General Disclaimer

One or more of the Following Statements may affect this Document

- This document has been reproduced from the best copy furnished by the organizational source. It is being released in the interest of making available as much information as possible.

- This document may contain data, which exceeds the sheet parameters. It was furnished in this condition by the organizational source and is the best copy available.

- This document may contain tone-on-tone or color graphs, charts and/or pictures, which have been reproduced in black and white.

- This document is paginated as submitted by the original source.

- Portions of this document are not fully legible due to the historical nature of some of the material. However, it is the best reproduction available from the original submission.

(NASA-CR-149101) THE DEEP SPACE NETWORK Progress Report, Jul. - Aug. 1976 (Jet Propulsion Lab.) 202 p HC A10/MF A01
CSCL 22D
N77-10091 THRU N77-10110
Unclas
G3/12 07281

NATIONAL AERONAUTICS AND SPACE ADMINISTRATION

The Deep Space Network
Progress Report 42-35

July and August 1976

JET PROPULSION LABORATORY
CALIFORNIA INSTITUTE OF TECHNOLOGY
PASADENA, CALIFORNIA

October 15, 1976

NATIONAL AERONAUTICS AND SPACE ADMINISTRATION

The Deep Space Network
Progress Report 42-35

July and August 1976

JET PROPULSION LABORATORY
CALIFORNIA INSTITUTE OF TECHNOLOGY
PASADENA, CALIFORNIA

October 15, 1976

Preface

Beginning with Volume XX, the Deep Space Network Progress Report changed from the Technical Report 32- series to the Progress Report 42- series. The volume number continues the sequence of the preceding issues. Thus, Progress Report 42-20 is the twentieth volume of the Deep Space Network series, and is an uninterrupted follow-on to Technical Report 32-1526, Volume XIX.

This report presents DSN progress in flight project support, tracking and data acquisition (TDA) research and technology, network engineering, hardware and software implementation, and operations. Each issue presents material in some, but not all, of the following categories in the order indicated.

Description of the DSN

Mission Support
- Ongoing Planetary/Interplanetary Flight Projects
- Advanced Flight Projects

Radio Science

Special Projects

Supporting Research and Technology
- Tracking and Ground-Based Navigation
- Communications—Spacecraft/Ground
- Station Control and Operations Technology
- Network Control and Data Processing

Network and Facility Engineering and Implementation
- Network
- Network Operations Control Center
- Ground Communications
- Deep Space Stations

Operations
- Network Operations
- Network Operations Control Center
- Ground Communications
- Deep Space Stations

Program Planning
- TDA Planning
- Quality Assurance

In each issue, the part entitled "Description of the DSN" describes the functions and facilities of the DSN and may report the current configuration of one of the five DSN systems (Tracking, Telemetry, Command, Monitor & Control, and Test & Training).

The work described in this report series is either performed or managed by the Tracking and Data Acquisition organization of JPL for NASA.

Contents

DESCRIPTION OF THE DSN

Network Functions and Facilities 1
N. A. Renzetti

MISSION SUPPORT

Ongoing Planetary/Interplanetary Flight Projects

DSN Mariner Jupiter-Saturn 1977 Prototype Radio Frequency Subsystem Compatibility Status and Test Report 4
A. I. Bryan and B. D. Madsen
NASA Code 311-03-23-10

Viking Mission Support 11
R. J. Amorose and D. W. Johnston
NASA Code 311-03-21-70

Pioneer Mission Support 20
T. P. Adamski
NASA Code 311-03-31-90

Helios Mission Support 24
P. S. Goodwin, W. G. Meeks, and R. E. Morris
NASA Code 311-03-21-50

SUPPORTING RESEARCH AND TECHNOLOGY

Station Control and Operations Technology

Hardware Additions to Microprocessor Architecture Aid Software Development 28
M. W. Sievers
NASA Code 310-30-68-09

512-Channel Correlator Controller 34
S. S. Brokl
NASA Code 310-30-69-10

Command Detector SNR Estimator and Lock Status Monitor Circuitry 42
R. F. Emerson
NASA Code 310-30-69-10

Three-Level Sampler Having Automated Thresholds 52
R. F. Jurgens
NASA Code 310-30-69-10

Network Control and Data Processing

An Algebraic Approach to Image De-smearing: Symmetries of Polynomials and Their Zeros 58
D. L. Johnson
NASA Code 310-40-70-02

NETWORK AND FACILITY ENGINEERING AND IMPLEMENTATION

Network

The Fast Decoding of Reed-Solomon Codes Using Number Theoretic Transforms 64
I. S. Reed and L. R. Welch
NASA Code 311-03-43-10

Deep Space Stations

LS 44—An Improved Deep Space Network Station Location Set for Viking Navigation 79
H. M. Koble, G. E. Pease, and K. W. Yip
NASA Code 311-03-42-54

High-Efficiency Solar Concentrator 99
F. L. Lansing and J. Dorman
NASA Code 311-03-41-08

A Two-Dimensional Finite-Difference Solution for the Transient Thermal Behavior of a Tubular Solar Collector 110
F. L. Lansing
NASA Code 311-03-41-08

Radio-Frequency Boresight Analysis of the Low-Cost 64-Meter Antenna 128
M. S. Katow
NASA Code 311-03-42-00

OPERATIONS

Network Operations

The Pioneer 11 1976 Solar Conjunction: A Unique Opportunity to Explore the Heliographic Latitudinal Variations of the Solar Corona . . 136
A. L. Berman, J. A. Wackley, S. T. Rockwell, and J. G. Yee
NASA Code 311-03-13-20

Viking 1 Planetary Phase Tracking Operations: Mars Orbit Insertion Through Landing 148
A. L. Berman and J. A. Wackley
NASA Code 311-03-13-20

PROGRAM PLANNING

TDA Planning

An Approach to Improve Management Visibility Within the Procurement and Financial Group at Goldstone 171
F. R. Maiocco and J. B. Rozek
NASA Code 311-03-32-10

A Technique for Generating Correlated X-Band Weather Degradation Statistics 180
E. C. Posner and F. J. Zeigler
NASA Code 311-03-31-30

Network Functions and Facilities

N. A. Renzetti
Office of Tracking and Data Acquisition

The objectives, functions, and organization of the Deep Space Network are summarized; deep space station, ground communication, and network operations control capabilities are described.

The Deep Space Network (DSN), established by the National Aeronautics and Space Administration (NASA) Office of Tracking and Data Acquisition under the system management and technical direction of the Jet Propulsion Laboratory (JPL), is designed for two-way communications with unmanned spacecraft traveling approximately 16,000 km (10,000 miles) from Earth to the farthest planets of our solar system. It has provided tracking and data acquisition support for the following NASA deep space exploration projects: Ranger, Surveyor, Mariner Venus 1962, Mariner Mars 1964, Mariner Venus 1967, Mariner Mars 1969, Mariner Mars 1971, and Mariner Venus Mercury 1973, for which JPL has been responsible for the project management, the development of the spacecraft, and the conduct of mission operations; Lunar Orbiter, for which the Langley Research Center carried out the project management, spacecraft development, and conduct of mission operations; Pioneer, for which Ames Research Center carried out the project management, spacecraft development, and conduct of mission operations; and Apollo, for which the Lyndon B. Johnson Space Center was the project center and the Deep Space Network supplemented the Manned Space Flight Network (MSFN), which was managed by the Goddard Space Flight Center (GSFC). It is providing tracking and data acquisition support for Helios, a joint U.S./West German project; and Viking, for which Langley Research Center provides the project management, the Lander spacecraft, and conducts mission operations, and for which JPL also provides the Orbiter spacecraft.

The Deep Space Network is one of two NASA networks. The other, the Spaceflight Tracking and Data Network, is under the system management and technical direction of the Goddard Space Flight Center. Its function is to support manned and unmanned Earth-orbiting satellites. The Deep Space Network supports lunar, planetary, and interplanetary flight projects.

From its inception, NASA has had the objective of conducting scientific investigations throughout the solar system. It was recognized that in order to meet this objective, significant supporting research and advanced technology development must be conducted in order to

provide deep space telecommunications for science data return in a cost effective manner. Therefore, the Network is continually evolved to keep pace with the state of the art of telecommunications and data handling. It was also recognized early that close coordination would be needed between the requirements of the flight projects for data return and the capabilities needed in the Network. This close collaboration was effected by the appointment of a Tracking and Data Systems Manager as part of the flight project team from the initiation of the project to the end of the mission. By this process, requirements were identified early enough to provide funding and implementation in time for use by the flight project in its flight phase.

As of July 1972, NASA undertook a change in the interface between the Network and the flight projects. Prior to that time, since 1 January 1964, in addition to consisting of the Deep Space Stations and the Ground Communications Facility, the Network had also included the mission control and computing facilities and provided the equipment in the mission support areas for the conduct of mission operations. The latter facilities were housed in a building at JPL known as the Space Flight Operations Facility (SFOF). The interface change was to accommodate a hardware interface between the support of the network operations control functions and those of the mission control and computing functions. This resulted in the flight projects assuming the cognizance of the large general-purpose digital computers which were used for both network processing and mission data processing. They also assumed cognizance of all of the equipment in the flight operations facility for display and communications necessary for the conduct of mission operations. The Network then undertook the development of hardware and computer software necessary to do its network operations control and monitor functions in separate computers. This activity has been known as the Network Control System Implementation Project. A characteristic of the new interface is that the Network provides direct data flow to and from the stations; namely, metric data, science and engineering telemetry, and such network monitor data as are useful to the flight project. This is done via appropriate ground communication equipment to mission operations centers, wherever they may be.

The principal deliverables to the users of the Network are carried out by data system configurations as follows:

- The DSN Tracking System generates radio metric data: i.e., angles, one- and two-way doppler and range, and transmits raw data to Mission Control.
- The DSN Telemetry System receives, decodes, records, and retransmits engineering and scientific data generated in the spacecraft to Mission Control.
- The DSN Command System accepts coded signals from Mission Control via the Ground Communications Facility and transmits them to the spacecraft in order to initiate spacecraft functions in flight.

The data system configurations supporting testing, training, and network operations control functions are as follows:

- The DSN Monitor and Control System instruments, transmits, records, and displays those parameters of the DSN necessary to verify configuration and validate the Network. It provides operational direction and configuration control of the Network, and provides primary interface with flight project Mission Control personnel.
- The DSN Test and Training System generates and controls simulated data to support development, test, training and fault isolation within the DSN. It participates in mission simulation with flight projects.

The capabilities needed to carry out the above functions have evolved in three technical areas:

(1) The Deep Space Stations, which are distributed around Earth and which, prior to 1964, formed part of the Deep Space Instrumentation Facility. The technology involved in equipping these stations is strongly related to the state of the art of telecommunications and flight-ground design considerations, and is almost completely multimission in character.

(2) The Ground Communications Facility provides the capability required for the transmission, reception, and monitoring of Earth-based, point-to-point communications between the stations and the Network Operations Control Center at JPL, Pasadena, and to the mission operations centers, wherever they may be. Four communications disciplines are provided: teletype, voice, high-speed, and wideband. The Ground Communications Facility uses the capabilities provided by common carriers throughout the world, engineered into an integrated system by Goddard Space Flight Center, and controlled from the communications Center located in the Space Flight Operations Facility (Building 230) at JPL.

(3) The Network Operations Control Center is the functional entity for centralized operational control of the Network and interfaces with the users. It has two separable functional elements; namely, Network Operations Control and Network Data Processing. The functions of the Network Operations Control are:

- Control and coordination of Network support to meet commitments to Network users.
- Utilization of the Network data processing computing capability to generate all standards and limits required for Network operations.
- Utilization of Network data processing computing capability to analyze and validate the performance of all Network systems.

The personnel who carry out the above functions are located in the Space Flight Operations Facility, where mission operations functions are carried out by certain flight projects. Network personnel are directed by an Operations Control Chief.

The functions of the Network Data Processing are:

- Processing of data used by Network Operations Control for control and analysis of the Network.
- Display in the Network Operations Control Area of data processed in the Network Data Processing Area.
- Interface with communications circuits for input to and output from the Network Data Processing Area.
- Data logging and production of the intermediate data records.

The personnel who carry out these functions are located approximately 200 meters from the Space Flight Operations Facility. The equipment consists of minicomputers for real-time data system monitoring, two XDS Sigma 5s, display, magnetic tape recorders, and appropriate interface equipment with the ground data communications.

DSN Mariner Jupiter-Saturn 1977 Prototype Radio Frequency Subsystem Compatibility Status and Test Report

A. I. Bryan
TDA Engineering Office

B. D. Madsen
Spacecraft Telecommunications Systems Section

The DSN Mariner Jupiter-Saturn 1977 prototype Radio Frequency Subsystem compatibility tests were the first hardware and software interface tests conducted between the DSN and the Project. These tests were conducted during May 24-27 1976 using the Compatibility Test Area for the DSN and the Telecommunications Development Laboratory for the prototype subsystem. This report describes these initial compatibility tests and reports the test results.

I. Introduction

The purpose of this report is to provide an assessment and status of telecommunications compatibility between the Radio Frequency Subsystem on the Mariner Jupiter-Saturn spacecraft and the Deep Space Network. This assessment and status is derived from test results obtained between the network, as represented in the Compatibility Test Area, and the subsystem located in the Telemetry Development Laboratory.

II. Test Objectives

The objectives of the tests with the radio frequency subsystem were to:

(1) Verify the capability of the network to receive S-band and X-band signals without degradation of receiver thresholds.

(2) Verify the capability to receive signals from the network without degradation of the subsystem receiver threshold.

(3) Determine the maximum network transmitter static offsets and the maximum-minimum network transmitter sweep rates for reliable subsystem acquisition.

(4) Determine the maximum network transmitter sweep rates for reliable subsystem tracking.

(5) Verify the capability of the network to receive and process uncoded high-rate telemetry without degradation.

(6) Verify the capability of the network to calibrate the subsystem group delays at S- and X-band with zero-delay devices.

III. Test Conditions

The radio frequency subsystem was configured for Receiver 2, Exciter 2, TWT 2, and high-gain antenna for both S- and X-band. A calibrated low-loss coaxial cable S-band link and an elliptical waveguide X-band link of approximately 113 m (370 ft) were used between the Telecommunications Development Laboratory and the Compatibility Test Area.

The ground station software consisted of uncoded telemetry and command processor test software and the planetary ranging assembly operational software.

IV. Test Results

The detailed test results are shown in Table 1 and a definition of terms in Table 2. Significant events and/or other items are noted in the following sections.

A. Radio Frequency Acquisition and Tracking Tests

1. Downlink threshold two-way X-band. The threshold was difficult to measure and was degraded two dB from the one-way measured threshold. This was due to X-band two-way phase jitter, a known problem.

2. X-band two-way residual phase jitter. Residual phase jitter could not be measured due to installation of new minicomputers being carried out at the Compatibility Test Area.

3. Sweep acquisition test. The radio frequency subsystem will acquire at -135 dBm with a rate of -200 Hz/s, but will not acquire at -135 dBm with a positive sweep rate greater than $+100$ Hz/s.

4. Tracking rate test. At high sweep rates (greater than 400 Hz/s), the radio frequency subsystem automatic gain control drops out and causes the transponder to switch to the auxiliary oscillator even though the voltage controlled oscillator remains in lock and continues to track the uplink. It appears to be an automatic gain control detector bandwidth problem.

5. Downlink Radio Frequency Spectrum Test. This test was not performed due to the lack of travelling wave tubes on the spacecraft.

B. Command Tests

No command tests were performed because of unavailability of both network and flight project subsystem equipment.

C. Telemetry Tests

1. Telemetry Processing Verification. This test was performed to the symbol signal-to-noise-ratio verification level using the telemetry command processor assembly. The bit error rate test was not performed due to a lack of hardware/software. This capability was not committed by the network for this subsystem test.

2. Telemetry Performance Test. The X-band Y-factor could not be measured due to low output level from the Block IV Receiver. Performance was verified by calculating received E_b/N_0 directly from unmodulated receiver power measurement to within $\pm$ 1 dB.

V. Future Activities

Additional compatibility tests will be performed on the proof test model, Flight 1 and Flight 2 spacecraft in the Spacecraft Assembly Facility at JPL during Thermal-Vac testing, and in the Spacecraft Assembly and Encapsulation Facility at the Kennedy Space Center, Cape Canaveral, Florida.

The problem of measurement of the X-band Y-factor at the Compatibility Test Area is in the process of being resolved by a modification. DSN engineering level software for Mariner Jupiter-Saturn will be available to support the prototype spacecraft testing now scheduled for the period of 11 October through 1 November, 1976.

Test software being developed for DSN telemetry tests requires a 2047-bit PN code sequence for bit error rate tests. At the present time, the modulation-demodulation subsystem support equipment does not provide the required code and has no provision for external code input. The possibility of providing either the correct code or an external code input port in the modulation-demodulation subsystem support equipment is being investigated.

VI. Assessment

These radio frequency subsystem tests did not indicate any design interface performance problems between the DSN radio frequency subsystems and those on the spacecraft.

The failure of the radio frequency subsystems to meet the pull-in range and acquisition parameters specified in the design requirements does not constitute an incompatibility with the DSN. These parameters determine the DSN acquisition rates and offsets which are controlled by operating procedures. The out-of-spec condition may be corrected by design change or by specification change with appropriate operational acquisition rate and offset limits.

Acknowledgment

The author wishes to thank the following members of the CTA 21 management and staff for their contribution to the successful completion of this series of DSN-MJS'77 Compatibility Tests: A. Salazar, R. Santiago, and L. Landers.

Test date	Test title	Deep Space Network						
		RCV	EXC	RNG Mod	CMD Mod	Uplink doppler	Uplink offset	CMA SUBC offset
5-24-76	Downlink threshold 1-way, S-band	BLK III	NA	Off	Off	NA	NA	NA
	Downlink threshold 1-way, X-band	BLK IV	NA	Off	Off	NA	NA	NA
	Downlink threshold 2-way, S-band	BLK III	BLK IV	Off	Off	0	0	NA
	Downlink threshold 2-way, X-band	BLK IV	BLK IV	Off	Off	0	0	NA
	Uplink threshold	NA	BLK IV	Off	Off	0	0	NA
	Receiver acquisition static offset	NA	BLK IV	Off	Off	0	±1200 Hz	NA
	Receiver acquisition	NA	BLK IV	Off	Off	±200 Hz/s	0	NA
	Receiver tracking	NA	BLK IV	Off	Off	100 Hz/s	±72.5 kHz	NA
	Spacecraft transmitter phase jitter, S-band	BLK III 1 & 2	BLK IV	Off	Off	0	0	NA
	Telemetry performance verification, X-band	BLK IV	BLK IV	Off	Off	0	0	NA
	Ranging delay performance	BLK IV	BLK IV	On	Off	0	0	NA
5-27-76	Ranging delay calibration	BLK IV	BLK IV	On	Off	0	0	NA

Table 1. DSN/MJS'77 prototype Radio Frequency Subsystem telecommunications compatibility test

Spacecraft									Test data	
TLM SUBC offset	EXC	RCV	Power	ANT	TWT	RNG	TMU	CDU	Performance	Criteria
NA	2S	2	NA	HGA	2S	Off	NA	NA	−159.5 dBm	−159.5 ± 0.5
NA	2X	2	NA	HGA	2X	Off	NA	NA	−153.0 dBm	−153.0 ± 0.5
NA	2S	2-100 dBm	NA	HGA	2S	Off	NA	NA	−159.5 dBm	−159.5 ± 0.5
NA	2X	2-100 dBm	NA	HGA	2X	Off	NA	NA	−151 (with difficulty)	−153.0 ± 0.5
NA	NA	2	NA	HGA	NA	Off	NA	NA	−151.5	−151.0 ± 0.5
NA	NA	2-130 dBm	NA	HGA	NA	Off	NA	NA	Frequency pushing	Acquisition at ± 2000 Hz
NA	NA	2-135 dBm	NA	HGA	NA	Off	NA	NA	+ 200 Hz/s, No acq −200 Hz/s, acq	Acquisition
NA	NA	2-110 dBm	NA	HGA	NA	Off	NA	NA	DPE = 6 deg	DPE ≤ 10 deg
NA	2S	2	NA	HGA	2S	Off	NA	NA	1.62 deg RMS	2.3 deg RMS
0	2X	2-100 dBm	NA	HGA	2X	Off	TLM SIM	NA	SER = 1.28×10^{-2} SSNR = 3.7 dB	SER = $1.5 \pm .5 \times 10^{-2}$
NA	2S 2X	2-100 dBm	NA	HGA	2S 2X	On	NA	NA	X zero delay S zero delay S range X range DRVID	X zero delay S zero delay S range X range DRVID
NA	2S 2X	2-100 dBm	NA	HGA	2S 2X	On	NA	NA	S = 657.9 ns X = 649.7 ns	<1000 ns <1000 ns

Table 2. Definitions of terms used in Table 1

ANT	Spacecraft antenna
Bit rate	Clock frequency of the telemetry bit information
BLK III exciter	The DSN S-band exciter equipment
BLK III receiver	The DSN S-band receiving equipment
BLK IV exciter	The DSN S-band exciter equipment
BLK IV receiver	The DSN S/X-band receiving equipment
CAR SUP	Downlink carrier suppression due to telemetry modulation
CDU	Command demodulation unit
CMA SUBC offset	Command modulation assembly subcarrier frequency offset relative to nominal
CMD MOD	Command processor assembly command modulation
EXC	Spacecraft S-band exciter equipment
HGA	High-gain antenna
LGA	Low-gain antenna
MGA	Medium-gain antenna
RNG MOD	Planetary ranging assembly modulation
PWR	Spacecraft transmitter power mode
RCV	Spacecraft S-band receiving equipment
RFS	Radio Frequency Subsystem
RNG	Spacecraft ranging channel
SDA SUBC offset	Subcarrier demodulator assembly subcarrier frequency offset relative to nominal
TLM SUBC offset	Subcarrier demodulator assembly frequency offset relative to nominal
TMU	Telemetry modulation unit
TWT	Traveling wave tube amplifier
UNC	Uncoded
Uplink doppler	Ramp rate of the uplink carrier frequency
Uplink offset	Uplink carrier frequency offset relative to the spacecraft receiver rest frequency

Viking Mission Support

R. J. Amorose and D. W. Johnston
DSN Network Operations Section

This report summarizes Deep Space Network support for the two Viking Missions to Mars and includes the Mars orbit insertions of Vikings 1 and 2 and the landing of Viking 1. Special procedures were employed during these critical events to minimize interruptions to the telemetry data return due to spacecraft data mode and attitude changes.

I. DSN Mission Operations and Status

A. Viking Operations Activities

The significant Viking 1 Planetary and Viking 2 Cruise activities supported by the DSN during this reporting period are listed in Table 1. Included in this support was the final Operational Readiness Test (ORT-3) prior to Mars Orbit Insertion (MOI) of Viking 1.

The Approach Midcourse Maneuver (AMC) of Viking 1 was performed in two steps due to a spacecraft pressurant leak problem. The original AMC was delayed one day to June 10 with a second AMC performed on June 15. DSS 63 (Madrid) successfully supported both AMC-1 and -2.

The Viking 1 MOI was successfully supported on June 19 by Goldstone, DSS 14 with DSS 11 as backup. A Mars Orbit Trim maneuver was performed on June 21 over DSS 63, which put the Viking 1 Orbiter in the proper orbit over the prime landing site. The first site certification pictures were taken on June 22, and for the next several weeks high-rate telemetry data were received periodically by the 64-meter subnet in support of this activity. The Viking 1 landing was delayed from the scheduled July 4 date to July 20, due to landing site requirements necessitating additional trim maneuvers and additional site certification photos. The successful landing was supported by DSS 63 with the initial surface pictures played back via the orbiter relay link to DSS 63 shortly after touchdown. On July 21, the daily direct link tracks of the Viking 1 lander started with DSS 43 (Australia) supporting through July 26. Then DSS 63 began a 10-day period of direct link lander support. In the mean time, Viking 2 approach science data were being gathered and the Approach Midcourse Maneuver was supported by DSS 43 on July 27.

B. DSS Support

The tracking hours per station of the Viking spacecraft and the number of commands transmitted from each station during this reporting period are listed in Table 2.

C. Intermediate Data Record Status

The Intermediate Data Records (IDRs) are generated by merging telemetry data received in real time and telemetry data recalled post pass from the Deep Space Stations. These data are then merged in the Network Data Processing Terminal, and the resultant IDR is then delivered to the Viking Project. During this reporting period the Deep Space Network Data Record capability provided the Viking Project Data Support Group with 177 telemetry Intermediate Data Records. The average delivery time for the 177 IDRs was 16 hours after the loss of signal at the end of a scheduled track. This average delivery time is within the 24-hour delivery commitment.

II. Special Planetary Procedures

In order to maximize the quantity of telemetry data that could be delivered to the Viking Project, under adverse conditions such as orbital maneuvers that required special spacecraft orientation, a special telemetry procedure was developed and used on both Viking 1 and 2 Mars Orbit Insertions. This special procedure insures that the orbiter engineering data are not interrupted when the orbiter spacecraft telemetry mode is switched from dual to single or single to dual subcarriers. When the spacecraft telemetry mode is switched, there is a power exchange that takes place between the subcarriers, and it is this telemetry power increase or decrease which must be controlled via the input attenuators on the subcarrier demodulators.

To verify the special procedure, a test was performed at the JPL Compatibility Test Area (CTA 21) and the following results were obtained:

(1) Telemetry data bit sync loop would lose lock when the spacecraft mode was switched from single to dual subcarriers or from dual to single subcarrier and the subcarrier demodulator input attenuator was reset in the usual manner.

(2) The telemetry data bit sync loop would remain in lock, if the subcarrier demodulator input attenuation was reset prior to mode change and the reset rate was 2 dB per second or less.

A special procedure based on these results was used successfully to enhance telemetry data return during Viking propulsive and non-propulsive maneuvers.

A backup Canopus loss contingency plan to supplement the standard star procedure was made available for Viking 1 and 2 Mars Orbit Insertions. The backup Canopus loss contingency plan could provide fast and accurate spacecraft orientation data in the event of loss of Canopus lock during the critical Mars Orbit Insertion phase of the mission. Although the procedure was available, it was not utilized except for verification of X-band in and out of lock times, since both spacecraft performed in a nominal manner.

A special procedure was developed and implemented to optimize data return when it became necessary to accomplish station transfers (1) during or near orbiter spacecraft periapsis, (2) under low signal conditions, or (3) because of a maneuver configuration of the spacecraft when accommodating special Mars surface photo mapping.

In order to maintain downlink receiver lock and minimize data degradation it was necessary to reduce the uplink tuning rates and optimize downlink receiver loop bandwidths. The uplink tuning rate and downlink receiver bandwidths used had to be adjusted for a number of receiver loop signal-to-noise ratios. This was accomplished by providing a table of uplink tuning rates and bandwidth combinations that could be used within specified signal level ranges.

The optimum tuning rate is available from Table 3. Depending on signal level and priority of S-band or X-band data, the optimum exciter tuning rate for maximum data return under adverse conditions could be selected.

A special modified code 1 configuration (Fig. 1) was used successfully for Mars Orbit Insertion of Viking Orbiters 1 and 2. This configuration provided complete telemetry data redundancy plus backup during the critical phase of Mars Orbit Insertion.

The modified code-1 configuration provides two independent processing streams of data being output via two (independently routed where possible) high-speed data lines. This parallel data processing concept is carried through all of the various ground data system interfaces to minimize the risk of data loss due to single-point failures.

III. DSN Support of Viking 1

A. Preseparation Checkout

DSN support of activities associated with the landing of Viking Lander 1 began on July 18, 1976 with DSS 63 supporting the separation minus 39-hour command update. The prime purpose of this command load was to prepare the mated lander for the preseparation checkout. DSS 63 was configured to code 15, the standard Orbiter-

Orbiter configuration with one Command Modulator Assembly initialized for Orbiter 1 and the other initialized for Lander 1 and mated lander commanding. The command load was successfully transmitted without incident.

The preseparation checkout occurred over DSS 43 on UTC day 201, July 19, 1976. A unique telemetry configuration was utilized during this pass in order to provide the Project with redundant data streams. During the major portion of preseparation checkout, the data rates were 1000 and 2000 bits per second. Redundant data streams were provided for these bit rates by specifying configuration code 24. This code provided two high-rate science data streams with channel 2 of Telemetry and Command Processor Alpha outputting data for the high-speed data line, and Telemetry and Command Processor Beta using channel 3 and outputting data to the wideband data line. This configuration provided dual processing channels at the station and also provided dual transmission paths to the Mission Control and Computing Center.

Following the completion of the 1000- and 2000-bit per second data, the spacecraft data rate changed to 4000 bits per second. At this data rate, channel 2 of the alpha string could no longer be used, as the rate exceeded the processing capability for this channel. At that time channel 2 of the alpha string was disabled and channel 3 enabled to provide redundant processing channels at the station with both data streams being transmitted via the wideband data line.

The non-conjoint 26-meter stations, DSS 62 (Madrid) and DSS 44 (Australia), provided backup command capability during the preseparation phase. Figure 2 shows the code 24 configuration used by DSS 43 for preseparation checkout.

B. Separation, Descent, and Landing

This phase of the landing activity was divided into two major events. The first event was the transmission of the separation "GO" command followed by the second event of separation, descent, and landing.

The telemetry configuration used by DSS 43 on the previous day for preseparation checkout (code 24) was used again for this pass.

Due to the importance of the "GO" command, special precautions were taken to insure that the command would be successfully transmitted. DSS 43 configured the two Command Modulator Assemblies for mated lander commanding. The two Telemetry and Command Processor command stacks were then loaded with "GO" commands. The prime Telemetry and Command Processor contained timed commands to be transmitted at separation minus 45 minutes while the backup Telemetry and Command Processor contained the identical commands, but untimed. The backup processor was to be used in the event problems developed in the prime string.

In addition to the commands loaded into the processor stacks, duplicate commands were also loaded into the manual buffer of each processor. These commands were to be transmitted if problems developed which would prevent transmission of the commands residing in the command stack.

A backup command capability was also provided by DSS 44. At this station the "GO" commands were loaded into the stack and manual buffer in the same way commands had been loaded in the backup string at DSS 43.

DSS 44 was to have been used following a failure at DSS 43. The exciter frequency at DSS 44 was chosen so that in the event of a transmitter or antenna failure at DSS 43 it would have only been necessary to turn on the transmitter at DSS 44 and tune to a new reference frequency, thus capturing the spacecraft receiver as it drifted towards its rest frequency. Command transmission could then be continued with only a slight delay.

The "GO" command was successfully transmitted by DSS 43 on July 20, 1976 using the prime transmission path.

The telemetry configuration chosen for support of separation, descent, and touchdown events was the standard two-orbiter configuration (code 15). In this configuration, both Telemetry and Command Processor strings were initialized for Orbiter 1, giving two redundant processing channels for engineering and science data. Since no commanding was anticipated during the descent phase, no special configurations or procedures were required. DSS 63 was the prime station for support of separation, descent, and touchdown.

A special procedure was used during the descent phase for telemetry processing at DSS 63. As the spacecraft began its descent and passed through the atmosphere of Mars, the 4000-bit per second data were transmitted in bursts of short duration. Between these data bursts were blocks of invalid data. In order to insure each of the 4000-bit per second bursts were processed at the station, the stations were instructed to initialize the two high-rate processing channels at the beginning of the burst data and

to remain initialized even though the data appeared as noise between bursts. Testing during compatibility tests and during operational tests both prior to launch and during cruise had proven this to be a feasible plan.

The separation, descent, and touchdown events were supported flawlessly.

C. Initial Lander S-Band Direct Link Support

The first Lander direct link took place during the DSS 43 view period on July 21, 1976. The Lander had landed in the Martian evening, and the direct link took place approximately 18 hours later during the Martian morning.

For the Lander direct link support a special telemetry and command configuration had been devised. This code 61 configuration provided for redundant Lander telemetry processing channels. Redundant command capability was provided by the use of two separate high-speed data lines connected to separate Command Modulator Assemblies. The code 61 configuration is shown in Fig. 3. The figure shows prime Lander engineering and science data provided by Telemetry and Command Processor 2, channels 1 and 2.

Backup processing was provided by Telemetry and Command Processor 2, channel 3, and Telemetry and Command Processor 1, channel 2. From this configuration, Lander data were supplied via three different transmission paths over high-speed data lines 1 and 2 and the wideband data line. The configuration minimized the possibility that a single-point failure would cause a loss of data.

Lander direct link support began with the beginning of the uplink acquisition sweep. A transmitter power output level of 20 kilowatts was used. The sweep was designed to take into account the uncertainties of the Lander best lock receiver frequencies and widened to insure the acquisition of both lander receivers. A total frequency range at S-band of 135648 hertz was swept at a rate of 43.2 hertz per second. The duration of the sweep lasted 52.2 minutes. Table 4 shows the uplink/downlink sweep, and ranging parameters used during the first direct link. Since the spacecraft transmitter was not turned on until the uplink acquisition sweep had been completed, the sweep was completed in the blind without benefit of downlink lock.

Command modulation was then turned on, but commanding was delayed until the results of the commands could be verified by the downlink telemetry. Commands were selected which would not alter any spacecraft parameter but which would allow the Lander Team to verify command capability.

At approximately 2 hours and 10 minutes following the start of the uplink acquisition sweep, DSS 43 obtained lock on the downlink. A special downlink acquisition sweep for the Block IV receiver had been devised which would guarantee lock in either the one-way or two-way tracking mode. The sweep covers a range of 105,600 hertz at S-band and was swept at a rate of 4800 hertz per second. Lock was obtained on the Block IV receiver in the two-way tracking mode. Following downlink acquisition it was discovered that uplink lock on spacecraft receiver 1 had not been attained. Several minutes following downlink lock, receiver 1 was observed to go into lock. The commands sent earlier were observed to be received and processed by both spacecraft receivers through monitoring of the command segment count. Ranging data were successfully obtained during the last 10 minutes of the downlink pass. At approximately 1 hour after the downlink acquisition took place, loss of lock was observed. No anomalies, except the initial failure to lock spacecraft receiver 1, occurred during the first direct link.

Table 1. Viking operations activities

Date	Spacecraft	Activity
June 1–2	Viking 1	8 kbps playback
June 2–3	Viking 1	Operational Readiness Test (ORT-3) for Mars Orbital Insertion (MOI)
June 3–6	Orbiter 1	Optical Navigation Sequences (ONS)
June 4	Lander 2	Initial Computer Load (ICL) update
June 10	Viking 1	Approach Midcourse Maneuver (AMC) scheduled for June 9 postponed until June 10
June 10, 11, 13	Orbiter 1	ONS
June 10	Lander 2	ICL update
June 10–13	Lander 2	Battery Conditioning Sequence
June 14	Orbiter 1	Visual Imaging Subsystem (VIS) and Infra Red Thermal Mapper (IRTM) alignment test playback
June 15	Viking 1	AMC 2. This maneuver was required because of the continued gas regulator leakage problem
June 16	Viking 1	Start of Viking 1 approach science
June 19	Viking 1	MOI
June 21	Viking 1	Mars Orbit Trim maneuver 1
June 21	Viking 1	Started Viking 1 site certification sequence
July 8	Orbiter 1	Mars Orbit Trim maneuver 5
July 9–15	Orbiter 1	Site certification photo sequence
July 13	Orbiter 1	Mars Orbit Trim 6
July 15	Orbiter 2	Optical Navigation Sequence 2
July 18–19	Lander 1	Pre-separation checkout
July 18	Viking 2	Completed Viking 2 Optical Navigation Sequence 2
July 20	Lander 1	Touchdown and start of landed operations
July 22	Viking 2	Start Viking 2 ONS
July 24	Viking 2	ONS
July 27	Viking 2	Viking 2 Approach Maneuver performed
July 28	Viking 2	Optical Navigation Sequence 4

Table 2. DSS support

Month	DSS	Number of passes	Hours tracked	Commands transmitted
June	11	25	194.24	413
	12	15	103	0
	14	18	165.52	504
	42	22	167.36	15
	43	28	220.53	3410
	44	11	89.56	43
	61	25	232.05	399
	62	9	93.11	32
	63	29	320.43	619
June total		182	1585.80	5435
July	11	29	239.10	358
	12	7	52.27	216
	14	40	336.03	1827
	42	26	205.29	183
	43	49	349.03	1641
	44	11	76.28	0
	61	26	260.20	1354
	62	7	58.53	92
	63	43	362.14	2276
July total		238	1938.87	7947
Report total		420	3524.67	13382

Table 3. Recommended uplink tuning rates

Downlink signal level, dBm	10-Hz bandwidth		30-Hz bandwidth	
	S-band tuning rate, Hz/s	X-band tuning rate, Hz/s	S-band tuning rate, Hz/s	X-band tuning rate, Hz/s
138 to −143	1.50	0.41	10.90	3.00
−143 to −148	1.25	0.34	9.10	2.50
−148 to −153	0.75	0.20	6.30	1.73
−153 to −158	0.50	0.14	1.50	0.40
−158 to −160	0.30	0.08	0.38	0.10
−160 to −163	0.19	0.05	—	—
−163 to −165	0.06	0.016	—	—

Table 4. Lander 1 initial acquisition: DSS 43, SOL 1

Uplink Acquisition Sweep	
Transmitter on	05:10:00 UTC
Transmitter power	20 kW
Frequency	44022494.0 Hz
Start tuning (Time 0)	05:10:40 UTC
Tune to	44020604.0 Hz
Tuning rate (rate 0)	−0.9000 Hz/s
Time (time 1)	05:45:40 UTC
Tune to TSF	44021540.0 Hz
Tuning rate (rate 1)	+0.9000 Hz/s
Stop tuning (time 2)	06:03:00 UTC
Command modulation on	06:03:29 UTC
Range modulation on	07:20:20 UTC
Sweep duration	52 min 20 s
Downlink Acquisition Sweep	
Start sweep	07:10:00 UTC
Sweep upper limit	44753046.55 Hz
Sweep lower limit	44751846.55 Hz
Sweep rate	100 Hz/s
Ranging Parameters	
Enter acquisition directive	07:20:40 UTC
T1	38 s
T2	9 s
T3	0 s
Round trip light time	38 min 5 s
Components	15

Notes: a. Receiver VCO = 23.8625 MHz. Bias receiver frequencies according to actual measurements.

b. Receiver to be swept in acquisition mode with ATZ (acquisition trigger at zero-beat) enabled.

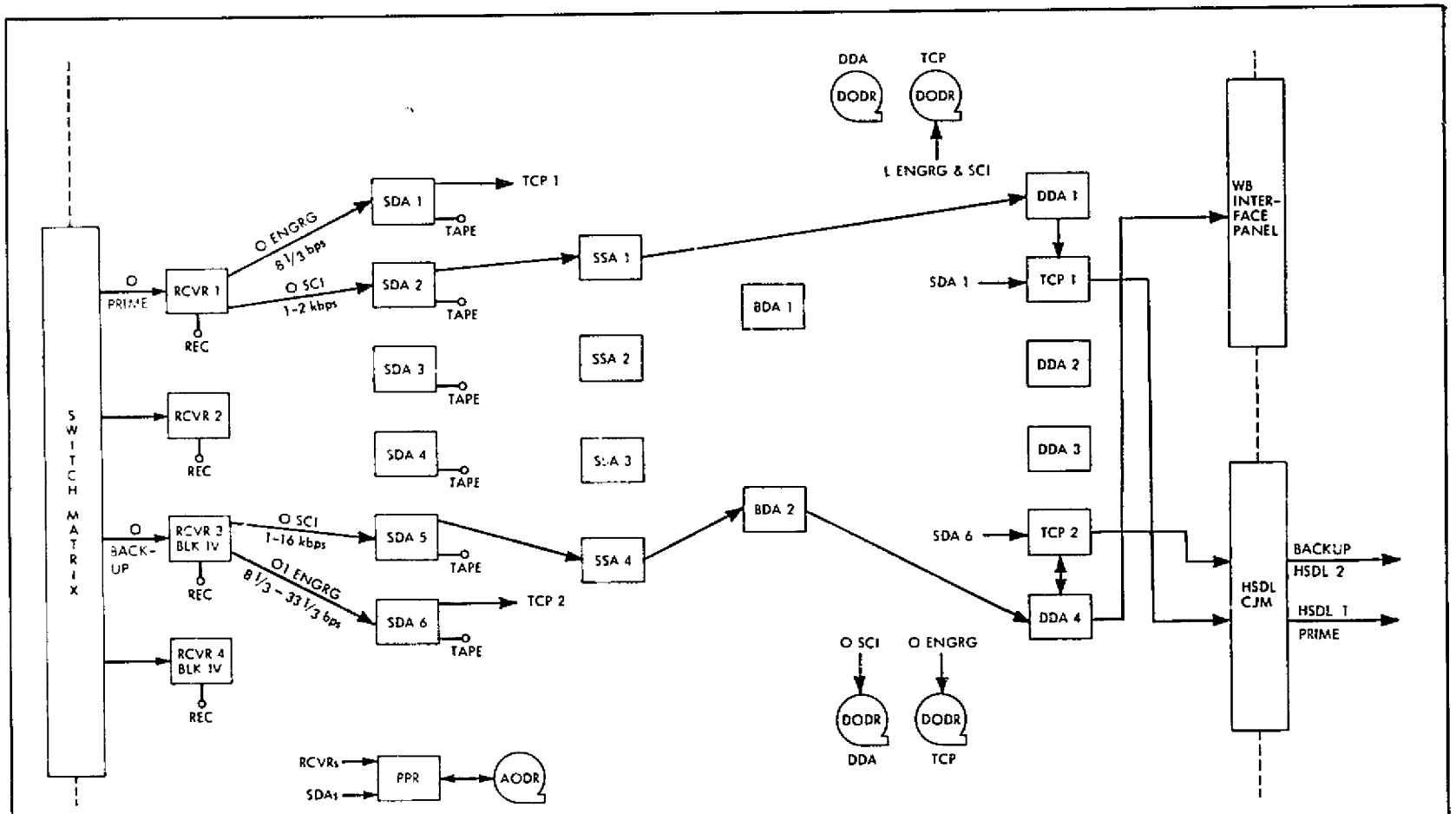

Code	Spacecraft	Receiver	Data Type	SDA	SSA	BDA	DDA	TCP
1 Modified	Orbiter Prime	1	Engrg	1	0	0	0	1
			Sci	2	1	0	1	
	Orbiter Backup	3	Sci	5	4	2	4	2
			Engrg	6	0	0	0	

Fig. 1. Modified planetary configuration, Orbiter–Orbiter—code 1

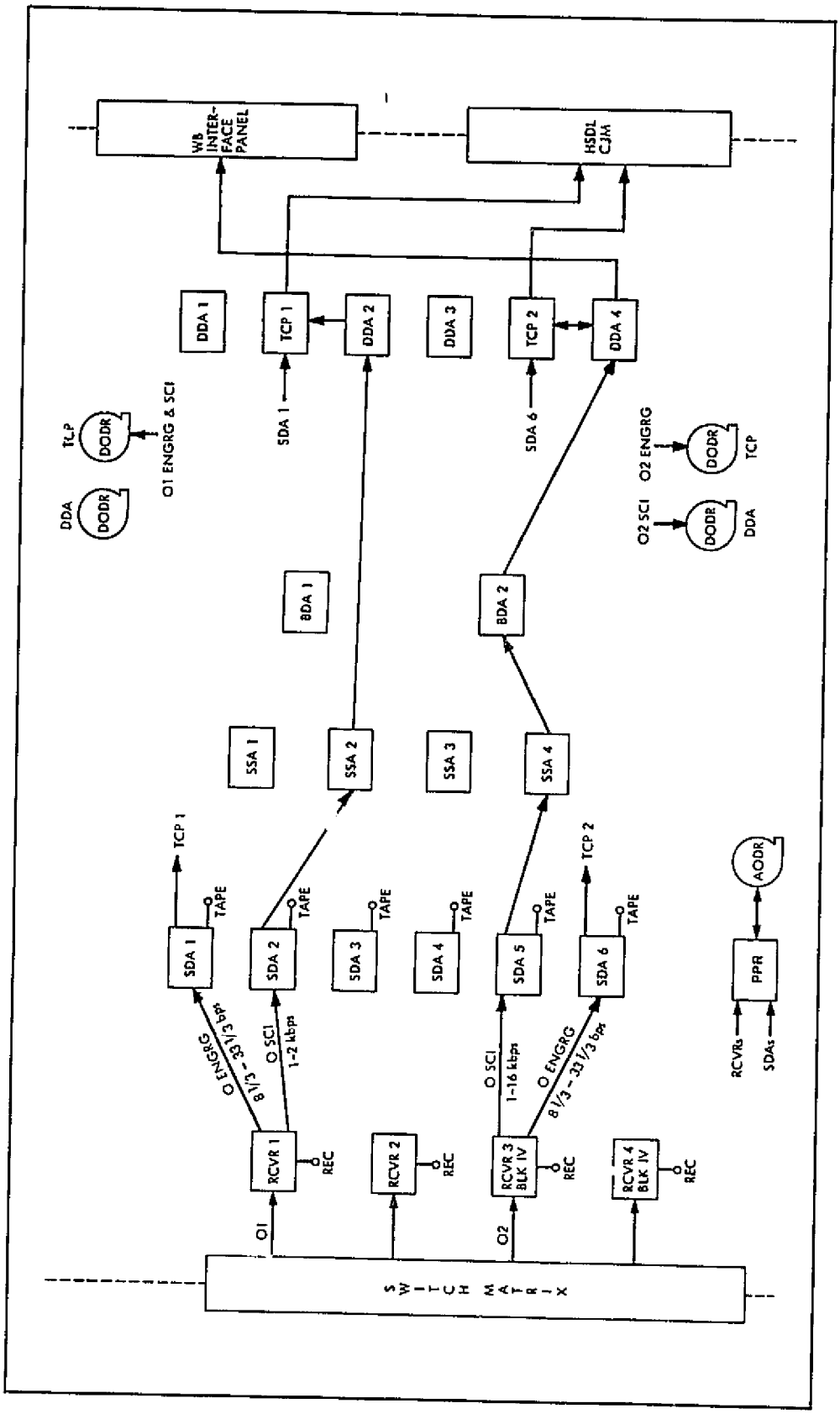

Fig. 2. Orbiter–Orbiter—code 24

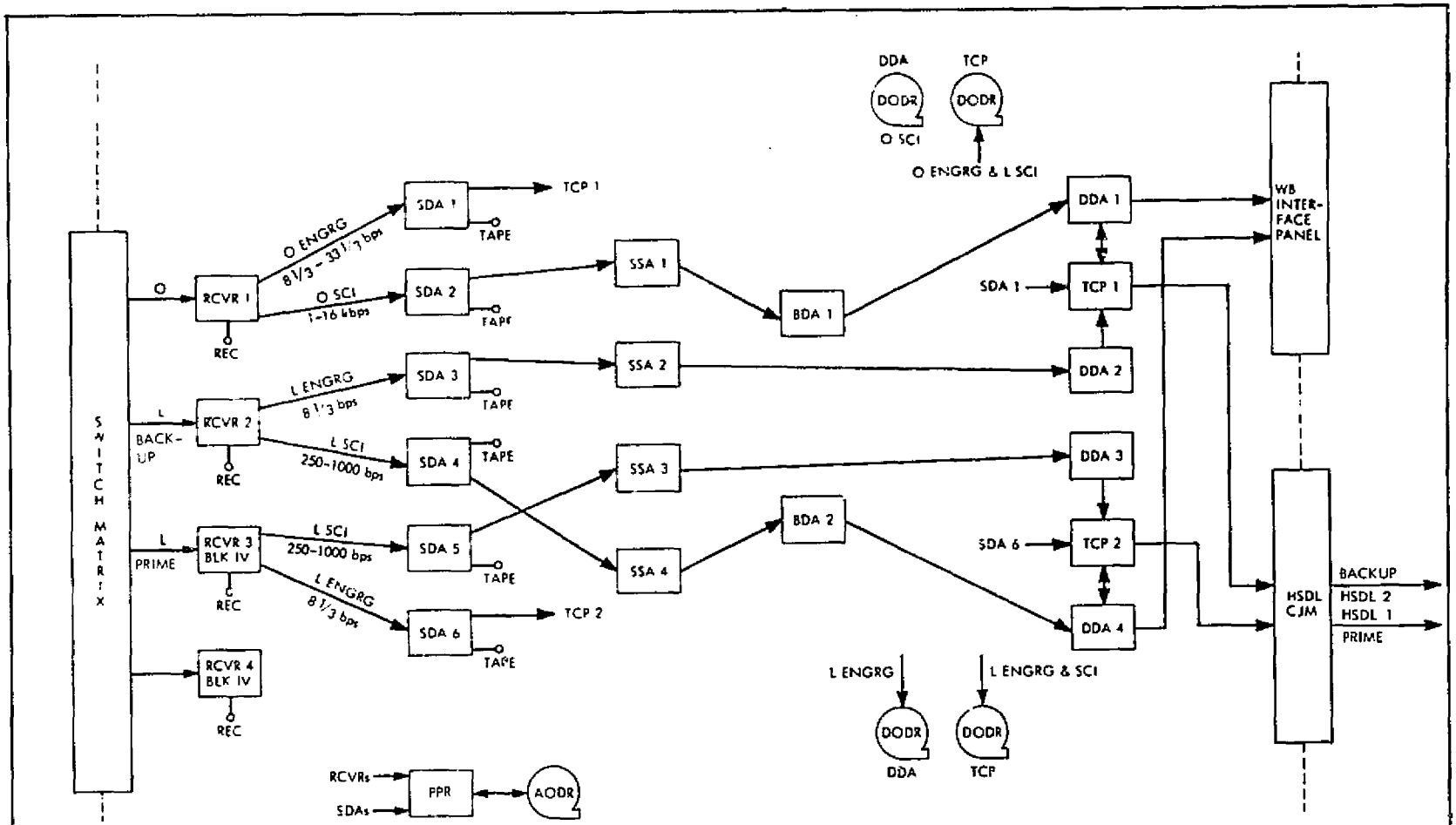

Code	Spacecraft	Receiver	Data Type	SDA	SSA	BDA	DDA	TCP
61	Orbiter	1	Engrg	1	0	0	0	1
			Sci	2	1	1	1	
	Backup Lander	2	Engrg	3	2	0	2	
			Sci	4	4	2	4	2
	Prime Lander	3	Sci	5	3	0	3	
			Engrg	6	0	0	0	

Fig. 3. Standard planetary configuration, Orbiter–Orbiter–Lander—code 61

Pioneer Mission Support

T. P. Adamski
Deep Space Network Operations

Status of the current Pioneer missions and initial operations planning for the Pioneer Venus Mission is given.

I. Pioneers 6, 7, 8, and 9

None of these spacecraft has been tracked during the last six months. Coverage is expected to continue at an extremely low level of support, although some tracking of Pioneers 6 and 9 will occur in October and November in support of radial alignments with the Helios spacecraft. The status of the spacecraft when each was last tracked was as follows:

All Pioneer 6 spacecraft systems were operating normally except for the failure of receiver 2 (which has restricted uplink to the low-gain antenna only), degradation of the solar array output and attitude-control sun sensors due to ultraviolet (UV) radiation and particulate impacts, and depletion of the attitude control gas supply. All instruments were also operating normally, except for the magnetometer and the radio propagation experiment. The magnetometer had failed in 1971, and the propagation instrument had been powered down due to the decommissioning of the experimenter's transmitting antenna at Stanford University.

Pioneer 7 was operating at reduced power due to severe degradation of the solar array. Transmitter (TWT) 1 and the roll index sun sensor were nonoperational and the performance of the attitude-control sun sensors was degraded. All other spacecraft systems were operational. The power limitation primarily affects the instruments, all of which are powered down. Only the plasma analyzer will be turned on when the spacecraft is next tracked.

Pioneer 8 was operating normally except for some degradation in solar array output and degradation in performance of the attitude-control sun sensors. Except for the cosmic dust and cosmic ray detectors, all instruments were operational. Although no data are being returned from the radio propagation experiment, the instrument remains on so that it may provide power to the electric field detector.

All Pioneer 9 spacecraft systems and instruments were operating normally except for one failed command decoder address and the lack of data from the radio propagation experiment, as described above for Pioneer 8.

II. Pioneers 10 and 11

A. Mission Status and Operations

Both spacecraft continue to operate normally except for some degradation in the performance of the Pioneer 10

star sensor and the failure of the Pioneer 11 spin-down thruster. The majority of instruments on board Pioneer 10 are operating normally, exceptions being the asteroid/meteoroid detector (powered down), the cosmic ray telescope (some radiation damage experienced at Jovian encounter), the infrared radiometer (powered down, no data in cruise phase), and the magnetometer (failed in November of 1975). Approximately half of the cells of the meteoroid detector have been punctured to date. The majority of the Pioneer 11 instruments are also operating normally. Exceptions are the asteroid/meteoroid detector (powered down in June of 1975 as the suspected cause of uncommanded spacecraft status changes), the imaging photopolarimeter (has some stepping problems at cone angles greater than 150 deg, but can be compensated for), the infrared radiometer (activated only once every eight months for checkout), the flux gate magnetometer (activated only once every two months for checkout) and the plasma analyzer (no output since April of 1975).

Tracking support of these spacecraft has been severely limited recently due to other commitments by the Deep Space Network. However, it has been possible to provide an average of one track per spacecraft per day to allow for monitoring of spacecraft health and acquiring scientific data. The majority of this coverage has been provided by the 26-meter stations, most notably those equipped with the 3-hertz tracking loop filters previously discussed in Ref. 1. The performance enhancement affected by these filters will allow recovery of Pioneer 10 telemetry at 16 bits per second until early 1977, when the spacecraft range will be approximately 11.5 AU. Since the Pioneer 11 Saturn encounter in September of 1979 will occur at a range of approximately 10.3 AU, the use of these filters will allow some off-loading of the 64-meter subnet during the pre-Saturn encounter period when Pioneer 11 will be competing for coverage with Pioneer Venus and the Jupiter encounters of the Mariner Jupiter-Saturn (MJS) mission.

B. Jovian Magnetic Tail Penetration

Pioneer 10 passed through the magnetic tail of Jupiter in March of this year, although the spacecraft was more than 4 AU from the planet (Fig. 1). The streaming out of the planet's magnetosphere into a tail-like shape due to the incident solar wind is a well-known phenomenon (Pioneer 7 observed Earth's magnetic tail in 1967) and it was anticipated that the Jovian tail would be detectable at a great distance because of the planet's extensive magnetosphere. Nevertheless, it was somewhat surprising to find that the tail extended almost 700 million kilometers from the planet.

The spacecraft crossed the orbit of Saturn in early February. By mid-March, when penetration occurred, it was slightly off the Sun-Jupiter line and 6 deg above the Jovian orbital plane. Although the exact period of immersion could not be determined because of non-continuous tracking coverage, the spacecraft was in the tail for at least 24 hours. For that interval, the plasma analyzer instrument observed no evidence of a solar wind, indicating that the wind had been blocked by the planet's magnetic field. The spacecraft magnetometer, having failed after the Jovian encounter, could not provide a measure of the change in magnetic field strength from interplanetary levels.

The extent of Jupiter's magnetic tail implies that Saturn should enter the tail every 20 years. If so, this will next occur in April of 1981 and may be observable by the MJS spacecraft.

C. Future Support

In all probability, coverage of the Pioneer 10 and 11 missions will continue at the current levels for the foreseeable future. Availability of the 64-meter stations should improve shortly before Pioneer 10 thresholds on the 26-meter subnets. However, available tracking time will be limited due to support of other ongoing and extended missions as well as by the lengthy periods of down-time required for implementation of the Mark III Data System.

One bright spot is the pending upgrade in late 1978 of the DSS 12 antenna at Goldstone to a diameter of 34 meters. The anticipated 2.2-dB gain improvement will considerably extend this station's ability to support Pioneer 11.

Possible improvements at the 64-meter stations were discussed in Ref. 1, and these will be especially significant for Pioneer 11, which may penetrate the heliospheric bow shock prior to exceeding the limits of communications with Earth. As shown in Fig. 2, the heliosphere is distended by the interstellar wind in much the same way that the solar wind causes the magnetospheres of Earth and Jupiter to be distorted. Although the bow shock's exact location cannot be determined until the spacecraft crosses it, it is of great scientific interest to know where the Sun's influence ends and interstellar space truly begins.

III. Pioneer Venus

Initial operations planning has begun for these missions, which are to be launched in 197[illegible] The most significant

operational problem area yet determined is the optimal method of supporting the multiprobe entry. The tentative station configuration for this phase of the mission has been presented elsewhere (Ref. 2), but a number of questions remain open; namely, which receivers should be operated from the Station Monitor and Control Console and which by individual operators, what is the optimal physical location for the extra receivers and their operators, and what options exist for failure mode recovery? The answers to these and related questions are being actively sought in the detailed formulation of the operations plan for the multiprobe entry. Future Progress Report articles in this series will report on progress as the Mission and DSN operations plans are developed.

References

1. Miller, R. B., "Pioneer 10 and 11 Mission Support," in *The Deep Space Network Progress Report 42—33*, pp. 21–25, Jet Propulsion Laboratory, Pasadena, California, June 15, 1976.
2. Miller, R. B., "Pioneer Venus 1978 Mission Support," in *The Deep Space Network Progress Report 42—27*, pp. 28–35, Jet Propulsion Laboratory, Pasadena, California, June 15, 1975.

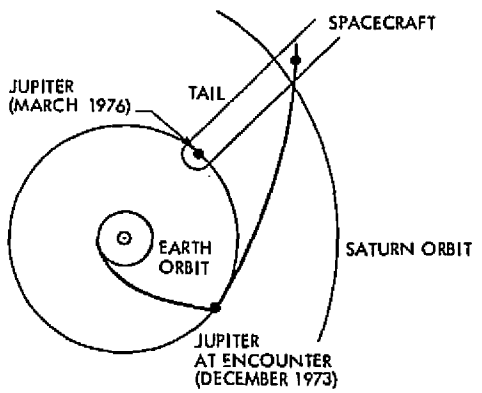

Fig. 1. Magnetic tail penetration geometry

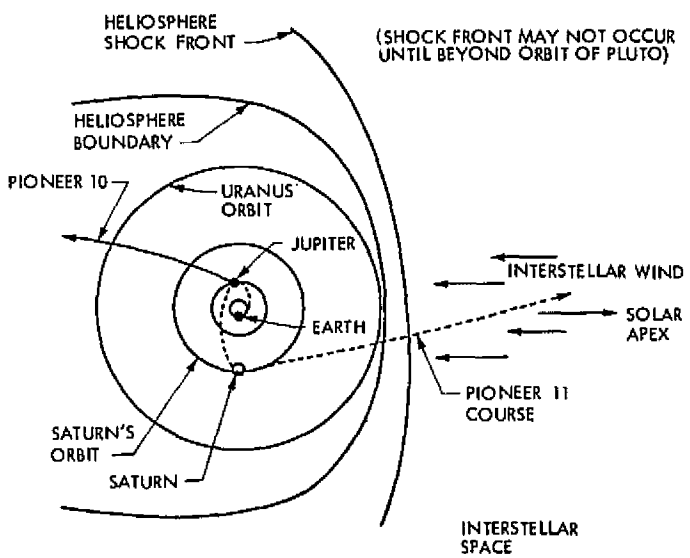

Fig. 2. Pioneer 11 enters interstellar space

Helios Mission Support

P. S. Goodwin
TDA Mission Support Office
W. G. Meeks and R. E. Morris
DSN Network Operations Section

Data from both Helios-1 and Helios-2 spacecraft in solar orbits continue to expand man's knowledge of our solar system. Having completed their third and first aphelions, respectively, the trajectories of both spacecraft will bring about perihelions in October 1976. Helios 2, while still in its five-month (May-September) superior conjunction, continues to supply valuable data for experiments 11 and 12 (Celestial Mechanics and Faraday Rotation). Helios 1 remains in cruise phase.

I. Introduction

This is the eleventh article in a series that discusses Helios-1 and -2 mission support. The previous article (Ref. 1) reported on Helios-1 and -2 cruise, radial and spiral alignments, Helios 2's entry into first superior conjunction, Spaceflight Tracking and Data Network (STDN) cross support, and DSN-STDN engineering tests. Also included were actual tracking coverage and DSN system performance. This article covers a Helios-1 spacecraft power anomaly, Helios-2 occultation, final DSN-STDN engineering test results, tracking coverage, and DSN performance for June and July 1976.

II. Mission Operations and Status

A. Helios-1 Operations

Approaching its third aphelion, the Helios-1 spacecraft was functioning normally (high power, high-gain antenna, power regulator 1, ranging-off) except for the spacecraft ranging temperature problem (Ref. 2). Comparisons between Helios-1 and -2 data were made as the spacecraft passed through spiral and radial alignments.

While DSS 44 (Australia) was tracking the Helios-1 spacecraft on pass 561 (21 June 1976), the downlink signal began to degrade. Within one-half hour the receivers could no longer maintain carrier lock. Following routine verification of proper station configuration and reporting to project personnel, short-term use of DSS 42 (Australia) was negotiated with the Viking Project. After reconfiguring for Helios 1, DSS 42 performed a spacecraft search; no signal was detected, thus verifying DSS 44 operations. Meanwhile telemetry data analysis at JPL revealed that the plus 26-volt power value in the telemetry data had changed from 26.98 volts (nominal) to 23.56 volts prior to loss of signal. About one hour later the 100-meter antenna at Effelsberg (DSS 67) was activated, but no downlink carrier could be detected. After careful ana' ' of the anomaly, the spaceflight team reasoned that the ...h-gain

antenna (HGA) pointing was incorrect. A command was sent to switch to the medium-gain antenna (MGA). After this, the German Effelsberg 100-meter station acquired a downlink signal. Spacecraft status showed that all instruments had been switched off; power regulator 2 was switched on; the spacecraft data handling system had gone to the "safe mode," and the HGA was pointing directly away from Earth. The spacecraft had apparently suffered a power overload (at 206 watts) and shut itself off (safe mode).

The next few days were spent in experiment turn-on and checkout, and reconfiguring the spacecraft as close as possible to the previous status while limiting total power consumption to 200 watts.

Present spacecraft status has all experiments back to normal, transmitting on the HGA at high power and high carrier suppression. The spacecraft is in cruise, having passed its third aphelion.

B. Helios-2 Operations

Still in superior conjunction, Helios 2 is following Helios 1 through aphelion. Plans were made to collect special data during this mission phase. Calibration procedures and data requirements for the 1 July to 5 October 1976 period were distributed to the Network. These data are being collected and preliminary analysis is presently underway.

Helios 2 experienced its second blackout (Sun–Earth–probe (SEP) angle ≤ 1 degree) from 3 through 17 July 1976 (the first blackout occurred on 16–17 May 1976). During this blackout, all communication with the spacecraft was lost — no station could maintain lock on the spacecraft carrier. A blackout timer onboard the spacecraft was set, causing the data to be stored. The memory contents will be read out as soon as higher data rates (64 b/s) are possible. With the spacecraft's trajectory keeping the Sun–Earth–probe angle less than 5 degrees from May through September, higher telemetry data rates are not expected until late August when the SEP angle is between 4–5 degrees.

The first aphelion was reached on Julian Day 200 (18 July) 1976 at 2200 GMT. All spacecraft experiments were functioning normally as the first orbit was completed.

Present spacecraft status indicates all experiments normal, transmitting on the HGA at high power and cruising toward its third blackout (approximately 25 September).

C. DSN-STDN Engineering Tests

The DSN engineering tests regarding STDN real-time telemetry and command cross-support for Helios (Ref. 1) were successfully completed during the month of June. The concept of utilizing interstation microwave links to send Helios modulated subcarriers (both telemetry and command) between the STDN receiver–transmitter and a DSN telemetry–command data processing computer string was demonstrated using live tracks of the Helios-1 spacecraft.

The last two tests were conducted between the STDN-Goldstone station and DSS 12 (Goldstone) on 17 and 25 June. Test results were very encouraging, demonstrating that it is possible to obtain 64 b/s coded telemetry from Helios 1 with a usable signal-to-noise ratio (SNR) (3 to 4 dB) at a 2-AU range from Earth.

A final report was assembled on the DSN-STDN engineering test results and forwarded to the U.S. Helios Project Manager. A decision is expected in September on whether to use the Goldstone STDN-DSN real-time microwave link configuration to support the Helios perihelion operations in October 1976.

D. Actual Tracking Coverage Versus Scheduled Coverage

This report covers tracking activities for a 63-day period from 7 June through 8 August 1976. Both Helios spacecraft were tracked a total of 123 times for a total of 801.8 hours. High Viking tracking requirements, plus Helios-2 solar occultation (spacecraft behind the Sun) accounted for the decrease in tracking hours from the last period. The Helios spacecraft received 47.8 percent of the DSN tracking time allotted to Pioneer and Helios after Viking requirements were satisfied. Helios 1 was tracked 82 times for a total of 576.6 hours. This represents a 21 percent decrease over the last report period. The average pass duration for Helios 1 was 7.03 hours compared to 7.6 hours for the last period. Helios 2 was tracked 41 times for a total of 225.2 hours with an average track time of 5.5 hours. Only 12.6 hours of 64-meter subnet support was allotted for Helios spacecraft during this period due to Viking requirements on the 64-meter subnet. Tracking

coverage will remain sparse until completion of the Viking primary mission in November 1976.

III. DSN System Performance

A. Command System

Helios command activity dropped considerably during this report period to a total of 2910 commands as compared to 7331 commands for the last period. Two factors account for this decrease: (1) Helios tracking time was reduced to only 47 percent of that received during the last report period, and (2) Helios 2 spent most of this period in, or very near, solar occultation. DSN resources have been largely allocated to the support of the Viking mission. The cumulative command totals are now 39,248 for Helios 1 and 13,428 for Helios 2.

There were no command system aborts during the months of June and July 1976. The cumulative command system abort count remains at 10 for Helios 1 and 3 for Helios 2.

Total command system downtime for the months of June and July was 6 hours and 45 minutes. Although this figure is only one-third of the last report period, tracking time for these months was also much less. Of the 10 failures reported, 5 were associated with the loss of transmitters at DSS 44 (3 each) and DSS 12 (2 each).

B. Tracking System

The Helios-1 spacecraft's ranging transponder remained inoperative throughout this reporting period due to a temperature-dependent malfunction (Ref. 2). The ranging capability is not expected to return until after September. This fact, together with the concentrated attention being devoted to Helios-2's first superior conjunction, made for a low level of Helios-1 activity.

Helios 2 entered its first superior conjunction (SEP $\leq$ 5 degrees) on 4 May 1976 and will remain there through 6 October. During this time the spacecraft will have been occulted by the Sun three times. This period is of extreme importance to the Helios radio science team. Special "receiver ramping" procedures are still being conducted in support of this trajectory phase. Only preliminary results have been published thus far. Final results will require further analysis.

C. Telemetry System

Computer analysis of Helios-2 inferior conjunction data, collected in March–April 1976, is in progress. From these data, curve fits of SNR degradation as a function of the system noise temperature (SNT) are to be generated per spacecraft and tracking subnet (26 or 64 meters). The next logical step is the development of the superior conjunction model which will utilize the basic inferior conjunction model as well as additional modeling of the spectral broadening test data. It is planned that these models will improve DSN telemetry predicts, thus helping to determine best allocation of DSN resources during future superior conjunctions.

IV. Conclusions

With the Helios-1 spacecraft's ranging system already inoperative because of an onboard temperature problem, the spacecraft switched to the "safe mode" on 21 June 1976 because of a power overload. After a few anxious hours, the downlink was commanded *ON* and the spacecraft reconfigured for normal operation.

Helios 2, while in its first superior conjunction, has experienced two total solar occultations and will have one more before its second perihelion in mid-October.

The last two DSN-STDN engineering tests to prove the interstation microwave link configuration to support Helios were completed during this report period. A final encouraging report was sent to Project management.

Due to DSN resource commitments to Project Viking, Helios tracking time was reduced by over 50 percent during the last report period. The DSN system performance remained at a high level with no significant anomalies.

Data collected during Helios-2 inferior conjunction in March and April of 1976 are being analyzed and used to build a model for future superior conjunctions by the Network Operations Analysis Group.

Due to Viking-1 and -2 prime missions the Helios DSN tracking schedule is expected to remain at present levels, sharing equally the remaining tracking time with Pioneers 10 and 11.

Acknowledgments

The authors wish to thank the following members of the Network Operations Analysis Group for their contribution of periodic Network Performance Reports:

Command:	R. Gillette, W. L. Tucker
Tracking:	A. L. Berman, R. S. Schlaifer, L. Bright
Monitor and RFI:	P. Low, C. Lunde

References

1. Goodwin, F. S., Meeks, W. G., and Morris, R. E., "Helios Mission Support," in *The Deep Space Progress Report 42-34*, pp. 21–26, Jet Propulsion Laboratory, Pasadena, Calif., Aug. 15, 1976.

2. Goodwin, P. S., Meeks, W. G., and Morris, R. E., "Helios Mission Support," in *The Deep Space Progress Report 42-33*, pp. 26–31, Jet Propulsion Laboratory, Pasadena, Calif., June 15, 1976.

Hardware Additions to Microprocessor Architecture Aid Software Development

M. W. Sievers
Communications Systems Research Section

Simple additions to a microprocessor's architecture provide a programmer with two powerful debugging aids. These aids are useful both for initial software development and for routine system integrity diagnostics. One of these aids may be expanded into a virtual machine system.

I. Introduction

The job of a hardware engineer is to design hardware, which, all too often, is done at the expense of the software engineer who must use the hardware. Whether through oversight or done intentionally to save space and hold down costs, hardware frequently lacks features not specifically required but that could simplify the task of the software engineer.

When designing microprocessor systems, whether they be simple dedicated controllers or complex general-purpose systems, the basic architecture can be constructed with increasingly fewer integrated circuit packages. A hardware engineer mesmerized by the simplicity of the architecture will put his design efforts into building interfaces for the devices the system must communicate with. The hapless programmer may be fortunate enough to get displays and single-step features to help him debug his software—but these are barely adequate when long and complex programs are being checked out.

In this article an Address Trap (breakpoint) mechanism and last-in-first-out (LIFO) Address Stack are suggested as two additions to the basic microprocessor architecture whose functions are solely to aid the programmer. These devices provide the programmer with the ability to specify address breakpoints and to trace program execution back through N instructions, where N is the depth of the stack. Both devices, plus interface logic and buffering, have been designed for an INTEL 8080-based system using approximately 25 integrated-circuit packages.

Section V is devoted to a proposal for implementing a microprocessor virtual machine system via data and address traps. The interested reader not familiar with virtual machine concepts should consult Refs. 1–7.

II. Basic Architecture

Consider Fig. 1 in which a basic microprocessor architecture is illustrated. Three buses, the Address Bus, Data Bus, and Control Bus, interconnect the Central

Processing Unit (CPU) and the various devices on the buses. This configuration is similar to the PDP-11 UNIBUS (Ref. 8) in which any device may be treated as memory or input-output at the hardware designer's option.

The Address Trap and Address LIFO are connected to the bus structure as shown. The Address Trap generates a one-bit DISABLE flag which is used to disable memory. This flag bit could properly be considered part of the Control Bus but is separated for clarity.

III. Address Trap

Frequently a programmer debugging new software desires to know if a given address in his program space is accessed. Further, it is often desirable to check partial results in the calculation of a complex function. In either case, the basic microprocessor instruction set does not lend itself to performing these tasks without considerable overhead.

An Address Trap which causes an interruption in the normal program stream is ideal for implementing the features described above. It is a very simple hardware device that jams an instruction on the Data Bus when the Address Bus contains an address equal to the one stored in a register in the trap. The advantage this device affords over inserting patches into the code being executed is that since the user program is left intact, no overhead is required for keeping track of where patches are made.

A block diagram of an Address Trap is shown in Fig. 2. The trap is assigned three sequential addresses in upper memory space making it appear as a memory device to the CPU. Two addresses are used for the Address Register which holds the address to be trapped. The third address is a register within the Control Unit that enables and disables the trap mechanism.

The Comparator compares the contents of the Address Register with the Address Bus. When the two are equal, the Comparator signals the Control Unit via EQUAL. If the trap is enabled, a Memory Disable signal is generated. This signal is used to turn the memory off so that the Data Bus is free for use by the trap. When the CPU signals its desire to read an instruction from memory, the trap jams its own instruction onto the Data Bus. In the case of an 8080, this instruction is an RST (RESTART) instruction which is a single-byte unconditional CALL.

The routine called by the trap could display the registers, dump memory, enter a new address into the trap, etc. If the trap address is set within a loop, for example, then the results of each pass through the loop could be displayed. Additionally, if input-output devices are placed in memory space, then attempts by the CPU to access these devices may be trapped.

IV. Address LIFO

There are two things that are certain in the life of a programmer: he will erase a file he shouldn't have and he will write a program that mysteriously branches to never-never land. Therefore, an Address LIFO is proposed as a means of tracing backward through a program to hasten finding the errant code in the solution of the latter problem.

Assume a special stack whose PUSH function was not under direct CPU control but whose POP function was. Each time the CPU references an instruction in memory, the address of the reference is pushed into the stack. At any time the CPU could disable the PUSH operation and examine the elements in the stack. This would permit a programmer to trace the steps of his program back to the depth of the stack. Should his program branch outside of its space, this stack could be examined to see where the program came from.

A block diagram of an Address LIFO is illustrated in Fig. 3. As with the Address Trap, it is assigned sequential addresses in upper memory. A Control Unit determines that the CPU is referencing an address within its allowed address space and pushes that address into the stack. A flip-flop within the Control Unit enables and disables the PUSH operation.

When the CPU desires to access the stack, it commands the Control Unit to cease the Push operation. It can then POP the stack without pushing the stack access routine addresses into the stack.

The LIFO may be used in conjunction with the trap described in Section III. Among other things, the trap routine could fetch the contents of the stack and display it for the programmer.

V. A Microprocessor Virtual Machine System

Before going into the proposed microprocessor virtual machine system architecture, a brief review of virtual machines will be offered. The interested reader should consult Refs. 1-7 for details.

A virtual machine (VM) is defined as an efficient, isolated copy of a real machine. This concept can be

explained by the virtual machine monitor (VMM) shown in Fig. 4. The VMM is a program that has the following characteristics:

(1) It provides an environment for other programs that is essentially identical to the real hardware environment of the original machine.

(2) Programs executing in this "virtual" environment suffer only small decreases in execution speed.

(3) The VMM exerts complete control over the system resources.

A virtual machine can be thought of as the environment created by the VMM.

A typical form of a VMM and VM implementation is to define a dual-state architecture. Two distinct modes of system operation are defined, privileged and nonprivileged, in which all critical functions are performed in the privileged state. The VMM operates in the privileged mode and performs such functions as direct handling of interrupts, performing input–output, and changing machine state. Each VM under the control of a VMM performs input–output to virtual devices and has the effects of its interrupts simulated by the VMM.

Instructions that must be executed in a privileged mode are called sensitive instructions. An instruction is control sensitive if it attempts to change the amount of resources available to the processor or affects the processor mode. An instruction is said to be behavior sensitive if its execution depends on a real memory address or the processor mode. All non-sensitive instructions are said to be innocuous.

In order for a machine to be virtualizable, the architecture must be such that when a sensitive instruction is executed in a non-privileged machine state, a trap occurs and the privileged state is entered. Consider Fig. 5 which shows the configuration of Fig. 1 in a slightly modified form. The Address Trap device now contains a Base and Bounds Register. The VMM loads these registers with the base and bounds of the VM it desires to execute. Should the VM attempt to access memory outside of these boundaries, an address trap occurs.

A Data Trap is similar in function to the Address Trap except it traps data rather than addresses. It contains a Content Addressable Memory (CAM), which holds the so-called sensitive instructions. When the Data Bus contains one of these instructions when the CPU is doing an instruction fetch, a trap occurs. The other use for this device is to implement instruction macros.

Upon power-up, the VMM can queue VMs and choose one for execution. Upon a trap or after a given delay, the VMM can suspend operation of one VM and start another. Although the details of the machine state switching have not been worked out, a little thought should prove them to be tractable.

References

1. Buzen, J. P., and Gagliardi, I. O., "The Evolution of Virtual Machine Architecture," *Proc. NCC*, AFIPS Press, Montvale, New Jersey, pp. 291–300, 1973.

2. Gagliardi, I. O., and Goldberg, R. P., "Virtualizable Architectures" *Proc. ACM AICA International Computing Symposium*, Venice, Italy, 1972.

3. Galley, S. W., "PDP-10 Virtual Machines," *Proc. ACM SIGARCH-SIGOPS Workshop on Virtual Computer Systems*, Cambridge, Massachusetts, 1969.

4. Coldberg, R. P., *Virtual Machine System*, Report No. MS-2686, MIT Lincoln Laboratory, Lexington, Mass., 1969.

5. Goldberg, R. P., "Hardware Requirements for Virtual Machine Systems," *Proc. Hawaii International Conference on Systems Sciences*, Honolulu, Hawaii, 1971.

6. Goldberg, R. R., "Architecture of Virtual Machines," *Proc. NCC*, AFIPS Press, Montvale, New Jersey, pp. 309–318, 1973.

7. Popek, G. J., and Goldberg, R. P., "Formal Requirements for Virtualizable Third Generation Architectures," *CACM*, Vol. 17, No. 7, July 1974.

8. *PDP-11 UNIBUS Interface Manual*, Digital Equipment Corporation, Maynard, Massachusetts, April 1970.

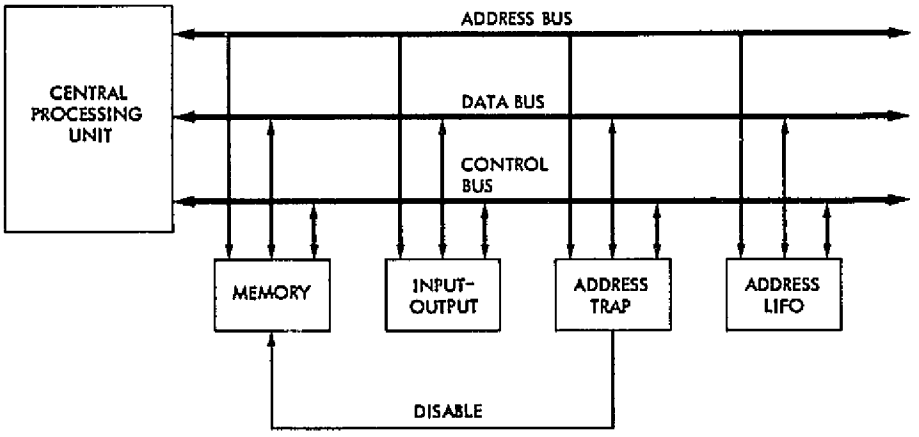

Fig. 1. Basic microprocessor architecture

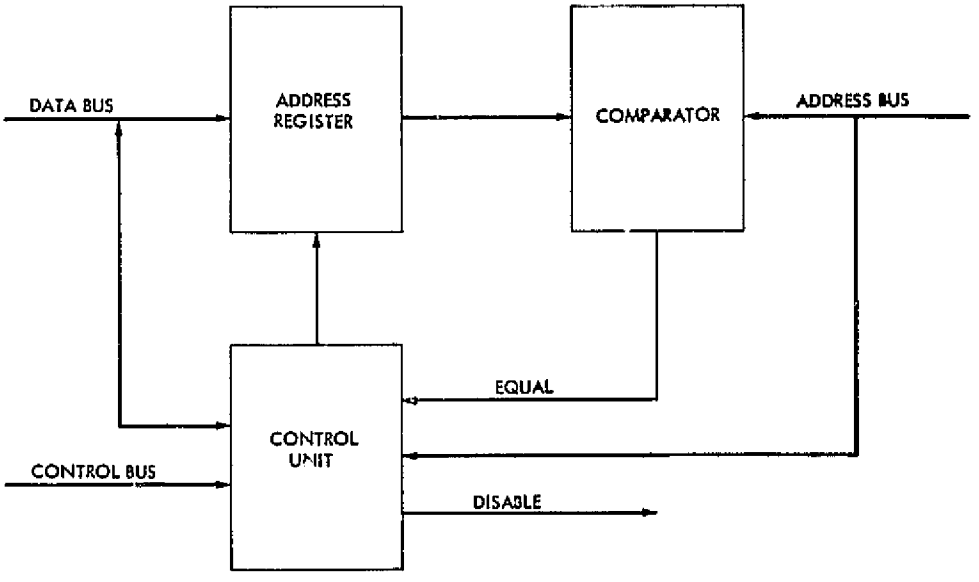

Fig. 2. Block diagram of Address Trap

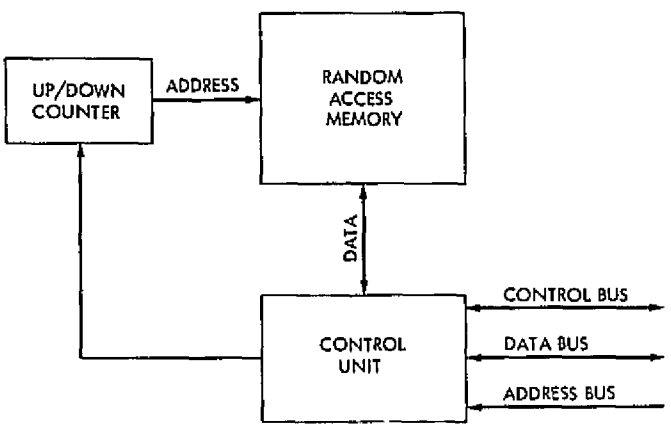

Fig. 3. Address LIFO

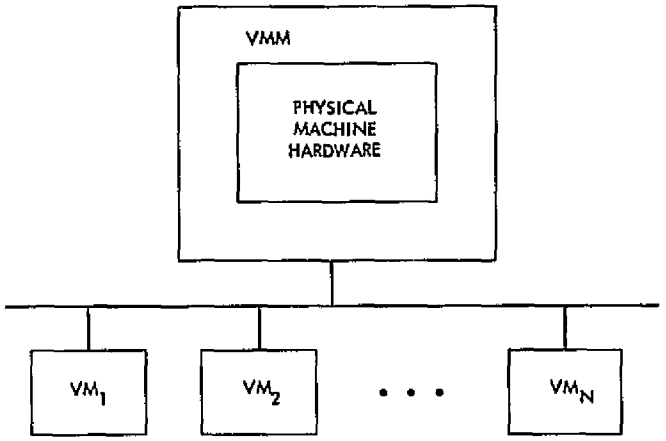

Fig. 4. Virtual machine monitor

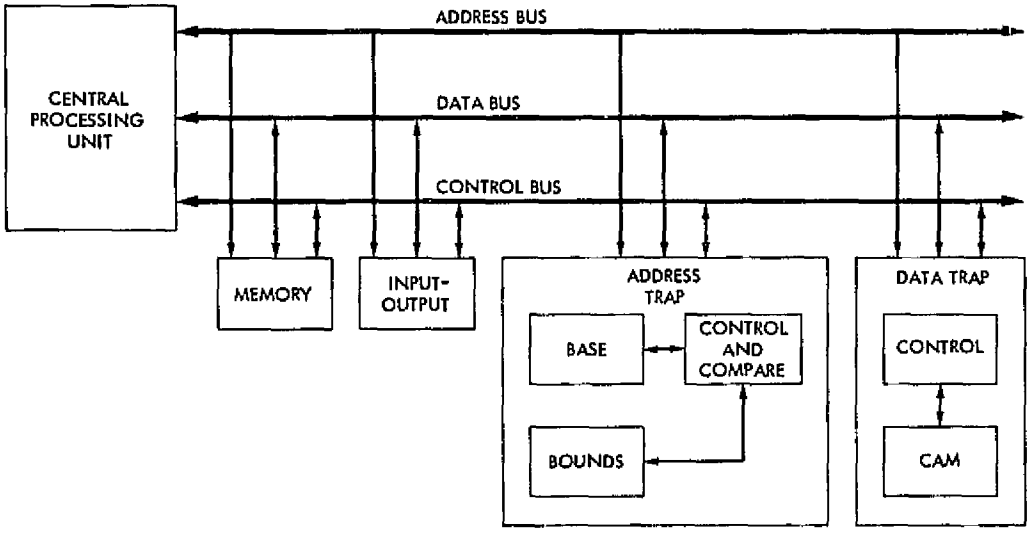

Fig. 5. Microprocessor based virtual machine system architecture

512-Channel Correlator Controller

S. S. Brokl
Communications Systems Research Section

JPL and the Haystack Observatory have developed a high-speed correlator for radio and radar observations. To ensure that the host computer could operate during the extended run times of the JPL–Haystack correlator, a controller was designed so that the correlator could run automatically without computer intervention. The correlator controller assumes the role of bus master and keeps track of data and properly interrupts the computer at the end of the observation.

I. Introduction

In 1972 JPL and the Haystack Observatory developed a 1024-Channel Solid State Correlator System, which consists of a control computer plus sixteen 64-channel correlator modules. It was decided that 512 channels of this correlator design could meet current JPL requirements for on-going radar experiments.

Each correlator module may be operated as a 64-channel "real" correlator or as a 32-channel "complex" correlator. The correlator may be used in either an autocorrelation mode or crosscorrelation mode. The maximum bandwidth is 10 MHz with a 20-MHz clock rate. Each module can accept quantized data in two-, three-, or five-bit formats.

The correlator controller was designed to allow the master computer to be free to carry on other tasks while the correlator accumulates the data. Once the computer loads the operating parameters into the correlator controller, the correlator is free to operate without the computer's central processor. The controller takes over the task of monitoring the most significant bits from each correlator channel accumulator and stores this overflow information in the computer's memory by way of a Direct Memory Access (DMA). An overflow is the process of detecting the "1" to "0" transition of the most significant bit of the accumulator. When a correlator run is complete, the controller will interrupt the computer with an "end-of-run" indication. At this time the computer takes over control and proceeds to unload the low order counts from the correlator accumulators and process the data.

II. Correlator Controller Requirements

The host computer chosen for this project is a Digital Equipment Corporation PDP 11-20. A block diagram illustrating the communications requirements of the controller is shown in Fig. 1. The controller is a moderator correctly formating communications between the computer and the correlator modules. In addition, when the

correlator is running, the controller takes charge of the unibus and becomes bus master. This is done to take advantage of the Direct Memory Access (DMA) feature of the PDP 11-20 computer. DMA allows a peripheral device to communicate directly with the computer's memory. With DMA an external device can run at memory cycle times and does not interfere with the computer central processor operation.

During long run times the controller computes the overflow of the accumulator of each channel and stores this information by way of the DMA in the computer's memory. With this feature of the controller, the maximum accumulation is increased from 24 to 40 bits. Integration times in excess of 8 hours with a 20-MHz clock rate can be realized by this method.

The correlator is structured in groups of 64 channels each (one module or unit). There are nine modules (units) that make up the correlator. In normal operation only eight units are used (512 channels), leaving one spare. The controller can specify any number of units up to eight to be used. These are called good units.

At the end of a correlator run, the controller signals the computer it is done. This is accomplished with an interrupt. An interrupt is a message to the central processor of a computer indicating a need to communicate. The PDP 11 has four interrupt priority levels. The controller is programmable in this area and can be set to any level of interrupt priority by the user.

III. Correlator Controller Operation

Figure 2 is a block diagram of the 512-channel correlator controller. The computer address and control buffers, priority BR/BG NPR/NPG, and data buffers are Digital Equipment Corporation suggested circuits and components (Ref. 1).

The address decoder allows computer access to the controller's control and status register and internal registers. Two codes alert the controller to either a control message transfer or data transfer. The decoder consists of manually setable dip switches and an 18-bit comparator. With this method the controller may be accessible with any two adjacent addresses selected by the user, and preset into the dip switches.

The control and status register (CSR) is a 16-bit programmable register. It is a pointer and allows data entering the controller to be channeled to internal registers and to the individual correlator modules. Additionally, it contains information on internal operations of the controller and correlator. When the end-of-run occurs, the four least-significant bits are automatically zeroed. This is done to allow the interrupt vector number contained in the interrupt vector address register to be presented to the PDP 11 central processor. The format of this register is in Fig. 3, and programming information can be obtained from Ref. 2.

The data multiplexer (MUX) receives its control information from the CSR and allows data from any of the internal controller registers or a selected correlator module to be read by the computer.

The interrupt vector register is a 16-bit programmable register that supplies the vector address during an interrupt at the end of a run.

The good units register is a 9-bit register with the format in Fig. 4. It controls the correlator unit counter by supplying information on which units are in use and allows the unit counter to stop at the proper unit during a run. The correlator unit counter controls end-of-overflow and which unit the overflow control is scanning. Either the PDP-11, by way of the control and status register, or the correlator unit counter supplies the unit address. The unit address source is selected by the PDP-11 or local address control multiplexer. When the correlator is running, the unit address is controlled by the correlator unit counter. When the correlator is being readied for a run or the data after a run is being unloaded, the unit address is supplied by the computer program through the controller control and status register.

The zero lag counter is a 40-bit-long high-speed counter which is loaded with the 1's complement of the *number* equal to the run time in seconds and multiplied by the clock frequency in hertz. Because the PDP-11 is a 16-bit word computer, the counter is segmented into three parts. It is segmented into 8-, 16-, 16-bit parts with the 8 bits being the most significant.

The start overflow sequence is initiated every 2^{18} count of the zero lag counter. Each correlator lag can store 2^{24} bits, and by running the controller overflow scanning faster ensures that no overflows in 512 lags will be missed. An additional overflow sequence is initiated when end-of-run occurs to ensure that no overflows happened since the last scan. The overflow scan time varies depending on how many accumulators overflowed. If all 512 bits overflowed, then the total scan time is approximately 1.2 ms. At the end of the zero lag count an interrupt is generated signalling the computer that a run is complete.

The overflow starting address register contains a 16-bit word, which is the starting address for the overflow array in the PDP-11 memory. This number is strobed into the 16-bit address counter at the beginning of each overflow sequence during a run. The address counter is incremented by the overflow control at the end of each lag "1" to "0" transition test.

The overflow control generates overflow read requests during a run and stores 16 overflow bits at a time in the overflow shift register. Each overflow bit is sequentially shifted from the shift register and tested for a "1" to "0" transition. This information is stored in a 512-bit scratch pad memory within the overflow controller. If an overflow is detected, the overflow controller generates a nonprocessor request (NPR) and upon receiving a nonprocessor grant (NPG) initiates a read request from the overflow array in the computer, stores these data in the overflow temporary storage register (overflow temp), increments overflow temp by one, and stores overflow temp back in the overflow array. If no overflows are detected, the computer array is not accessed.

Figure 5 is the format for the correlator bus function word. The correlator control buffer contains 12 line drivers for this bus. Additionally, the correlator control buffer contains line drivers for run control, high-speed clock, bus control strobe, connect clock, and the unit address. The bus control strobe and connect clock are signals generated during a load and control operation from the control and status register or from a read request from the overflow control.

Figure 6 is the format of the correlator data word. The correlator data register in the controller holds this 24-bit word while the computer reads data. The computer program first sets the control and status register to point to the high order 16 bits and then to the low order 8 bits.

The run control distributes the master clock to the zero lag counter and the correlator when commanded to be in run by the computer. The run control is turned off by an interrupt or a stop command from the computer. Additionally, the run control supplies both a true run and extended run signals. The true run disables the front end counters in the correlator so that additional data are suppressed; the extended run disables the master clock after the final overflow scan is completed.

The interrupt control can be programmed to act on any priority level. The interrupt control automatically zeros the four least-significant bits of the control and status register when an end-of-run occurs. This is done so that the interrupt vector address is presented to the data bus during the interrupt. The interrupt control also sends a bus request and waits for a bus grant before executing the interrupt to the computer.

When the correlator is not in the run condition, all data transfer is under control of the computer. The controller has two addresses, one (164000) allows data to be transferred into and out of the controller control and status register (CSR). The other address (164002) allows data to be transferred from registers or modules being pointed to by the CSR. To read data from a correlator module, first set all units to the read mode by setting 13606_8 into the CSR. Follow this by a data transfer word from the correlator controller to the unit array within a program. The read request to correlator module via bit D_4 of the CSR must go to a "one" and then to a "zero" state between data transfer requests. The following is an example of a machine language program (Ref. 3). All numbers are in octal.

Example: Correlator Unit #1 Read

First set all correlator modules to read mode

```
MOV #13606 @ #164000 (sets all units
CLR @ #164002          to read mode)
```

Word

```
#1 MOV #14236 @ #164000 (send a read request to
                         unit #1)
#2 MOV #164002 @ #XXXX (XXXX =location; reads
                        data from 8 low order
                        bits into an array)
#3 MOV #14217 @ #164000 (satisfies 0 condition for
                         read request and pre-
                         pares to read high order
                         register bits)
#4 MOV #164002 @ #XXXX  (XXXX = location;
                         reads data from 16
                         high order bits into an
                         array)
```

Each module contains its own address counter which is zeroed when a run is completed. To read all 64 lags, 64 read requests per module must be made. The first program word in the above example sends a read request to the module pointed to in the CSR word and the module unloads its 24-bit word into the correlator data register within the controller. The second word transfers the 8 *least*-significant bits from this register into an array within the computer. The third word sets the CSR pointer to read the 16 high order bits from the correlator data

register. The fourth word transfers the 16 *most*-significant bits from this register into an array within the computer.

IV. Summary

The correlator controller may assume the roll of master only after the computer has issued a run command. At that time the controller keeps track of overflows and ensures proper updating within the overflow array in the computer's memory without interrupting the computer's processor. At the end of a run, the controller interrupts the computer and releases itself to operate as a slave.

The first operation of the 512-channel correlator was successfully accomplished during joint experiments in January 1976 between Aricibo and Goldstone, when Aricibo transmitted signals to Saturn and Goldstone received.

References

1. *Interfacing Handbook, PDP-11/05, 10, 35, 40*, Digital Equipment Corporation, 1974.
2. Jurgens, R. F., "Theory, Operation, and Computer Programming of the 512-Lag Correlator System, " in *The Deep Space Network Progress Report 42-32*, pp. 164–177, Jet Propulsion Laboratory, Pasadena, Calif., Apr. 15, 1976.
3. *Processor Handbook, PDP-11/05, 10, 35, 40*, Digital Equipment Corporation, 1973.

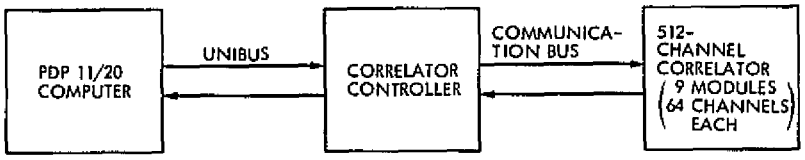

Fig. 1. Correlator system block diagram

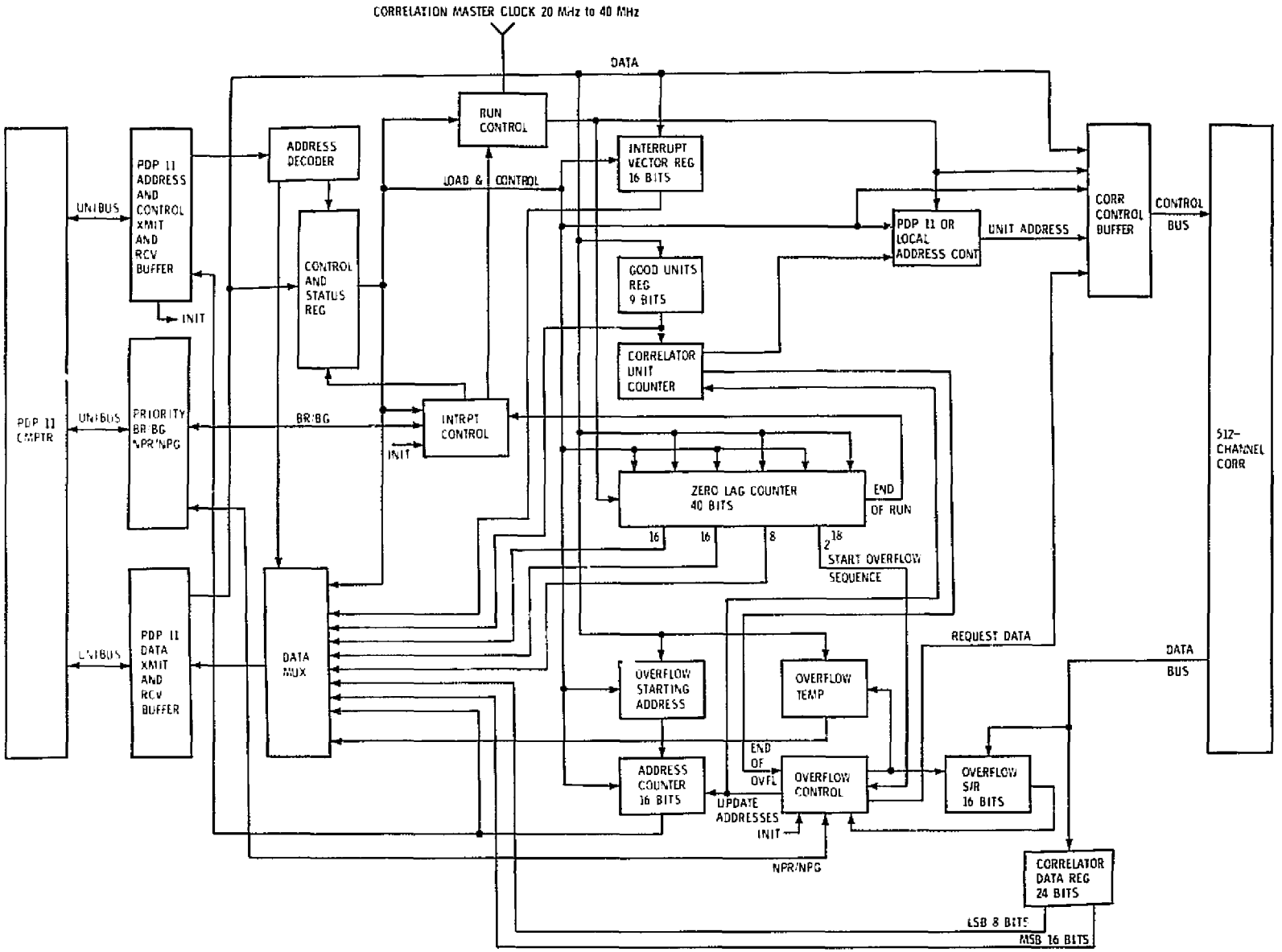

Fig. 2. 512-channel correlator controller block diagram

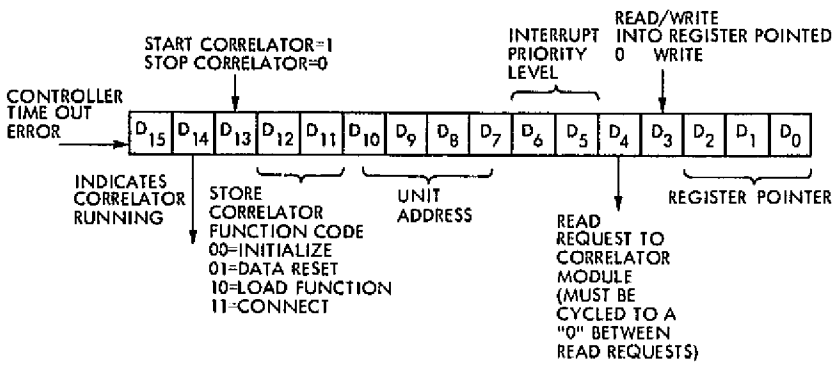

REGISTER POINTER CODES:

000 = INTERRUPT VECTOR 16 BITS
001 = GOOD UNITS 9 BITS
010 = OVERFLOW STARTING ADDRESS 16 BITS
011 = ZERO LAG COUNTER 16 LSB
100 = ZERO LAG COUNTER MIDDLE 16 BITS
101 = ZERO LAG COUNTER 8 MSB
*110 = CORRELATOR LOW ORDER 8 BITS IN READ ONLY
111 = CORRELATOR HIGH ORDER 16 BITS IN READ ONLY

INTERRUPT PRIORITY

00 = 4
01 = 5
10 = 6
11 = 7

UNIT ADDRESS

0001 THRU 1001 = BCD UNIT 1 THRU 9
1111 = ADDRESS ALL UNITS

*IN THE WRITE MODE THE DATA TRANSFER PORT LOADS DATA DIRECTLY INTO THE UNIT ADDRESSED AND CAN ONLY BE READ IN THE OVERFLOW READ MODE. THIS ALLOWS LOADING OF THE 12 FUNCTION BITS IN EACH CORRELATOR MODULE.

Fig. 3. Control and status register format

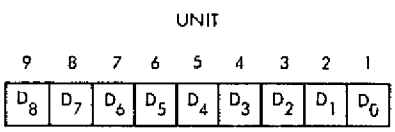

NOTE: A "1" IN ANY BIT POSITION INDICATES THAT THE UNIT IS GOOD.

Fig. 4. Good units register format

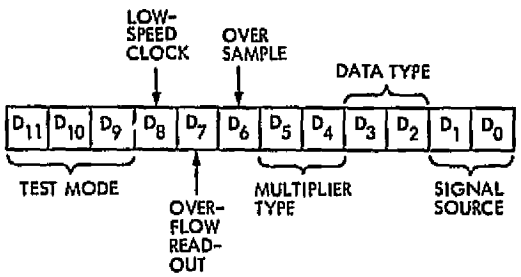

BIT ASSIGNMENTS		OCTAL CODE	FUNCTION
BITS 0-1	SIGNAL SOURCE	0	FROM STAGE N-1
		1	FROM STAGE N-2
		2	FROM DATA SAMPLER
		3	FROM AUX UNIT
BITS 2-3	DATA TYPE	0	REAL TWO LEVEL
		1	REAL THREE LEVEL
		2	COMPLEX TWO LEVEL
		3	COMPLEX THREE LEVEL
BITS 4-5	MULTIPLIER TYPE	0	TWO LEVEL
		1	THREE LEVEL
		2	FOUR LEVEL
		3	FIVE LEVEL
BIT 6	OVERSAMPLE	0	NYQUIST RATE
		1	2 x NIQUIST RATE
BIT 7	OVERFLOW READ	0	DATA READ MODE
		1	OVERFLOW READ MODE
BIT 8	LOW-SPEED CLOCK	0	HIGH-SPEED CLOCK
		1	LOW-SPEED CLOCK
BITS 9-11	TEST MODES	0	OPERATE
		1	DISABLE DATA BUS
		2	BUS TRANSMIT 1's
		3	BUS TRANSMIT 0's
		4	MEMORY LOAD 1's
		5	MEMORY LOAD 0's
		6	SPARE
		7	FAULT INDICATOR ON

Fig. 5. Correlator bus function word format

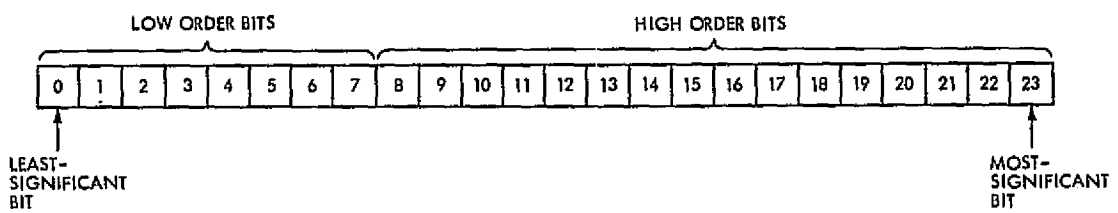

NOTES:
1. IN THE READ MODE THE 24-BIT REGISTER REPRESENTS ONE ACCUMULATOR CHANNEL. 64 READ REQUESTS ARE REQUIRED TO UNLOAD EACH MODULE.
2. IN THE OVERFLOW READ MODE THE 16 HIGH ORDER BITS REPRESENT THE MOST-SIGNIFICANT BIT OF EACH ACCUMULATOR CHANNEL. FOUR OVERFLOW READ REQUESTS ARE REQUIRED TO UNLOAD EACH MODULE. THE 8 LOW ORDER BITS REPRESENT D_0 THROUGH D_7 OF THE CORRELATOR BUS FUNCTION REGISTER FOR THE MODULE BEING UNLOADED.

Fig. 6. Correlator data word format

Command Detector SNR Estimator and Lock Status Monitor Circuitry

R. F. Emerson
Communications Systems Research Section

A breadboard of the command detector signal-to-noise-ratio estimator and lock status monitor was built on a wire-wrap card. The breadboard was integrated with the Standard Command Detector, and its performance was measured. The design, design constraints, and construction of the breadboard are described. The performance is shown to agree with the theoretical model

I. Introduction

The command detector signal-to-noise-ratio estimator and lock status monitor (SNORE–LOCK) was developed from work centering around data-aided tracking receivers (Ref. 1). The advantage of this approach is that it is insensitive to the magnitude of the input signal. This is particularly important in connection with the multiple rate command detector activity (Ref. 2).

The SNORE–LOCK circuit was designed to interface with, and become a part of, the Standard Command Detector being developed for the NASA Low Cost Systems Office. The circuit accepts values from the matched filters of the command detector and calculates a signal-to-noise-ratio (SNR) estimate (SNORE). Using several values of this estimate, it decides the lock status of the detector.

II. Theory of Operation

The design of the SNORE–LOCK circuit will be described below starting at the functional level and progressing to the logic level. A description as if it were a computer program is presented to clarify the sequencing of events within the circuit.

A. Functional Description

A functional block diagram of the SNORE–LOCK circuit is shown in Fig. 1. The diagram illustrates the data flow and functional processing within the circuit.

Starting at the left of the diagram, N values of each of two data types are accumulated in magnitude. The value of DATA represents an inphase correlation when the detector is locked. Likewise the value of ERROR represents the quadrature phase correlation. The inphase value is a measure of the signal, while the quadrature phase value is a measure of the noise.

A ratio of the accumulated values is then computed. This computed value is called SNORE. SNORE values are both accumulated for telemetry use and compared with a fixed digital threshold for lock detection. K successive comparisons are used in the lock indication algorithm.

In the breadboard version of the circuit, the values of N,K and the threshold are digitally selectable. In the flight unit these values would be fixed at manufacture.

B. Logical Description

The logic block diagrams of Figs. 2 and 3 expand upon the above functional description of the previous section. All arithmetic operations within the processor are bit-serially performed.

Values of DATA and ERROR received from the detector are scaled to fit within the accumulator registers of the processor. Since a resolution of 0.25 in SNORE is required, the value of ERROR is divided by 4 before it is accumulated. This permits the use of an integer division algorithm.

At the correct time, the values in the scaling registers are transferred through conditional complementors (C/C) and accumulated. The multiplexor at the input of each accumulator selects the source of information depending upon the phase of processor operation.

During the accumulation phase, the C/C outputs are the sources for the accumulators. During the division or "compute" phase, the value of the divisor is added to the dividend. Since ERROR was accumulated as a negative absolute value, this results in a subtraction. For each successful subtraction (that is, where the result is still greater than zero), the quotient is incremented. This incrementing is accomplished with the adder previously used to obtain the divisor. The sharing of this adder reduces the package count and power requirements at a small cost in complexity—the addition of a multiplexor.

The timing logic provides the signals and clocks used to control operations within the processor. After N accumulations are performed, the division process is started. Should the detector present new values of DATA and ERROR before the division is complete, the operation reverts back to the accumulation phase. This limits the maximum value of SNORE at high symbol rates (above 500 symbols/s). This does not affect the lock indicator operation as the maximum is about twice the nominal value for threshold lock indication.

The value of SNORE is used by the lock indicator (Fig. 3), and is accumulated for presentation to the telemetry subsystem.

The quotient or SNORE value is compared with a fixed digital threshold. K successive values that are greater set the detector lock indicator, while K successive values that are not greater reset the lock indicator. When set, the lock indicator indicates in-lock. K successive decisions which are not members of these two groups cause no change in lock indication.

C. SNORE–LOCK Algorithm

The SNORE calculation is performed in two steps or phases. During the first phase, a number of samples of the DATA and ERROR register values from the detector are accumulated. During the second phase, the accumulated results are used to obtain a ratio which is a measure of the SNR. In addition to these two active phases, there is a quiescent phase in which no processing is performed.

In order to place the relationships in a logical order, the following discussion will treat the SNORE–LOCK processing as a computer program. The flow chart of Fig. 4 would represent the actual processing if each action could be accomplished in "no" time. Since the processing action requires a finite amount of time, some elements in the hardware implementation have been included to provide for "multiprocessor" capability. Each element of the flowchart, identified by number, is presented below.

Block 1 illustrates a waiting function. Waiting is necessary to synchronize data transfers between the detector and the SNORE processor. The detector has data ready for transfer 32,000 times a second. The only data transfer that is used by the SNORE processor occurs at the end of a symbol time. (Here "symbol" represents one unit of information in the command message. The term "symbol rate" will be used for command bit rate to prevent confusion.) Each data transfer is saved except the one at the beginning of the symbol period (see Blocks 2 and 3). By this method the values of the DATA and ERROR registers in the detector at the end of a symbol period are available for use at the correct time.

Block 4 tests the "First Sum Flag." If successful, it indicates that a value of SNORE is available and must be processed. The processing is added to the loop once for every N accumulations (see Block 18). In Block 5 this flag is reset, the "SNORE counter" is incremented, and, if the counter value equals 16 (Block 6), the value in the "SNORE accumulator" is made available to the telemetry subsystem. At the same time both the counter and

accumulator are cleared (Block 7). In Block 8 the new value of SNORE, indicated by the flag, is accumulated.

Block 9 represents the lock detector test of SNORE against the fixed threshold. If the value is not greater than the threshold, "Flag" is set (set = 1) (see Blocks 10 and 11). The lock indicator is reset if the last K "Flags" were one. This is shown in Blocks 12 through 15. The value of the latest "Flag" is added to storage and the $(K + 1)$st value is dropped (Block 16). After this is complete, the flow returns to the main loop.

The values saved by the operations of Block 3 are summed, in absolute value, in the dividend and divisor registers. The "symbol counter" is also incremented (Block 17). If this count has not reached the present value N (Block 18), processing is returned to the wait loop at Block 1. If it has reached N, "First Sum Flag" is set (Block 19) and the quotient register is cleared (Block 20).

The value of SNORE is computed by an integer division algorithm. This algorithm is illustrated in Blocks 21, 22, and 23. The value in the dividend register, representing an accumulation of ERROR values, is repeatedly subtracted from the value in the divisor register. The results of each subtraction are returned to the divisor register. If this result is greater than zero, the quotient is incremented; if not, the processing is completed and the flow is returned to Block 1.

Two other conditions will stop the division process. If the quotient will overflow on the next successful cycle (Block 24) or if time has run out—indicated by the signal "Last Sample" (Block 25)—division is stopped and the flow returned to the wait loop at Block 1.

III. Description of Hardware

The breadboard SNORE-LOCK circuit was designed to provide a test vehicle for the algorithm and to approach, as closely as possible, the flight qualifiable form of the circuit. These are somewhat contradictory constraints.

The following paragraphs will expand upon the constraints and illustrate, briefly, the resulting equipment.

A. Implementation Constraints

In order to minimize the flight qualification development phase of the Standard Command Detector, including the SNORE-LOCK circuit, the design of the breadboard was constrained to use those circuit elements which had already passed Preferred Part Qualification. The second most important consideration was that of power dissipation. Therefore, 54L series logic elements were used, except where speed considerations prevented their use. Finally, package count, a measure of complexity, was used to constrain the design.

The breadboard design included parameter entry logic which would not be used in the flight design. This was done to facilitate the optimization of those parameters.

B. Construction

The breadboard was built on a wire-wrap card (type B). A photograph of the completed breadboard is presented as Figs. 5 and 6. This approach was used because of extensive experience with it for both breadboard and finished systems. In addition, the "Card" is supported by mounting and interconnect hardware and support software to permit rapid and accurate construction and documentation. Further, the wire-wrap approach facilitates changes while maintaining stable "brass board" quality.

IV. Integration and Preliminary Performance Tests

The design, construction, and functional testing of the SNORE-LOCK was performed independently of that performed for the command detector. The interface between the two sections was the only aspect of the total system design that required mutual and coordinated effort.

A. Integration

The integration of the SNORE-LOCK was accomplished in an orderly manner with no difficulties. Certain signals of the system were inspected after integration to validate that the interface had been done properly.

B. Preliminary Performance Tests

Preliminary performance tests of the SNORE-LOCK circuit were performed using the command detector, a simulated signal channel, and specialized instrumentation. Two types of tests were conducted: (1) the value of computed SNORE was compared with that of the input SNR, and (2) the probability of falsely indicating the lock status at an input of 10.5 dB SNR.

1. SNORE Value Tests. The value of SNORE was measured as a function of bit rate and input SNR. At the time of the tests the detector loss had been measured to be 1.5 dB. Figure 7 presents the results of these tests. Ten values of DATA and ERROR were accumulated for each SNORE computation. The 8-bit per second results are thought to be caused by truncation errors. This has not been modeled as yet (Ref. 3).

2. **Lock Indicator Tests.** The performance of the lock indicator was measured at one bit rate and one input signal level. Ten accumulations of DATA and ERROR and two successive comparisons were used for the lock indication (See Fig. 8). In addition, the bit error rate (BER) at the output was measured. This allowed a closer comparison of the results with the theoretical model (Ref. 4).

From these results it would appear that the false-in-lock (FIL) probability is better than that predicted by theory. Unfortunately, this results from a design decision which resulted from truncation problems. The error accumulation is set to −1 at the start of an accumulation cycle to prevent dividing by zero. This lowers the values of SNORE and results in shifting the lock probabilities curves to the left. At low values of threshold, truncation errors affect the P_{FIL} result.

V. Conclusions

The results of the preliminary tests indicate that the operation of the SNORE and lock circuits is as predicted by the theory. Extensive and expensive discrete simulations would be required to improve upon these results.

References

1. Simon, M. K., and Springett, J. C., *The Theory, Design, and Operation of the Suppressed Carrier Data-Aided Tracking Receiver*, Technical Report 32-1583, pp. 44–46, Jet Propulsion Laboratory, Pasadena, Calif., June 15, 1973.
2. Emerson, R. F., "A Multiple-Rate Command System," in *The Deep Space Network Progress Report 42-25*, pp. 94–107, Jet Propulsion Laboratory, Pasadena, Calif., Feb. 15, 1975.
3. Lipes, R. G., "Analysis of Command Detector Signal-to-noise Ratio Estimator," in *The Deep Space Network Progress Report 42-31*, pp. 75–83, Jet Propulsion Laboratory, Pasadena, Calif., Feb. 15, 1976.
4. Lipes, R. G., "Analysis of Command Detector In-Lock Monitoring," in *The Deep Space Network Progress Report 42-32*, pp. 70–73, Jet Propulsion Laboratory, Pasadena, Calif., Apr. 15, 1976.

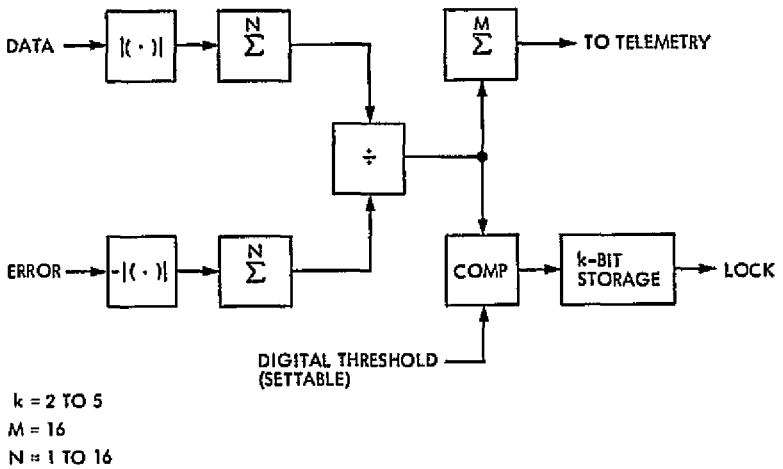

Fig. 1. Functional block diagram of SNORE-LOCK

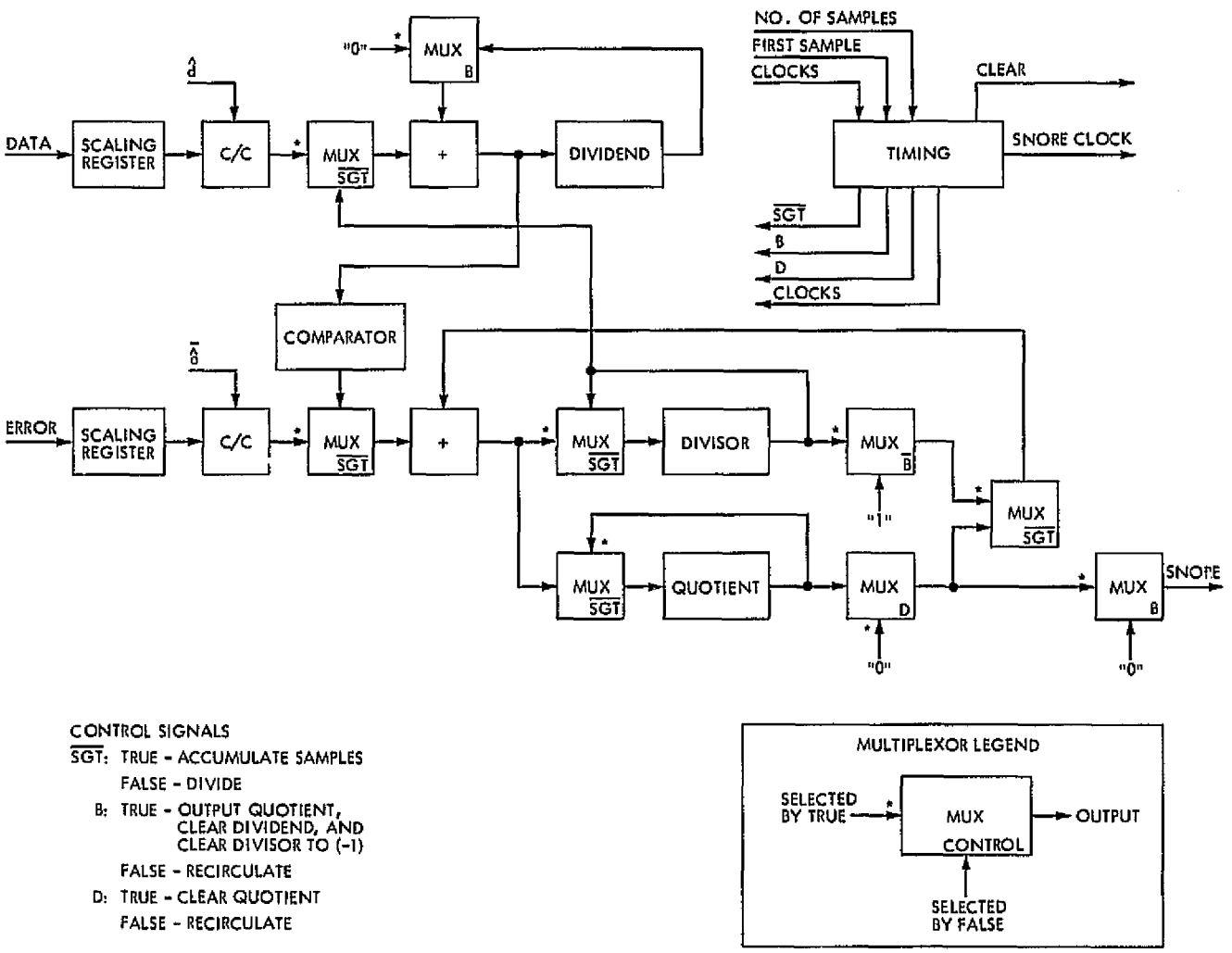

Fig. 2. Logic block diagram of accumulators and divider

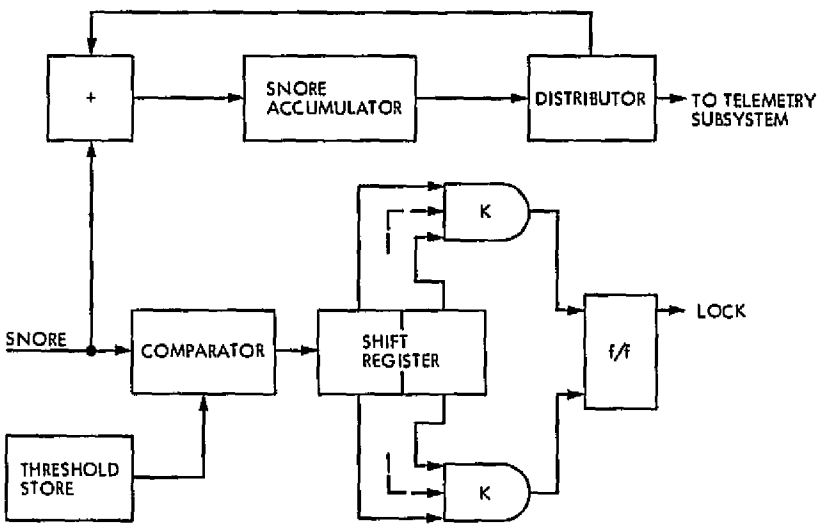

Fig. 3. Logic block diagram of SNORE accumulator and LOCK indicator

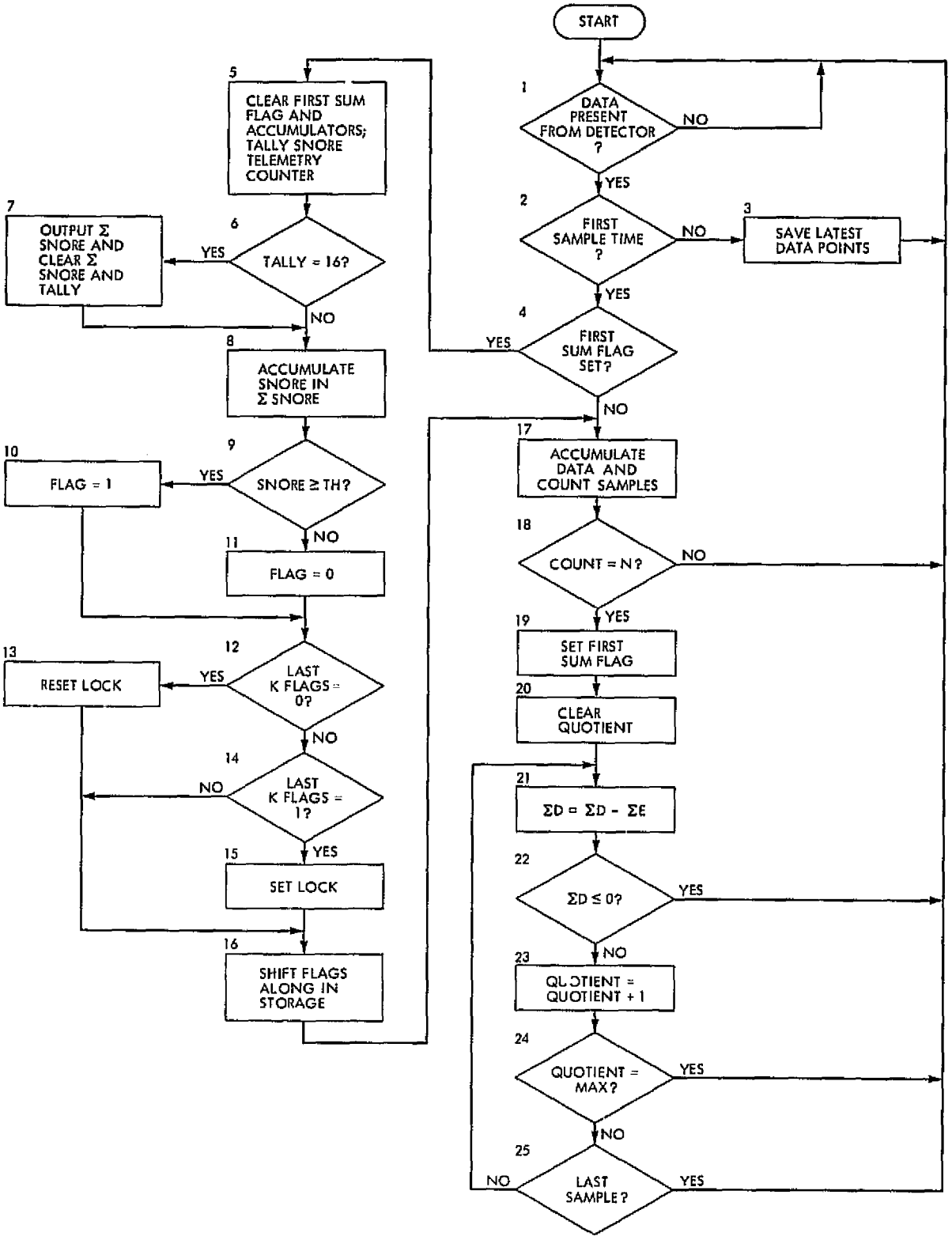

Fig. 4. SNORE–LOCK algorithm flowchart

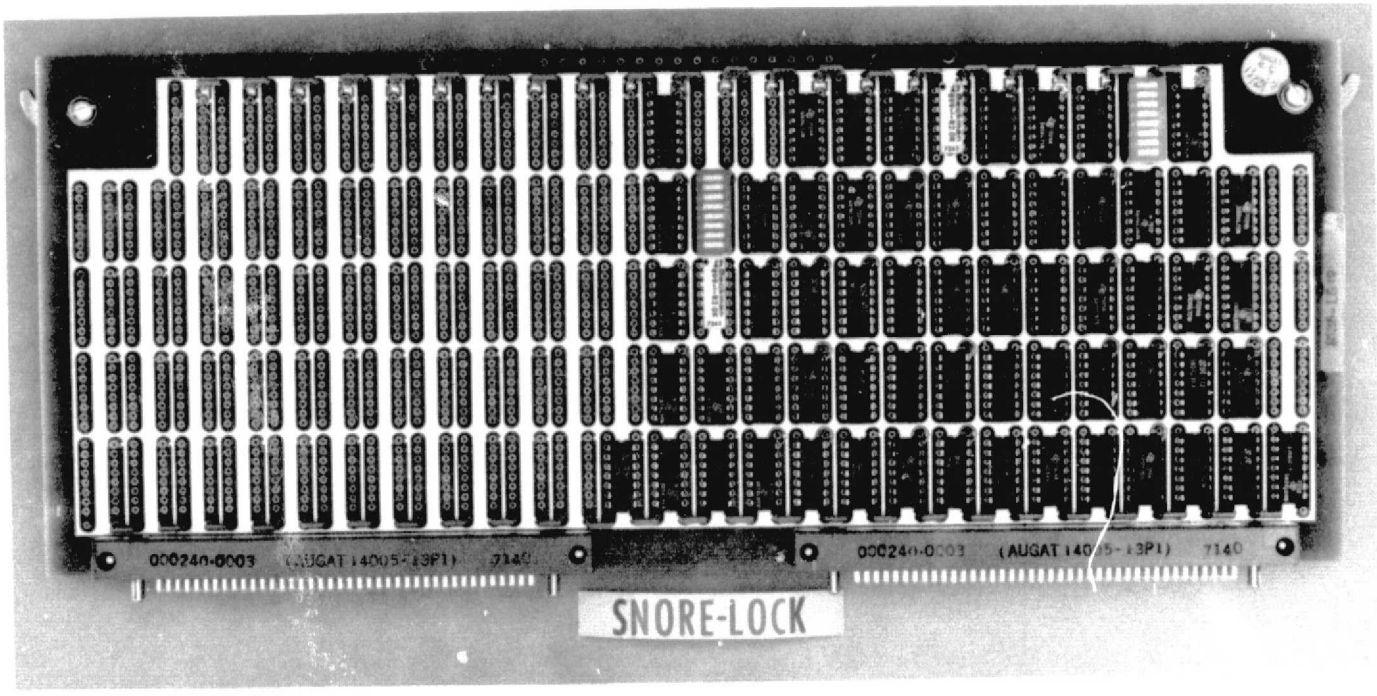

Fig. 5. Component side of SNORE-LOCK wire-wrap card

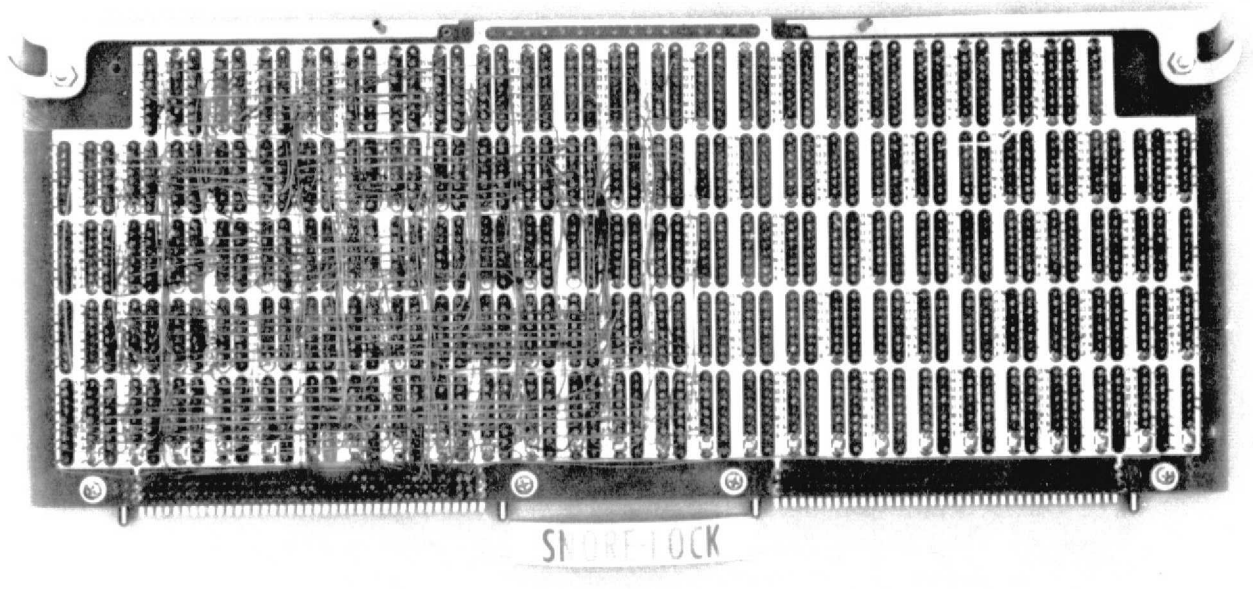

Fig. 6. Wiring side of SNORE-LOCK wire-wrap card

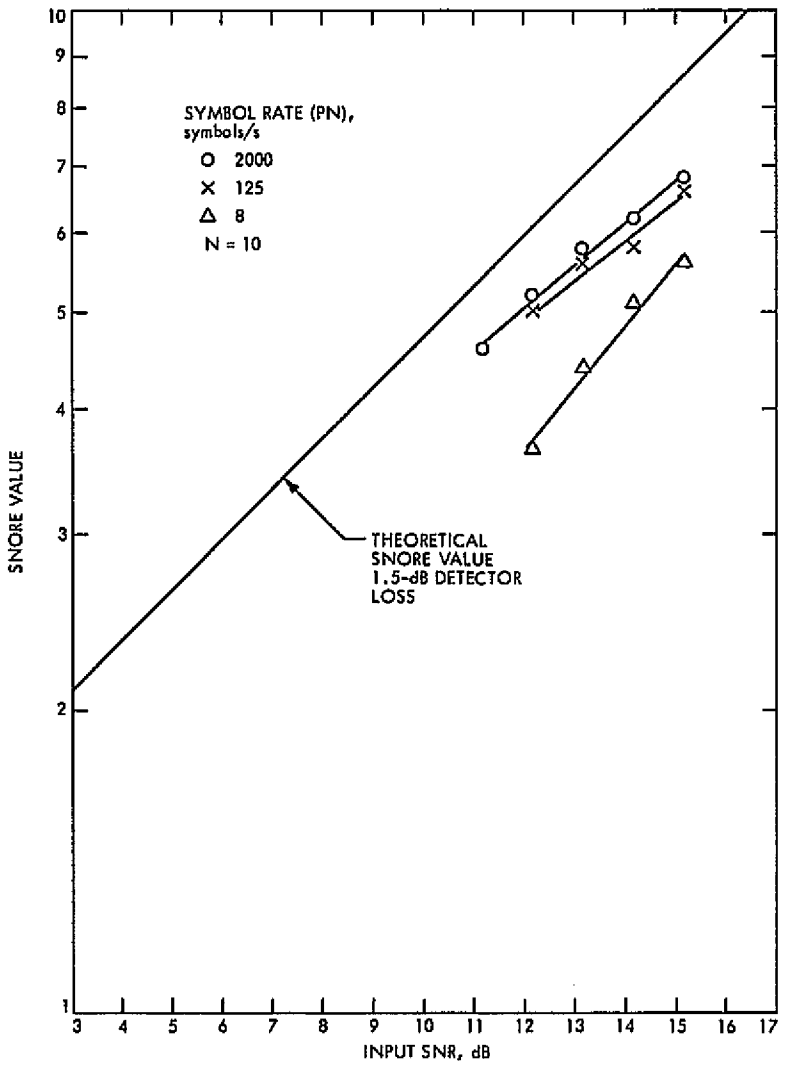

Fig. 7. Input SNR vs SNORE at several symbol rates

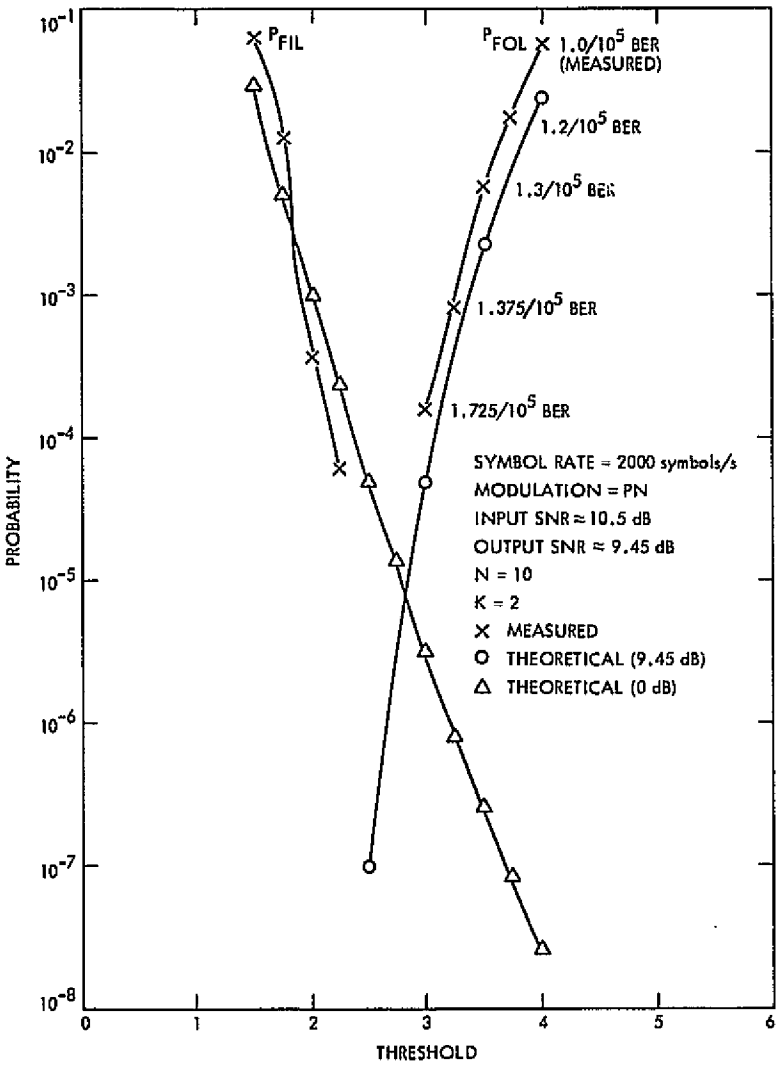

Fig. 8. LOCK indicator tests

Three-Level Sampler Having Automated Thresholds

R. F. Jurgens
Communications Systems Research Section

A three-level sampler is described that has its thresholds controlled automatically so as to track changes in the statistics of the random process being sampled. In particular, the mean value is removed and the ratio of the standard deviation of the random process to the threshold is maintained constant. The system is configured in such a manner that slow drifts in the level comparators and digital-to-analog converters are also removed. The ratio of the standard deviation to threshold level may be chosen within the constraints of the ratios of two integers N and M. These may be chosen to minimize the quantizing noise of the sampled process. Proper ratios have been given by Rodemich for gaussian random processes.

The advantages of computing autocorrelation functions from hard-clipped noise processes were originally formulated by VanVleck (Ref. 1). This procedure results in a degradation of the power spectra by a factor of $\pi/2$ and is usually offset by increasing the observing time by a factor of nearly 2.5. Rodemich demonstrated that considerable improvement could be made by extending the number of quantizing levels (Ref. 2). The new JPL-Haystack autocrosscorrelator system (HAC) can support 2×2 (usual hard-clipped mode), 3×2, and 3×3 level products in the formation of the autocorrelation function. This system has been described by Jurgens (Ref. 3). A one-bit data sampler having automated dc removal has been described by Brokl and Hurd (Ref. 4). Their procedure has been extended to a three-level sampler having automated dc removal and threshold tracking to remove amplifier gain variations in the receiver system and to establish optimum thresholds for minimizing the quantizing noise. The resulting sampler is designed with Motorola emitter-coupled logic (MECL) and operates in excess of 100 MHz. This note describes the operation of the sampler and the dynamics of the feedback loops.

Let $x(t)$ be a stationary zero-mean gaussian random process having variance σ_x^2. This process is assumed to be contaminated by drifts in the receivers and amplifiers such that a new time varying process $y(t)$ is formed, where $y(t) = a(t)x(t)+b(t)$. $a(t)$ and $b(t)$ are slowly varying, and $a(t)$ is always assumed to be greater than zero. The process $y(t)$ is to be sampled; however, the sampling thresholds may be chosen so as to remove the drifts $a(t)$ and $b(t)$ simultaneously. Figure 1 shows a simple three-level sampler which may be extended to operate for any number of levels. The voltages v_+ and v_- control the upper

and lower thresholds of the comparators, respectively. The comparator C_1 gives a 1 state output when clocked if $y(t) > v_+$ and zero otherwise. The comparator C_2 gives a 1 state output if $y(t) < v_-$ and zero otherwise, three sample levels result and will be called 1, 0, and −1. The threshold voltages may be determined from certain running averages calculated from the outputs v_{10} and v_{20}. The system then acts simultaneously as an automatic gain control and a dc removal control.

Any number of schemes can be used to establish the feedback signals v_+ and v_-, but perhaps the simplest scheme is to force the average ratio of 1's to (0's plus −1's) to be a fixed ratio while simultaneously forcing the number −1's to (1's plus 0's) to maintain the same ratio as suggested by E. R. Rodemich. Figure 2 shows a simple scheme to accomplish this. The NOR gate, G1, yields a 1 state for 0's of the truth table of Fig. 1, and the 1's and 0's are merged by the OR gate G_2, and likewise the −1's and 0's by the gate G_3. The divide by N and divide by M counters establish a proper balance between the 1's and everything else and the −1's and everything else. If the counts going into the up-down counters UD1 and UD2 are on the average equally up and down the output count remains nearly constant and the voltage at the output of the digital-to-analog converters (DAC) remains constant. If, for example, the rate of 1's relative to the 0's and −1's is too large, UD1 will count upward increasing the output of DAC1 which raises the threshold voltage v_+ and decreases the 1's count rate. DAC2 generates the lower reference voltage which is normally negative.

The dynamics of the system may be modeled by observing that the up–down counters combined with the digital-to-analog converters act as integrators of the average rates of up counts minus the down counts. The equation for the v_+ signal may be written in terms of the rate of 1's, r_1, and the rate of 0's or −1's, r_0.

$$v_+(t) = S \int_0^t [r_1(u) - r_0(u)]\,du$$

where S is the sensitivity of the DAC, and the counters are assumed to be set to 0 at $t = 0$. $r_1(t)$ is clock rate times the probability of 1's divided by N, while $r_0(t)$ is the clock rate times the probability of 0's or −1's divided by M. Therefore if C_k is the clock rate, then

$$v_+ = s \int_0^t C_k P\{y > v_+(u)\}/N - C_k P\{y \le v_+(u)\}/M\,du \qquad (1)$$

If the random process $x(t)$ is gaussian the probabilities in Eq. (1) may be calculated from the probability density functions of either x or y.

$$p(x) = \frac{1}{\sqrt{2\pi}\sigma_x} \exp\,[-1/2(x/\sigma_x)^2] \qquad (2)$$

and

$$p(y) = \frac{1}{\sqrt{2\pi}a\sigma_x} \exp\,[-(x-b)^2/2a^2\sigma_x^2] \qquad (3)$$

Thus

$$P\{y \le v_+(t)\} = P\left\{x \le \frac{v_+(t) - b}{a}\right\} = F_x\left(\frac{v_+ - b}{a}\right) \qquad (4)$$

where

$$F_x\left(\frac{v_+ - b}{a}\right) = \int_{-\infty}^{\frac{v_+ - b}{a}} \frac{1}{\sqrt{2\pi}\,\sigma_x} \exp\,[-1/2(x/\sigma_x)^2]\,dx \qquad (5)$$

and

$$P\{y > v_+(t)\} = 1 - F_x\left(\frac{v_+ - b}{a}\right) \qquad (6)$$

Replacing the probabilities in Eq. (1) with Eqs. (4) and (6) and differentiating both sides yields:

$$\frac{dv_+}{dt} = SC_k\left\{\frac{1}{N} - \left(\frac{1}{N} + \frac{1}{M}\right) F_x\left(\frac{v_+ - b}{a}\right)\right\} \qquad (7)$$

A somewhat more convenient form may be obtained by replacing $F_x(x)$ with

$$\frac{1}{2}\left[1 + \operatorname{erf}\left(\frac{x}{2\,\sigma_x}\right)\right]$$

giving

$$\frac{dv_+}{dt} = -1/2\,SC_k\left\{\left(\frac{1}{N} + \frac{1}{M}\right)\operatorname{erf}\left(\frac{v_+ - b}{\sqrt{2}\,a\sigma_x}\right) - \left(\frac{1}{N} - \frac{1}{M}\right)\right\} \qquad (8)$$

Likewise, the differential equation for $v_-(t)$ may be obtained:

$$\frac{dv_-}{dt} = -1/2\,SC_k\left\{\left(\frac{1}{N}+\frac{1}{M}\right)\operatorname{erf}\left(\frac{v_- - b}{\sqrt{2}\,a\sigma_x}\right) + \left(\frac{1}{N}-\frac{1}{M}\right)\right\} \tag{9}$$

The arithmetic mean of v_+ and v_- is the effective mean or dc feedback signal, and one half the distance between the thresholds is the effective threshold or gain feedback signal, i.e.

$$v_{dc} = (v_+ + v_-)/2 \tag{10}$$

and

$$v_g = (v_+ - v_-)/2 \tag{11}$$

Equations (8) and (9) are first-order nonlinear differential equations having nonconstant coefficients and driving functions. If $a(t)$ is constant and greater than zero, the system is stable for all values of the product SC_k and the function $b(t)$. In practice, the up-down counters can overflow if the required threshold voltages fall outside the range of the DACs. In this case a continuous hunt condition is established until the values of a and b are restored to a range for which steady state may be achieved.

The steady-state conditions are found by setting dv_-/dt and dv_-/dt to zero in Eqs. (8) and (9). This yields

$$v_{+ss} = \sqrt{2}\,a\sigma_x \operatorname{erf}^{-1}\left(\frac{M-N}{M+N}\right) + b \tag{12}$$

$$v_{-ss} = \sqrt{2}\,a\sigma_x \operatorname{erf}^{-1}\left(\frac{M-N}{M+N}\right) + b \tag{13}$$

$$v_{dc} = b$$

$$v_g = \sqrt{2}\,a\sigma_x \operatorname{erf}^{-1}\left(\frac{M-N}{M+N}\right) \tag{15}$$

The ratio of $v_g/a\sigma_x$ is usually established to minimize the quantizing error in some manner. The values of M and N are chosen in Eq. (15) to closely approximate this ratio; however, large values of M and N increase the time constant of the system which may or may not be desirable. Rodemich has shown that a ratio of 0.612 yields a minimum variance for power spectra computed from the sampled data when quantized to 3 levels (Ref. 3). Values of $N = 4$ and $M = 11$ give a close approximation to this value and are sufficiently small as to permit a fairly rapid response time.

The effective cutoff frequency of the system may be determined by determining the small signal time constant of the differential equation near the steady-state operating point. This may be accomplished by letting $v_+ = v_{+ss} + \Delta v$ in Eq. (8). This leads to a first-order linear differential equation given as Eq. (16). The effective

$$\frac{d\Delta v}{dt} = -SC_k\left(\frac{1}{N}+\frac{1}{M}\right)\frac{1}{a\sigma_x} \exp\left(-\left[\operatorname{erf}^{-1}\left(\frac{M-N}{M+N}\right)\right]^2\right)\Delta v \tag{16}$$

time constant is the reciprocal of the multiplier of Δv in Eq. (16) and is dependent upon the standard deviation of the input noise process, $\sigma_y = a\sigma_x$, as well as the physical parameters of the system. Figure 3 shows the response of the system when $b(t)$ is a unit step function. Note that $v_g(t)$ is disturbed momentarily by the positive step because $v_+(t)$ and $v_-(t)$ do not respond equally to a positive excitation. Also shown is the step response for $a(t)$ between 1.0 and 1.75 for b equal to zero. Digital computer simulation of the system using pseudorandom gaussian noise yields essentially the same results.

Frequency analysis of the sampled function verifies that the dc components of y are removed and that the thresholds are properly established. The threshold signals exhibit a jitter caused by the stochastic nature of the sampled signal and due to the finite resolution of the digital-to-analog converters. The low-frequency components of the signal are, of course, tracked out causing the system to act as a high-pass filter having a cutoff frequency defined by the time constant of Eq. (16). If N and M are made arbitrarily large with the proper ratio maintained, the cutoff frequency may be made arbitrarily low. The dc offsets and slow drifts would be tracked out, and the fluctuation of the threshold voltages v_+ and v_- would be due primarily to the finite resolution of the DACs and equal in peak-to-peak voltage to the voltage resolution of the DACs.

References

1. VanVleck, J. H., *The Spectrum of Clipped Noise*, Lab. Report No. 51, Harvard Radio Research, 1943.

2. Rodemich, E. R., "Spectral Estimates Using Nonlinear Functions," *Annals of Math. Stat.*, Vol. 37, pp. 1237–1256, 1965.

3. Jurgens, R. F., "Theory, Operation, and Computer Programming of the 512-Lag Correlator System," *The Deep Space Network Progress Report* 42-32, pp. 164–77, Jet Propulsion Laboratory, Pasadena, Calif., April 1976.

4. Brokl, S. S., and Hurd, W. J., "Digital DC Offset Compensation of Analog-To-Digital Converters," in *The Deep Space Network*, Technical Report 32-1526, Vol. XVII, pp. 45–47, Jet Propulsion Laboratory, Pasadena, Calif., Oct. 15, 1973.

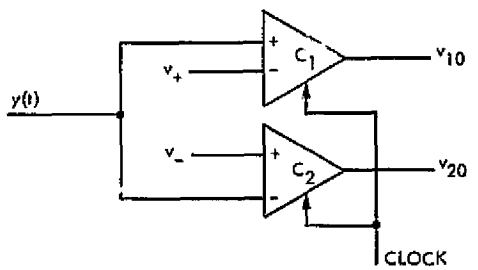

v_{20}	v_{10}	SAMPLE STATE
0	0	0
0	1	1
1	0	−1
1	1	NOT POSSIBLE

Fig. 1. Simple three-level sampler and output truth table defining the three states in terms of the comparator output signals v_{10} and v_{20}

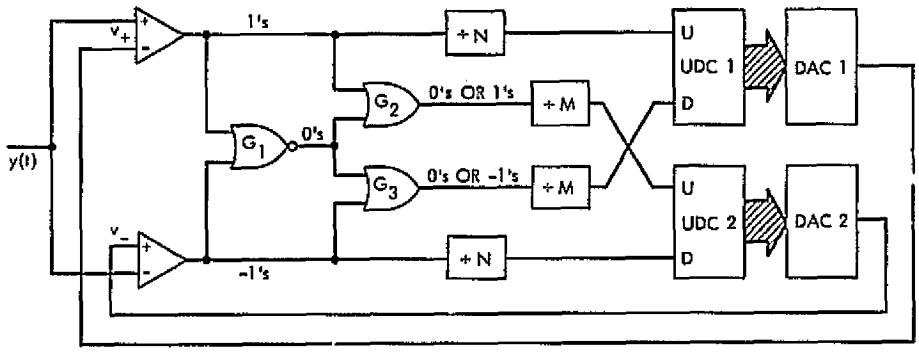

Fig. 2. Block diagram of a simple feedback controlled designed to establish the threshold voltages v_+ and v_- so as to remove dc offsets and gain variations in the input signal

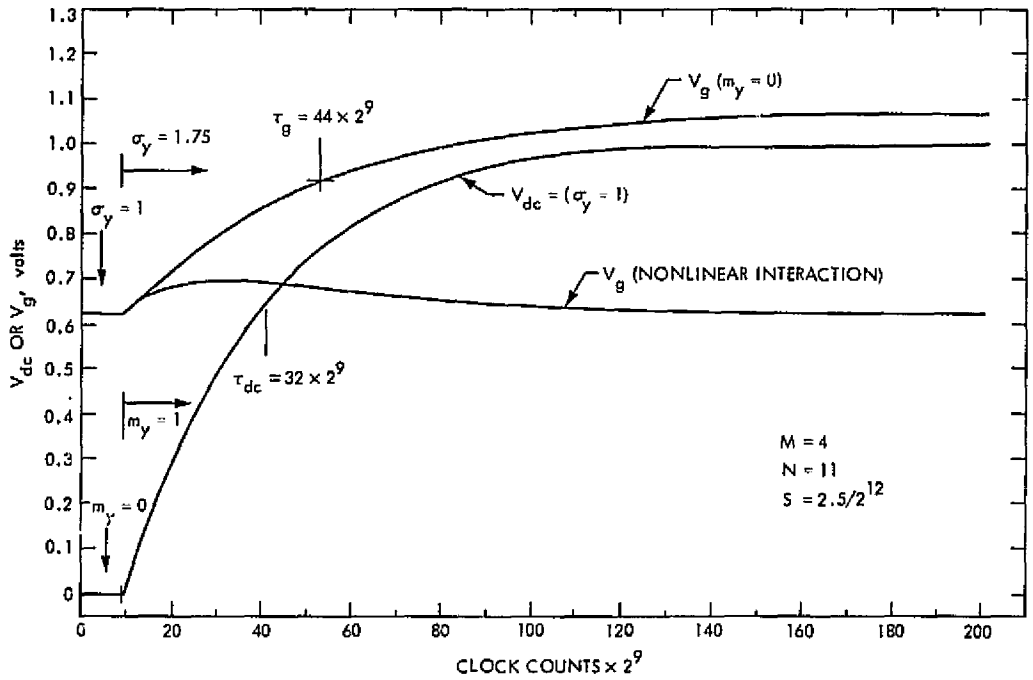

Fig. 3. Response of effective feedback signals v_y and v_{dc} to step function excitations in the mean m_y and the standard deviation σ_y. The interaction of v_y for a step in m_y is also shown. The relative size of the interaction becomes smaller as the step size is decreased.

N77 10101

An Algebraic Approach to Image De-smearing: Symmetries of Polynomials and Their Zeros

D. L. Johnson
Communications Systems Research Section

Frequently a photograph received from a spacecraft will be "smeared" by some process, e.g., by camera motion. Algebraically such smearing can be represented as $p = \sigma f$, where σ is the true picture, p is the received picture, and f is the smearing function. (p, σ, and f are polynomials in two variables x and y.) Thus, in principle, σ can be recovered by multiplying p by $1/f$. However, there are problems involved in computing $1/f$; this paper investigates some of them.

I. Introduction

It is often the case that a photograph received from a spacecraft will be "smeared" by some process, e.g., by the motion of the camera while the shutter is open. In this article we will study one aspect of the problem of smear compensation.

We assume the original picture is uniformly sampled, and thereby discretized into cells which are labeled with coordinates (a,b); we shall represent the picture by a polynomial in two abstract variables x,y:

$$\sigma(x,y) = \sum_{a,b} \sigma_{a,b}\, x^a y^b$$

This representation means simply that the pixel with integer coordinates (a,b) has brightness level $\sigma_{a,b}$. We further assume that the smearing process can be represented by a *point-smear polynomial* $f(x,y)$, i.e., that the smeared version of the original picture is given by

$$p(x,y) = \sigma(x,y)\, f(x,y)$$

(In particular, $f(x,y)$ itself represents the smeared version of the "unit impulse signal," $\sigma(x,y) = 1$.) If we are given p (the received picture) and f (which can be computed from knowledge of spacecraft geometry), we can hope to recover the original picture σ as

$$\sigma = p(x,y)/f(x,y)$$

So we need a practical representation of the rational function $p(x,y)/f(x,y)$.

One approach is to expand $1/f(x,y)$ as a power series in x and y (with negative powers permitted). This power series can then be multiplied formally by p to recover σ. However, in order for this procedure to give physically meaningful results, it is necessary (for technical reasons we shall omit) that the power series (a) has coefficients approaching 0 as $|a|$ or $|b| \to \infty$, or, even better, (b) con-

verges for all values on the "unit torus" = $\{(x,y):|x| = |y| = 1\}$ (Condition (b) implies condition (a).) These two conditions turn out to be equivalent to (a) f has only a finite number of zeros on the unit torus; (b) f has no such zeros.

The purpose of this paper is then to study the zeros of a polynomial on the unit torus.

II. L-Polynomials

I want to examine the zeros of a polynomial $f(x,y)$ in two (complex) variables lying on the "unit torus," that is, the points (x,y), where $|x| = |y| = 1$ (this is the generalization of the "unit circle" to two complex variables; I shall call such zeros "unimodular"). We shall find that a certain symmetry operation is useful in this context, and in fact that certain "symmetric" polynomials always do have roots.

First note the following: the function $kx^ay^bf(x,y)$, where $k \neq 0$ is a constant and a,b are integers, has exactly the same zeros on the unit torus U^2 as does f (this is true even when a or b is less than zero); for this reason we will call two polynomials f,g *equivalent*, written $f \simeq g$, if $g = kx^ay^bf$. It will be convenient to include in our considerations not only polynomials in x,y, but all functions of the form $x^ay^bf(x,y)$, where f is a polynomial function, and a,b may be negative—that is, polynomials in x,y, $1/x$, and $1/y$. Our notion of equivalence clearly extends to these functions, which we will call *L-polynomials*. Every equivalence class of *L-polynomials* has an obvious representative, namely, a *polynomial* having *no factors of x or y*. That is, if f is an L-polynomial, multiply it (if there are negative degree terms) or divide it (if the degrees of the terms are all positive) by suitable powers of x and y to achieve a function equivalent to f and having the above italicized properties. This polynomial (which is only determined up to a constant multiple) will be called the *reduced form* of f, and any polynomial without factors of x or y, *reduced*.

We introduce these definitions:

(a) The *x-degree* of f (an L-polynomial), written $\deg_x f$, is the highest power of x occurring in f; likewise $\deg_y f$.

(b) The x-subdegree $\mathrm{sbdg}_x f$ is the *lowest* power of x occurring in (the terms of) f; likewise $\mathrm{sbdg}_y f$.

(c) The range of x (in f), written $\mathrm{rng}_x f$, is $\mathrm{rng}_x f = \deg_x f - \mathrm{sbdg}_x f$; likewise for $\mathrm{rng}_y f$.

Note that if f is a *polynomial*, then $\mathrm{sbdg}_x f$ is just the largest power of x dividing f; in fact more generally, we have for any L-polynomial f, $x^{-\mathrm{sbdg}_x f} \cdot y^{-\mathrm{sbdg}_y f} \cdot f$ is a reduced form of f.

The set of L-polynomials form a *ring*, that is, the product, sum, and difference of two L-polynomials is another L-polynomial. In this ring we have a greatest common divisor (GCD)) d of any two elements f,g; we write $d = (f,g)$. The GCD here is the usual GCD of polynomials, but as in all rings, it is only defined up to a multiple by a *unit*; a unit is an L-polynomial u such that $1/u$ is *also* an L-polynomial. Later we will need to work with the GCD of L-polynomials, and we will have use for the following:

If u is a unit in the ring L of L-polynomials, then u is a *monomial*, that is, $u = kx^ay^b$.

Proof: Let $1/u = v$, v an L-polynomial. Then $uv = 1$. Let U,V be reduced forms of u, v, with $U = x^\alpha y^\beta u$ and $V = x^\gamma y^\delta v$: then $UV = x^{\alpha+\gamma}y^{\beta+\delta}$. Since U and V are *polynomials*, the unique factorization of polynomials tells us that U must be of the form kx^ay^b, as well as V. Q.E.D.

The above has the following corollary: The GCD $d = (f,g)$ of two L-polynomials is only defined up to multiple by a unit; but the units are kx^ay^b: thus d is defined up to the *equivalence* of L-polynomials. Hence we would be more correct to write: $d \simeq (f,g)$.

III. The Adjoint Operation

We now introduce our main tool in investigating the unimodular zeros of $(L-)$ polynomials, an operation * on L-polynomials which we call the *adjoint*, defined by:

$$f^*(x,y) = \overline{f(1/\bar{x}, 1/\bar{y})}$$

where the bar denotes complex conjugation This operation simply replaces x by $1/x$ and y by $1/y$, and conjugates all the coefficients of f. Thus, f^* is also an L-polynomial in x,y. We also have:

(1) $(f^*)^* = f$

(2) $(f + g)^* = f^* + g^*$

(3) $(fg)^* = f^*g^*$

(4) $\deg_x f^* = -\mathrm{sbdg}_x f$ (ditto y)

(5) $(f,g)^* \simeq (f^*,g^*)$

The first four are clear. To prove the last statement, suppose d divides f and g, with $f = Fd$, $g = Gd$, where d, F, G are also L-polynomials. Then we have, using (3),

$$f^* = F^*d^*, \qquad g^* = G^*d^*$$

i.e., d^* divides f^* and g^*, *i.e.*, d^* divides (f^*,g^*). In particular, putting $d = (f,g)$, we get $(f,g)^*$ divides (f^*,g^*). Replacing f by f^* and g by g^* and using (1), we have then also:

$$(f^*,g^*)^* \text{ divides } (f,g), \text{ and so } (f^*,g^*) \text{ divides } (f,g)^*$$

Thus, $(f,g)^*$ and (f^*,g^*) divide each other, that is, they are unit multiples of each other, or as we saw in Section II, $(f,g)^* \simeq (f^*,g^*)$. Q.E.D.

The connection of the unimodular zeros of f and the adjoint operation lies in the following:

Proposition 1: If $(x,y) = (\alpha,\beta)$ is a root of $f(x,y) = 0$ on U^2, i.e., $f(\alpha,\beta) = 0$ and $|\alpha| = |\beta| = 1$, then $f^*(\alpha,\beta) = 0$ also.

Proof: $f^*(\alpha,\beta) = \overline{f(1/\bar{\alpha}, 1/\bar{\beta})}$; but $|\alpha| = |\beta| = 1$ means $1/\bar{\alpha} = \alpha$, $1/\bar{\beta} = \beta$, so

$$f^*(\alpha,\beta) = \overline{f(\alpha,\beta)} = \bar{0} = 0$$

Corollary: If f is an L-polynomial, then the unimodular roots of f lie among the common roots of f and f^*. Hence, either these roots are *finite* in number, or f and f^* have a common polynomial factor.

Proof: We may assume f is reduced, and replace f^* by its reduced form g, since these have the same unimodular roots. Then the zeros of f on U^2 are also zeros of g. It is well known (Bezout's theorem) that two polynomials in x,y have either a common factor or otherwise only a finite number of common roots; in the latter case, there are *a fortiori* only a finite number of zeros of f on U^2.

IV. Self-Adjoint Polynomials

The previous proposition told us that if f and f^* have no (nontrivial) common divisor, that is, $(f,f^*) \simeq 1$, then f has only a finite number of zeros on U^2. If f has an infinite number of zeros, then $d \simeq (f,f^*)$ is not $\simeq 1$ (that is, d is not a monomial kx^ay^b). Let's see how this d behaves under the adjoint operation. We have:

$$d^* \simeq (f,f^*)^* \simeq (f^*,f^{**}) \simeq (f^*,f) \simeq (f,f^*) \simeq d$$

That is, d is *equivalent to its adjoint.* This gives rise to the *Definition:* An L-polynomial f is called self-adjoint if $f^* \simeq f$, that is, if $f^* = kx^ay^bf$ for some constant $k \neq 0$ and integers a,b. The triple (k,a,b), which indicates how f must be changed to get f^*, we will call the *translation character* of f.

Note that this definition entails that $|k| = 1$: for if $r > 0$ is the maximum absolute value of the coefficients in f, then it is also that of f^*, since these coefficients are conjugate to those of f. But the maximum absolute value of the coefficients of kx^ay^bf is clearly $|k|r$: so $|k|r = r$ and $|k| = 1$. In particular, if f is a *real* L-polynomial (i.e., real coefficients), then k is clearly also real and so $k = \pm 1$.

Here are some examples of self-adjoint polynomials:

(a) $f = x^2 + 1$: $f^* = x^{-2} + 1 = x^{-2}(x^2 + 1)$: so $(k,a,b) = (1, -2,0)$.

(b) $f = \alpha x^2 + e^{i\theta}\bar{\alpha}y$: $f^* = \bar{\alpha}x^{-2} + e^{-i\theta}\alpha y^{-1} = e^{-i\theta}x^{-2}y^{-1}(e^{i\theta}\bar{\alpha}y + \alpha x^2)$ so $(k,a,b) = (e^{-i\theta},-2,-1)$.

(c) For any L-polynomial g, $f = g + g^*$; then $f^* = f$, and $(k,a,b) = (1,0,0)$.

(d) For any L-polynomial g, $f = g - g^*$; then $f^* = g^* - g = -f$ so $(k,a,b) = (-1,0,0)$.

(e) For any L-polynomial g,$f = g \pm xg^*$; then $f^* = g^* \pm x^{-1}g = \pm x^{-1}(g \pm xg^*)$: so $(k,a,b) = (\pm 1,-1,0)$.

Other examples can be formed in this way.

Let's now see how self-adjointness behaves under equivalence. We have:

Proposition 2: If f is self-adjoint with translation character (k,a,b), then $g = \lambda x^\alpha y^\beta f$ is also self-adjoint, with translation character

$$\left(\frac{\bar{\lambda}}{\lambda}k, a - 2\alpha, b - 2\beta\right)$$

Proof:

$$g^* = \bar{\lambda}x^{-\alpha}y^{-\beta}f^* = \bar{\lambda}x^{-\alpha}y^{-\beta}(kx^ay^bf)$$

$$= \bar{\lambda}x^{-\alpha}y^{-\beta}\left(kx^ay^b\,\frac{1}{\lambda x^\alpha y^\beta}\,g\right)$$

$$= \frac{\bar{\lambda}}{\lambda}\,kx^{a-2\alpha}y^{b-2\beta}g$$ Q.E.D.

The above shows us that $g \simeq f$ and f self-adjoint $\rightarrow g$ self-adjoint; further, if we are permitting complex coefficients, by appropriately choosing λ, we can "normalize" f so that its k is 1: in fact if k_f is $e^{i\theta}$, then choose $\lambda = e^{i\theta/2}$. Then the k for $g = \lambda_f$ is

$$\frac{\bar{\lambda}}{\lambda} k = \frac{e^{-i\theta/2}}{e^{i\theta/2}} e^{i\theta} = 1$$

If we are restricting to real coefficients, however (as when f itself is real), then λ will be real, $\bar{\lambda}/\lambda = 1$, and so $k = \pm 1$ is *unchanged* under equivalence: k is thus an invariant of the self-adjoint equivalence class. We can also see that there are two other invariants of this class: the translation exponents a and b, while not invariant themselves, *are* invariant *mod* 2 since $a - 2\alpha \equiv a \bmod 2$, $b - 2\beta \equiv b \bmod 2$. Thus, in the complex case, the vector $[(a,b) \bmod 2]$ of numbers mod 2 gives us an invariant of the self-adjoint type of f, which we will call simply the *character* of f. If f is real, k is also an invariant, and if we define $\epsilon = 0 \bmod 2$ for $k = 1$, $\epsilon = 1 \bmod 2$ for $k = -1$, then we have a "character" for f consisting of *three* mod 2 numbers (ϵ,a,b). These "characteristic vectors" for f depend only on the equivalence class of f. Recall that the unimodular zero set of f also depends only on its equivalence class; it should not be surprising then that (as we shall see) the character of f influences the behavior of its zero set.

Here is a table of real examples (in some sense minimal ones) showing that every mod 2 vector (ϵ,a,b) actually occurs as the character of some polynomial:

Polynomial	Mod 2		
	ϵ	a	b
1	0	0	0
$x^2 - 1 \left(\text{or } x - \frac{1}{x}\right)$	1	0	0
$x + 1$	0	1	0
$x - 1$	1	1	0
$y + 1$	0	0	1
$y - 1$	1	0	1
$x + y$	0	1	1
$x - y$	1	1	1

Here now is how the character influences the zero set of a self-adjoint f:

Proposition 3: If the character of a self-adjoint L-polynomial f is not 0 (that is, the zero vector, mod 2), then f has zeros on U^2.

Proof: In the complex case we have seen that we may assume $k = 1$; then

$$f^*(x,y) = \overline{f(1/\bar{x}, 1/\bar{y})} = \overline{f(x,y)} \text{ for } (x,y) \epsilon U^2$$

But since f is self-adjoint,

$$f^*(x,y) = x^a y^b f(x,y) \qquad (k = 1)$$

Hence,

$$\overline{f(x,y)} = x^a y^b f(x,y)$$

Were f never zero on U^2, we could write uniquely

$$f(x,y) = r(x,y) \cdot u(x,y),$$

where $r = |f| > 0$ and $u = f/r$ is of unit modulus, and r and u are continuous functions of $(x,y) \epsilon U^2$. We have then

$$x^a y^b = \frac{\bar{f}(x,y)}{f(x,y)} = [\bar{u}(x,y)]^2$$

Now, as (x,y) travels around any closed curve in the unit torus U^2, u will travel around the unit circle U an integral number of times, by continuity, and hence u^2 will travel around U an *even* integral number of times. But if we let x travel once around the unit circle while holding $y = 1$, $x^a y^b$ goes a times around U, and likewise let $x = 1$ and y move around U, $x^a y^b$ goes b times around U. Hence a and b must both be *even*, i.e., the character (a,b) mod 2 is zero.

In the real case we have a simpler proof: for now f is real when x and y are, i.e., when x and y are ± 1. We have, then, for such x and y,

$$\overline{f(x,y)} = f(x,y) = k x^a y^b f(x,y)$$

so $f(x,y) \neq 0 \rightarrow k x^a y^b = 1$. But if either a or b is odd, or $k = -1$, we can clearly choose $(x,y) = (\pm 1, \pm 1)$ so that $k x^a y^b = -1$, which implies $f = 0$. Q.E.D.

V. The Case of Infinite Zeros

Henceforth, we are going to confine our attention to the case when f has an *infinite number of zeros* on U^2, which

implies $d = (f,f^*)$ is not $\simeq 1$. We can strengthen this statement to:

Proposition 4: f has an infinite number of zeros on U^2 iff the self-adjoint L-polynomial $d \simeq (f,f^*)$ does; in fact, all but a finite number of the zeros of f are zeros of d.

Proof: Putting $f = Fd$, $f^* = Gd$, where F,G are also L-polynomials, then

$$f^* = F^*d^* \simeq F^*d \text{ and } f^* = Gd$$

so

$$G \simeq F^*$$

Hence also $(F,F^*) \simeq (F,G) \simeq 1$: so F and F^* have no common factor, and by the Corollary to Proposition 1, F has only a finite number of zeros on U^2. The zeros of f (on U^2) are the union of those of F and those of d. Q.E.D.

Thus, the zeros of f consist of those of the "self-adjoint part" of f (that is, d), plus a finite number of other, isolated, zeros; so henceforth we shall spend our time elucidating the structure of the zeros of a self-adjoint polynomial d. We already know that if d has non-zero character, it has zeros; the results below will actually show that if d has any zeros, it has an infinite number.

Proposition 5: Let d be a self-adjoint L-polynomial; then its zero set on U^2 consists of a finite number (possibly zero) of real, closed curves on U^2. If the algebraic curve given by $d(x,y) = 0$ is non-singular, or, more generally, if its singularities do not lie on U^2, then these curves are smooth and disjoint.

Proof: We will only prove this for the case when the singularities are off U^2—the full statement follows from an overdose of algebraic geometry. In any case, the locus of $d = 0$ in the complex projective plane* is (a) compact, (b) outside of the singularities, a smooth orientable surface M. The zeros of d on U^2 are simply all points of M satisfying $x = 1/\bar{x}$, $y = 1/\bar{y}$.

Let's consider in more detail the transformation I of the plane given by $x \to 1/\bar{x}$, $y \to 1/\bar{y}$. First of all, I takes M into itself: for $d(x,y) = 0 \to d^*(x,y) = 0$ (since $d^* \simeq d$ and $(x,y) \epsilon U^2$), i.e., $\overline{d(1/\bar{x}, 1/\bar{y})} = 0$, i.e., $d(1/\bar{x}, 1/\bar{y}) = 0$, i.e., $(1/\bar{x}, 1/\bar{y}) \epsilon M$. Second, the fixed points of I are precisely the points of the unit torus, and so if we consider I to be a mapping of M into itself, its fixed points are precisely the zeros of d in U^2. For any non-singular (finite) point (α,β) of M (in particular, for $(\alpha,\beta) \epsilon U^2$, which was by assumption non-singular), either x or y is an analytic function on M which is one to one on a neighborhood (in M) of (α,β): thus, we may examine the behavior of M and the transformation I in a neighborhood (in M) of (α,β) by examining either the x-values alone or the y-values alone. (That is: either the x-values or y-values *determine* the point in a neighborhood of (α,β), so we may identify it from this one value alone, as well as what I has done to it, if I takes it into the same neighborhood.)

In particular, suppose $(\alpha,\beta) \epsilon U^2$, so $|\alpha| = |\beta| = 1$, I fixes (α,β), and x sends (α,β) to α and a neighborhood of (α,β) in M to a neighborhood of α in the complex number line C. The way I acts in this neighborhood in M is faithfully mirrored by the transformation $I_x: x \to 1/\bar{x}$ in C. This I_x fixes α (as it should, since I fixes (α,β) and everything is mirrored faithfully in C), but also a smooth arc passing through α in the x-plane, namely, all points x in a neighborhood α for which $|x| = 1$; the same is thus true in M: the inverse image of these fixed points of I_x in C are fixed points of I, and are a smooth arc in M. Since they are fixed by I, they are also *in* U^2: thus, we have shown that, if $(\alpha,\beta) \epsilon M \cap U^2$ (i.e., is a zero of d in U^2), then there is a smooth arc passing through (α,β), entirely in $M \cap U^2$; also, in our neighborhood of (α,β) these arc's points are the only points in $M \cap U^2$ (again, because this is true of α in C): Thus, $M \cap U^2$ consists locally of smooth arcs; since it is also compact (both M and U^2 are so in the projective plane), then $M \cap U^2$ must be a finite collection of disjoint smooth closed (real) curves.

As an easy Corollary: if d is self-adjoint and has one zero on U^2, then it has an infinite number. Also: d has no isolated zeros. (These apply, for example, to any d with non-zero character.)

VI. Winding Numbers

Let us think of the smooth closed curves of $M \cap U^2$ as *curves on* U^2. We would like to investigate a bit more thoroughly how these curves are situated in U^2. If then α is any closed curve on U^2, it may be parameterized as

$$\alpha(u) = (x(u), y(u)), \quad |x(u)| = |y(u)| = 1$$

*The *complex plane* means here the set of all pairs (x,y) with x and y *complex*; the *real* plane has x,y *real*. Thus, the real plane is two-dimensional, but the complex plane is 4-dimensional (over the *reals*). The real dimension is always twice the complex dimension; thus, an algebraic curve over the *complexes* is two *real* dimensions, although the very word "curve" means one-dimensional.

and u is a parameter, which we may assume travels around the unit circle once as $\alpha(u)$ travels the closed curve once. We then have the *winding numbers of* α, $W_x(\alpha)$ = the number of times $x(u)$ goes around U (in the positive sense) as u goes around U once (also in the positive sense); likewise for $W_y(\alpha)$.

Note that we have chosen an orientation of α in this definition, namely, via our parameterization. If we were to change the parameterization by $u \to \bar{u}$, the curve would be traced in reverse, likewise $x(u)$ and $y(u)$, and so both winding numbers would negate. These winding numbers are, however, well defined mod 2, independent of this choice of orientation.

Likewise, if we have a collection $A = \{\alpha_i\}$ of closed curves (not necessarily disjoint) on U^2, we may define their *total winding numbers*

$$W_x(A) = \sum_i W_x(\alpha_i)$$

and

$$W_y(A) = \sum_i W_y(\alpha_i)$$

The orientations of the various α_i may be chosen in various ways, so the total winding numbers are not well defined (even up to sign); they *are* still, however, well-defined mod 2.

A winding number may be computed in various ways; we shall do it as follows: $W_x(\alpha)$ = the number of times $x(u)$ passes any fixed point $\theta \epsilon U$ in the *positive direction*, counting -1 for passing it in the negative (i.e., clockwise) direction. Modulo 2, this total sum of $+1$'s and -1's is just the number of times $x(u)$ takes any particular value $\theta \epsilon U$ on the curve α; that is, the number of roots u of $x(u) = \theta$.

In particular, let $A = \{\alpha_i\}$ be the collection of curves given by the equation $d = 0$ on U^2, where d is a self-adjoint L-polynomial with translation character (k,a,b). If we put $x = \theta$ in d, we get an L-polynomial

$$Y_\theta(y) = d(\theta,y)$$

an L-polynomial in y alone. The total mod 2 winding number $W_x(A)$ is the number (mod 2) of points on A with $x = \theta$; i.e., it is just the number of solutions of $Y_\theta(y) = 0$ with $|y| = 1$. We have now the following two lemmas:

Lemma 1. $Y_\theta(y)$ is an L-polynomial which for general θ has the same degree, subdegree, and range as that of y in d. Furthermore, Y is self-adjoint in y, with translation monomial $k\theta^a y^b$.

Proof: The first statement is clear (if we just choose θ to be a non-root of the coefficients of the highest and lowest powers of y). As to the second:

$$\begin{aligned} Y^*(y) &= (\text{by definition})\ \overline{Y(1/\bar{y})} = \overline{d(\theta,1/\bar{y})} \\ &= d(1/\bar{\theta},1/\bar{y})\ (\text{since } |\theta| = 1) = d^*(\theta,y) \\ &= k\theta^a y^b d(\theta,y) = k\theta^a y^b\, Y(y) \end{aligned}$$ Q.E.D.

Lemma 2. If $Y(y)$ is a self-adjoint L-polynomial of range r, then the number of roots of Y on the unit circle $|y| = 1$ is $\equiv r \bmod 2$.

Proof: The non-zero roots of Y are just the roots of the reduced form of Y: $y^{-\text{sbdg}_y Y} \cdot Y(y)$; also r is the degree of this reduced form. Hence we may assume Y is already reduced, and $\deg_y Y = r$. In this case $Y^* = \overline{Y(1/\bar{y})} = ky^{-r}Y$. Since the roots of Y are non-zero (it is reduced, after all, and has no y-factors), any root y_0 inside the unit circle corresponds to a root $1/\bar{y}_0$ of Y^*, and hence also Y, *outside* the unit circle. Thus, the total number of roots of Y is (the # on $|y| = 1$) + 2 · (# roots inside $|y| = 1$); this is, of course, also the *degree* of Y (double roots are counted twice). Hence we have:

$$r \equiv \#\ \text{roots on } |y| = 1 \bmod 2$$ Q.E.D.

Applying this to $Y_\theta(y) = d(\theta,y)$, we have

$$\begin{aligned} W_x(A) &\equiv \#\ \text{roots of } Y_\theta(y) \text{ on } |y| = 1 \equiv \text{rng}_y Y(y) \\ &= \text{rng}_y d = \deg_y d - \text{sbdg}_y d \\ &\equiv -\deg_y d - \text{sbdg}_y d \bmod 2 \end{aligned}$$

If now (k,a,b) is the translation character of d, then note that $b = -\deg_y d - \text{sbdg}_y d$: for the higher power of y in d, that is, $\deg_y d$, becomes the lowest power $-\deg_y d$ in d^*, that is, the subdegree term; to bring the subdegree term of d down to $y^{-\deg_y d}$, we must clearly multiply by $y^{-\deg_y d - \text{sbdg}_y d}$, that is, $b = -\deg_y d - \text{sbdg}_y d$.

Thus, we have, finally,

$$W_x(A) \equiv b \bmod 2$$

Similarly, we find $W_y(A)$ mod 2, and thus our final

Proposition 6: The winding numbers (W_x,W_y) of the zero set (in U^2) of a self-adjoint L-polynomial d with (complex) character (a,b) satisfy:

$$(W_x,W_y) \equiv (b,a) \bmod 2$$

The Fast Decoding of Reed-Solomon Codes Using Number Theoretic Transforms

I. S. Reed and L. R. Welch
University of Southern California

T. K. Truong
DSN Systems Engineering Office

It is shown that Reed-Solomon (RS) codes can be encoded and decoded by using a fast Fourier transform (FFT) algorithm over finite fields. A Fourier-like transform is defined over finite fields of type $I_{F_n}(\sqrt[8]{2})$, where F_n is a Fermat prime for $n \leq 4$. The field $I_{F_n}(\sqrt[8]{2})$ is used to extend the length of the original Fermat number transforms by a factor of 8. The arithmetic utilized to perform these transforms over the field of type $I_{F_n}(\sqrt[8]{2})$ requires only integer additions, circular shifts and a minimum number of integer multiplications by powers of $\sqrt[8]{2}$. The computing time of this transform encoder-decoder for RS codes is less than the time of the standard method for RS codes.

More generally, the field GF(q) is also considered, where q is a prime of the form $K \times 2^n + 1$ and K and n are integers. GF(q) can be used to decode very long RS codes by an efficient FFT algorithm with an improvement in the number of symbols. The arithmetic needed for these more general transforms requires only slightly modified binary integer additions and multiplications.

Transforms can be defined also over the Galois field $GF(q^2)$, a finite field analogous to the complex number field, where $q = 2^p - 1$ is a Mersenne prime. The arithmetic needed for this case requires integer complex multiplications mod q and additions mod q.

It is shown in this paper that a radix-8 FFT algorithm over $GF(q^2)$ can be utilized to encode and decode very long RS codes with a large number of symbols. For eight symbols in $GF(q^2)$, this transform over $GF(q^2)$ can be made simpler than any other known number theoretic transform with a similar capability. Of special interest is the decoding of a 16-tuple RS code with four errors.

I. Introduction

Recently Gore (Ref. 1) extended Mandelbaum's methods (Ref. 2) for decoding Reed-Solomon (RS) codes (Ref. 3). He proposed the usage of a finite field transform over $GF(q^n)$, where q is a prime and n is an integer, for decoding RS codes. Michelson (Ref. 4) has implemented Mandelbaum's algorithm and showed that the decoder, using the transform over $GF(q^n)$, is faster than a more standard decoder (Ref. 5). The first disadvantage of the transform method over $GF(q^n)$ is that the transform length is an odd number, so that the most efficient FFT algorithm cannot be used to yield a fast transform decoder. The second disadvantage is that the arithmetic required to perform these transforms over $GF(q^n)$ still requires a substantial number of multiplications in $GF(q^n)$. The arithmetic used to implement this transform was performed in the extended field, $GF(q^n)$.

Schonhage and Strassen (Ref. 6) defined Fourier-like transforms over the ring of integers modulo the Fermat number $2^{2^n}+1$ to yield convolutions for performing fast integer multiplications. Rader (Ref. 7) proposed transforms over rings of integers modulo both Mersenne and Fermat numbers that can be used to compute error-free convolutions of real integer sequences.

Agarwal and Burrus (Refs. 8 and 9) extended Rader's Fermat number theoretic transform by using the generator $\alpha = \sqrt{2}$ for the transform, rather than $\alpha = 2$. In this case the usual FFT algorithm can be used to calculate transforms with as many as 2^{n+2} points of integer data. This transform was shown to be over the residue classes of quadratic integers $I_{F_n}(\sqrt{2})$, where $\sqrt{2}$ is a root of $x^2 - 2 = 0$ and I_{F_n} denotes the set of integers mod F_n (Ref. 10).

McClellan (Ref. 11) has realized recently the hardware for the Fermat number theoretic transforms. He showed that the arithmetic used to perform these transforms requires only integer additions and circular shifts. The primary advantage of the Rader transform is that multiplications by powers of two are performed by simple bit rotations. Of course, this advantage must be weighed against the difficulty of the numeric constraints relating word length, length of sequence d, and the compositeness of d, imposed by the choices of Mersenne prime and Fermat numbers.

Recently, the authors (Refs. 12 and 13) extended the number theoretic transform (NTT) to a complex integer field by taking transforms over a Galois field $GF(q^2)$, where q is a Mersenne prime. This field is analogous to the field of complex numbers. Such a complex number theoretic transform (CNT) offers more choices in transform length than can be obtained by other methods for the computing fast transform of the complex numbers. The arithmetic used to perform this transform requires integer complex multiplications and additions, mod q. In Ref. 14 it was shown that the binary arithmetic in $GF(q^2)$ is simpler than complex number arithmetic. For example the components of the eighth roots of unity in $GF(q^2)$ are fixed powers of 2. This latter fact was used to develop a fast radix–8 FFT algorithm over $GF(q^2)$. The transforms over $GF(q^2)$ were extended also to operate over the direct sum of Galois fields (Ref. 15). Such transforms can be used to compute transforms with improved dynamic range.

It was proposed (Ref. 16) also that number theoretic transforms could be defined in the Galois field $GF(q)$, where the prime q was of form $q = k \times 2^n + 1$, where k and n are integers. For this class of primes, the FFT algorithm can be utilized to realize transforms of integers that are not quite as fast as the Fermat number transforms. However, such transforms offer a substantial variety of transform and word lengths beyond what is possible with the Fermat transforms of Schonhage, Strassen, and Rader.

The arithmetic used to perfom the FFT over $GF(q)$ requires only slightly modified binary integer additions and multiplications. It should be noted that in Ref. 16, a method to perform arithmetic modulo $k \times 2^n + 1$ is developed specifically for the case $k = 3$. It was shown (Ref. 17) that a radix–2 FFT over $GF(q)$ is slightly faster than the efficient algorithm (Ref. 18) for the conventional FFT of real data when programmed on a PDP-10 computer. This speed could be considerably improved on computer hardware appropriately specialized to perform modulo q arithmetic.

Recently, Justesen (Ref. 19) proposed that transforms over fields of Fermat primes can be used to encode and decode RS codes. Since $\sqrt{2} \in GF(F_n)$ for $n = 2, 3, 4$ (see Ref. 10) is an element of order 2^{n+2} in $GF(F_n)$, the RS code of as many as 2^{n+2} symbols can be generated in $GF(F_n)$. Hence, using an argument similar to Gore's transform decoding method, mentioned above, the Fermat number theoretic transform is used to decode RS codes. Since the arithmetic in this new transform decoder is performed in $GF(F_n)$, such a number theoretic trans-

form decoder for RS codes can handle as many as 2^{n+2} symbols for $n = 2, 3, 4$. Encoding, and decoding can be accomplished faster and simpler than any other known standard decoder for RS codes of the same symbol range.

To treat longer RS codes in $GF(F_n)$, the transform is extended here to the finite field of type $I_{F_n}(\sqrt[8]{2})$, where $\sqrt[8]{2}$ is a root of the polynomial $P(x) = x^8 - 2$ over $GF(F_n)$ and I_{F_n} denotes the set of integers modulo F_n. If F_n is a Fermat prime, then $I_{F_n} = GF(F_n)$. The field $I_{F_n}(\sqrt[8]{2})$ is obtained by taking the residue classes of polynomials modulo $P(x)$. That is,

$$I_{F_n}(\sqrt[8]{2}) = \{a + b(\sqrt[8]{2}) + c(\sqrt[8]{2})^2 + d(\sqrt[8]{2})^3 + e(\sqrt[8]{2})^4 + f(\sqrt[8]{2})^5 + g(\sqrt[8]{2})^6 + h(\sqrt[8]{2})^7 \mid a, b, c, d, e, f, g, h \epsilon GF(F_n)\}$$

It will be shown that 2 is an octadic residue of a Fermat prime F_n for $n = 3, 4$. Thus, $I_{F_n}(\sqrt[8]{2})$ is a field of F_n elements isomorphic to $GF(F_n)$. The transform over $I_{F_n}(\sqrt[8]{2})$ extends the length of Rader's original Fermat number theoretic transform by a factor of 8. The arithmetic used to perform this transform requires only integer additions, circular shifts and a minimum number of integer multiplications by powers of $\sqrt[8]{2}$.

To decode very long RS codes over $GF(F_n)$ (from Refs. 9 and 10), one can use the fact that 3 is a primitive element in $GF(2^{2^n} + 1)$. Thus a FFT over $GF(F_n)$ can be used to decode a 2^{2^n}-tuple RS code. The arithmetic used to perform this transform requires integer multiplications by powers of 3 and integer additions mod F_n.

Since the Fermat primes F_n exist only for $n \leq 4$, the dynamic range of the transforms associated with these primes is severely limited. To remedy this it may be possible to use transforms over the direct sum of Galois fields, $GF(F_n)$ to decode RS codes with an improved number of symbols.

A special case of the radix-8 FFT over $GF(q^2)$ where $q = 2^p - 1$ is a Mersenne prime is developed in some detail to encode and decode a very long nonsystematic RS code with a large number of symbols. Recall that the 8th root of unity in $GF(q^2)$ is $\pm 2^{(p-1)/2}(1 + \hat{i})$, where p is a prime. Hence, the arithmetic used to perform 8-point transforms requires only circular shifts and additions. This transform is used to decode a 16-tuple error correcting RS code faster and simpler than any other similar code.

II. A Transform Over $I_{F_n}(\sqrt[8]{2})$ Where F_n is a Fermat Prime

Let q be a prime and let $GF(q^n)$ be the Galois field and suppose that integer d divides $q^n - 1$. Also let the element $\gamma \epsilon GF(q^n)$ generate the cyclic subgroup of d elements, G_d in the multiplicative group of $GF(q^n)$. Then, by Ref. 12, a transform over this subgroup G_d can be defined by

$$A_K = \sum_{n=0}^{d-1} a_n \gamma^{Kn} \qquad \text{for } 0 \leq K \leq d-1 \qquad \text{(1a)}$$

where d divides $q^n - 1$ and $a_n \epsilon GF(q^n)$ for $n = 0, 1, 2, \cdots, d-1$ and the inverse of transform of A_K is

$$a_n = (d)^{-1} \sum_{K=0}^{d-1} A_K \gamma^{-Kn} \qquad \text{(1b)}$$

where (d) denotes the residue of d mod q, and $(d)^{-1}$ is the inverse of (d). In the present case, attention is restricted to $n = 1$. Thus, the transform over $G_d \epsilon GF(q)$ can be defined by

$$A_K = \sum_{n=0}^{d-1} a_n \gamma^{Kn} \qquad \text{for } 0 \leq K \leq d-1 \qquad \text{(2a)}$$

where $d \mid q - 1$ and $a_n, A_K \epsilon GF(q)$ and the inverse transform of A_K still holds. That is,

$$a_n = (d)^{-1} \sum_{K=0}^{d-1} A_K \gamma^{-Kn} \qquad \text{for } 0 \leq n \leq d-1 \qquad \text{(2b)}$$

where (d) denotes the residue of d mod q and $(d)^{-1}$ is the inverse of (d).

It is shown in the Appendix that 2 is an octadic residue of a Fermat prime F_n. As a consequence, $\sqrt[8]{2}$ is an element of $GF(F_n)$. Thus, by the same procedure used in the proof of theorem 6 of Ref. 21, $I_{F_n}(\sqrt[8]{2})$ for $n = 3, 4$ is isomorphic to $GF(F_n)$.

If $q = F_n$ is a Fermat Prime, the above transform (Eq. (2)) can be defined in $GF(F_n) \cong I_{F_n}(\sqrt[8]{2})$ for $n = 3, 4$. Since $I_{F_n}(\sqrt[8]{2})$ is isomorphic to $GF(F_n)$ and $(\sqrt[8]{2})^{2^{n+3}} \equiv -1$ mod F_n, then by the theorem 1 of Ref. 12, $\gamma = \sqrt[8]{2}$, is an element of order 2^{n+4} in $I_{F_n}(\sqrt[8]{2})$. Thus the FFT over $I_{F_n}(\sqrt[8]{2})$ can be defined to compute the transform of a sequence of as many as $d = n + 4$ points of input data. It should be noted that this fact extends the length of Rader's original Fermat number theoretic transform by a factor of 8.

Since $\gamma = \sqrt[8]{2}$ $GF(F_n)$ is an element of order 2^{n+4}, it is well known (see for example Ref. 12) that the FFT algorithm over $GF(F_n)$ is composed of $d = n + 4$ stages of computation. The first $d - 3$ stages require only multiplications by the powers of 2, i.e., circular shift. By Ref. 9, $\sqrt{2} = 2^{3\cdot 2^{n-2}} - 2^{2^{n-2}}$. Thus, the $(d-2)$-st stage requires integer multiplications by powers of $\sqrt[8]{2}$, i.e., circular shifts. Only the last two stages require integer multiplications by powers of $\sqrt[8]{2}$. Hence the number of arithmetic operations used to perform this transform are $d \cdot \log d$ integer additions $((d-3)\cdot \log d + 2\log d) = (d+1)\log d$ circular shifts and $2\cdot \log d$ integer multiplications by powers of $\sqrt[8]{2}$. This implies that the FFT over $I_{F_n}(\sqrt[8]{2})$ for $n = 3, 4$ is faster and simpler than any other number theoretic transforms of the same transform length and dynamic range.

III. Fast Decoding of Systematic Reed-Solomon Codes Using the Transform Over $I_{F_n}(\sqrt[8]{2})$

It was shown in the previous section that the field of type $I_{F_n}(\sqrt[8]{2})$ is isomorphic to $GF(F_n)$ for $n = 3, 4$ and the $\alpha = \sqrt[8]{2} \in GF(F_n)$ is an element of order 2^{n+4}. A systematic Reed-Solomon code can be specified in $GF(F_n)$ as follows.

Assume the code length for the RS code is $N = 2^{n+1}$. Let a codeword be represented by $f(x)$, a polynomial of degree $N - 1$ over $GF(F_n)$. The generator polynomial of $f(x)$ is defined as

$$g(x) = \prod_{i=1}^{d-1}(x - \alpha^i)$$

where $d = 2^K < N = 2^{n+1}$, $\alpha = \sqrt[8]{2}$, $\alpha^2 = (\sqrt[8]{2})^2, \cdots, \alpha^d = (\sqrt[8]{2})^d$ are the roots of $g(x)$ in $GF(F_n)$. The resultant RS code with N symbols, which is a multiple of the generator polynomial, is composed of $d - 1$ parity check symbols and $n - (d - 1)$ information symbols. d is the minimum distance of the RS code. If t is the number of errors the code will correct, then for an RS code $d = 2t + 1$.

Suppose that the code $f(x) = f_0 + f_1 x + \cdots + f_{N-1}x^{N-1}$ is transmitted over a noisy channel. The received code $R(x) = \gamma_0 + \gamma_1 x + \gamma_2 x^2 + \cdots + \gamma_{N-1}x^{N-1}$ is composed of the original code with the addition of possible errors, i.e.,

$$\gamma(x) = f(x) + e(x)$$

where $e(x) = e_0 + e_1 x + e_2 x^2 + \cdots + e_{N-1}x^{N-1}$ is the error polynomial.

Upon receiving the message $\gamma(x)$, one may decode the message symbols by first using the FFT over $I_{F_n}(\sqrt[8]{2})$. The transform is taken over the received N-tuple message $(\gamma_0, \gamma_1, \cdots, \gamma_{N-1})$, the coefficients of the polynomial $\gamma(x)$. This transform is

$$\begin{aligned} S_K &= \sum_{n=0}^{N-1}\gamma_n(\sqrt[8]{2})^{Kn} \qquad \text{for } K = 0,1,\cdots,N-1 \\ &= \sum_{n=0}^{N-1}(f_n + e_n)(\sqrt[8]{2})^{Kn} \\ &= \sum_{n=0}^{N-1}f_n(\sqrt[8]{2})^{Kn} + \sum_{n=0}^{N-1}e_n(\sqrt[8]{2})^{Kn} \\ &= F_K + E_K \end{aligned}$$

Since $f(x)$ is a multiple of $g(x)$, $f(\alpha^i) = 0$ for $i = 1,2,\cdots,d-1$. Hence,

$$\begin{aligned} S_K = E_K &= e((\sqrt[8]{2})^K) = \sum_{n=0}^{N-1}e_n(\sqrt[8]{2})^{Kn} \\ &= \sum_{n=0}^{N-1}e_n((\sqrt[8]{2})^n)^K \qquad \text{for } K = 1,2,\cdots,d-1 \end{aligned} \tag{3}$$

Let Y_i and X_i be the ith error magnitude and the ith error location, respectively. Then the syndrome in Eq. (3) becomes

$$S_K = E_K = \sum_{i=1}^{t}Y_i X_i^K \qquad \text{for } K = 1,2,\cdots,d-1 \tag{4}$$

The error locator polynomial $\sigma(x)$ is defined as usual by

$$\sigma(x) = \prod_{i=1}^{t}(1 - X_i x) = 1 - \sigma_1 x + \sigma_2 x^2 + \cdots, (-1)^t \sigma_t x^t$$

where σ_i are the elementary symmetric functions.

It follows that

$$\sigma(X_i^{-1}) = 0 = 1 - \sigma_1 X_i + \sigma_2 X_i^{-2} + \cdots, + (-1)^t \sigma_t X_i^{-t}$$
$$\text{for } i = 1,2,\cdots,t$$

Multiplying the above equation by $Y_i X_i^{j+t}$, one gets

$$Y_i X_i^{j+t} - \sigma_1 Y_i X_i^{j+t-1} + \sigma_2 Y_i X_i^{j+t-2} + \cdots, + (-1)^t \sigma_t Y_i X_i^{j+t-t}$$

Summing on i for $i = 1,2,\cdots,t$, then

$$\sum_{i=1}^{t}Y_i X_i^{j+t} - \sigma_1 \sum_{i=1}^{t}Y_i X_i^{j+t-1} + \cdots (-1)^t \sigma_t \sum_{i=1}^{t}Y_i X_i^j = 0$$

Using Eq. (4), we have

$$S_{j+t} - \sigma_1 S_{j+t-1} + \cdots + (-1)^t \sigma_t S_j = 0 \qquad \text{for } j \leq t \tag{5}$$

and

$$E_{j+t} - \sigma_1 E_{j+t-1} + \cdots + (-1)^t \sigma_t E_j = 0 \qquad \text{for } j > t \tag{6}$$

If $S_1 = E_1, S_2 = E_2, \cdots, S_{d-1} = E_{d-1}$ are known, the σ_i for $i = 1, 2, \cdots, t$ in Eq. (5) can be calculated by using Berlekamp's (Ref. 22) iterative algorithm. If σ_i is known, Eq. (6) is then used to obtain $E_0, E_d, E_{d+1}, \cdots, E_{N-1}$, and the transform of the N-tuple error pattern, i.e., $(E_0, E_1, E_2, \cdots, E_{N-1})$ is obtained. Thus, the N-tuple error pattern $(e_0, e_1, \cdots, e_{N-1})$ is found by taking the inverse transform over $I_{F_n}(\sqrt[8]{2})$ of E_K for $K = 0, 1, \cdots, N-1$. Finally, the original N-tuple symbols code can be computed by subtracting e_n from received code γ_n.

To recapitulate, the decoding of systematic Reed-Solomon codes using the transform over $I_{F_n}(\sqrt[8]{2})$, is composed of the following three steps:

(1) Compute the transform over $I_{F_n}(\sqrt[8]{2}) \cong GF(F_n)$ for $n = 3,4$ of the received code N-tuple, i.e.,

$$S_K = \sum_{n=0}^{N-1} \gamma_n \alpha^{nk}$$

where $\gamma_n \epsilon GF(F_n)$ and $\alpha = \sqrt[8]{2} \epsilon GF(F_n)$ is an element of order $N = 2^{n+4}$.

(2) Use Berlekamp's iterative algorithm (Refs. 19 and 22) to determine σ_i from the known $S_j = E_j$ for $i = 1, 2, \cdots, t$ and $j = 1, 2, \cdots, d-1$. Then compute the remaining E_j.

(3) Compute the inverse of the transform over $I_{F_n}(\sqrt[8]{2})$ of $(S_K - E_K)$ to obtain the corrected code.

An advantage of this decoding algorithm over other methods is that a FFT over $GF(F_n)$ can be used to compute the syndromes and error magnitudes. Also the Berlekamp's algorithm can be performed in the arithmetic of $GF(F_n)$. The arithmetic used to perform the FFT over $GF(F_n)$ only requires integer additions, circular shifts, and a minimum number of multiplications; thus, such a Fermat number theoretic transform decoder for an RS code of as many as 2^{n+4} symbols can be accomplished faster and simpler than other RS decoders. Since this new transform decoding algorithm is independent of code rate, it is more efficient for correcting a large number of errors in an RS code. The FFT over $GF(F_n)$ becomes more efficient for the longer RS codes.

A disadvantage of this decoding method is that the Fermat primes F_n exist only for $n \leq 4$ and the lengths and dynamic ranges of the transforms associated with these primes are often severly limited. To remedy this it is well known (Ref. 9) that such transforms can be defined over rings of integers modulo a Fermat numbers $F_n = 2^{2^n} + 1$ for $n = 5, 6$, i.e., I_{F_n}. The syndromes can be evaluated by using transforms over this ring. If one knows the S_j, the inverse element in the ring is needed to evaluate the σ_i. However, the inverse of an element in this resulting ring does not exist unless $(a, F_n) = 1$. For this reason, transforms over I_{F_n} cannot be used directly to decode RS codes.

It should be pointed out that a word length of $2^n + 1$ bits is required to represent a number in $GF(F_n)$. However, the word length in the transmitted word is often a multiple 4 bits. Thus, the values of the symbols in $GF(F_n)$ cannot be represented easily as a 2^n bit word. To remedy this, suppose the information symbols are represented in the range from 0 to $2^{2^n} - 1$. After encoding the information symbols, the parity check symbols may occur in the range between 0 and 2^{2^n}. If 2^{2^n} is observed as a parity check symbol, deliberately change this value to 0, now an error. The transform decoder will correct this error automatically.

A simple example of the above decoding procedure for an RS code in $GF(F_n)$ is now presented.

Example. Let $GF(2^{2^2} + 1)$ be the field of integers modulo the Fermat prime $F_2 = 17$. We consider a 2-error correcting 8-tuple RS code in $GF(17)$.

Since $2^{2^2} \equiv -1 \bmod 17$, by (Ref. 12 theorem 1) $\alpha = 2$ is an element of order 8 in $GF(17)$. The cyclic subgroup of 8 elements with generator $\alpha = 2$ in GF (17) follows:

$$\alpha = 2$$

$$\alpha^2 = 2^2 = 4$$

$$\alpha^3 = 2^3 = 8$$

$$\alpha^4 = 2^4 = -1$$

$$\alpha^5 = 2^5 = 15$$

$$\alpha^6 = 2^6 = 13$$

$$\alpha^7 = 2^7 = 9$$

$$\alpha^8 = 2^8 = 1$$

The block length of the RS code is $N = 8$. It can correct at most $t = 2$ errors. This implies that the minimum distance of the code is $d = 2t + 1 = 5$. Then the information symbols are $N - (d - 1) = 8 - (5 - 1) = 4$. The generator polynomial is defined as

$$g(x) = \prod_{i=1}^{d-1} (x - \alpha^i) = \prod_{i=1}^{5-1} (x - 2^i)$$
$$= x^4 + 4x^3 + 8x^2 + 9x + 4$$

Assume the information symbols are $1, 2, 3, 2 \epsilon GF(17)$, i.e., $I(x) = 1x^7 + 2x^6 + 3x^5 + 2x^4$. Recall that the code word is a multiple of $g(x)$. By the division algorithm, one gets

$$I(x) = q(x)g(x) + R(x)$$

where $R(x)$ is the remainder of polynomial of degree less than the degree of $g(x)$. It follows that

$$f(x) = I(x) - R(x) = q(x)g(x)$$

Hence the encoding of $I(x)$ is the polynomial

$$f(x) = 5 + 2x + 12x^2 + 15x^3 + 2x^4 + 3x^5 + 2x^6 + x^7$$
$$= (5, 2, 12, 15, 2, 3, 2, 1)$$

Suppose that two errors occur in the received word, e.g.,

$$\gamma(x) = 5 + 2x + 9x^2 + 15x^3 + 2x^4 + 1x^5 + 2x^6 + 1x^7$$
$$= (\gamma_0, \gamma_1, \gamma_2, \gamma_3, \gamma_4, \gamma_5, \gamma_6, \gamma_7)$$
$$= (5, 2, 12 - 3, 15, 2, 3 - 2, 2, 1)$$

Then the error pattern $e(x)$ is

$$e(x) = \gamma(x) - f(x)$$
$$= 0 + 0 \cdot x^1 - 3x^2 + 0 \cdot x^3 + 0 \cdot x^4 - 2x^5 + 0 \cdot x^6 + 0 \cdot x^7$$
$$= (e_0, e_1, e_2, e_3, e_4, e_5, e_6, e_7)$$
$$= (0, 0, 14, 0, 0, 15, 0, 0)$$

The syndrome can be calculated, using an FFT over $GF(F_n)$. That is,

$$S_K = E_K = \sum_{n=0}^{8-1} \gamma_n 2^{nK}$$
$$= \sum_{n=0}^{8-1} (f_n + e_n) 2^{nK}$$
$$= \sum_{n=0}^{8-1} f_n 2^{nK} + \sum_{n=0}^{8-1} e_n 2^{nK}$$
$$= F_K + E_K$$

Since

$$\sum_{n=0}^{8-1} f_n 2^{nK} = 0 \qquad \text{for } K = 1, 2, 3, 4$$

then

$$S_K = E_K = \gamma(x) = e(x) = \sum_{n=0}^{8-1} e_n \cdot 2^{nK} = \sum_{i=1}^{2} Y_i X_i^K$$

$$\text{for } K = 1, 2, 3, 4$$

Hence,

$$S_1 = e(2) = E_1 = -3 \cdot 2^2 - 2 \cdot 2^5 = -8$$
$$S_2 = e(2^2) = E_2 = -3(2^2)^2 - 2(2^2)^5 = -5$$
$$S_3 = e(2^3) = E_3 = -3(2^3)^2 - 2(2^3)^5 = 11$$
$$S_4 = e(2^4) = E_4 = -3(2^4)^2 - 2(2^4)^5 = -1$$

The error locator polynomial $\sigma(x)$ is

$$\sigma(x) = \prod_{i=1}^{r} (1 - X_i x) = \prod_{i=1}^{2} (1 - X_i x)$$
$$= 1 - (X_1 + X_2)x + X_1 X_2 x^2$$
$$= 1 - \sigma_1 x + \sigma_2 x^2$$

where

$$\sigma_1 = X_1 + X_2, \sigma_2 = X_1 X_2$$

It follows that

$$\sigma(X_i^{-1}) = 0 = 1 - \sigma_1 X_i^{-1} + \sigma_2 X_i^{-2} \qquad \text{for } i = 1, 2$$

Multiplying by $Y_i X_i^{j+1}$,

$$Y_i X_i^{j+2} - \sigma_1 Y_i X_i^{j+2-1} + \sigma_2 Y_i X_i^{j+2-2} = 0 \qquad \text{for } i = 1, 2$$

Summing on i for $i = 1, 2$, one has

$$\sum_{i=1}^{2} Y_i X_i^{j+2} - \sigma_1 \sum_{i=1}^{2} Y_i X_i^{j+1} + \sigma_2 \sum_{i=1}^{2} Y_i X_i^{j} = 0$$

i.e.,

$$S_{j+2} - \sigma_1 S_{j+1} + \sigma_2 S_j = 0, \qquad \text{for } j \leq 2 \tag{7}$$

and

$$E_{j+2} - \sigma_1 E_{j+1} + \sigma_2 E_j = 0 \qquad \text{for } j > 2 \tag{8}$$

It follows from Eq. (7) that for $j = 1, 2$

$$S_3 - \sigma_1 S_2 + \sigma_2 S_1 = 0$$

$$S_4 - \sigma_1 S_3 + \sigma_2 S_2 = 0$$

or

$$-5\sigma_1 + \sigma_2 8 \equiv 11 \bmod 17 \tag{9a}$$

$$11\sigma_1 + \sigma_2 5 \equiv 1 \bmod 17 \tag{9b}$$

Since

$$\begin{vmatrix} -5, 8 \\ 11, 5 \end{vmatrix} = -25 - 11 \cdot 8 \equiv 6 \not\equiv 0 \bmod 17$$

Equation (9) has a solution. To obtain the solution, multiply Eq. (9a) by 11 and Eq. (9b) by 5, then

$$-55\sigma_1 + \sigma_2 88 = 36$$

$$55\sigma_1 + \sigma_2 25 = -5$$

The solutions of above equations are

$$\sigma_2 = \frac{-3}{11} \equiv -3 \cdot 11^{-1} \equiv -3 \cdot 14 \equiv 9 \bmod 17$$

and

$$\sigma_1 = \frac{-46}{11} \equiv 5 \cdot (-3) \equiv 2 \bmod 17$$

Equation (8) becomes

$$E_{j+2} - 2E_{j+1} + 9E_j = 0 \qquad \text{for } j > 2 \tag{10}$$

From Eq. (10), one gets the rest of the transform E_j of the error pattern, i.e.,

$$E_5 = 2E_4 - 9E_3 \equiv 2(-1) - 9(11) \equiv 1 \bmod 17$$

$$E_6 = 2E_5 - 9E_4 \equiv 2(1) - 9(-1) \equiv 11 \bmod 17$$

$$E_7 = 2E_6 - 9E_5 \equiv 2(11) - 9(1) \equiv 13 \bmod 17$$

$$E_8 = 2E_7 - 9E_6 \equiv 2(13) - 9(11) \equiv 12 \bmod 17$$

The inverse transform over $GF(2^2 + 1)$ of the E_j is

$$e_n = (8)^{-1} \sum_{K=0}^{8-1} E_K 2^{-nK} \qquad \text{for } 0 \leq n \leq 7$$

$$= (-2)(E_0 2^0 + E_1 2^{-n} + E_2 2^{-2n} + E_3 2^{-3n} + E_4 2^{-4n} + E_5 2^{-5n} + E_6 2^{-6n} + E_7 2^{-7n})$$

$$= (-2)(12 \cdot 2^0 + 9 \cdot 2^{-n} + 12 \cdot 2^{-2n} + 11 \cdot 2^{-3n} + 16 \cdot 2^{-4n} + 1 \cdot 2^{-5n} + 11 \cdot 2^{-6n} + 13 \cdot 2^{-7n})$$

Using the FFT algorithm, we have finally

$$(e_0, e_1, e_2, e_3, e_4, e_5, e_6, e_7) = (0, 0, 14, 0, 0, 15, 0, 0)$$

The corrected codeword is

$$f(x) = R(x) - e(x)$$

$$= (5, 2, 9, 15, 2, 1, 2, 1) - (0, 0, 14, 0, 0, 15, 0, 0)$$

$$= (5, 2, 12, 15, 2, 3, 2, 1)$$

IV. A Fast Transform Over $GF(F_n)$ for the Nonsystematic Reed-Solomon Codes

The transform over finite field $GF(q)$, where q is a prime, can be also used to decode nonsystematic Reed-Solomon codes. The nonsystematic Reed-Solomon code is defined in Ref. 5. Let $\alpha \epsilon GF(q)$ be an element of order N. Consider the information polynomial $I(x)$ with coefficients $\epsilon GF(q)$, i.e.,

$$I(x) = i_0 + i_1 x + \cdots, + i_{K-1} x^{K-1}$$

The transmitted code word is the following polynomial:

$$f(x) = I(\alpha^0) + I(\alpha^1)x + I(\alpha^2)x^2 + \cdots, + I(\alpha^{N-1})x^{N-1}$$

$$= F_0 + F_1 x + F_2 x^2 + \cdots, + F_{N-1} x^{N-1}$$

where the $I(\alpha^i)$ are obtained by using the transform over $GF(F_n)$. That is,

$$I(\alpha^K) = F_K = \sum_{n=0}^{N-1} i_n (\alpha^K)^n \qquad \text{for } K = 0, 1, 2, \cdots, N-1$$

where

$$i_0 = i_0, i_1 = i_1, \cdots, i_{K-1} = i_{K-1}, i_K = 0, i_{K+1} = 0, \cdots, i_{N-1} = 0$$

The inverse transform over $GF(q)$ of F_K is

$$i_n = (N)^{-1} \sum_{K=0}^{N-1} F_K \alpha^{-nK} \qquad \text{for } n = 0, 1, \cdots, N-1$$
$$= (N)^{-1} f(\alpha^{-n})$$

It follows that

$$(N)^{-1} f(\alpha^{-n}) = i_n \qquad \text{for } n = 0, 1, \cdots, K-1$$
$$= 0 \qquad \text{for } n = K, \cdots, N-1$$

Suppose the received word in the transform domain is

$$\gamma(x) = f(x) + e(x)$$
$$= f(x) + \sum_{j=0}^{N-1} e_j \alpha^{jn}$$

where $e(x)$ is the transform of the error pattern. Then, the inverse transform of $\gamma(x)$ is

$$S_n = (N)^{-1} \sum_{K=0}^{N-1} \gamma_k \alpha^{-Kn}$$
$$= (N)^{-1} \sum_{K=0}^{N-1} -f_k \alpha^{-Kn} + (N)^{-1} \sum_{K=0}^{N-1} \left(\sum_{j=0}^{N-1} e_j \alpha^{jn} \right) \alpha^{-Kn}$$
$$= (N)^{-1} f(\alpha^{-n}) + e_n$$

or

$$S_n = i_n + e_n \qquad \text{for } n = 0, 1, \cdots, K-1$$
$$= 0 + e_n \qquad \text{for } n = K, \cdots, N-1$$

Thus, the syndrome is

$$S_n = e_n \qquad \text{for } n = K, K+1, \cdots, N-1 \qquad (11)$$

Hence $t = (N - K)/2$ errors in N-tuple can be corrected in the nonsystematic RS code. By the same procedure, used in the derivation of Eq. (5), one gets

$$S_{N-j} - \sigma_1 S_{N-j-1} + \cdots + \sigma_t (-1)^t S_{N-j-t} = 0 \qquad (12)$$
$$\text{for } 1 \leq j \leq t$$

and

$$e_{N-j} - \sigma 1 e_{N-j-1} + \cdots + (-1)^t \sigma_t e_{N-j-t} = 0 \qquad (13)$$
$$\text{for } j \geq t$$

Using the Berlekamp's algorithm, σ_i can be computed for the syndromes. The error pattern can be obtained by using Eq. (13). We see that a fast transform over $GF(q)$ for the nonsystematic RS code can be implemented by using only one inverse transform. However, encoding is accomplished by a forward transform. Hence for the nonsystematic RS codes the FFT over $GF(F_n)$ is both to encode and to decode the codes.

V. A Transform Decoder Over the Finite Field, $GF(K \cdot 2^n + 1)$

In the previous section, transforms over the field of type $I_{F_n}(\sqrt[8]{2})$ were defined to decode RS code. However, Fermat primes existed only for $n \leq 4$, and the lengths and dynamic ranges of the transforms associated with these primes were often severely limited. Also it was found that a word length, 4m could not always be represented adequately in $GF(F_n)$. To alleviate such difficulties another approach was proposed recently (Refs. 16 and 17). High-speed number theoretic transforms were defined on the Galois field $GF(q)$, where the prime q was of form $q = K \times 2^n + 1$, where n and K are integers.

In Ref. 16, an FFT algorithm over $GF(q)$ was utilized to realize transforms of integers. Such transforms offer a substantial variety of possible transform lengths and dynamic ranges. However, the arithmetic needed was often somewhat more extensive than required for the Fermat primes.

If q is a prime of the form $K \cdot 2^n + 1$, by Eqs. (2a) and (2b), a transform can be defined on $GF(K \times 2^n + 1)$. The order of the multiplicative group with generator of $GF(q)$ is given by

$$t = q - 1 = K \cdot 2^n$$

Since t has the factor 2^n the usual radix-2 FFT algorithm can be utilized to calculate the transform of as many as $d = 2^n$ points. If $d = 2^m$, $1 \leq m \leq n$ and α is the primitive element of $GF(q)$, then the generator of G_d is evidently $\gamma = \alpha^{2^{n-m}}$. Primes of the form $K \cdot 2^n + 1$ can be found in the table of Ref. 23. Thus primes of the form $K \cdot 2^n + 1$ can be chosen to fit into the word lengths of different digital computers.

To fit a transform defined by Eq. (2a) in the PDP-10 computer, which has a word length of 36 bits, the largest prime number of the form $K \times 2^n + 1$ was found to be the prime $45 \times 2^{29} + 1$. By Fermat's theorem, $2^{45 \times 2^{29}} \equiv 1 \mod q$, where $q = 45 \times 2^{29} + 1$. This is equivalent to $(2^{45})^{2^{29}} \equiv 1 \mod q$. It can be verified by a computer program that $(2^{45})^{2^{28}} \equiv -1 \mod q$. Thus, by theorem 1 of

Ref. 12, $2^{45} \equiv 8589933136 \bmod q$ is an element of order 2^{28}, where $q = 45 \times 2^{20} + 1$. It follows that $\gamma \equiv 2^{45 \cdot 2^{28-K}} \bmod q$ is an element of order 2^K where $0 \leq K \leq 28$. A detailed discussion for finding the index or order of an element modulo a prime of form $K \cdot 2^n + 1$ can be found in Ref. 16.

Multiplication modulo of the prime number $q = 45 \times 2^{20} + 1$ is straightforwardly performed in assembly language software in the PDP-10 computer. To perform addition modulo q, let $A + C = A + (C - q)$, where $(C - q) \leq 0$. Then if $A + (C - q) \leq 0$, the addition is accomplished by the add command, otherwise it equals $A + (C - q) + q$. Another method for performing addition modulo $K \cdot 2^n + 1$ was developed for small K in Ref. 16.

Subtraction modulo q, if $A - C \leq 0$, is accomplished by the subtract command; otherwise, it equals $A - C + q$. For a more detailed discussion for implementing the transform over $GF(45 \times 2^{20} + 1)$ in software, see Ref. 17. It was shown (Ref. 17) that the arithmetic used to perform this transform requires $d \log d$ integer multiplications mod q and $d \log d$ integer additions mod q. Hence, using the same procedure described in the previous section, a transform over $GF(q)$ where $q = K \cdot 2^n + 1$ can be used to decode a very long RS code with improved symbol range.

VI. A Transform Decoder Over $GF(q^2)$ Where q is a Mersenne Prime

In the previous sections, transforms were defined in $GF(K \times 2^n + 1)$. In this section, a transform is defined on $GF(q^2)$ where q is a Mersenne Prime. It will be shown that the radix-8 FFT over $GF(q^2)$ can be used to decode very long RS code with a goodly number of symbols. Of special interest is the radix-8 FFT algorithm over $GF(q^2)$.

In Ref. 12, Reed and Truong extended previous transforms of Rader (Ref. 7) by developing a Fourier-like transform over the Galois field $GF(q^2)$, a finite field of q^2 elements, where q is a prime, of the form

$$A_K = \sum_{n=0}^{d-1} a_n \gamma^{kn} \qquad \text{for } 0 \leq K \leq d-1 \qquad (14a)$$

In Eq. (14a) the transform length, d, divides $q^2 - 1$, $a_n \epsilon GF(q^2)$ and γ is a primitive dth root of unity that generates the d-element cyclic subgroup

$$G_d = \{\gamma, \gamma^2, \cdots, \gamma^{d-1}, 1\}$$

in the multiplicative subgroup of $GF(q^2)$. The inverse transform of Eq. (14a) is

$$a_m = (d)^{-1} \sum_{k=0}^{d-1} A_K \gamma^{-Km} \qquad \text{for } 0 \leq m \leq d-1 \quad (14b)$$

where $(d)^{-1}$ denotes the multiplicative inverse of the residue of d modulo q in $GF(q^2)$.

It is shown in Eq. 12 that if q is a Mersenne prime of the form

$$q = 2^p - 1 \qquad \text{for } p = 2, 3, 5, 7, 13, 17, 19, 31, 61, 127, \cdots$$

then the polynomial

$$p(x) = x^2 + 1$$

is always irreducible in $GF(q)$, a finite field of q elements. Since every irreducible quadratic polynomial over $GF(q)$ must split over $GF(q^2)$ (Ref. 24), the existence of a root $\hat{i}$ of the polynomial

$$p(x) = x^2 + 1 = 0$$

is guaranteed in the extension field $GF(q^2)$. Hence $GF(q^2)$ can be constructed as the set

$$GF(q^2) = \{a + \hat{i}b \mid a, b \epsilon GF(q)\}$$

Furthermore, since the mapping from the complex integer field C composed of the set

$$C = \left\{\alpha + \hat{i}\beta \mid \alpha, \beta \text{ integers and } -\frac{q-1}{2} \leq \alpha, \beta \leq \frac{q-1}{2}\right\}$$

where $\hat{i} = \sqrt{-1}$, to $GF(q^2)$ is one-to-one and onto, circular convolutions of complex integers can be performed either in C or in $GF(q^2)$. It is also shown in Ref. 12 that FFTs of as many as 2^{p+1} points can be carried out in $GF(q^2)$.

It was shown (Ref. 14) that the arithmetic operations for performing the transform pair, Eqs. (14a) and (14b), in $GF(q^2)$ requires only modulo q additions, modulo q multiplications, circular shifts of a p-bit register, and complement operations. Also because of the symmetry properties of the dth roots of unity in $GF(q^2)$, where d divides 2^{p+1}, algorithms analogous to the conventional twiddle factor FFT algorithms can be used to compute transforms over $GF(q^2)$.

It was shown (Ref. 14) that when d divides 2^{p+1}, the components of $\gamma^{kd/8}$, where γ is a primitive dth root of unity in $GF(q^2)$ and k is an odd integer, are fixed powers of 2. As a consequence, complex multiplications involving $\gamma^{kd/8}$ can be accomplished merely by additions and circular shifts of $(p-1)/2$ bits in a p-bit register. Therefore, these new FFT algorithms can be made faster and simpler than the conventional FFT algorithm. Of particular interest is a new radix-8 FFT algorithm that requires no multiplications at all when evaluating the set of 8-point discrete Fourier transforms (DFTs) before referencing with the twiddle factor. Hence, using a procedure similar to that discussed in Section 3, a radix-8 FFT over $GF(q^2)$ can be developed to decode RS code of as many as 2^{p+1} symbols.

Observe that the element $c = a + \hat{i}b$ in $GF(q^2)$ can be used to represent two symbols a, b in $GF(q)$. Thus, the transform over $GF(q^2)$ can be used to decode a 2^{p+2}-tuple in $GF(q)$ RS code. By theorem 1 of Ref. 14, we know that an 8th root of unity in $GF(q^2)$ is $\pm 2^{(p-1)/2}(1+\hat{i})$. If special interconnections are made between the inputs and outputs of the p-bit register, the $(p-1)/2$-bit circular shift could be performed readily in one clock time. This fact makes possible an 8-point FFT over $GF(q^2)$, which requires only circular shifts and additions. This FFT over $GF(q^2)$ can be used to decode a special 4-error correcting 16-tuple RS code faster and simpler than any other code of comparable error correcting capability.

The flow chart (Fig. 1) illustrates transform decoding over $GF(q^2)$ for correcting this RS code.

Example: Let $GF(q^2) = \{a + \hat{i}b \mid a, b \in GF(q)\}$ be a Galois field, where $q = 2^3 - 1 = 7$. The information symbols are the 4-tuple $(1+\hat{i},\ 1+2\hat{i},\ 2+\hat{i},\ 1+\hat{i}0)$. Encode this 4-tuple into an 8-tuple by using the FFT over $GF(q^2)$. This code corrects at most two-symbol errors.

From Ref. 14, $\alpha = 2^{(p-1)/2}(1+\hat{i}) = 2^{(3-1)/2}(1+\hat{i}) = 2(1+\hat{i})$ is an element of order 8. That is,

$$\alpha = 2(1+\hat{i})$$
$$\alpha^2 = 2^2(1+\hat{i})^2 = \hat{i}$$
$$\alpha^3 = \hat{i}2(1+\hat{i}) = 2(-1+\hat{i})$$
$$\alpha^4 = -1$$
$$\alpha^5 = 2(-1-\hat{i})$$
$$\alpha^6 = -\hat{i}$$
$$\alpha^7 = -\hat{i}2(1+\hat{i}) = 2(1-\hat{i})$$

The information polynomial is

$$E(x) = i_0 + i_1x + i_2x^2 + i_3x^3 + i_4x^4 + i_5x^5 + i_6x^6 + i_7x^7$$
$$= ((1+\hat{i}), (1+2\hat{i}), (2+\hat{i}), (1+\hat{i}0), (0+\hat{i}0), (0+\hat{i}0), (0+\hat{i}0), (0+\hat{i}0))$$

Encoding is performed by taking the FFT over $GF(7^2)$ of i_n That is,

$$F_K = \sum_{n=0}^{8-1} i_n \alpha^{nK}$$
$$= (1+\hat{i}) + (1+2\hat{i})\alpha^K + (2+\hat{i})\alpha^{2K} + (1+\hat{i}0)\alpha^{3K}$$

this implies

$$f(x) = F_0 + F_1x + F_2x^2 + F_3x^3 + F_4x^4 + F_5x^5 + F_6x^6 + F_7x^7$$
$$= ((5+4\hat{i}), (3+4\hat{i}), 4, (-2-\hat{i}), 1, (4+2\hat{i}), 1, (-\hat{i}-1))$$

Suppose the received word associated with two errors is

$$\gamma(x) = \gamma_0 + \gamma_1x + \gamma_2x^2 + \gamma_3x^3 + \gamma_4x^4 + \gamma_5x^5 + \gamma_6x^6 + \gamma_7x^7$$
$$= ((1+\hat{i}), (3+4\hat{i}), 4, (-2-\hat{i}), 1, (2+\hat{i}), 1, (-\hat{i}-1))$$
$$= f_n + e_n$$
$$= ((5+4\hat{i}), (3+4\hat{i}), 4, (-2-\hat{i}), 1, (4+2\hat{i}), 1, (-\hat{i}-1))$$
$$+ ((-4-3\hat{i}), 0, 0, 0, 0, (-2-\hat{i}), 0, 0)$$

The inverse transform over $GF(q^2)$ of γ_n is defined as

$$S_n = 2^{-3}\sum_{K=0}^{8-1} \gamma_K \alpha^{-nK} = \sum_{K=0}^{8-1} \gamma_K \alpha^{-nK}$$

Using the FFT algorithm, one gets,

$$S_0 = 2 + 4\hat{i}$$
$$S_1 = -4 - 3\hat{i}$$
$$S_2 = -3$$
$$S_3 = 2 + 5\hat{i}$$
$$S_4 = e_4 = -2 - 2\hat{i}$$
$$S_5 = e_5 = -3 - \hat{i}$$
$$S_6 = e_6 = -3 + 2\hat{i}$$
$$S_7 = e_7 = -2 + 3\hat{i}$$

Substituting S_i for $i = 4, 5, 6, 7$ in Eq. (12), yields

$$\left.\begin{aligned} \sigma_1 S_5 - \sigma_2 S_4 &= S_6 \\ \sigma_1 S_6 - \sigma_2 S_5 &= S_7 \end{aligned}\right\} \qquad (15)$$

Since

$$\begin{aligned} \begin{vmatrix} S_5 & -S_4 \\ S_6 & -S_5 \end{vmatrix} &= -S_5^2 + S_4 S_6 \\ &= -(-3 - \hat{i})^2 + (-2 - 2\hat{i})(-3 + 2\hat{i}) \\ &= 2 + 3\hat{i} \neq 0 \end{aligned}$$

Eq. (15) has a solution. Thus

$$\begin{aligned} \sigma_1 &= \frac{-S_6 S_5 + S_4 S_7}{-S_5^2 + S_4 S_6} \\ &= \frac{-(-3 + 2\hat{i})(-3 - \hat{i}) + (-2 - 2\hat{i})(-2 + 3\hat{i})}{2 + 3\hat{i}} \\ &= \frac{-1 + \hat{i}}{2 + 3\hat{i}} \\ \sigma_2 &= \frac{S_5 S_7 - S_6^2}{-S_5^2 - S_4 S_6} = \frac{-3 - 2\hat{i}}{2 + 3\hat{i}} \end{aligned}$$

To find the inverse element $(a + \hat{i}b)$ of $(2 + 3\hat{i})$ in $GF(7^2)$

$$(2 + 3\hat{i})(a + \hat{i}b) \equiv 1 \bmod 7$$

which implies

$$\begin{aligned} 2a - 3b &\equiv 1 \bmod 7 \\ 2b + 3a &\equiv 0 \bmod 7 \end{aligned} \qquad (16)$$

The solutions of Eq. (16) are

$$\begin{aligned} a &= -2 \\ b &= 3 \end{aligned}$$

Thus,

$$(2 + 3\hat{i})^{-1} = (-2 + \hat{i}3)$$

Hence

$$\begin{aligned} \sigma_1 &= (-1\hat{i})(2 + 3\hat{i})^{-1} = -1 + 2\hat{i} \\ \sigma_2 &= (-3 - 2\hat{i})(2 + 3\hat{i})^{-1} = 5 + 2\hat{i} \end{aligned}$$

From Eq. (13),

$$e_{j+2} = (-1 + 2\hat{i})e_{j+1} - (5 + 2\hat{i})e_j \qquad \text{for } j = 6, 7, 8, 9$$

It follows that

$$\begin{aligned} e_0 &= \sigma_1 e_7 - \sigma_2 e_6 \\ &= (-1 + 2\hat{i})(-2 + 3\hat{i}) - (5 + 2\hat{i})(-3 + 2\hat{i}) \\ &= 1 + 3\hat{i} \\ e_1 &= \sigma_1 e_0 - \sigma_2 e_7 \\ &= (-1 + 2\hat{i})(1 + 3\hat{i}) - (-2 + 2\hat{i})(-2 + 3\hat{i}) \\ &= 2 + 2\hat{i} \\ e_2 &= \sigma_1 e_1 - \sigma_2 e_0 \\ &= (-1 + 2\hat{i})(2 + 2\hat{i}) - (-2 + 2\hat{i})(1 + 3\hat{i}) \\ &= 2 - 2\hat{i} \\ e_3 &= \sigma_1 e_2 - \sigma_2 e_1 \\ &= (-1 + 2\hat{i})(2 - \hat{i}) - (-2 + 2\hat{i})(2 + 2\hat{i}) \\ &= -2\hat{i} + 1 \end{aligned}$$

Hence the error pattern is

$$\begin{aligned} e_0 &= 1 + 3\hat{i} \\ e_1 &= 2 + 2\hat{i} \\ e_2 &= 2 - \hat{i} \\ e_3 &= 1 - 2\hat{i} \\ e_4 &= -2 - 2\hat{i} \\ e_5 &= -3 - \hat{i} \\ e_6 &= -3 + 2\hat{i} \\ e_7 &= -2 + 3\hat{i} \end{aligned}$$

Since $S_n = i_n + e_n$, the corrected code is

$$\begin{aligned} i_n &= S_n - e_n \\ &= (2 + 4\hat{i}, -4 - 3\hat{i}, -3, 2 + 5\hat{i}, -2 - 2\hat{i}, \\ &\quad -3 - \hat{i}, -3 + 2\hat{i}, -2 + 3\hat{i}) - (1 + 3\hat{i}, 2 \\ &\quad + 2\hat{i}, 2 - \hat{i}, -2\hat{i} + 1, -2 - 2\hat{i}, -3 - \hat{i}, \\ &\quad -3 + 2\hat{i}, -2 + 3\hat{i}) \\ &= (1 + \hat{i}, 1 + 2\hat{i}, 2 + \hat{i}, 1 + 0\hat{i}, 0 + \hat{i}0, 0 + \hat{i}0, \\ &\quad 0 + \hat{i}0, 0 + \hat{i}0) \end{aligned}$$

Appendix

A Method for Determining Octadic Residue and Octadic Nonresidues of a Prime

To define the field of type $I_{F_n}(\sqrt[8]{2})$, it is necessary to determine whether 2 is either an octadic residue or an octadic nonresidue of F_n. Towards this end, the following definition and theorems are needed.

Definition. Suppose m is an integer and q is a prime such that $(m, q) = 1$. Let $[m/q]_2$ be the Gauss-Legendre symbol. Then $[m/q]_{2^n}$ is the symbol, defined by

$$\left[\frac{m}{q}\right]_{2^n} = +1 \qquad \text{if } X^{2^n} \equiv m \bmod q \text{ has an integer solution in } GF(q)$$

$$= -1 \qquad \text{if } X^{2^n} \equiv m \bmod q \text{ has not an integer solution in } GF(q) \text{ for which } [m/q]_{2^{n-1}} = 1$$

Theorem 1. Let $q = a^2 + b^2 = 4n + 1$ be a prime for a odd and b even. If $[2/q]_2 = 1$, then $[2/q]_4 = (-1)^{b/4}$.

Theorem 2. Let $q = a^2 + b^2 = 8n + 1$ be a prime, a odd and b even. If $[2/q]_4 = 1$, then

$$\left[\frac{2}{q}\right]_8 = (-1)^{b/8} \qquad \text{if } n \text{ is even}$$

$$= (-1)^{(b/8)+1} \qquad \text{if } n \text{ is odd}$$

For the proof of these two theorems, see Ref. 20.

Let q be a Fermat prime, i.e., $F_n = 2^{2^n} + 1 = 4 \cdot 2^{2^n-2} + 1 = (2^{2^{n-1}})^2 + 1 = a^2 + b^2$ for $n = 1, 2, 3, 4$.

By Theorem 1,

$$\left[\frac{2}{F_n}\right]_4 = (-1)^{2^{2^n-1}/4} = +1 \text{ for } n = 3, 4$$

Also by theorem 2,

$$\left[\frac{2}{F_n}\right]_8 = (-1)^{2^{2^n-1}/8} = 1 \qquad \text{for } n = 3, 4$$

Thus, 2 is an octadic residue modulo F_n for $n = 3, 4$.

Acknowledgment

The authors wish to thank Mr. B. Mulhall and Dr. B. Benjauthrit of JPL for their early support, suggestions, and encouragement of the research that led to this paper.

References

1. Gove, W. C., *Transmitting Binary Symbols with Reed-Solomon Code.* Johns Hopkins EE Report No. 73-5, April 1973.

2. Mandelbaum, D., "On Decoding Reed-Solomon Codes," *IEEE Transactions on Information Theory,* Vol. IT-17, No. 6, pp. 707–712, November 1971.

3. Reed, I. S., and Solomon, G., "Polynomial Codes over Certain Finite Fields," *SIAM J. Appl. Math.,* Vol. 8, pp. 300–304, June 1960.

4. Michelson, A., *A New Decoder for the Reed-Solomon Codes Using a Fast Transform Technique.* Systems Engineering Technical Memorandum No. 52, Electronic Systems Group Eastern Division GTE Sylvania, August 1975.

5. Peterson, W. W., *Error-Correcting Codes.* MIT Press, Cambridge, Mass., 1961, pp. 168–169.

6. Achonhage, S., and Strassen, V., "Schnelle Multiplikation Grosser Zahlem," *Computing 7,* pp. 281–292, 1971.

7. Rader, C. M., "Discrete Convolution via Mersenne Transforms," *IEEE Trans. on Computers,* Vol. C-21, No. 12, December 1972.

8. Agarwal, R. C., and Burrus, C. S., "Fast Convolution Using Fermat Number Transforms with Applications to Digital Filtering," *IEEE Trans. on Acoustics. Speed, and Signal Processing,* Vol. ASSP-22, No. 2, April 1974.

9. Agarwal, R. C., and Burrus, C. S., "Number Theoretic Transforms to Implement Fast Digital Convolutional," *Proceedings of the IEEE,* Vol. 63, No. 4, April 1975.

10. Reed, I. S., and Truong, T. K., "Convolution Over Residue Classes of Quadratic Integers," in *IEEE Trans. Inf. Theory,* July 1976.

11. McClellan, J. H., "Hardware Realization of a Fermat Number Transform," *IEEE Trans. on Acoustics, Speech, and Signal Processing,* Vol. Assp. 24, No. 3, June 1976.

12. Reed, I. S., and Truong, T. K., "The Use of Finite Fields to Compute Convolutions," *IEEE Trans. Inf. Theory,* Vol. IT-21, No. 2, pp. 208–212, March 1975.

13. Reed, I. S., *The Use of Finite Fields and Rings to Compute Convolutions,* Laboratory Technical Memorandum No. 24L-0012, MIT Lincoln Laboratory, October 1973.

14. Liu, K. Y., Reed, I. S., and Truong, T. K., "Fast Algorithms for Complex Integer Transforms," submitted to *IEEE Trans. on Acoustics, Speed, and Signal Processing.*

15. Reed, I. S., and Truong, T. K., "Complex Integer Convolutions over a Direct Sum of Galois Fields," *IEEE Trans. Inform. Theory,* Vol. IT-21, November 1975.

16. Golomb, S. W., Reed, I. S., and Truong, T. K., "Integer Convolutions Over the Finite iFeld *GF* $(3 \cdot 2^n + 1)$," to be published in *SIAM Journal on Applied Mathematics.*

17. Reed, I. S., Truong, T. K., Kwoh, Y. S., and Hall, E. L., "Image Processing by Transforms over a Finite Field," submitted to *IEEE Transactions on Computers*, January 1976. Available from the Computer Society Repository.

18. Singleton, R. C., "An Algorithm for Computing the Mixed Radix Fast Fourier Transform," *IEEE Trans. Audio Electroacoust.*, Vol. AU-17, pp. 93–103, June 1969.

19. Justesen, J., "On the Complexity of Decoding of Reed-Solomon Codes," *IEEE Trans. Inform. Theory*, Vol IT-22, March 1976.

20. Ping-Yuan Wu, *A Rational Reciprocity Law*, Ph.D. dissertation, Dept. of Mathematics, University of Southern California, August 1975.

21. Reed, I. S., and Truong, T. K., "Convolutions over Quartic Integer Residue Classes," submitted to *IEEE Trans. Inf. Theory*.

22. Berlekamp, E. R., *Algebraic Coding Theory*, New York, McGraw Hill, 1968, Chapter 7.

23. Robinson, R. M., "A Report on Primes of the Form $K \cdot 2^n + 1$ and on Factors of Fermat Numbers," *Proceedings of the American Mathematical Society*, Vol. 9, No. 5, October 1958.

24. Herstein, I. N., *Topics in Algebra*, Blaisdell Publishing Co., 1964.

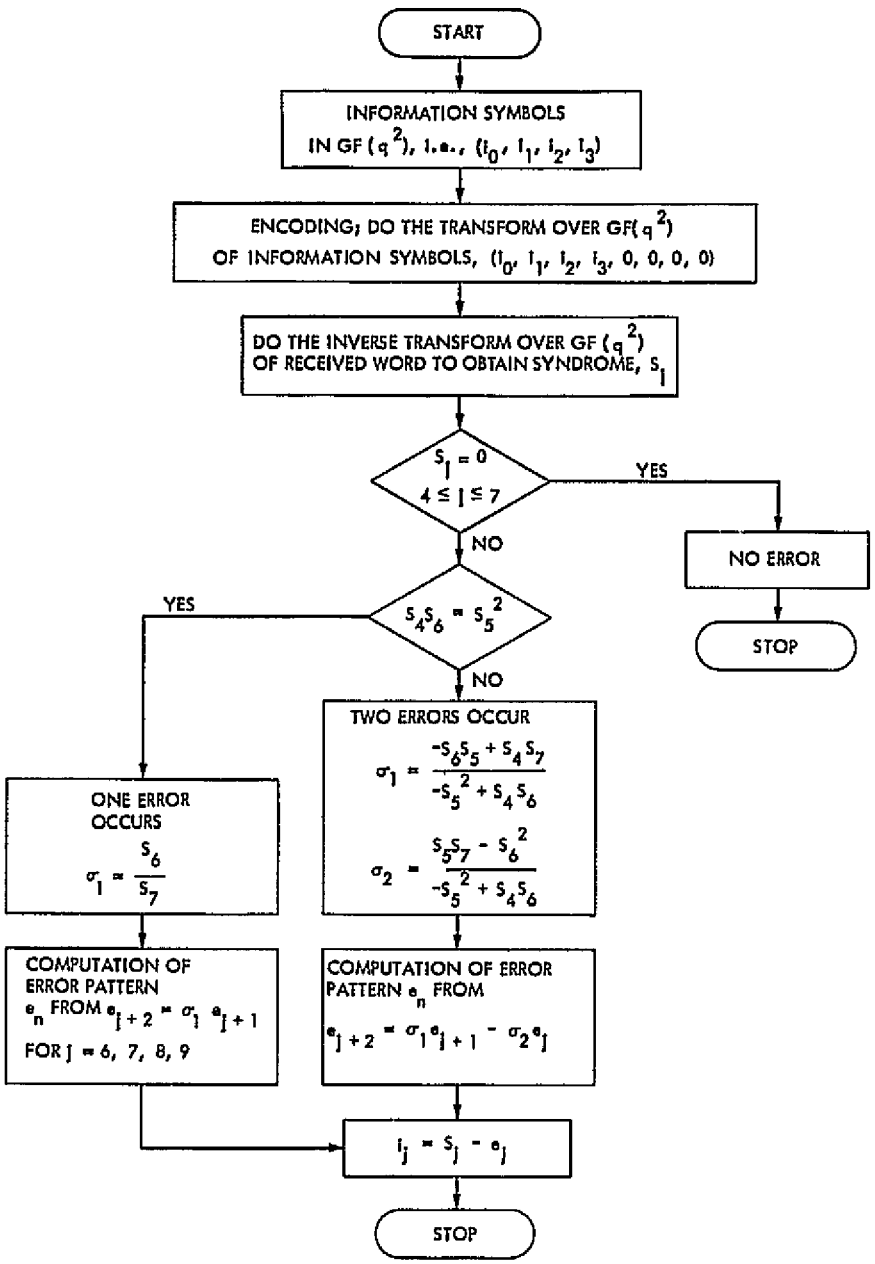

Fig. 1. Transform over GF (q^2) encoder and decoder for correcting at most 2 errors of 8-tuple RS code

LS 44 — An Improved Deep Space Network Station Location Set for Viking Navigation

H. M. Koble, G. E. Pease, K. W. Yip
Navigation Systems Section

Improved estimates for the spin axis and longitude components of the Deep Space Network station locations have been obtained from post-flight processing of radio metric data received from various Mariner planetary missions. The use of an upgraded set of ionospheric calibrations and the incorporation of near-Venus and near-Mercury radio metric data from the Mariner 10 spacecraft are the principal contributing effects to the improvement. These new estimates, designated Location Set (LS) 44, have supported Viking navigation activities in the vicinity of Mars. As such, the station locations have been determined relative to the planetary positions inherent in JPL Development Ephemeris (DE) 84, which has been used throughout the Viking mission. The article also presents and discusses a version of LS 44 based upon the latest planetary ephemeris, DE 96.

I. Introduction

This article primarily focuses on an update which has recently been made to the location estimates for the Deep Space Network (DSN) tracking stations. The new solutions, designated Location Set (LS) 44, fulfill a requirement to provide the Viking mission with a "best" set of estimates to support critical navigation operations in the vicinity of Mars. As such, they replace LS 43 which had supported the launch and much of the interplanetary cruise phases of the mission.

The update was obtained by combining the absolute station location information inherent in radio metric data arcs received from five previous deep space probes (Mariners 4, 5, 6, 9, and 10) with relative position information from geodetic surveys at the various complexes. Adjustments were made only to the LS 43 estimates of each station's geocentric distance from the Earth's spin axis r_s and geocentric longitude λ. The data under consideration, as expected, did not provide a sufficiently accurate absolute determination of the third coordinate, the geo-

centric height above Earth's equatorial plane Z, to warrant an update to the LS 43 values.[1]

Herein, emphasis will be placed on the differences between LS 43 and 44 with the intent of justifying why, in our view, the latter represents an improved spin axis and longitude determination. In brief, there are two principal reasons. First, the processing of radio metric data used to determine LS 43 has been improved, particularly in the area of calibrating the data to account for ionospheric charged particle effects. Second, new radio metric data have been incorporated into the combined data set solution thereby permitting the first accurate absolute determination of the locations for Deep Space Stations (DSS) 43 and 63. The new data, which are from the Mariner 10 mission, also enhance the estimates for other stations in the network.

Any set of DSN station location solutions is associated with some particular JPL planetary ephemeris. Both LS 43 and 44 are referenced to JPL Development Ephemeris (DE) 84. The second portion of the article will briefly discuss some results in connection with determining the effect of a planetary ephemeris update on the station location estimates, LS 44.

At present, if a new ephemeris is adopted during a mission, a *complete* reprocessing of the radio metric data must be performed in order to determine a set of station location estimates relative to the new ephemeris. A research project is currently in progress to develop an analytically based procedure that will enable us to adjust a set of station location estimates for ephemeris changes and circumvent the need for expensive data processing. Preliminary results have indicated that the Brouwer and Clemence Set III ephemeris partial derivatives can represent ephemeris differences to a level of accuracy commensurate with required station location accuracies. Therefore, a linear correction scheme using these partial derivatives appears promising. No matter what procedure is eventually developed, it will be necessary to test its accuracy against the complete reprocessing approach. Anticipating that this test will be made in the near future, the LS 44 data set was reprocessed using JPL Development Ephemeris 96, and a combined data solution was once again obtained for the spin axis and longitude components. The final portion of this article will compare the individual and combined solutions for DE 84 and DE 96.

[1]The coordinate system in question will be more fully described at the beginning of Section II.

II. Background on Station Location Development Procedures

The locations of the DSN tracking stations are computed in a geocentric coordinate system whose axes are defined by the Earth mean pole (axis of rotation), equator, and prime meridian of 1903.0. A variety of coordinate parameters may be used to locate a given station within this system. At JPL, the cylindrical triplet r_s, λ, and Z is most often used,

where

r_s = distance from the axis of rotation, km

λ = longitude as measured east from the prime meridian, deg

Z = height above the equatorial plane, km

Figure 1 depicts the coordinate system and location parameters for one station.

Current station location development procedures are guided by a simplified, yet quite valuable theoretical analysis of the information content in the available radio metric data (primarily two-way doppler plus a relatively small number of range points). Details may be found in Refs. 1 and 2. The following discussion summarizes the general conclusions contained therein.

A. Spin Axis Determination

In these references it is shown that uncertainties in the probe's absolute position (more precisely in the probe's declination) will degrade the spin axis estimate. Analysis reveals that if data are processed from either or both of two specific geometries, this correlation effect can be circumvented.

The first favorable geometry is one from which the probe's absolute position can be inferred independent of Earth-based parameters such as station locations. In theory, this can be done from data taken during the period of a probe's closest approach to a target body other than Earth—the so-called planetary encounter phase. During this period, a complete orbit estimate can be independently made because of the bending effect exerted on the probe's motion by the target planet's gravitational field. Processing the data only provides an accurate estimate of the probe's position *relative* to this planet. However, the necessary absolute reference is provided by the planetary ephemeris in usage.

Upon more careful study of the simplified, theoretical model used in this analysis, it can be noted that when the probe is at zero declination, an uncertainty in its position does not have an appreciable degrading effect on the information content of radio metric data for estimating r_s. Consequently, an absolute determination of the station's spin axis component can also be made if a short span of radio metric data is processed which includes a period when the probe's declination passes through zero degrees.

B. Longitude Determination

In Ref. 2 it was demonstrated that station longitude accuracy depends heavily on the observability of the spacecraft's geocentric range rate, and the precision in the longitude estimate markedly improves as the range rate determination becomes more exact. Again, a planetary encounter geometry spanning a period of roughly encounter ± 5 days should be useful for longitude work because the spacecraft absolute velocity can also be determined independent of Earth-based parameters. Unfortunately, in practice, the probe's encounter orbit velocity estimate may be degraded due to incomplete usable doppler tracking coverage, particularly from the post-encounter period. For example, if a large ΔV is required for orbit insertion (as in Mariner 9 and Viking), the post-insertion data cannot be combined with pre-insertion data to improve station location estimates. To reduce the velocity uncertainty and thereby improve the station longitude determination, a useful tactic is to supplement the usable doppler data with range measurements taken near the planetary encounter. This follows because range measured over time determines the mean range rate.

The Hamilton-Melbourne simplified, theoretical analysis (Ref. 1) indicates that the zero declination arc is not useful for determining accurate absolute longitude estimates. However, the relative difference in longitude between various stations will be preserved if solutions are obtained from this type of data arc.

C. Z Height Determination

The Z component of station position is not well determined by doppler data. In order to produce a complete set of location estimates, it has been necessary to rely on data provided by sources outside JPL. Currently, we are using the results of geodetic surveys (Ref. 3) made at the various complexes and geocentric-geodetic differences prepared by Wolf Research Corporation (Ref. 4) using optical and laser data to obtain Z values. The Z height estimates were not changed from LS 43 to LS 44, and the values in current usage at JPL are displayed in Table 1. The use of existing Mariner range data and near-simultaneous range data from the Viking orbiters is currently being contemplated to improve the Z height determination.

D. General Guidelines

Based on this theoretical analysis and past experience processing radio metric data, we can establish some general guidelines for determining the spin axis and longitude estimates.

(1) Define tracking arcs from the various missions that reflect the planetary encounter or zero declination geometry.

(2) For each arc, obtain the best set of calibrations for ionospheric charged particle effects, tropospheric refraction, and timing and polar motion which are currently available. Of course, our ability to obtain high-quality station spin axis and longitude estimates depends on minimizing the errors introduced by each of these sources.

(3) For each arc, obtain as accurate a spacecraft trajectory as possible.

(4) Given the best trajectory, obtain estimates for the spacecraft state at the initial epoch of each arc and estimates for the DSN stations which participated in tracking the given spacecraft during the defined time period. In this regard, it is usually necessary to simultaneously estimate one or more other parameter types such as solar pressure, planetary oblateness, range biases, attitude-control accelerations, planetary mass, etc.

(5) Combine the individual arc absolute station location determinations and any relative information from ground surveys to obtain a final set of estimates. Historically, the procedure used to perform this last step has varied, and we will defer any additional commentary until LS 43 and 44 are discussed.

III. Location Set 43

The previous best set of station locations, Location Set 43, was announced in May 1975 and used to support the Viking mission during the launch and interplanetary cruise phase.

Table 2A and 2B summarizes the tracking arc geometry and radio metric data that provided the basis for the

spin axis and longitude estimates. As indicated, encounter arc data were used from the Mariner 4, 5, 6, and 9 missions along with a pre- and post-encounter zero declination phase of the Mariner 5 trajectory. The asymmetry relative to planetary encounter for Mariner 6 was due to unusable data caused by a gas-venting cooling operation; for Mariner 9 it was due to the Mars orbit insertion maneuver.

Each arc was processed using the orbit determination program of the Mariner 10 mission (Ref. 5); the same planetary ephemerides, JPL Development Ephemeris 84; the same source for UT1 (universal time) and Earth polar motion, the Bureau International de l'Heure (BIH); and the same model for tropospheric refraction calibrations.[2]

All doppler data were calibrated for the effects of ionospheric charged particles *with the exception* of the Mariner 4 data. Unfortunately, at the time of radio metric data processing for LS 43, calibrations were available only for a data set that was too small to provide reliable station location solutions. It was estimated that the errors introduced into the Mariner 4 solution by ignoring the ionospheric effect would be no more than 0.5×10^{-5} deg (approximately ½ m) in longitude and 1.6 m in spin axis. The actual longitude error proved to be slightly larger than this prediction (see Table 8, right-most column).

Once the final individual arc solutions were obtained, LS 43 was produced by combining these six determinations in a least squares fashion. The final solution involved simultaneous estimation of 72 parameters: a six-dimensional spacecraft state vector for each arc (36 parameters); a three-dimensional solar pressure model vector for each arc (18 parameters); one range bias parameter for the Mariner 6 and 9 missions (2 parameters); and spin axis and longitude parameters for each of the eight stations, DSSs 11, 12, and 14 at Goldstone, 41 and 42 in Australia, 51 in South Africa, and 61 and 62 in Spain, which provided tracking coverage during the time periods in question (16 parameters).

In determining this final estimate, a priori information on station locations was included based on relative coordinate differences determined from ground-based geodetic surveys at the various complexes.[3] The geodetic data were transformed to the geocentric coordinate system defined in Fig. 1, and the results are presented in Table 3. The a priori spin axis and longitude absolute values conformed exactly with these differences, and the statistics on these values were defined by: standard deviation of the spin axis a priori values for survey-constrained stations, 1000 m, and for stations not constrained, 50 m; standard deviation of the longitude a priori values for survey-constrained stations, 1000×10^{-5} deg, and for stations not constrained, 50×10^{-5} deg; correlation coefficients determined to reflect a survey accuracy of 0.3 m and 0.3×10^{-5} deg, respectively.

The final spin axis and longitude estimates are given in Table 4, and the differences between the individual data arc solutions and these values may be found in Table 5.

To provide a complete set of estimates for all stations in the Network, values for those which did not track (DSSs 13, 43, 44, and 63) were computed by adding the relative differences shown in the lower portion of Table 3 to the LS 43 solutions for the base stations at each site (DSSs 12, 42, and 61).

Using the data from Table 5, we conclude that for stations whose solution was based on more than one data arc, the consistency in spin axis estimates range from 1.090 m for DSS 51 to a worst case of 4.545 m for DSS 41. The Mariner 4 spin axis solutions are low because calibrations for ionospheric charged particle effects were not included.

The scatter for the encounter arc longitude estimates range from 1.200×10^{-5} deg (~1.2 m) for DSS 41 to 4.296×10^{-5} deg for DSS 51. The reader will note that the absolute longitude determinations from the zero-declination arcs are not consistent with the encounter arc solutions, particularly for the Mariner 5 postencounter case. These solutions, were included in the final LS 43

[2]JPL Development Ephemeris 84 was announced by E. M. Standish and M. S. W. Keesey of the Systems Division, Tracking System and Applications Section in an internal document, Interoffice Memorandum 391.5-553. The document is entitled, "Development Ephemeris 84 — Announcement," and was published on August 22 1973.

A description of the data-gathering and data-processing system by which the timing and polar motion calibrations were obtained may be found in (Ref. 6).

Details concerning the mathematical model for tropospheric calibrations may be found in (Ref. 7). The "dry" and "wet" tropospheric zenith range error polynomials for each data arc were based on results discussed in a JPL document, Engineering Memorandum 391-506, prepared by F. B. Winn, C. C. Chao, and M. J. Richter.

[3]The survey data was obtained from (Ref. 3) and subsequent private communications between the DSN and N. A. Mottinger of the Systems Division, Navigation Systems Section.

determination; however, their formal uncertainties as computed by the orbit determination program are three to four times larger than the encounter arc statistics for comparable amounts of data. When LS 43 was prepared, the final estimates were interpreted to mean that these zero-declination longitude solutions would have minimal influence on the combined data estimates. Recent analysis has confirmed this hypothesis.

IV. Location Set 44

Location Set 44 was announced in late April 1976 and has been used to support Viking mission activities since that time. This new set of station locations represents an update to the LS 43 spin axis and longitude estimates discussed in Section III. The differences between these solutions are primarily due to two factors: (1) the inclusion of radio metric data for two new encounter arcs and (2) an improved processing of the four encounter and two zero-declination arcs used to determine LS 43.

A. New Radio Metric Data

Post-flight analysis of encounter arc data from the Mariner 10 mission had not been completed at the time the bulk of data processing for LS 43 was performed. A preliminary determination of station location estimates from the Venus and first Mercury encounters revealed that this new data would have a significant effect. By including it, the number of radio metric points on which a combined data arc solution would be based would more than double. Furthermore, since DSS 43 and 63 provided tracking coverage during these encounter arcs, the previous geodetic survey-based solutions could be augmented by absolute information from radio metric data.

The preliminary solutions for *both* encounter arcs indicated that a correction of approximately 3 m was warranted for the spin axis component of both DSS 42 and 43. This was due to the fact that the LS 43 value for DSS 42 was based on a paucity of ionospheric calibrated radio metric data from that station. As indicated in Table 2B, 358 points were incorporated; however, 276 of these from the Mariner 4 mission were uncalibrated. Since the LS 43 estimate for DSS 43 was obtained by adding a survey difference to the DSS 42 spin axis coordinates, we can say that the DSS 43 value was also based on primarily uncalibrated radio metric data.

A summary of the Mariner 10 data incorporated into the LS 44 solution is provided in Tables 6A and 6B. Range data were available for the Venus encounter arc, but analysis of a range + doppler based solution could not be completed in time to include in the LS 44 determination. Analysis subsequent to the generation of LS 44 revealed that if the doppler-only solution were replaced by this range + doppler solution, the effect on LS 44 would be to perturb the values by at most 0.09 m in spin axis and 0.31×10^{-5} deg in longitude. An effort was also made to include data from the third encounter arc with Mercury. Unfortunately, examination of the residuals associated with filtering this data revealed that the quality of the fit was not very good and that further analysis and data processing would be needed before the Mercury 3 encounter could be included.

The doppler-only solution from the Venus encounter and the range + doppler solution from the first Mercury encounter will be discussed shortly.

B. Improved Processing of LS 43 Data

The most significant factor which prompted a reprocessing of the radio metric data used to develop LS 43 was an upgrading of the set of calibrations for ionospheric charged particle effects. A complete discussion of these calibrations may be found in (Ref. 8). In summary, the following changes were made to the LS 43 data sets.

1. Mariner 4 mission. As noted in Section III, the radio metric data which were processed to obtain station location estimates from the Mariner 4 encounter arc were not calibrated for the ionospheric effect. For the LS 44 determination, calibrations were prepared directly from ionospheric total electron content (TEC) data wherever possible. Other radio metric data points were also calibrated by averaging available TEC data and mapping the resultant values to the appropriate time intervals and tracking stations-spacecraft lines of sight. Whereas 1015 uncalibrated doppler points were used in the LS 43 solution for the Mariner 4 mission, only 899 of these could be accurately calibrated for use in an LS 44 solution.

2. Mariner 6 mission. An analysis of the calibrations used for DSS 62 data revealed that the underlying TEC data were noisy and of poorer quality than data for other stations which tracked during the encounter arc period. It was decided to replace these calibrations with a new set prepared by averaging the available TEC data over the period from 7/26/69 to 7/30/69 and applying these averages to all of the radio metric data for DSS 62. These data were taken on 7/26 and 7/28. By using averaged

rather than actual TEC values, an additional 15 points could be calibrated.

3. Mariner 9 mission. At the time the Mariner 9 encounter arc data were processed for the LS 43 solution, calibrations were unavailable for one pass of data from DSS 41 taken on 11/11/71. A set of calibrations were prepared by averaging the total electron contents for the week including this date. In so doing, 39 additional points could be calibrated.

No modifications were made to the LS 43 ionospheric calibrations for any of the three Mariner 5 tracking arcs. In Table 7, we summarize the modifications which were made to the data sets used in preparing LS 43 (c.f. Table 2B).

Some minor modifications were made to the tropospheric calibrations, but the same planetary ephemeris DE 84 and timing and polar motion decks described previously for LS 43 were used in preparing LS 44.

C. Procedure and Discussion of Individual Data Arc Solutions

Whereas the LS 43 solutions were obtained using the orbit determination program for the Mariner 10 mission, it was decided to use the corresponding program for the Viking mission to perform the data processing for LS 44. This was logical because LS 44 would be used to support the critical navigation activities for both Viking spacecraft in the vicinity of Mars.

As a first step, an effort was made to reproduce the individual data arc solutions of Table 5 (which were generated by the Mariner 10 orbit determination program) using the Viking software. That is to say, the upgraded calibrations for tropospheric and ionospheric effects were not initially used and internal constants from the Viking program were overridden by the corresponding Mariner values. In general, reproduceability was achieved to a very high accuracy (on the average, less than 0.2 meters in spin radius and 0.2×10^{-5} degrees in longitude) with the notable exception of the Mariner 9 data arc. Extensive analysis (Ref. 8) revealed that the models for gas leaks did not correspond between the two programs, and that the Mariner 10 program did not handle the integration of its model in an entirely accurate manner. The discrepancy between the solutions from the two programs was as large as 0.26 meters in spin radius and 0.72×10^{-5} deg in longitude.

In Table 8, we present a summary of the improved individual station location solutions which resulted from reprocessing the LS 43 data using the new software, upgraded calibrations for ionospheric and tropospheric effects, but same planetary ephemeris and timing and polar motion models. The left-hand columns contain the differences between these solutions and the LS 43 values of Table 4. The right-hand columns contain the differences between these solutions and the corresponding solutions from the original processing (i.e., the results of Table 5).

As anticipated, the average change in the solutions for the three Mariner 5 data arcs is much smaller than the adjustments to the Mariner 4-6-9 solutions. The sizeable increases in the spin radius and longitude estimates for Mariner 4, the dramatic change in the DSS 62 longitude estimate for Mariner 6, and the decreases in longitude estimates for Mariner 9 are, however, consistent with the ionospheric, tropospheric, and software gas leak model modifications discussed earlier.

The two Mariner 10 encounter arcs defined by Table 6A-B were also processed using the Viking software; the same ephemeris, JPL Development Ephemeris 84; BIH data for universal time and polar motion; and calibrations for ionosphere and troposphere generated by the same models which provided calibrations for the other data arcs. Table 9 summarizes the Mariner 10 solutions. The most significant effects are: (1) a large positive correction to the LS 43 spin axis estimates at DSS 42 and 43 and (2) a negative correction to the LS 43 longitude estimates of more than one meter. The apparent anomalies in the Mariner 10 Mercury 1 encounter solutions for r_s at DSS 12 and λ at DSS 42 are compensated by comparatively large uncertainties in these estimates (Table 9).

D. Final Combined Solution

Once the final individual arc solutions were obtained, LS 44 was produced by combining these eight determinations in a direct, least squares fashion. The final solution involved estimation of: spin axis and longitude parameters for each of the ten stations, DSS 11, 12, 14, 41, 42, 43, 51, 61, 62, and 63 which provided tracking coverage during the time periods in question and the following set of parameters from the individual data arcs (these were the parameters which were simultaneously estimated with the participating stations in determining the individual arc estimates):

Mariner 4 encounter—a six-parameter spacecraft state

Mariner 5 preencounter—a six-parameter spacecraft state and a three-parameter solar pressure model vector

Mariner 5 encounter—same as Mariner 5 preencounter

Mariner 5 postencounter—same as Mariner 5 preencounter

Mariner 6 encounter—a six-parameter spacecraft state and one range bias parameter

Mariner 9 encounter—a six-parameter spacecraft state and one range bias parameter

Mariner 10 Venus encounter—a six-parameter spacecraft state, Venus oblateness, and mass of Venus

Mariner 10 Mercury 1 encounter—a six-parameter spacecraft state, Mercury oblateness, mass of Mercury, a nine-parameter solar pressure model vector, and four range bias parameters

In determining the final estimates, relative coordinate differences based on geodetic survey information were again included as a priori data. The a priori spin axis and longitude absolute values conformed exactly with the results of Table 8, and the statistics on these values were defined by: standard deviation of the spin axis a priori values, 50 m; standard deviation of the longitude a priori values, 50×10^{-5} deg; correlation coefficients were determined to reflect an assumed survey accuracy of 0.3 m and 0.3×10^{-5} deg, respectively.

The final spin axis and longitude estimates appear in Table 10. Since DSS 13 and 44 did not provide tracking coverage during the time periods in question, their estimates were computed by other means. For DSS 13, the geodetic survey-based relative spin axis and longitude differences (Table 3) were added to the LS 44 estimates for DSS 12. However, a different strategy was employed for DSS 44. This station provided tracking coverage for the Pioneer 10 spacecraft during its interplanetary cruise. Estimates for DSS 44 were obtained from this radio metric data, and it was found that they were not consistent with a spin axis and longitude determination based on the survey differences between DSS 42 and 44 as shown in Table 3. When solutions based on interplanetary cruise arc data from the Viking spacecrafts tended to confirm the Pioneer values, it was decided to abandon the survey information for DSS 44 minus DSS 42 in favor of this radio metric based solution. Consequently, the LS 44 values are the Pioneer absolute estimates.

Earlier we discussed the various factors which contribute to the differences between the LS 43 and 44 station location estimates. In Table 11, these differences are documented quantitatively. For each station in the network, we have computed the spin axis and longitude changes between the two location sets. These values appear in the left-most column of this table. In the center column, we show the effect of reprocessing the LS 43 data. A combined solution was obtained from the improved individual determinations documented in Table 8 using techniques identical to those for computing LS 44. The result was then differenced with the LS 43 solution. Finally, the right-most column of Table 11 shows the effect of adding Mariner 10 data to the combined solution resulting from the improved processing of LS 43 individual arcs. In other words, these values represent the difference between the left and center columns.

The most significant change between the LS 43 and 44 spin axis estimates occurs at DSS 42 and 43. Approximately 80% of this large positive increase is due to the Mariner 10 data. As noted earlier, this is not surprising; it had been predicted in preliminary post-flight analysis of this data. Most of the changes at the Goldstone complex (DSSs 11, 12, and 14) and South Africa (DSS 51) are due to reprocessing of LS 43 data. A glance at Table 8 reveals that the principal contributing factor was the addition of ionospheric calibrations for the Mariner 4 data arc.

The longitude changes from LS 43 to LS 44 are consistently negative. From the results of Table 9, it is clear that the Mariner 10 solutions would force the combined estimates in this direction. However, it is a little surprising to see that the reprocessing of LS 43 data also led to a negative shift in longitudes. Examining the Table 8 data, it would appear that the positive correction to the Mariner 4 estimates due to the ionospheric effect has been swamped by the large negative corrections in Mariner 9 resulting from proper handling of the gas leak model by Viking software and also by the very large change in the DSS 62 estimate for Mariner 6.

Recall that Table 8 and 9 also displayed the differences between the individual data arc solutions and the LS 43 estimates. We have represented the differences between these same solutions and the LS 44 estimates pictorially in Figs. 2 and 3. These differences are plotted against the number of Julian days past 1950.0. The time axis is an exact scale, and we have endeavored to center the results for each encounter arc about the encounter date. The Mariner 5 pre- (labeled M5C in the figures) and postencounter (labeled M5P in the figures) results have been placed in close proximity to the encounter arc

solutions for that mission. The horizontal line in the middle of each vertical bar represents the actual difference between the individual data arc solution for the indicated station and the LS 44 value. The size of the vertical bars reflect the formal 1-σ (standard deviation) uncertainties for each individual solution which were produced by the Viking orbit determination program.

The longitude residuals appear to be drifting in a negative direction with time, although the slope seems to change following the Mariner 5 encounter. Although further analysis is needed, the spin axis residuals may be exhibiting a sinusoidal behavior.

V. Effect of an Ephemeris Change on LS 44 Values

The set of station location estimates which we have designated as Location Set 44 were computed relative to the absolute planetary positions inherent in JPL Development Ephemeris 84. These estimates will not be valid if changes are made to the relative position of the Earth with the various encounter planets during the time periods specified by the data arcs used to obtain LS 44. A *rough* estimate of the changes in station locations due to an update of the adopted planetary ephemeris can be obtained from the differences in the respective geocentric right ascensions and declinations of the target planets at the times of spacecraft encounter. These numbers translate into equivalent changes in the DSS spin axis and longitude estimates according to

$$\Delta r_s = \frac{\Delta\delta}{206265} r_s \tan\delta$$

$$\Delta\lambda = \Delta\alpha$$

where Δr_s is the change in spin axis for a given station due to the ephemeris change, $\Delta\lambda$ is the change in longitude for that station, r_s is the spin axis estimate relative to the old ephemeris, δ is the target planet declination in degrees as defined by the old ephemeris, $\Delta\delta$ is the change in target planet declination between the old and new ephemeris in seconds of arc, and $\Delta\alpha$ is the change in target planet right ascension between the old and new ephemeris.

To illustrate this rough approximation scheme, let us assume the old ephemeris is DE 84, and the new ephemeris is JPL Development Ephemeris 96 (Ref. 9). The spin axis estimates r_s relative to the old ephemeris will be the LS 44 values of Table 10. DE 84 based target planet declinations δ and the changes in planet declination $\Delta\delta$ and right ascension $\Delta\delta$ between the old and new ephemeris appear in Table 12A. These were computed at the various spacecraft encounter times. Using this data and the expressions for Δr_s and $\Delta\lambda$ defined above, the approximate effect of this ephemeris change on the LS 44 spin axis and longitude values has been computed and appears in Table 12B.

However, a precise evaluation of the induced changes requires the "brute force" approach of reprocessing the individual arc tracking data to obtain station location estimates relative to the new ephemeris and combining the individual determinations to obtain a final location set. This has been done to the data which defines LS 44. For each arc, the inputs to the orbit determination program were not changed with the exception of replacing the DE 84 ephemeris and planetary partial derivative files with the corresponding ones for DE 96. Target planet centered initial conditions were used for the spacecraft state vector on each of the six encounter arc solutions. Heliocentric initial conditions were used for the Mariner 5 pre- and post-encounter solutions.

In Table 13, we show the actual differences between the individual data arc solutions for the DE 84 and DE 96 cases. Notice that for each data arc subsequent to and including the Mariner 5 post-encounter, the changes in spin axis and longitude induced by the ephemeris update are very nearly constant as the predictions of Table 12B suggest. However, there is no consistency to the changes in spin axis and longitude for each data arc preceding the Mariner 5 post-encounter. At present, we do not have a satisfactory explanation for this phenomenon.

The DE 96 based individual solutions have been combined using a procedure identical to the formation of LS 44. The resulting spin axis and longitude estimates appear in Table 14, and their differences with LS 44 are shown in Table 15.[4] The changes in spin axis are seen to be statistically insignificant. Consequently, from a station location viewpoint DE 96 induces a pure rotation of approximately 2.5×10^{-5} deg East relative to DE 84 values.

[4]The DE 96 based station location solutions discussed herein have been computed using a value for the speed of light of 299792.5 km/sec. In the export version of DE 96 (Ref. 9) an updated value of 299792.458 km/s has been adopted. If the reader uses the updated value in all computations, we recommend that the Z values of Table 1 and the r_s values of Table 14 be multiplied by the ratio 299792.458/299792.5 to obtain a DE 96 based station location set that is consistent with this new speed of light constant.

VI. Summary

A preliminary determination of spin axis and longitude estimates based on radio metric data from the Viking 1 spacecraft indicates perturbations to the LS 44 values of, on the average, 1 m or less in r_s and 1×10^{-5} deg or less in λ. This tends to confirm our belief that the LS 44 spin axis and longitude values appearing in Table 10 represent an improved station location estimate. Previous deficiencies in calibrating the radio metric for ionospheric charged particle effects have been minimized and new, useful data from the Mariner 10 mission have been incorporated. As summarized by Table 11, the net effect has been to increase previous spin axis estimates, particularly for DSSs 42 and 43, and to shift the longitude estimates westward.

Our study also reveals that if the latest planetary ephemeris, JPL Development Ephemeris 96 is adopted, the effect on station location estimates, as summarized in Table 15, will be to rotate the system approximately 2.5×10^{-5} degrees eastward.

Acknowledgement

The authors wish to acknowledge N. A. Mottinger for his contributions to the determination of LS 43, the reduction of geodetic survey information, and the development of combination software for LS 44. G. C. Rinker served as the primary consultant for Viking software used in the individual data arc processing. K. H. Rourke designed and coordinated the activities for developing the improved station locations described in this article.

References

1. Hamilton, T. W., and Melbourne, W. G., "Information Content of a Single Pass of Doppler Data from a Distant Spacecraft," in *The Deep Space Network*, Space Program Summary 37-39, Vol. III, pp. 18–23. Jet Propulsion Laboratory, Pasadena, Calif., May 31, 1966.

2. Rourke, K. H., and Mottinger, N. A., "Resolution of an Inconsistency in Deep Space Station Longitude Solutions," in *The Deep Space Network Progress Report 42-44*, pp. 132–143. Jet Propulsion Laboratory, Pasadena, Calif., December 15, 1974.

3. NASA Directory of Observation Station Locations, Vol. 1, 3rd Ed., Goddard Space Flight Center, November 1973.

4. Marsh, J. G., Douglas, B. C., and Losko, S. M., *A Global Station Coordinate Solution Based upon Camera and Laser Data—Goddard Space Flight Center 1973*, Report X-592-72-177, p. 61, May 1973.

5. MVM'73 MOS Software Orbit Determination Program (ODP) Requirements, SRD-73-3-482, July 11, 1972 (JPL internal document).

6. Fliegel, H. F. and Wimberly, R. N., *Tracking System Analytic Calibration Activities for the Mariner Mars 1971 Mission*, Technical Report 32-1587, pp. 77–82. Jet Propulsion Laboratory, Pasadena, Calif., March 1, 1974.

7. Chao, C. C., *Tracking System Analytic Calibration Activities for the Mariner Mars 1971 Mission*, Technical Report 32-1587, pp. 61–77, Jet Propulsion Laboratory, March 1, 1974.

8. Yip, K. W., "LS 43 Updates for LS 44," to appear in *The Deep Space Network Progress Report.*

9. Standish, E. M., Keesey, M. S. W., and Newhall, X. X., *JPL Development Ephemeris Number 96*, Technical Report 32-1603, Jet Propulsion Laboratory, Pasadena, Calif., Feb. 19, 1976.

Table 1. Current Z heights estimates LS 43 and LS 44

DSS	Z, km
11	3673.765
12	3665.629
13	3660.957
14	3667.053
41	−3302.189
42	−3674.589
43	−3674.756
44	−3691.410
51	−2768.744
61	4114.879
62	4116.902
63	4115.105

Table 2A. Summary of tracking arc geometry, LS 43

Mission	Tracking arc	Encounter date	Target planet	[a]	[b]	[c]
Mariner 4 encounter	1965 7/6–7/28	1965 7/15	Mars	12 h 31 min	1.45	−3
Mariner 5 preencounter	1967 7/22–9/16	–	–	–	–	−8 to 8
Mariner 5 encounter	1967 10/14–10/25	1967 10/19	Venus	10 h 46 min	0.53	6
Mariner 5 postencounter	1967 10/29–11/21	–	–	–	–	2 to −2
Mariner 6 encounter	1969 7/25–7/31	1969 7/31	Mars	16 h 10 min	0.64	−24
Mariner 9 encounter	1971 11/9–11/13	1971 11/14	Mars	22 h 27 min	0.81	−12

[a]Apparent right ascension of target plane at encounter date, JPL Development Ephemeris 84

[b]True distance from Earth to target planet at encounter date (AU), JPL Development Ephemeris 84

[c]Spacecraft declination (deg)

Table 2B. Number of data points for each station, LS 43

Mission	Participating DSS	Number of data points by type	
Mariner 4 encounter	11	501 F2	
	42	276 F2	
	51	238 F2	
Mariner 5 preencounter	11	104 F2	
	12	44 F2	
	14	101 F2	
	42	82 F2	
	61	504 F2	
	62	151 F2	
Mariner 5 encounter	12	148 F2	
	14	388 F2	
	41	48 F2	
	62	175 F2	
Mariner 5 postencounter	12	242 F2	
	14	121 F2	
	41	99 F2	
	62	242 F2	
Mariner 6 encounter	12	283 F2	
	14	53 F2	332 Tau
	41	201 F2	
	51	26 F2	
	62	64 F2	
Mariner 9 encounter	12	152 F2	6 Mu
	14	29 F2	
	41	155 F2	
	62	423 F2	

F2 = two-way doppler, S-band
Tau = Tau range data
Mu = Mu range data

Table 3. Relative coordinate differences based on geodetic survey information

Station pair	Δr_s, km	$\Delta\lambda$, deg
11–12	−5.71166	−0.0439311
14–12	−8.05467	−0.0840455
62–61	−1.79030	−0.1188072
13–12	3.43285	0.0105998
43–42	−0.10110	0.0
44–42	−11.37185	−0.0034758
63–61	−0.15712	−0.0010142

Table 4. Spin axis and longitude values, LS 43

DSS	r_s, km	λ, deg East
11	5206.340339	243.1505977
12	5212.052093	243.1945268
14	5203.997323	243.1104843
41	5450.203649	136.8874971
42	5205.349548	148.9812787
51	5742.939590	27.6854314
61	4862.608422	355.7509853
62	4860.818264	355.6321788
13	5215.484943	243.2051266
43	5205.248448	148.9812787
44	5193.977698	148.9778029
63	4862.451302	355.7519995

Table 5. Individual data arc solutions minus LS 43 values

DSS	Mission	Δr_s, m	$\Delta\lambda$, 10^{-6} deg
11	Mariner 4 encounter	−0.972	2.044
	Mariner 5 preencounter	1.403	1.856
12	Mariner 5 preencounter	1.750	1.939
	Mariner 5 encounter	0.672	−1.322
	Mariner 5 postencounter	0.274	9.192
	Mariner 6 encounter	−2.562	0.262
	Mariner 9 encounter	−1.035	−1.090
14	Mariner 5 preencounter	0.470	2.807
	Mariner 5 encounter	−0.127	−1.833
	Mariner 5 postencounter	−1.361	9.699
	Mariner 6 encounter	−1.362	0.257
	Mariner 9 encounter	1.997	−1.703
41	Mariner 5 encounter	−2.373	−0.332
	Mariner 5 postencounter	−1.985	10.692
	Mariner 6 encounter	−1.680	−0.195
	Mariner 9 encounter	2.172	−1.395
42	Mariner 4 encounter	0.042	1.295
	Mariner 5 preencounter	1.733	2.368
51	Mariner 4 encounter	0.174	1.641
	Mariner 6 encounter	1.264	−2.655
61	Mariner 5 preencounter	0.060	2.127
62	Mariner 5 preencounter	0.091	0.441
	Mariner 5 encounter	−0.482	−1.563
	Mariner 5 postencounter	−0.840	9.918
	Mariner 6 encounter	0.066	2.215
	Mariner 9 encounter	1.818	−1.507

Table 6A. Summary of tracking arc geometry from the Mariner 10 mission used in LS 44

Mission	Tracking date	Encounter date	Target planet	a	b	c
Mariner 10 Venus encounter	1974 1/28–2/14	1974 2/5	Venus	19 h 51 min	0.29	−13
Mariner 10 1st Mercury encounter	1974 3/21–4/10	1974 3/29	Mercury	22 h 52 min	0.98	−9

[a]Apparent right ascension of target planet at encounter date, JPL Development Ephemeris 84

[b]True distance from Earth to target planet at encounter date (AU), JPL Development Ephemeris 84

[c]Spacecraft declination (deg)

Table 6B. Number of data points for each station Mariner 10 encounter arcs

Mission	Participating DSS	Number of data points by type	
Mariner 10 Venus encounter	12	384 F2	
	14	934 F2	
	42	121 F2	
	43	1415 F2	
	62	347 F2	
	63	961 F2	
Mariner 10 1st Mercury encounter	12	181 F2	3 Plop
	14	425 F2	43 Mu2
	42	62 F2	
	43	575 F2	30 Plop
	62	64 F2	
	63	564 F2	35 Plop

F2 = two-way doppler, S band
Mu2 = Mu2 range data
Plop = planetary operational ranging points

Table 7. Modifications to the number of data points for each station, LS 43 vs. LS 44

Mission	Participating DSS	Number of data points by type			
		LS 43		LS 44	
Mariner 4 encounter	11	501 F2		473 F2	
	42	276 F2		245 F2	
	51	238 F2		181 F2	
Mariner 6 encounter	12	238 F2		283 F2	
	14	53 F2	332 Tau	53 F2	322 Tau
	41	201 F2		201 F2	
	51	26 F2		26 F2	
	62	64 F2		79 F2	
Mariner 9 encounter	12	152 F2	6 Mu	152 F2	6 Mu
	14	29 F2		29 F2	
	41	155 F2		194 F2	
	62	423 F2		423 F2	

Table 8. Changes due to improved processing of LS data

Mission	Participating DSS	Comparison of improved solutions with LS 43 values[a]		Comparison of improved solutions with individual solutions used in LS 43[b]	
		Δr_s, m	$\Delta\lambda$, 10^{-5} deg	Δr_s, m	$\Delta\lambda$, 10^{-5} deg
Mariner 4 encounter	11	0.522	2.940	1.494	0.896
	42	0.485	2.107	0.443	0.812
	51	0.846	2.376	0.672	0.735
Mariner 5 preencounter	11	1.549	1.952	0.146	0.096
	12	1.966	1.850	0.216	0.089
	14	0.666	2.939	0.196	0.132
	42	1.844	2.515	0.111	0.147
	61	0.292	2.226	0.232	0.099
	62	0.377	0.799	0.286	0.358
Mariner 5 encounter	12	0.700	−1.488	0.028	−0.166
	14	−0.062	−1.715	0.065	0.118
	41	−2.196	−0.363	0.177	−0.031
	62	−0.393	−1.708	0.089	−0.145
Mariner 5 postencounter	12	0.227	9.396	−0.047	0.204
	14	−1.427	9.948	−0.066	0.249
	41	−1.976	10.664	0.009	−0.028
	62	−0.749	10.100	0.091	0.182
Mariner 6 encounter	12	−2.199	−0.183	0.363	−0.445
	14	−1.203	−0.078	0.159	−0.335
	41	−1.811	−0.580	0.069	−0.385
	51	1.192	−2.895	−0.072	−0.240
	62	−0.234	0.270	−0.300	−1.945
Mariner 9 encounter	12	−1.093	−1.760	−0.058	−0.670
	14	1.731	−2.431	−0.266	−0.728
	41	2.120	−1.731	−0.052	−0.336
	62	1.707	−2.303	−0.111	−0.796

[a] Δr_s = r_s (improved) − r_s (LS 43)
$\Delta\lambda$ = λ (improved) − λ (LS 43)

[b] Δr_s = r_s (improved) − r_s (original)
$\Delta\lambda$ = λ (improved) − λ (original)

Table 9. Mariner 10 station location solutions used in LS 44

Mission	Participating DSS	Δr_s, m[a]	Std Dev, m[a]	$\Delta\lambda$, 10^{-5} deg[b]	Std Dev, 10^{-5} deg[c]
Mariner 10 Venus encounter	12	0.571	0.618	−1.723	0.755
	14	0.249	0.550	−2.296	0.697
	42	2.815	1.243	−1.673	1.090
	43	3.212	0.305	−1.460	0.660
	62	0.968	0.651	−2.539	0.837
	63	0.961	0.403	−1.486	0.712
Mariner 10 1st Mercury encounter	12	2.685	2.093	−2.776	1.240
	14	0.628	0.486	−1.981	0.308
	42	4.808	1.555	4.808	1.413
	43	3.443	0.322	−0.279	0.275
	62	1.132	1.035	−0.677	0.817
	63	0.282	0.352	−2.230	0.292

[a]Δr_s = r_s (individual solution) − r_s (LS 43)

[b]$\Delta\lambda$ = λ (individual solution) − λ (LS 43)

[c]These are the formal standard deviations (1-σ) of the non-consider parameter estimates of the station locations as produced by the Viking orbit determination program.

Table 10. Spin axis and longitude values, LS 44

DSS	r_s, km	λ, deg East
11	5206.340852	243.1505848
12	5212.052472	243.1945123
14	5203.997735	243.1104678
41	5450.203703	136.8874855
42	5205.352165	148.9812708
43	5205.251697	148.9812726
51	5742.940160	27.6854256
61	4862.608849	355.7509710
62	4860.818670	355.6321631
63	4862.451845	355.7519840
13	5215.485322	243.2051121
44	5193.986790	148.9778162

Table 11. Analysis of the spin axis and longitude update

	Participating DSS	LS 44–LS 43	Effect of improved processing of LS 43 data	Effect of Mariner 10 data
Spin axis, m	11	0.51	0.44	0.07
	12	0.38	0.28	0.10
	14	0.41	0.28	0.13
	41	0.05	0.12	−0.07
	42	2.62	0.56	2.06
	43	3.15	0.46	2.69
	51	0.57	0.63	−0.06
	61	0.43	0.23	0.20
	62	0.41	0.14	0.28
	63	0.56	0.28	0.28
Longitude, 10^{-5} deg	11	−1.29	−0.64	−0.65
	12	−1.45	−0.70	−0.75
	14	−1.65	−0.65	−1.00
	41	−1.16	−0.47	−0.69
	42	−0.79	−0.58	−0.21
	43	−0.61	−0.58	−0.03
	51	−0.59	−0.46	−0.13
	61	−1.43	−0.75	−0.68
	62	−1.57	−0.80	−0.77
	63	−1.58	−0.77	−0.81

Table 12A. Target planet ephemeris parameters

Mission	Target planet declination, DE 84, deg	Δδ, arc-sec	Δα, arc-sec
Mariner 4 encounter	−3.1897	−0.0265612	0.0684338
Mariner 5 encounter	6.2464	−0.0301313	0.0727104
Mariner 6 encounter	−24.4210	−0.0530386	0.0708131
Mariner 9 encounter	−11.505	−0.0267841	0.1103786
Mariner 10 Venus encounter	−13.2284	−0.0492917	0.109137
Mariner 10 1st Mercury encounter	−9.3958	0.0308986	0.0905302

Target planet declinations are relative to spacecraft encounter times.

α = target planet right ascension, δ = target planet declination.

$\Delta\alpha = \alpha(\text{DE 96}) - \alpha(\text{DE 84})$, at spacecraft encounter time.

$\Delta\delta = \delta(\text{DE 96}) - \delta(\text{DE 84})$, at spacecraft encounter time.

Table 12B. Predicted effect of an ephemeris update on station Location Set 44 (DE 96 minus DE 84 individual data arc solutions)

	Participating DSS	Mariner 4 encounter	Mariner 5 encounter	Mariner 6 encounter	Mariner 9 encounter	Mariner 10 encounter	Mariner 10 Mercury 1 encounter
Spin axis, m	11	0.04					
	12		−0.08	0.61	0.14	0.29	−0.13
	14		−0.08	0.61	0.14	0.29	−0.13
	41		−0.09	0.64	0.14		
	42	0.04				0.29	−0.13
	43					0.29	−0.13
	51	0.04		0.67			
	61						
	62		−0.08	0.57	0.13	0.27	−0.12
	63					0.27	−0.12
Longitude, 10^{-5} deg	11	1.90					
	12		2.02	1.97	3.07	3.03	2.51
	14		2.02	1.97	3.07	3.03	2.51
	41		2.02	1.97	3.07		
	42	1.90				3.03	2.51
	43					3.03	2.51
	51	1.90		1.97			
	61						
	62		2.02	1.97	3.07	3.03	2.51
	63					3.03	2.51

Table 13. True effect of an ephemeris update on station Location Set 44 (DE 96 minus DE 84 individual data arc solutions)

	Participating DSS	Mariner 4 encounter	Mariner 5 pre-encounter	Mariner 5 encounter	Mariner 5 post-encounter	Mariner 6 encounter	Mariner 9 encounter	Mariner 10 Venus encounter	Mariner 10 Mercury 1 encounter
Spin axis, m	11	−0.585	0.200						
	12		0.151	−0.410	0.000	0.284	0.278	0.279	−0.164
	14		−0.005	−0.250	0.004	0.326	0.234	0.261	−0.119
	41			0.598	−0.040	0.395	0.254		
	42	0.330	0.054					0.284	−0.168
	43							0.272	−0.122
	51	−0.094				0.398			
	61		0.018						
	62		0.176	−0.052	0.004	0.407	0.216	0.260	−0.141
	63							0.267	−0.101
Longitude, 10^{-5} deg	11	3.502	1.937						
	12		2.661	1.648	2.345	2.141	3.412	3.142	2.537
	14		1.943	1.495	2.339	2.166	3.390	3.121	2.496
	41			1.826	2.292	2.146	3.350		
	42	2.354	1.615					3.152	2.434
	43							3.107	2.503
	51	2.634				2.213			
	61		1.921						
	62		3.333	1.728	2.338	2.187	3.404	3.186	2.498
	63							3.111	2.493

Table 14. Spin axis and longitude values — combined solution for DE 96

DSS	r_s, km	λ, deg East
11	5206.340775	243.1506103
12	5212.052461	243.1945377
14	5203.997723	243.1104930
41	5450.203863	136.8875110
42	5205.352285	148.9812947
43	5205.251765	148.9812975
51	5742.940200	27.6854493
61	4862.608909	355.7509964
62	4860.818730	355.6321890
63	4862.451921	355.7520093
13	5215.485311	243.2051375

Table 15. Effect of an ephemeris update on station locations (combined DE 96 solution minus LS 44 values)

DSS	Δr_s, m	$\Delta\lambda$, 10^{-5} deg
11	−0.077	2.55
12	−0.011	2.54
14	−0.012	2.52
41	0.160	2.55
42	0.120	2.39
43	0.068	2.49
51	0.040	2.37
61	0.060	2.54
62	0.060	2.59
63	0.076	2.53

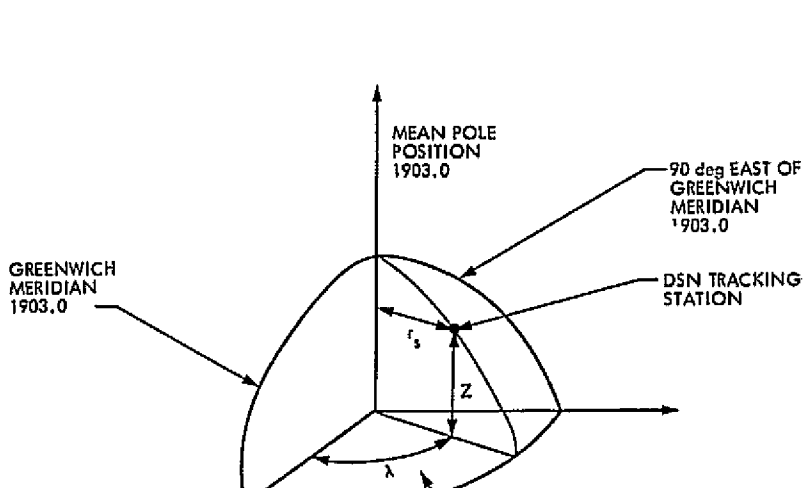

Fig. 1. A cylindrical coordinate system for locating a DSN station

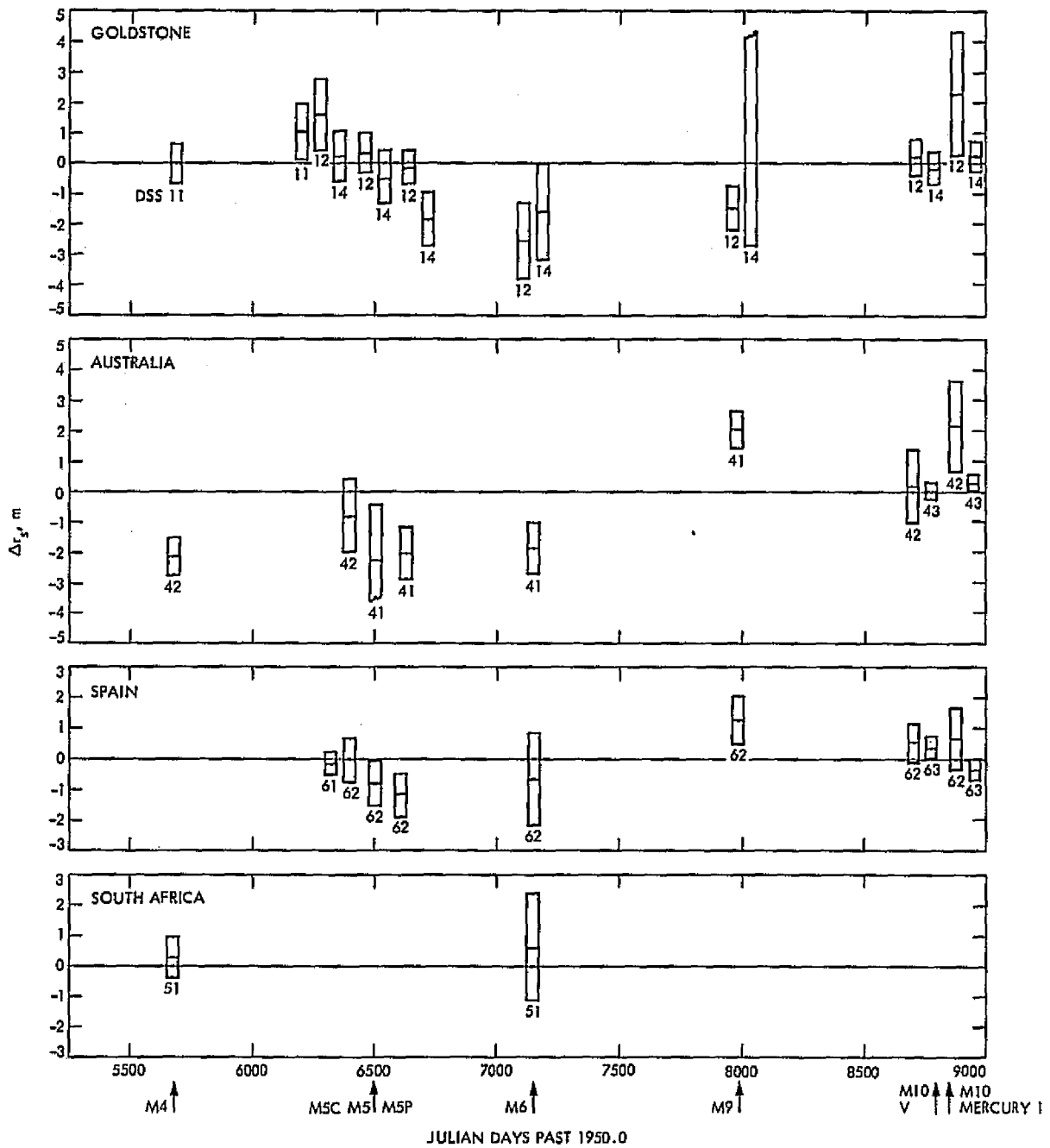

Fig. 2. Differences between individual data arc spin axis estimates and LS 44 values

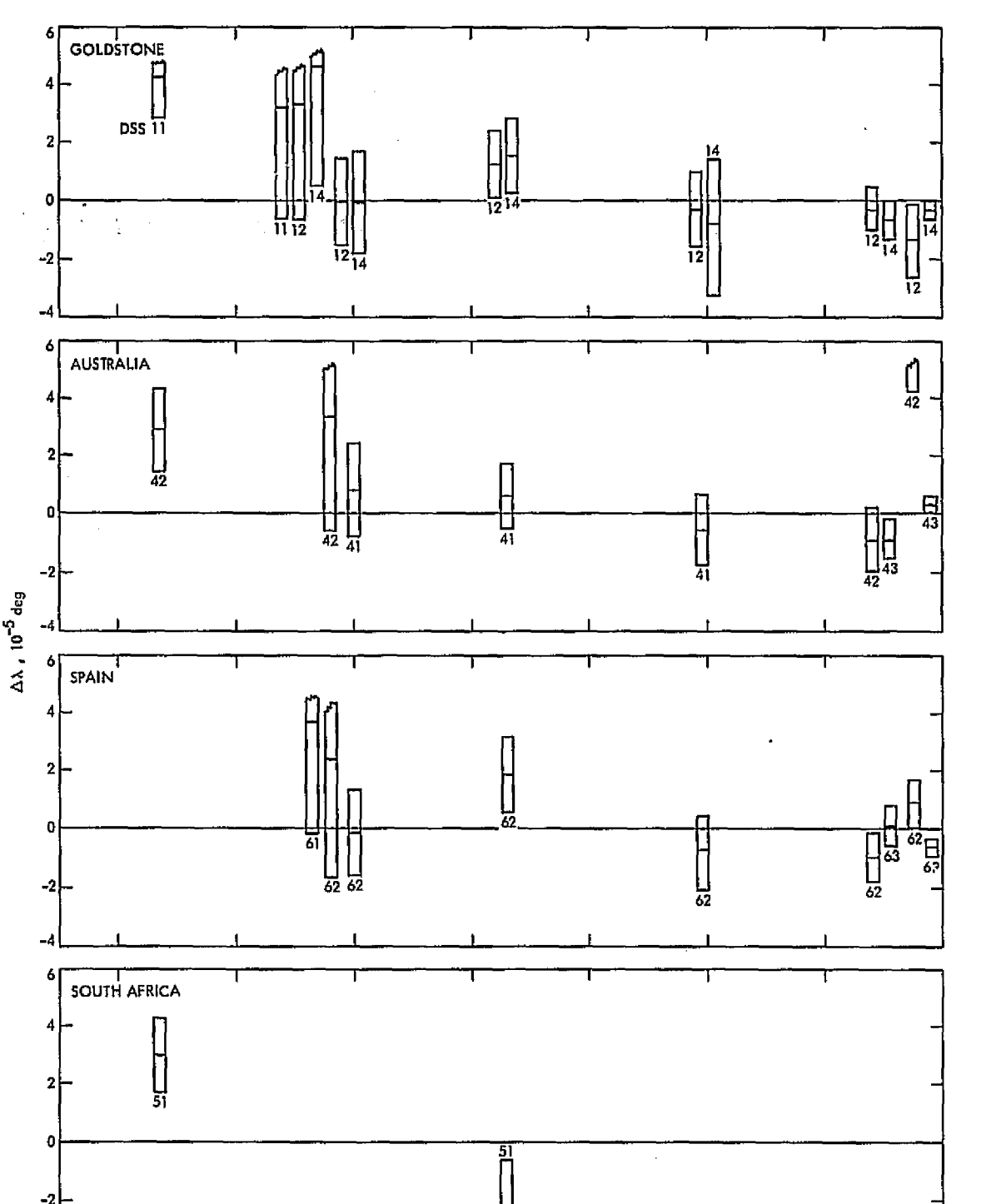

Fig. 3. Differences between individual data arc longitude estimates and LS 44 values

High-Efficiency Solar Concentrator

F. L. Lansing and J. Dorman
DSN Engineering Section

A new type of solar concentrator is presented using liquid lenses and simple translational tracking mechanism. The concentrator achieves a 100:1 nominal concentration ratio and is compared in performance with a flat-plate collector having two sheets of glazing and non-selective coating. The results of the thermal analysis show that higher temperatures can be obtained with the concentrator than is possible with the non-concentrator flat-plate type. Furthermore, the thermal efficiency far exceeds that of the comparative flat-plate type for all operating conditions.

I. Introduction

One of the fundamental problems associated with the effort to replace conventional energy sources by solar energy is to achieve high-temperature collection at very low cost. High temperature is feasible if the solar energy is concentrated and delivered to a collecting medium such as a gas or liquid. The greater the energy concentration, the greater the temperature of the collecting medium and the more useful the energy collected for heating, airconditioning, and electric power generation. Unfortunately, low-cost flat-plate solar collectors cannot operate efficiently at temperatures above 100°C, and presently available higher temperature concentrators are very expensive (approximately 5 to 10 times the cost of flat-plate collectors).

This article describes a low-cost method of manufacturing a high-temperature solar concentrator. There are two main features of the design that are unique: (a) a liquid lens construction of optimum shape with 100:1 nominal concentration ratio, and (b) a translational rather than rotational tracking mechanism. There is a resemblance between the construction of this design to that of a simple, non-concentrating flat-plate solar collector having two sheets of glazing, and it is estimated that it will cost only approximately 25 percent more for the liquid lens construction.

II. Description

The main features of the solar concentrator are indicated in Fig. 1. The major elements of the device are the lens assembly, working medium tubes, and the tracking mechanism. The lens assembly forms a series of individual lenses arranged side by side and is fabricated from transparent plastic or glass, as illustrated in Fig. 2. The curvature of the upper and lower shells of the lens assembly is designed for minimum focal length and optimum concentration ratio. The space between shells is filled with liquid. The initial design used water as the filling medium

for its low cost. The refraction index of water (1.33) closely approximates that of glass (1.5) so that the lens optical transmissivity closely approximates that achieved by a solid lens manufactured from glass. It is foreseen that other transparent liquids or additives may enhance the performance of the concentrator for different applications. The lens assembly design also includes compensation for expansion and the contraction of the liquid filler in addition to means for filling, draining, and cleaning (not shown in figures). The outer shells of the lens assembly are inexpensive to manufacture and light in weight for easy shipment and site installation.

The working medium tubes can be made of copper, steel, or aluminum and are placed on a thermal insulation layer at the focal lines of the individual lenses. There is no fin or plate connection of the tubes as is normal with flat-plate solar collectors. The tube surface is coated with a mat black paint for maximum absorption. A nominal concentration ratio of 100:1 was demonstrated experimentally on the single lens shown in Fig. 2. The resulting high temperatures can lead to a feasible application in electric power generation through solar-Rankine power cycles.

The function of the unique tracking mechanism adopted in this concentrator is to maintain the focal line at the working medium tubes independent of the Sun's incidence angle as indicated in Fig. 3. A simple drive system consisting of a fractional horsepower electric motor, reduction gear and an eccentric disk moves the lens assembly on its rollers in a translational motion with simple harmonic motion at a frequency of one cycle per day. Compensation for differences between summer and winter solstice and intermediate seasonal variations is achieved by eccentricity adjustments of the disk.

An important feature of the design is the absence of environmental impact. If water is chosen as the liquid filler for the lenses, it represents little or no hazard in case of leakage failure.

III. Thermal Analysis

This is performed by applying the first law of thermodynamics and the heat rate equations at steady-state condition to the unit concentrator shown in Fig. 2, which is composed of one 2-dimensional lens, a single tube at the lens focal line and the working fluid. After manipulating the energy balance equations for the lens, the tube, and the working fluid, the fluid temperature difference between the inlet and the outlet sections can be written as

$$(T_{out} - T_{in})_1 = [\alpha \tau_1 IR - U_{e1}(T_{in} - T_a)] \frac{1}{U_{e1}} \left[1 - \exp\left(\frac{-U_{e1}U_{pf1}}{RG_f c_f (U_{e1} + U_{pf1})}\right)\right] \quad (1)$$

where U_{pf1} is the tube surface-to-fluid conductance coefficient expressed by Whillier (Ref. 1) for laminar water flow in tubes in the form

$$U_{pf1} = \frac{2.484}{d_i} + \left| \frac{0.0854\left(\frac{m_f}{Ld_i}\right)}{1 + 0.0684\left(\frac{m_f}{L}\right)^{2/3}} \right| \quad (2)$$

The concentrator thermal efficiency is then given by

$$\eta_{th1} = \frac{G_f c_f (T_{out} - T_{in})_1}{I} \quad (3)$$

For comparison, the performance of a flat-plate type collector is given, based on analysis by Whillier (Ref. 1). The comparative flat-plate design is shown in Fig. 4 and includes double glazing and a metallic plate integral with the tubes. The tube's dimensions, lateral spacing, and the optical properties of their coating material are taken the same as for the concentrator. The resulting fluid temperature difference can be written as

$$(T_{out} - T_{in})_2 = [\alpha \tau_2 I - U_{e2}(T_{in} - T_a)] \frac{1}{U_{e2}} \left[1 - \exp\left(\frac{-U_{e2}U_{pf2}}{G_f c_f (U_{e2} + U_{pf2})}\right)\right] \quad (4)$$

where U_{pf2} is the "equivalent" conductance coefficient between the fluid and the combined fin and tubes, given by the following relation

$$\frac{1}{U_{pf2}} = \frac{(d_o + 2\ell)}{\pi d_i U_{pf1}} + \frac{2\ell(1-F)}{U_{e2}(d_o + 2\ell F)} \quad (5)$$

where F is the fin efficiency determined from

$$F = \frac{\tanh \ell\sqrt{\frac{U_{e2}}{K\delta}}}{\ell\sqrt{\frac{U_{e2}}{K\delta}}} \quad (6)$$

The corresponding thermal efficiency is then expressed as

$$\eta_{th2} = \frac{G_f c_f (T_{out} - T_{in})_2}{I} \quad (7)$$

Table 1 presents the results of a numerical comparison between the concentrator and the double-glazing collector, and is constructed from the following assumed operating conditions:

Solar radiation intensity	I	= 700 kcal/(h·m²)
Ambient air temperature	T_a	= 20°C
Inlet fluid temperature	T_{in}	= 30°C
Tube surface absorptivity	α	= 0.9
Tube surface emissivity	ϵ	= 0.9
Water-lens transmissivity[1]	τ_1	= 0.78
"Effective" transmissivity of double glazing[2]	τ_2	= 0.83
Water specific heat	c_f	= 1 kcal/kg°C
Tube length	L	= 1.2 m
Tube inner diameter	d_i	= 0.007 m
Tube outer diameter	d_o	= 0.010 m
Half width of fin	ℓ	= 0.075 m
Plate thickness	δ	= 0.0015 m
Tube material conductivity	K	= 45 kcal/(h·m°C) (galvanized steel)
Lens/tube area ratio	R	= 16 (actual concentration ratio)
Number of lens/collector panels		15
Heat loss coefficient between tube (or plate) surface and ambient air[3]	U_{e1}	= 7.33 kcal/h·m²°C
	U_{e2}	= 3.42 kcal/h·m²°C

The above operating conditions were abstracted from the experimental results of flat-plate solar collectors to yield a practical evaluation of their comparison. The efficiency results are plotted as shown in Figs. 5 and 6.

[1]Calculated based on a lens average thickness of 3.81 cm, a refraction index of 1.33 and on extinction coefficient of 0.08 cm⁻¹

[2]Based on 0.32 cm thickness for each panel, an extinction coefficient of 0.08 cm⁻¹ and a refraction index of 1.526

[3]U_{e1} is based on an average temperature of 120°C and U_{e2} is based on an average temperature of 70°C.

IV. Conclusions

(1) The improved efficiency of the concentrator compared with the double-glazing collector at a given radiation intensity and a wide range of fluid mass flux is plotted in Fig. 5. The percentage improvement in efficiency is also included for comparison in Table 1. It appears that the thermal efficiency obtained from the concentrator exceeds that of the comparative double-glazing collector for all operating conditions. As an example, for a high temperature application where the fluid is heated by 175°C, the corresponding mass flux is 2.5 kg/(h·m²) and an improvement in the thermal efficiency of 76 percent is obtained. On the other hand, for a high efficiency operation, Table 1 indicates that a large mass flux of 100 kg/(h·m²) gives an efficiency improvement of 13 percent over the double-glazing collector, which is still considered a useful gain in collector performance.

(2) The performance curve expressing the thermal efficiency vs. the variable $(T_{in} - T_a)/I$ at a selected mass flux of 30 kg/(h·m²) is as shown in Fig. 6. The straight line relationship is evident from the fluid temperature rise expressions given by Eqs. (1) and (4). For the concentrator, the thermal efficiency can be written as

$$\eta_{th1} = 0.684 - 0.447\left(\frac{T_{in} - T_a}{I}\right) \tag{8}$$

and that for the double-glazing collector as

$$\eta_{th2} = 0.619 - 2.835\left(\frac{T_{in} - T_a}{I}\right) \tag{9}$$

The "zero-efficiency" condition, with a radiation intensity of 700 kcal/(h·m²), corresponds to an inlet fluid temperature of 1072°C for the concentrator and 153°C for the double-glazing collector. This result shows that the maximum temperatures that can be reached by the concentrator are much higher than is possible with the comparative double-glazing type.

(3) The slope of the performance curves of Fig. 6, which is a measure of the heat loss, is shown to have a smaller value for the concentrator compared with the double-glazing collector. This is due to the fact that in the case of the concentrator the heat loss coefficient between the tube and the ambient air per unit area of the collector is given

by U_{e1}/R, while that for the double-glazing type is U_{e2}. This means that the reduction in heat losses to the surroundings, brought by focusing the incident energy on a smaller area, outweighs its increase due to higher temperatures obtained.

(4) Practical examples of the utilization of the present concentrator in airconditioning and/or power generation applications, are taken from Table 1 as follows:

(a) For an electric-power generation application, a mass flux of 2.5 kg/(h·m²) is chosen for each concentrator panel (1.2 × 2.4 m) which results in an exit fluid temperature of 204.7°C. If a Rankine power cycle is operated between 204.7°C and an ambient temperature 20°C as its temperature limits at 50 percent relative efficiency to the Carnot cycle, it will give a thermal efficiency of 19 percent. This means that one concentrator panel can produce a mechanical work equivalent to 0.28 kW per panel for every hour of operation.

(b) It appears feasible for the airconditioning load of a normal residence (3 tons of refrigeration) to be carried out totally by solar energy. For example, if the airconditioner used is a mechanical vapor compression refrigeration unit that is driven by a solar-Rankine cycle it will consume about 3.6 kW. In this case, 12.8 concentrator panels are needed with a total area of 37 m² (400 ft²).

On the other hand, if the airconditioner used is of the absorption type, a collector temperature in the order of 100°C is sufficient. A mass flux of 5 kg/(h·m²) from Table 1 will result in a fluid temperature of 121.3°C, which is adequate for full-load operation (coefficient of performance is about 0.65). In this case, only 10.6 concentrator panels are needed for airconditioning the house with a total area of 30.6 m² (328 ft²). Both cases indicate that the required collection area for airconditioning is adequate and does not exceed that of a south-facing roof in most houses.

Definition of terms

c_f	fluid specific heat, kcal/kg·°C
d_i	inner tube diameter, m
d_o	outer tube diameter, m
F	fin efficiency
G_f	fluid mass flux (flow rate per unit collector area), kg/h·m²
I	solar radiation intensity, kcal/(h·m²)
K	conductivity, kcal/(h·m°C)
ℓ	half width of fin, m
L	tube length, m
m_f	mass flow rate per tube, kg/hr
R	lens area/concentrator tube projected area
T_{in}	inlet fluid temperature, °C
T_{out}	outlet fluid temperature, °C
T_a	ambient temperature, °C
U_e	"effective" heat loss coefficient between tube (or plate) surface and ambient, kcal/(hr·m²·°C)
U_{pf}	tube (or plate) surface to fluid conductance coefficient, kcal/h·m²·°C)
α	absorptivity
τ	transmissivity
δ	plate thickness, m
ϵ	emissivity
η_{th}	thermal efficiency

Subscripts

1	concentrator
2	double-glazing collector

Reference

1. Whillier, A., "Design Factors Influencing Solar Collector Performance," *Low Temperature Engineering Application of Solar Energy*, ASHRAE Publication, 1967, Chap. III, pp. 27–40.

Table 1. Numeric comparison between solar concentrator and analogous flat-plate double-glazing collector

G_f, kg/(h·m²)	Flow rate per tube, kg/h	Fluid temperature rise, $(T_{out}-T_{in})$ °C		Thermal efficiency η, %		% Improvement in efficiency
		Concentrator	Double-glazing	Concentrator	Double-glazing	
0	0	1062.6	142.9	00.0	00.0	0
2.5	0.48	174.7	99.1	62.4	35.4	76
5	0.96	91.3	63.8	65.2	45.6	43
10	1.92	46.7	36.6	66.7	52.4	27
20	3.84	23.6	19.7	67.5	56.4	20
30	5.76	15.8	13.5	67.8	57.9	17
50	9.6	9.5	8.3	68.1	59.2	15
100	19.2	4.8	4.2	68.4	60.5	13

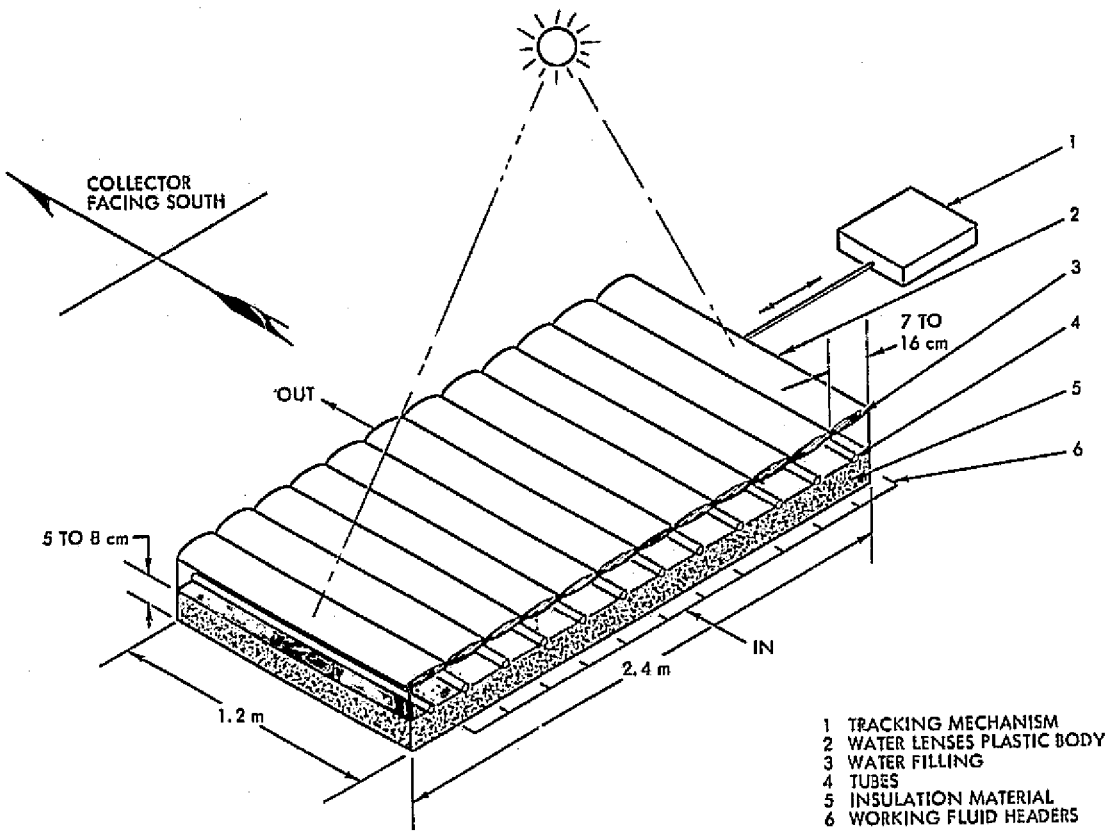

Fig. 1. Overall view of the solar concentrator

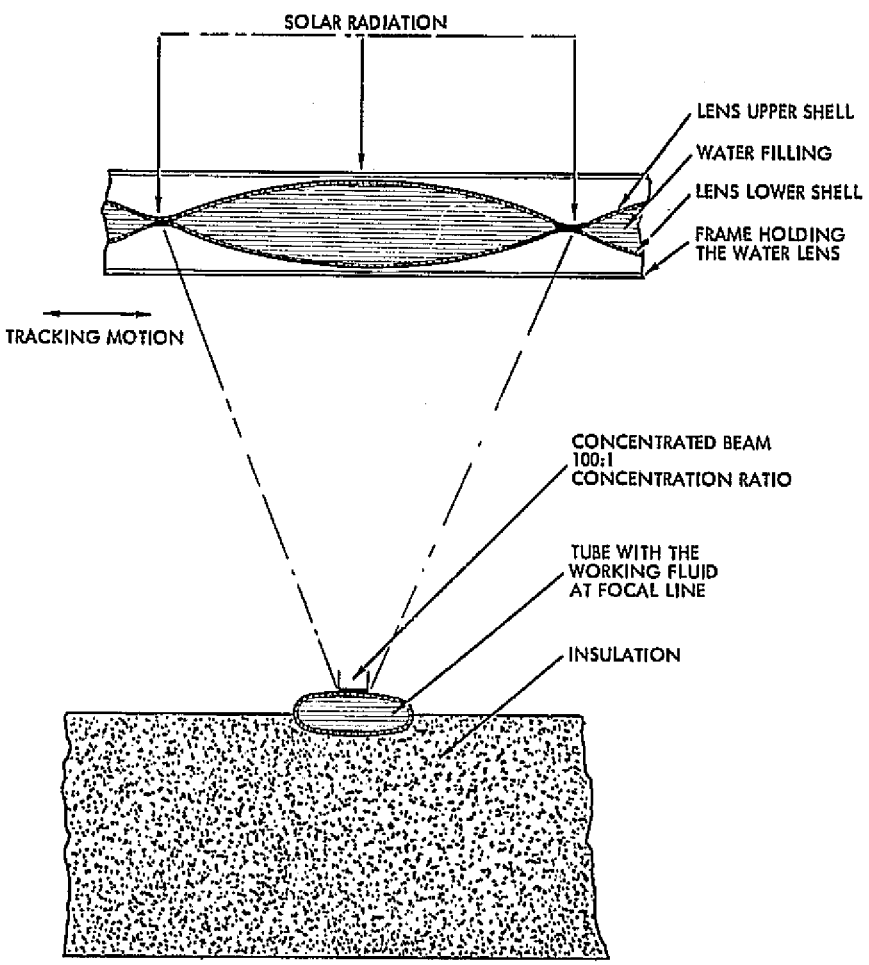

Fig. 2. Working principle of a "liquid" lens

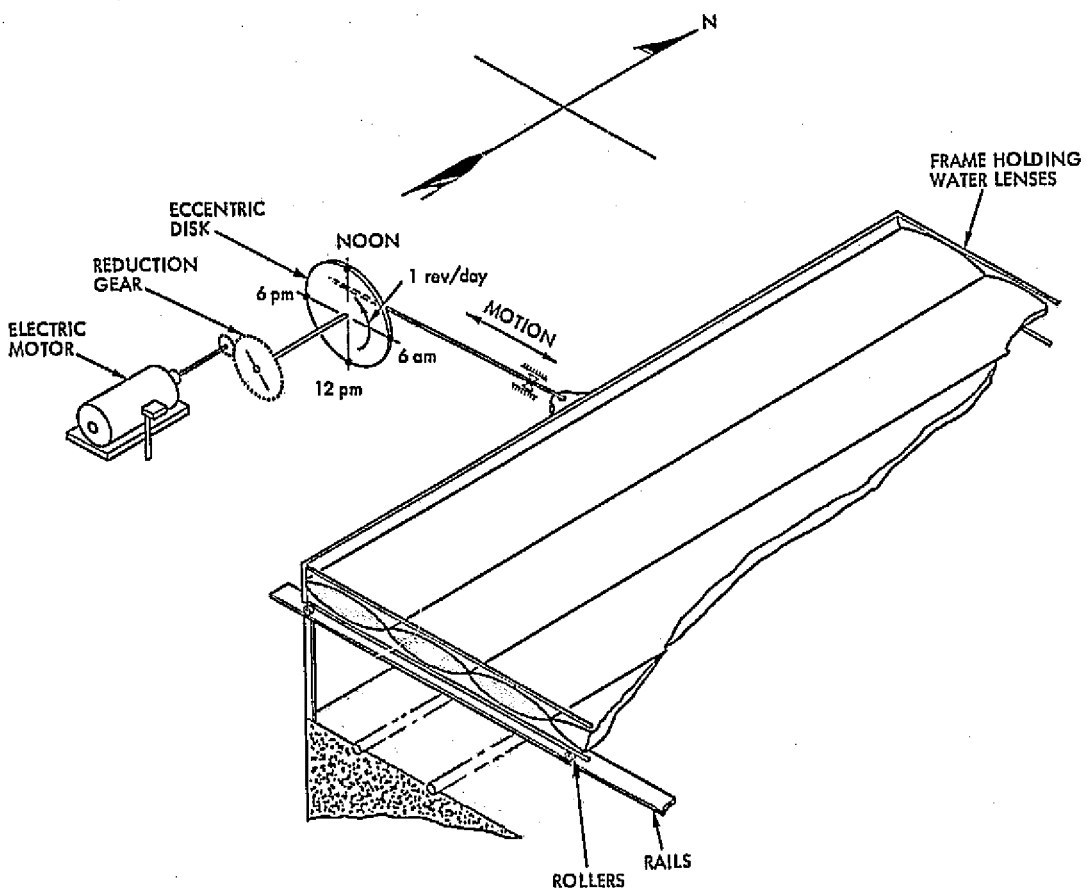

Fig. 3. Details of translational tracking mechanism

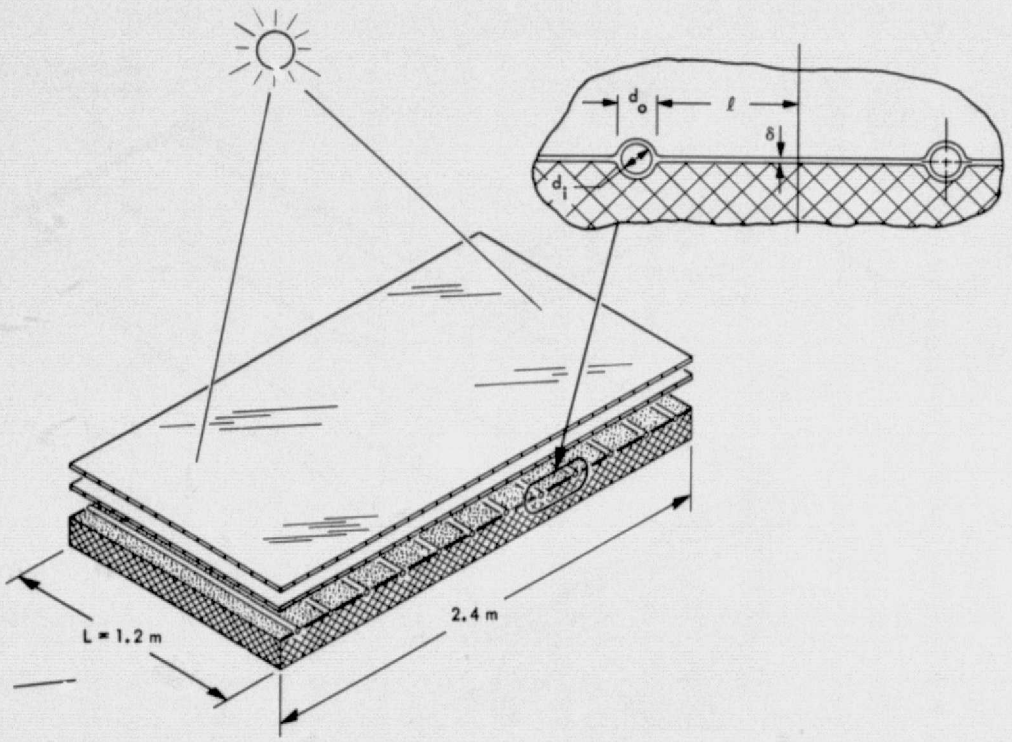

Fig. 4. Double-glazing flat-plate solar collector

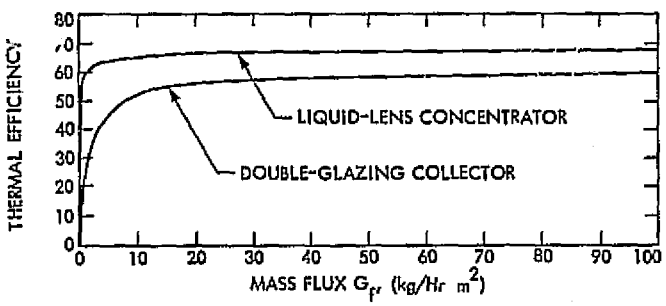

Fig. 5. Effect of varying the mass flux on the collector thermal efficiency

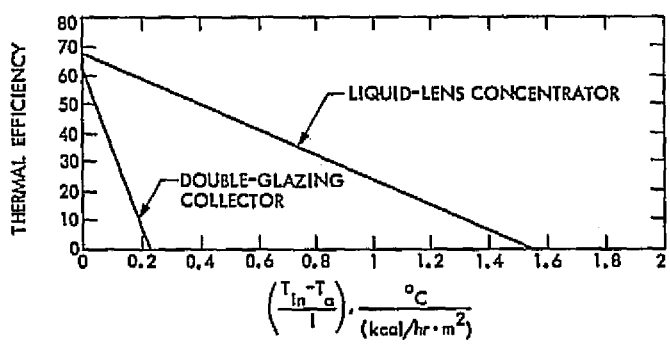

Fig. 6. Efficiency curves for a flow flux G_f = 30 kg/h • m^2

A Two-Dimensional Finite-Difference Solution for the Transient Thermal Behavior of a Tubular Solar Collector

F. L. Lansing
DSN Engineering Section

A numerical procedure was established using the finite-difference technique in the determination of the time-varying temperature distribution of a tubular solar collector under changing solar radiancy and ambient temperature. Three types of spatial discretization processes were considered and compared for their accuracy of computations and for selection of the shortest computer time and cost. The stability criteria of this technique was analyzed in detail to give the critical time increment to ensure stable computations. The results of the numerical analysis were in good agreement with the analytical solution previously reported. The numerical method proved to be a powerful tool in the investigation of the collector sensitivity to two different flow patterns and several flow control mechanisms.

I. Introduction

The need for an accurate prediction of the thermal behavior of solar collectors, to be used as a basic tool for their performance comparison, has become increasingly important with the rapid development of solar energy technology. For example, imposing changes on a specific solar collector such as introducing a new geometrical configuration, having a different control mechanism for its working fluid or developing new optical properties for the glazing and coating, require a sufficiently general analytical model which is both an adequate idealization of the physical system and capable of reasonably simple mathematical description.

The common procedure in analyzing the time-varying response of solar collectors has been based on a sequence of events of equal time intervals that range from 30 to 60 minutes, at the end of which the solar collector is assumed to have reached a quasi steady-state condition. This procedure cannot be generalized for all types of solar collectors and is restricted to those which possess very small thermal capacitance or very short response time (approximately 10 minutes) to the solar radiancy changes. The procedure would fit most flatplate collectors.

The solar collector under study has been selected as a candidate for Goldstone DSCC energy conservation pro-

jects. The time taken by this collector to reach quasi steady-state condition, measured experimentally by the solar simulator team at NASA Lewis Research Center, was approximately one hour. Accordingly, a new investigation was required for an accurate procedure to study its transient thermal behavior.

The possibility of finding an exact analytical solution was not excluded from the investigation and was reported in a previous article (Ref. 1). The first results indicated that the problem can be solved by a closed algebraic form, but it is highly complicated. To facilitate the computations, numerical solutions are preferred. The finite-difference method was then selected for the transient thermal study to supplement the analytical methods for additional coverage for this type of solar collector at all operating conditions.

II. Numerical Analysis

The numerical solution using the finite-difference method has become more popular in solving heat-transfer problems with the availability of high-speed digital computers and their associated technology. This method is used if a high degree of accuracy is required or if the problem is of considerable size and complexity.

In the finite-difference method, space and time discretization processes lead to a set of algebraic equations (nodal equations) instead of the partial differential equations that characterize the system. The nodal equations can be derived by purely mathematical methods or by energy consideration at the node of each spatial segment.

A. Collector Description and Flow Patterns

The tubular collector unit, as shown schematically in Figs. 1 and 2, is composed of three concentric tubes; an inner tube, an absorber tube, and a cover tube. The annulus space between the absorber and cover tubes is evacuated to minimize convection and conduction losses. The absorber tube surface is coated with a selective material to reduce the outward long-wave radiation losses. In flow pattern (1), as shown in Fig. 1 (a), the circulating fluid starts from the open-end section of the inner tube. At the closed end of the collector, the fluid reverses its direction and passes in the annulus spacing between the inner and absorber tubes. In flow pattern (2), as shown in Fig. 1 (b), the fluid path is reversed from the above. Each collector module consists of 24 collector units formed from flow patterns (1) and (2) in an alternate series as shown in Fig. 2. For more irradiancy augmentation, the set of collectors is mounted with lateral spaces separating them from each other with a highly reflective back reflector.

B. Program Procedure

Figure 3 illustrates one axisymmetric segment of the collector tube and the nodal and edge temperatures used throughout the analysis. The segment has a thickness ΔX and is bounded by sections (J) and $(J + 1)$ perpendicular to the axis of symmetry. The nodal temperatures of the Jth segment are located at the midsection of the segment and are denoted by TM_J. Four nodal temperatures are assigned to each segment, one for each of the following: the inner fluid pass, the outer fluid pass, the absorber tube surface, and the cover-tube surface temperatures. Because of the constrained boundary conditions at the open end and the closed end of each collector unit, as well as between the different flow patterns in series, the nodal temperatures of the fluid in the inner and outer passes only are converted back to the edge temperatures, after each computation process with an increment of time $\Delta\theta$. This results in a two-dimensional temperature distribution for the axisymmetric collector unit; in the axial direction and in the radial direction. No allowance is made for circumferential temperature differences between the upper tube's surface of the collector unit facing the Sun and the bottom tube's surface facing the back reflector. This means that the temperatures are uniform circumferentially.

The energy balance equations are listed in Appendix A for convenience. The present set of nodal and edge temperatures at time θ are then grouped together in a matrix format, and the corresponding future set of temperatures at time $(\theta + \Delta\theta)$ is then computed and updated using matrix multiplication algebra. The computations proceed in the above sequence after preassigning an initial set of temperatures. The latter can be arbitrarily determined based on past experience or can be given as a result of measurements.

III. Results and Conclusions

One of the obstacles that is met during the execution of the computations is the numerical instability. In Appendix B, the necessary stability criteria are derived and presented for each flow pattern. This shows that the increment time $\Delta\theta$ and the spatial increment ΔX cannot be arbitrarily chosen, but must be calculated from the above criteria to ensure stable computations. It can be shown from the critical stability condition Eq. (B-2), that

the smaller the size of each segment, ΔX, leads to a smaller allowable increment of time $\Delta\theta$ and a larger program execution time. This is due to the doubling of complexity; first due to the increased size of the matrices with larger number of segments, and second to the increased number of repetitions with smaller time intervals. Several program runs were made and the results are listed as follows:

(1) The time-varying temperature distribution of the working fluid in a unit collector at some given operating condition is plotted in Figs. 4 and 5 for flow patterns (1) and (2), respectively. The collector fluid temperature is assumed to be uniform at 70°C before a sudden step of solar radiancy of 0.75 kW/m² is imposed and remains constant thereafter. In both flow patterns, the steady-state exit fluid temperature reaches the same value of 78°C as shown in frame (d) of Figs. 4 and 5. It is clear from the time frames (a), (b) and (c) of Figs. 4 and 5, the distinct difference in responding to changes of the solar radiation between the different flow patterns. The exit fluid temperature of flow pattern (1) responds by a much faster rate in the early stages since the fluid leaves the collector as soon as it absorbs the useful energy from the annulus area facing the Sun. On the other hand, the exit fluid temperature of flow pattern (2) is not significantly increased until the relatively colder fluid in the center tube is discharged. This results in a much higher fluid temperature at the closed end of the collector which may cause some local degradations of the selective coating for this type of flow pattern.

(2) The exit fluid temperature obtained from the numerical results of the previous unit collector runs is plotted in Fig. 6. Superimposed on Fig. 6 is the analytical solution previously reported in Ref. (1) for the same operating conditions, optical and geometrical properties. Although the analytical solution was made with the assumption of zero tube thermal capacitance, it is in good agreement with the numerical solution which considers such a thermal capacitance with only a maximum deviation of $\pm$ 0.5°C. The deviation between the numerical and analytical solutions in the first 5 min in Fig. 6 is due to the different estimates of the initial temperature profile. The analytical solution considers an initial steady-state temperature profile with inlet fluid temperature of 70°C, which results in an exit temperature of 69.2°C, (Ref. 1), while the numerical solution arbitrarily assigns a uniform fluid temperature of 70°C in the two fluid passes.

(3) The finite-difference numerical solution is then applied to two collector units connected in series as shown in Fig. 2. In this case, the following two important criteria have been studied:

(a) The effect of changing the diameter of the inner tube on the rate of temperature growth is plotted as shown in Fig. 7. The manufacturer's specification of the inner diameter, D_i, is 10.5 mm, which makes the fluid velocity in the inner fluid pass seventeen times larger than the fluid velocity in the annulus pass. The reason for that selection is to shorten the residence time inside the center tube for faster extraction of the hot fluid, though it causes an excessive impulse force at the closed-end of the collector. On the other hand, the minimization of these impulsive forces requires that the velocity in each fluid pass should be equal and the inner diameter in this case would be 29 mm. It is clear from Fig. 7 that reducing the diameter D_i will hasten the response of the collector after about 20 min, though it has no effect on the steady-state temperature that could be reached.

(b) The rate of cooling of the collector at zero solar radiation is illustrated in Fig. 8. The fluid in the two collector units is assumed uniform at 87°C when a sudden drop of the solar radiation to zero value is imposed and remains constant thereafter. The rate of cooling amounts to 2.9°C/h to an ambient temperature of 30°C. This shows the very low heat loss coefficient that this collector possesses over flat plate types. This is mainly due to the vacuum employed and the use of selective coatings.

(4) The application of the numerical solution has been extended further to study a complete module, consisting of 24 collector units connected in series with alternating flow patterns. Three different computer programs have been written corresponding to three different space discretization processes for $N = 4$, 2 and 1. This results in a substantial reduction of computer time and cost as the number of segments per tube is reduced. For example, the computer time is approximately in the ratio of 16:4:1 as the number of segments N goes from 4:2:1, respectively. This is due to the squared-reduction effects of matrices size and the number of time loops required. Regarding accuracy, it has been found that increasing the space segments has an insignificant effect as shown in Fig. 9. The temperature deviation is shown to be $\pm$ 1 percent as the number of segments N is reduced from 2 to 1 which was done to obtain a 75 percent reduction of the computer time and cost.

(5) The practical use of the tubular solar collector has indicated that the maximum end-to-end temperature rise across one module can reach as high as 50°C or approxi-

mately 2°C for each collector unit. This low temperature differential of the working fluid results in an insignificant temperature gradient across both the cover and absorber tube ends. Several module runs with three types of spatial divisions (four, two and one-segment per tube) indicate that the one-segment solution is more than adequate for the temperature profile prediction without sacrificing accuracy. The four-segment solution is not recommended as it consumes excessive computer time (at least 16 times that of a one-segment solution). The two-segment solution may or may not be used for further studies, depending on the allowable program funds.

(6) The collector circulating fluid may be stopped during operation at the following two time periods as a temperature vs. flow control technique: (a) from midnight to about 8:00 a.m. when the sun starts to rise, and (b) from the sunset at about 7:00 p.m. to midnight. The control system is designed to conserve what is collected during the sunshine hours. The actual hours of operation vary from day to day, depending on the type of application and the solar radiation time.

To allow for this, the numerical analysis program is provided with two extra computational controls. The first handles the periods of shut-down when all the 24 collector units behave as a single collector unit regardless of flow patterns, as occurs when the module end-to-end temperature difference is zero or 2°C at the maximum. The second computational control deals with sudden diurnal shut down after operation with a module end-to-end temperature difference exceeding 2°C.

(7) In Fig. 10 the results of six different flow control processes are plotted for a collector module (24 units in series) under variable solar radiancy and ambient temperatures. The total incident solar radiation falling on a plane surface at 20°C with the horizontal and facing south is registered and plotted for June 2, 1975 at the Goldstone DSCC, California. The accumulated solar irradiancy for that day was 10.465 kWh/m^2 and with a collector module projected area of 2.602 m^2, the total incident energy amounted to 27.228 kWh. The numerical analysis provided a valuable assistance in exposing the transient thermal behavior of the collector under several flow controls and the understanding of its important features. The flow control processes are as follows:

(a) *Flow Control* (1): The fluid is left stagnant starting at midnight with a temperature of 20°C equal to the ambient temperature. During the sunshine period, the temperature rises and reaches a maximum of 230°C at around 4:00 a.m. under the given solar radiancy. The slow rate of cooling as discussed in item (3) b, will keep the fluid hot most of the time, and the temperature will reach about 130°C at the following midnight. Since no drainage of hot water is assumed in this control, the overall thermal collection efficiency will be zero.

(b) *Flow Control* (2): This is similar to flow control (1) except that the fluid is left stagnant starting midnight at a temperature of 70°C. At about 6:00 a.m. the fluid temperature drops by 13°C due to night cooling, and then starts to pick up some heat as the sun rises. The maximum temperature is found to be 244°C at 4:00 p.m. and it drops to 130°C at the following midnight as in flow control (1). The overall thermal collection efficiency is also zero with this control. The results from flow controls (1) and (2) indicate that the no-flow maximum fluid temperature, though not significantly varying with the temperature of the residing fluid at midnight, can reach excessive values that cause severe thermal stresses and coating degradation problems.

(c) *Flow Control* (3): This is a modification of flow control (1) whereby the fluid is left stagnant starting midnight with 20°C temperature and after reaching a temperature of 70°C at about 9 a.m., a fluid circulating pump is turned on and a uniform flow rate of 22 kg/h from the storage tank flows into the collector. The fluid temperature oscillates around 130°C for 5½ hours (10:30 a.m. to 4:00 p.m.) and then drops to 70°C at about 7:00 p.m. The peak of the accumulated thermal energy for the day occurs at 7:00 p.m. and reaches 36.23 percent of the total incident solar energy.

(d) *Flow Control* (4): This is the same as flow control (3) except that the pump is rated at 33 kg/h. The fluid temperature thus oscillates about 110°C for 5½ h (10:30 a.m. to 4:00 p.m.); a temperature and a range most suitable for running an absorption type of air conditioner. The peak of the accumulated thermal energy for the day occurs at 6:30 p.m. and reaches 37.39 percent of the total incident solar energy.

(e) *Flow Control* (5): This is a modification of flow control (2) whereby the fluid is left stagnant starting midnight with 70°C temperature and after reaching a temperature of 70°C at 8:00 a.m., a fluid circulating pump is turned on and a uniform flow rate of 33 kg/h from the storage tank flows into the collector. The fluid temperature oscillates around 110°C for about 7 h (9:15 a.m. to 4:00 p.m.) which is longer than the range given by flow control (4). The peak of the accumulated thermal

energy for the day occurs at 6:30 p.m. and reaches 42.34 percent of the total incident solar energy.

(f) *Flow Control* (6): This is a continuous pumping operation for 24 h with a flow rate of 33 kg/h of the fluid at 70°C starting at midnight. The temperature drop for the period from midnight to 5:00 a.m. is only 5°C. As the Sun rises, the fluid temperature starts to increase and matches the temperatures reached by flow controls (4) and (5). The peak of the accumulated thermal energy occurs at 6:30 p.m. and reaches 41.72 percent of the total incident solar energy.

It is clear from the above six trials of flow control that flow control (5) provides the highest accumulated thermal efficiency (42.34%) as well as the required hot temperature (110°C) for an airconditioning application over a period of about 7 h (9:15 a.m. to 4:00 p.m.).

Definition of Terms

C Specific heat of tube material, kWh/kg • °C

C_f Specific heat of flowing fluid, kWh/kg • °C

D Tube diameter, m

F Augmented radiation factor, ≥ 1

G_{mn} Thermal conductance, kW/m²

I Direct solar radiancy, kW/m²

L Tube length, m

m_f Fluid mass flow rate, kg/h

N Number of space elements per tube,

Q_{in} Nodal internal heat generation, kWh

r Reflectivity,

T Edge temperature, K

TM Nodal temperature, K

T_{sky} Sky temperature, K

T_{amb} Ambient temperature, K

U_{ac} Radiative heat transfer coefficient between the absorber and the cover tubes, kW/m² • °C

U_{ao} Overall heat transfer coefficient between the absorber tube and the outer fluid in the annulus, kW/m² • °C

U_{cv} Convective heat transfer coefficient between the cover tube and the ambient air, kW/m² • °C

U_{oi} Overall heat transfer coefficient between the outer fluid and the inner fluid, kW/m² • °C

U_{rd} Radiative heat transfer coefficient between the cover tube and sky, kW/m² • °C

V Volume, m³

X Distance measured from the inlet tube section, m

θ Time, h

α Absorptivity

ϵ Emissivity

τ Transmissivity of cover tube

δ Tube thickness, m

ρ Density, kg/m³

Δ Increment

Subscripts

a absorber tube

c cover tube

f fluid

i inner fluid, in the center tube

o outer fluid, in the annulus area

Acknowledgement

The author would like to acknowledge Dr. C. L. Hamilton who provided valuable assistance in the technical analysis and R. J. Wallace and K. P. Bartos who made a number of helpful suggestions.

References

1. Lansing, F. L., "The Transient Thermal Response of a Tubular Solar Collector," *Technical Memorandum 33-781*, Jet Propulsion Laboratory, Pasadena, Calif., July 15, 1976.
2. Razelos, P., "Methods of Obtaining Approximate Solutions," *Handbook of Heat Transfer*, edited by Rohsenow, W. M., and Hartnett, J. P., Sec. 4, McGraw Hill Book Co., N. Y., 1973.

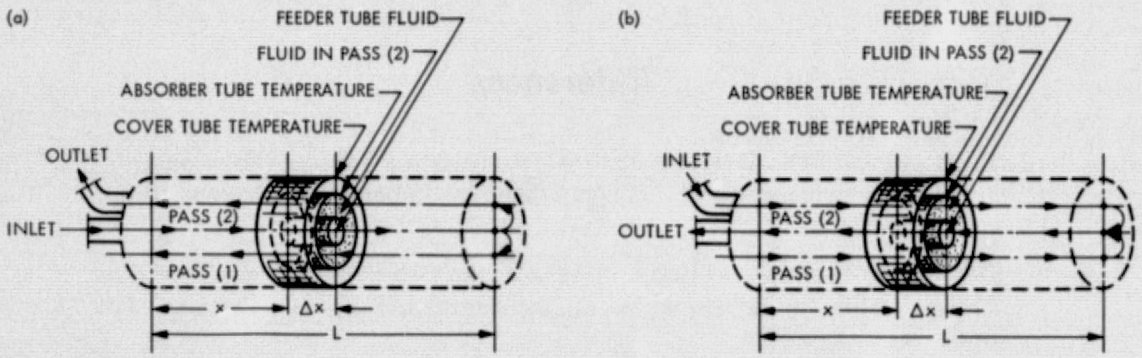

Fig. 1. Collector configuration (a) flow pattern (1) (b) flow pattern (2)

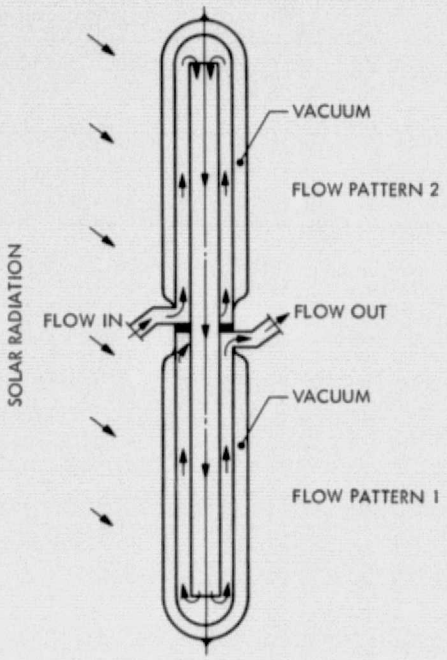

Fig. 2. Two collector units in series

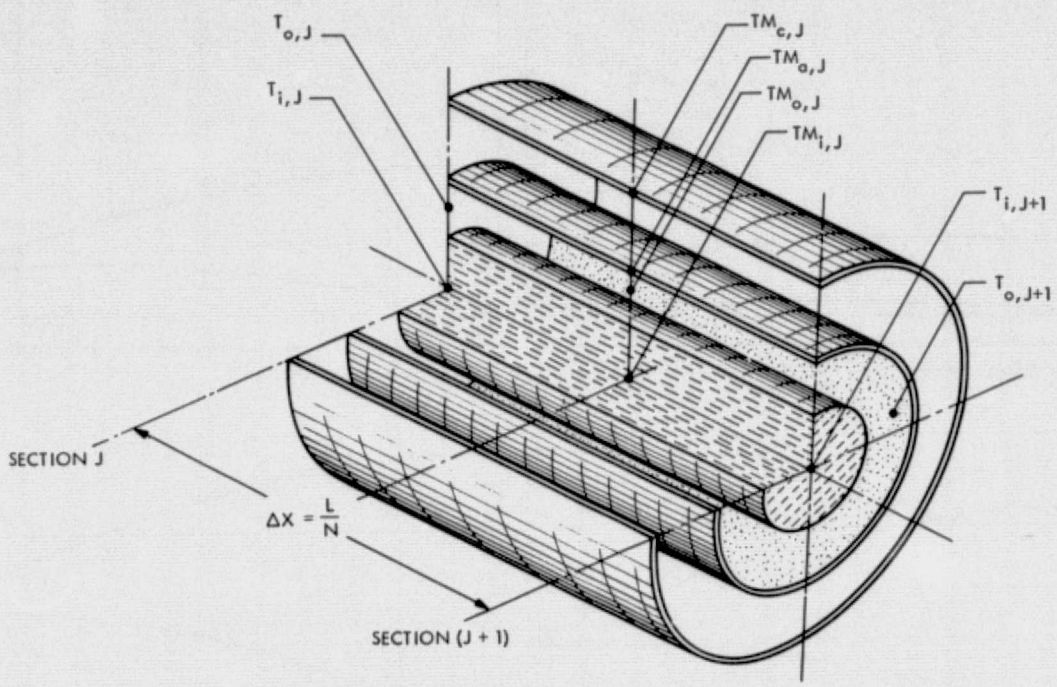

Fig. 3. Nodal and edge temperatures of the Jth segment

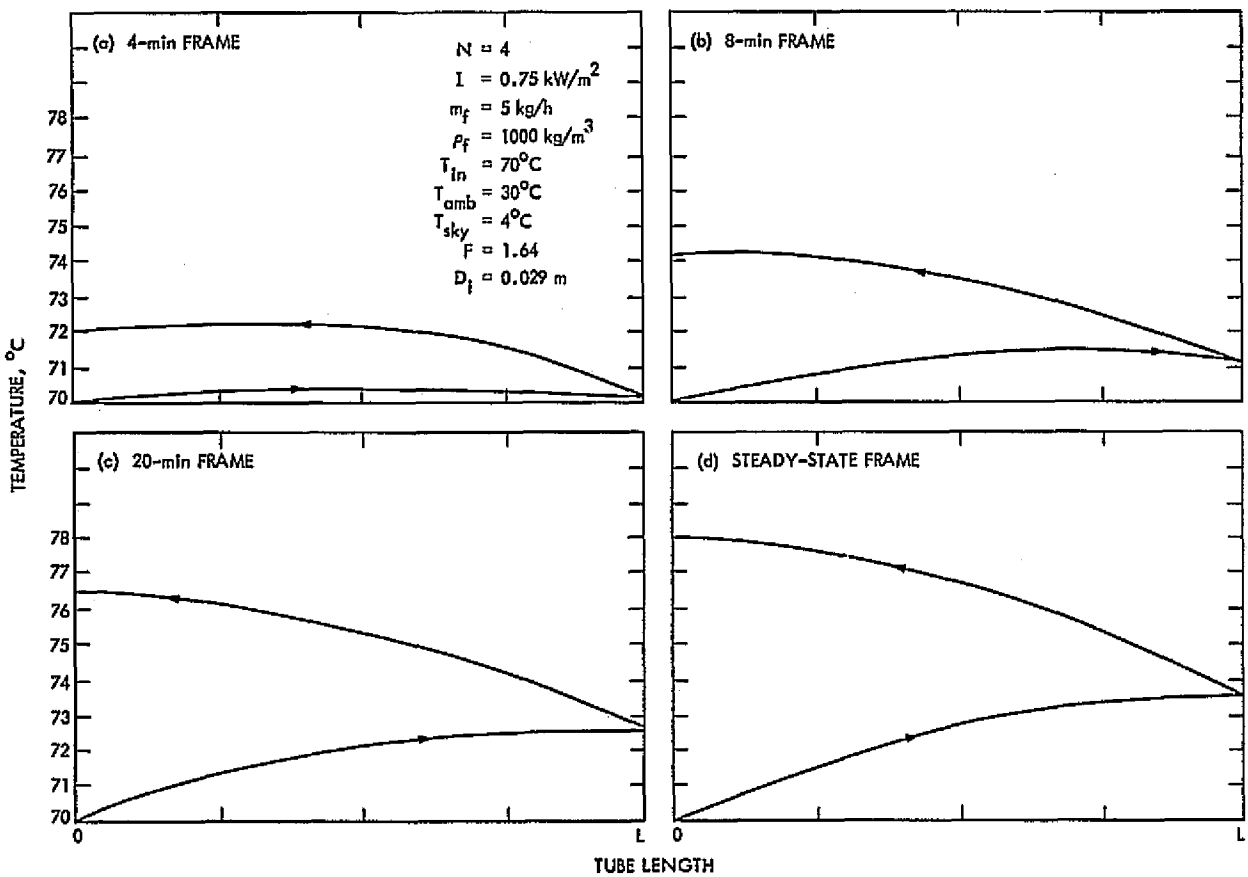

Fig. 4. Different time frames for one collector unit of flow pattern (1) showing the growth of the temperature profile

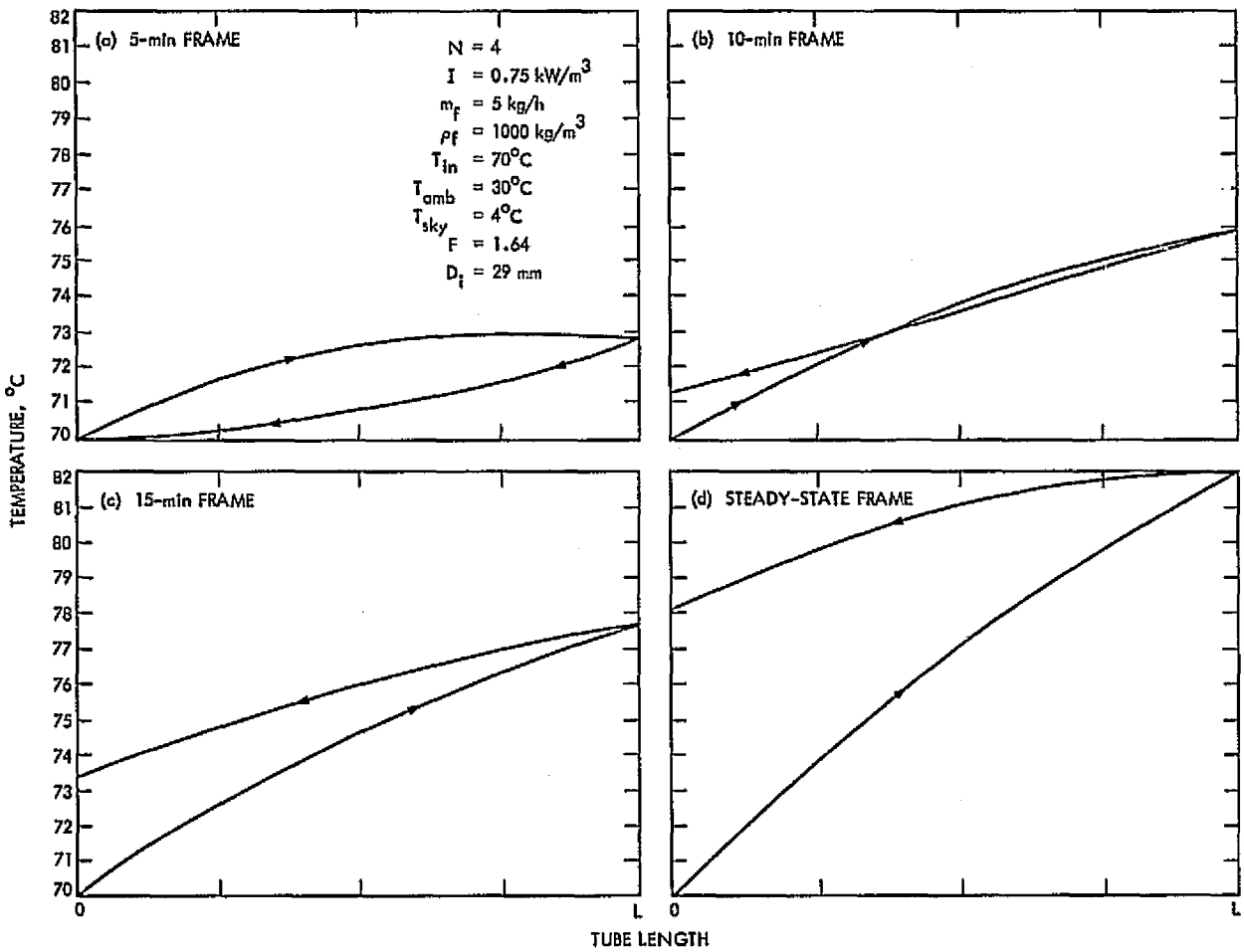

Fig. 5. Different time frames for one collector unit of flow pattern (2) showing the growth of the temperature profile

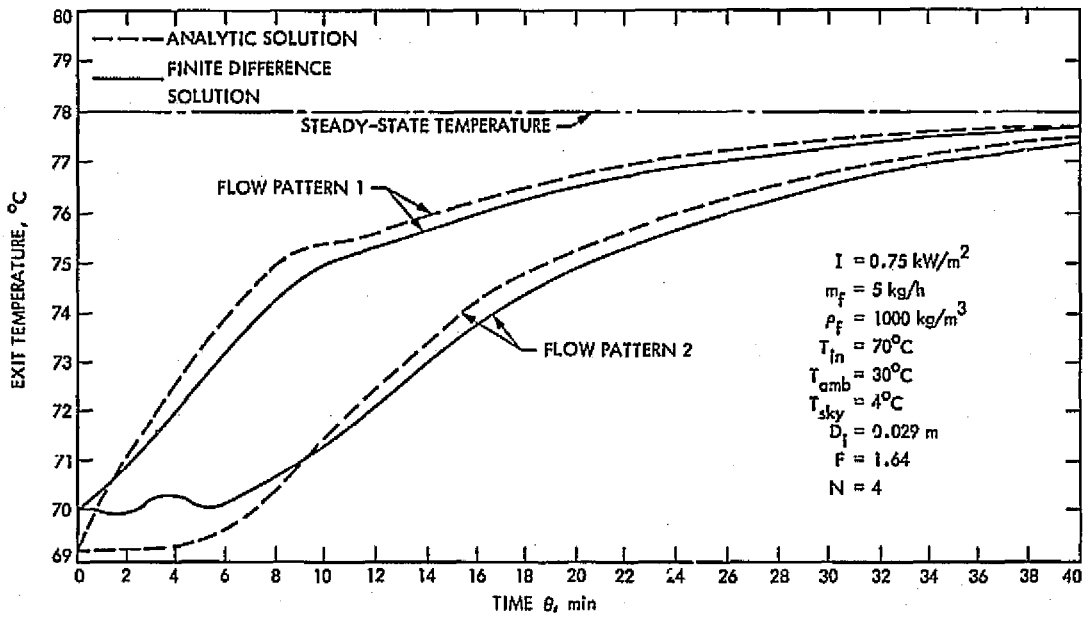

Fig. 6. Comparison between the finite difference solution and the analytical solution for a single tube and two different flow patterns

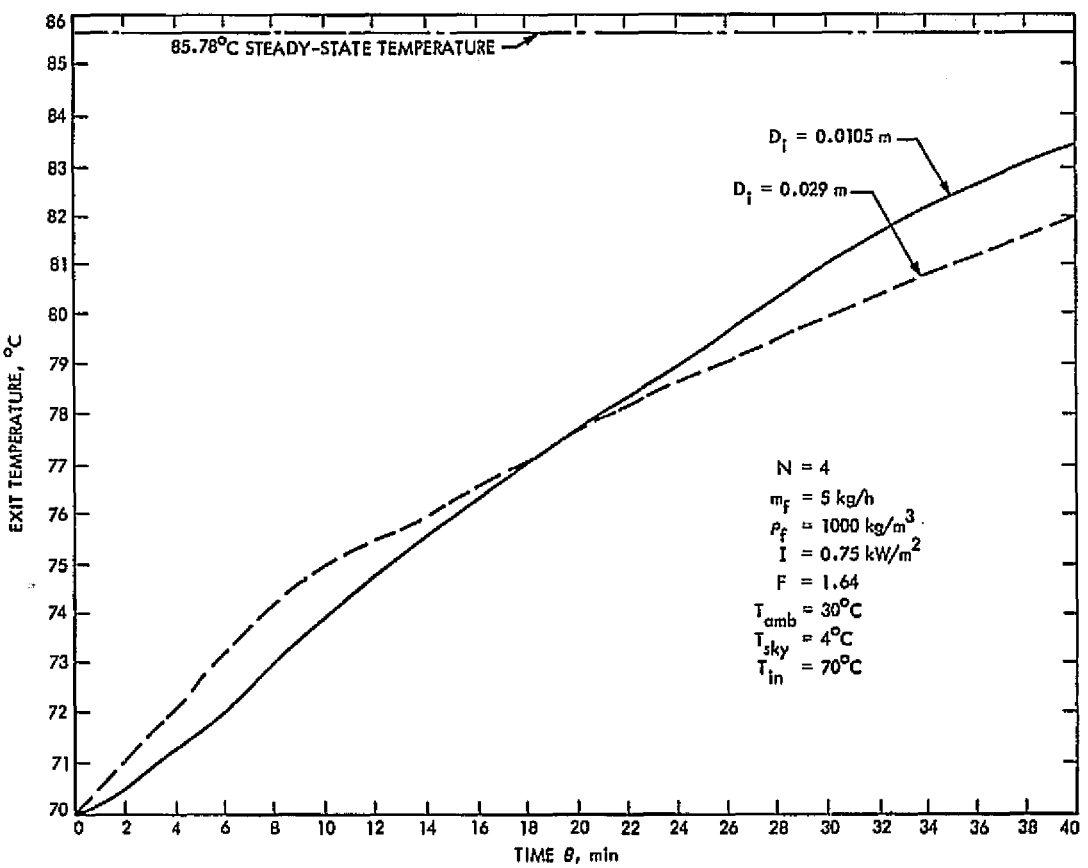

Fig. 7. Effect of increasing the inner tube diameter on thermal response for two collector units in series

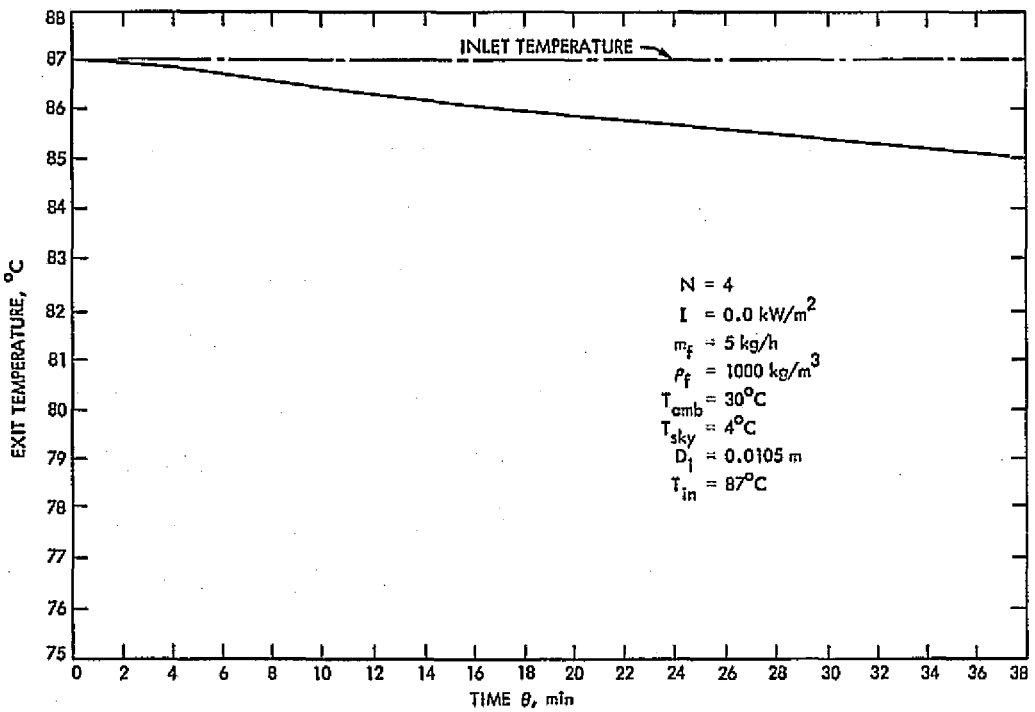

Fig. 8. Rate of cooling of two collector units in series at zero radiancy and constant inlet fluid temperature

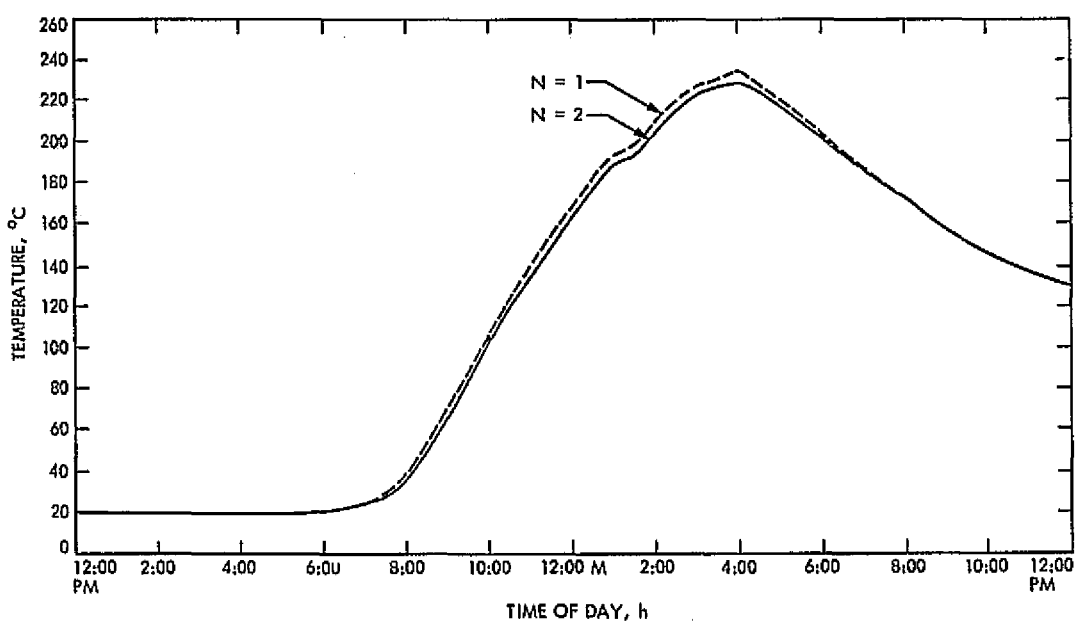

Fig. 9. Temperature deviations as calculated numerically for two finite-difference schemes with different space segments for 24 collector units at zero flowrate

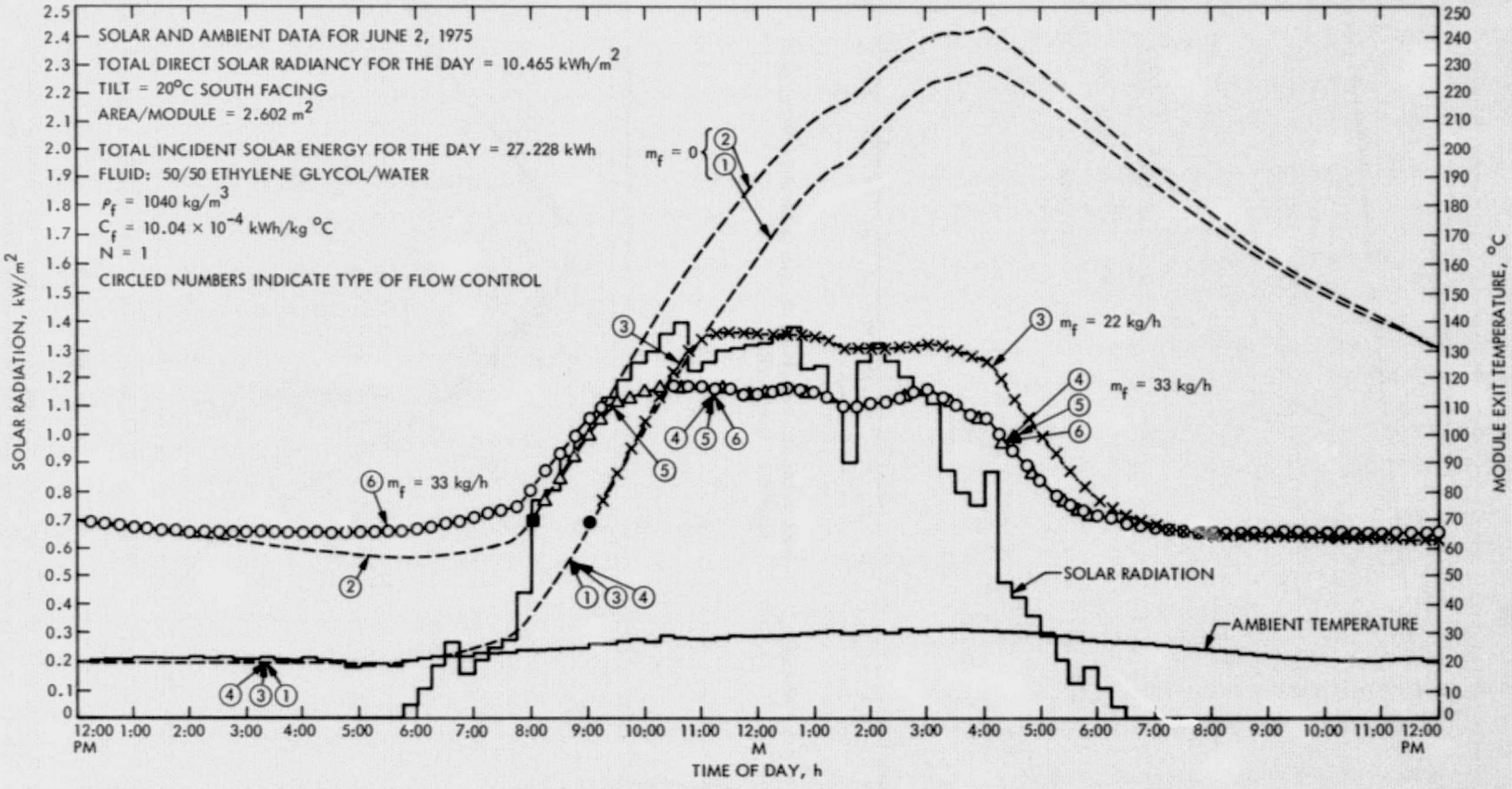

Fig. 10. Complete day performance of a collector module (24 units) under variable solar radiancy, ambient temperature and six flow control mechanisms

Appendix A

Nodal Energy Equations

I. General Remarks

The first step in obtaining the nodal equations is to subdivide the collector tubes into spatial segments by sections as shown in Fig. 3, locate a node in the center of each segment and then calculate the conductances between adjacent nodes. The energy balance for the mth node which is surrounded by n adjacent nodes, is then considered during a small time interval $\Delta\theta$. During this time interval, the temperatures of the n nodes are assumed to remain constant. Accordingly,

$$\rho_m C_m V_m \frac{\Delta T_m}{\Delta\theta} = \sum_n G_{mn}[T_n(\theta) - T_m(\theta)] + Q_{in} \tag{A-1}$$

where V_m is the volume assigned to the segment whose node is m, G_{mn} is the thermal conductance between nodes m, n, and Q_{in} is the rate of heat generation in the node if any. The difference ΔT_m may be expressed in terms of either a forward, a backward or a mid-difference (Ref. 2) which will yield different forms of Eq. (A-1). The simplest form is obtained using the "forward" difference and is chosen for the present work, i.e.,

$$\Delta T_m = T_m(\theta + \Delta\theta) - T_m(\theta) \tag{A-2}$$

In this case, the future temperature $T_m(\theta + \Delta\theta)$ is explicitly obtained from the knowledge of the present temperatures $T_m(\theta)$ and $T_n(\theta)$ at time θ. Combining Eqs. (A-1) and(A-2) gives the future temperature $T_m(\theta + \Delta\theta)$ as follows:

$$T_m(\theta + \Delta\theta) = T_m(\theta) + \left[\sum_n G_{mn}[T_n(\theta) - T_m(\theta)] + Q_{in}\right]\frac{\Delta\theta}{\rho_m C_m V_m} \tag{A-3}$$

It is important to note that the conductances G_{mn} include, in general, the energy conducted across the tube boundaries of the elements as well as the energy transported between neighboring nodes in case of an open system node with a fluid flowing across the segment (Lagrangian control volume approach).

II. Boundary Conditions

(1) For both flow patterns the closed-end temperature of the inner and the outer fluid must be equal.

(2) For flow pattern (1), the open-end temperature of the fluid in the inner tube is a known value.

(3) For flow pattern (2), the open-end temperature of the fluid in the annulus area is a known value.

(4) For a collector composed of two tubes of flow pattern (1) and (2) in series, the open end-to-end temperatures must be equal.

III. Energy Equations

The application of Eq. (A-3) ot the inner fluid, outer fluid, absorber tube and the cover tube segments yield the following:[1]

A. Inner Fluid

$$TM_{i,j}(\theta + \Delta\theta) = TM_{i,j}(\theta) + \left[G_{oi}[TM_{o,j}(\theta) - TM_{i,j}(\theta)] \pm G_{ff}[T_{i,j+1}(\theta) - T_{i,j}(\theta)]\right]\frac{\Delta\theta}{\rho_f C_f \frac{V_i}{N}} \tag{A-4}$$

where the (+) sign is for flow pattern (2) and the (−) sign is for flow pattern (1).

Expressing the inner fluid nodal temperatures in terms of the edge temperatures as

$$TM_{i,j}(\theta) = \frac{T_{i,j}(\theta) + T_{i,j+1}(\theta)}{2}$$
$$TM_{o,j}(\theta) = \frac{T_{o,j}(\theta) + T_{o,j+1}(\theta)}{2} \tag{A-5}$$

Then

$$\begin{aligned} TM_{i,j}(\theta + \Delta\theta) = {} & T_{i,j}(\theta)[0.5 - (0.5\,G_{oi}\Delta\theta_i \pm G_{ff}\Delta\theta_i)] \\ & + T_{i,j+1}(\theta)[0.5 - 0.5\,G_{oi}\Delta\theta_i \pm G_{ff}\Delta\theta_i] \\ & + T_{o,j}(\theta)\{0.5\,G_{oi}\Delta\theta_i\} \\ & + T_{o,j+1}(\theta)\{0.5\,G_{oi}\Delta\theta_i\} \end{aligned} \tag{A-6}$$

[1]See Appendix A of Ref. (1) for the explanation and the derivation of the heat flux distribution.

where

$$G_{oi} = U_{oi}\frac{\pi D_i L}{N}$$

$$G_{ff} = m_f C_f$$

$$V_i = \frac{\pi}{4} D_i^2 L$$

$$\Delta\theta_i = \frac{\Delta\theta \cdot N}{\rho_f C_f \cdot \frac{\pi}{4} D_i^2 L} \tag{A-7}$$

and the (+) sign is for flow pattern (2) and the (−) sign is for flow pattern (1).

B. Outer Fluid

$$TM_{o,j}(\theta + \Delta\theta) = TM_{o,j}(\theta) + \left[\left(U_{ao}\frac{\pi D_a L}{N}\right)[TM_{a,j}(\theta) - TM_{o,j}(\theta)] - \left(U_{oi}\frac{\pi D_i L}{N}\right)[TM_{o,j}(\theta) - TM_{i,j}(\theta)] \mp (m_f C_f)[T_{o,j+1}(\theta) - T_{o,j}(\theta)]\right] \cdot \frac{\Delta\theta}{\rho_f C_f \frac{V_o}{N}} \tag{A-8}$$

where the (+) sign is for flow pattern (1) and the (−) sign for flow pattern (2).

Expressing the outer fluid nodal temperatures in terms of edge temperatures as

$$TM_{o,j}(\theta) = \frac{TM_{o,j}(\theta) + TM_{o,j+1}(\theta)}{2}$$

$$TM_{i,j}(\theta) = \frac{TM_{i,j}(\theta) + TM_{i,j-1}(\theta)}{2} \tag{A-9}$$

Then

$$\begin{aligned} TM_{o,j}(\theta + \Delta\theta) = {} & T_{o,j}(\theta)\{0.5 - (0.5\,G_{ao}\Delta\theta_o \\ & + 0.5\,G_{oi}\Delta\theta_o \mp G_{ff}\Delta\theta_o)\} \\ & + T_{o,j+1}(\theta)\{0.5 - 0.5\,G_{ao}\Delta\theta_o \\ & - 0.5\,G_{oi}\Delta\theta_o \mp G_{ff}\Delta\theta_o\} \\ & + TM_{a,j}(\theta)\{G_{ao} \cdot \Delta\theta_o\} \\ & + T_{i,j}(\theta)\{0.5\,G_{oi}\Delta\theta_o\} \\ & + T_{i,j+1}(\theta)\{0.5\,G_{oi}\Delta\theta_o\} \end{aligned} \tag{A-10}$$

where

$$G_{ao} = U_{ao} \cdot \frac{\pi D_a L}{N}$$

$$G_{oi} = U_{oi}\frac{\pi D_i L}{N}$$

$$G_{ff} = m_f C_f$$

$$V_o = \frac{\pi}{4}(D_o^2 - D_i^2)L$$

$$\Delta\theta_o = \frac{\Delta\theta \cdot N}{\rho_f C_f (D_o^2 - D_i^2)L} \tag{A-11}$$

and the (+) sign is for flow pattern (1) and the (−) sign is for flow pattern (2).

C. Absorber Tube

$$TM_{a,j}(\theta + \Delta\theta) = TM_{a,j}(\theta) + \left[I \cdot F \cdot \left(\frac{\alpha_a \tau_c}{1 - r_a r_c}\right) \cdot \frac{D_c L}{N} - \left(U_{ao}\frac{\pi D_a L}{N}\right)[TM_{a,j}(\theta) - TM_{o,j}(\theta)] - \left(U_{ac}\frac{\pi D_a L}{N}\right)[TM_{a,j}(\theta) - TM_{c,j}(\theta)]\right] \times \frac{\Delta\theta}{\rho_a C_a \frac{V_a}{N}} \tag{A-12}$$

Expressing the outer fluid nodal temperatures in terms of edge temperatures as

$$TM_{o,j}(\theta) = \frac{T_{o,j}(\theta) + T_{o,j+1}(\theta)}{2} \tag{A-13}$$

Hence

$$\begin{aligned} TM_{a,j}(\theta + \Delta\theta) = {} & TM_{a,j}(\theta)\{1 - G_{ao}\Delta\theta_a - G_{ac}\Delta\theta_a\} \\ & + TM_{c,j}(\theta)\{G_{ac}\Delta\theta_a\} \\ & + T_{o,j}(\theta)\{0.5\,G_{ao}\Delta\theta_a\} \\ & + T_{o,j+1}(\theta)\{0.5\,G_{ao}\Delta\theta_a\} \\ & + \left\{I \cdot F \cdot \frac{\alpha_a \tau_c}{1 - r_a r_c} \cdot \frac{D_c L}{N} \cdot \Delta\theta_a\right\} \end{aligned} \tag{A-14}$$

where

$$V_a = \pi D_a \delta_a L$$

$$\Delta\theta_a = \frac{\Delta\theta \cdot N}{\rho_a C_a \cdot (\pi D_a \delta_a L)} \tag{A-15}$$

D. Cover Tube

$$TM_{c,j}(\theta + \Delta\theta) = TM_{c,j}(\theta) + \left\{\left\{I \cdot F \cdot \left(\alpha_c + \frac{\alpha_c r_a r_c}{1 - r_a r_c}\right) \cdot \frac{D_c L}{N}\right\} + U_{ac}\frac{\pi D_a L}{N}[TM_{a,j}(\theta) - TM_{c,j}(\theta)] - U_{cv} \cdot \frac{\pi D_c L}{N}[TM_{c,j}(\theta) - T_{amb}] - U_{rd} \cdot \frac{\pi D_c L}{N}[TM_{c,j}(\theta) - T_{sky}]\right\} \frac{\Delta\theta}{\rho_c C_c \frac{V_c}{N}} \tag{A-16}$$

or

$$TM_{c,j}(\theta+\Delta\theta) = TM_{c,j}(\theta)[1 - G_{ac} \cdot \Delta\theta_c - G_{cb}\Delta\theta_c - G_{cs}\Delta\theta_c] + TM_{a,j}(\theta)[G_{ac} \cdot \Delta\theta_c] + \Delta\theta_c \left\{\left\{I \cdot F \cdot \left(\alpha_c + \frac{\alpha_c r_a \tau_a}{1 - r_a r_c}\right)\frac{D_c L}{N}\right\} + (G_{cb} \cdot T_{amb}) + (G_{cs} \cdot T_{sky})\right\} \tag{A-17}$$

where

$$V_c = \pi D_c \delta_c L$$

$$\Delta\theta_c = \frac{\Delta\theta \cdot N}{\rho_c C_c (\pi D_c \delta_c L)}$$

$$G_{cb} = U_{cv}\frac{\pi D_c L}{N}$$

$$G_{cs} = \frac{U_{rd} \cdot \pi D_c L}{N} \tag{A-18}$$

Appendix B

Convergence and Stability of Computations

I. General Remarks

In the numerical computations, the term error refers to the difference between the approximate solution obtained by the finite difference scheme and the exact solution of the original partial differential equations. Accordingly, there exists two types of errors.

(1) Truncation error due to the replacement of the derivatives by finite differences. This depends on the given initial and boundary conditions.

(2) Round-off error caused by carrying out the computations to a finite decimal place.

Apart from the above errors, the most serious problem associated with the finite difference scheme is the phenomena of instability. This means that the temperatures oscillate with an increasing magnitude as the computation progresses. Therefore, the space and time increments ΔX, $\Delta\theta$, respectively, cannot be selected arbitrarily but rather constrained to satisfy certain stability criteria. For practical applications, the following elementary argument (Ref. 2) has been used for obtaining simple and adequate stability conditions.

The mth node temperature can be expressed in terms of the surrounding n nodes in the format:

$$T_m(\theta + \Delta\theta) = K_{mm}T_m(\theta) + \sum_n K_{mn}T_n(\theta) \qquad \text{(B-1)}$$

where the coefficients K_{mn} are set to be positive. If the coefficient K_{mm} was negative then the higher temperature $T_m(\theta)$ at the present time θ, the lower the temperature $T_m(\theta + \Delta\theta)$ at the future time $(\theta + \Delta\theta)$. This would be in violation of the thermodynamics principles. Therefore, the increment of time $\Delta\theta$ for a given space subdivision ΔX should be chosen so that the coefficient K_{mm} is positive or at least zero. Applying the above simple rule to the finite difference equations developed earlier for each node, the following critical stability conditions are established.

II. Case of Flow Pattern (1)

For the inner fluid temperature stability

$$0.5 - 0.5\,G_{oi}\Delta\theta_i - G_{ff}\Delta\theta_i \geq 0 \qquad \text{(B-2)}$$

For the outer fluid temperature stability

$$0.5 - 0.5\,G_{ao}\Delta\theta_o - 0.5\,G_{oi}\Delta\theta_o - G_{ff}\Delta\theta_o - 0.5\,G_{oi}\Delta\theta_i \geq 0 \qquad \text{(B-3)}$$

For the absorber tube temperature stability

$$1 - (G_{ao} + G_{ac})\,\Delta\theta_a \geq 0 \qquad \text{(B-4)}$$

For the cover tube temperature stability

$$1 - (G_{ac} + G_{cb} + G_{cs})\,\Delta\theta_c \geq 0 \qquad \text{(B-5)}$$

III. Case of Flow Pattern (2)

For the inner fluid temperature stability

$$0.5 - G_{ff}\Delta\theta_i - 0.5\,G_{oi}\Delta\theta_i - 0.5\,G_{oi}\Delta\theta_o \geq 0 \qquad \text{(B-6)}$$

For the outer fluid temperature stability

$$0.5 - 0.5\,G_{ao}\Delta\theta_o - 0.5\,G_{oi}\Delta\theta_o - G_{ff}\Delta\theta_o \geq 0 \qquad \text{(B-7)}$$

For the absorber tube temperature stability

$$1 - (G_{ao} + G_{ac})\,\Delta\theta_a \geq 0 \qquad \text{(B-8)}$$

For the cover tube temperature stability

$$1 - (G_{ac} + G_{cb} + G_{cs})\,\Delta\theta_c \geq 0 \qquad \text{(B-9)}$$

IV. Case of a Series Connection of Flow Patterns (1) and (2)

The foregoing conditions are combined and listed as follows:

For the inner fluid temperatures stability, a comparison of conditions (B-2) and (B-3) shows that condition (B-4) predominates, thus leaving

$$0.5 - G_{ff}\Delta\theta_i - 0.5\,G_{oi}\Delta\theta_i - 0.5\,G_{oi}\Delta\theta_o \geq 0$$

or

$$\Delta\theta \leq \frac{\rho_f C_f}{(4U_{oi}/D_i) + (8N\,C_f m_f/\pi D_i^2 L) + \left[4U_{oi}/(D_a^2/D_i)\left(1-\left(\frac{D_i}{D_a}\right)^2\right)\right]} \tag{B-10}$$

For the outer fluid temperature stability, a comparison of conditions (B-3) and (B-7) shows that condition (B-7) predominates, thus

$$0.5 - 0.5\,G_{ao}\Delta\theta_o - 0.5\,G_{oi}\Delta\theta_o - G_{ff}\Delta\theta_o - 0.5\,G_{oi}\Delta\theta_i \geq 0$$

or

$$\Delta\theta \leq \frac{\rho_f C_f}{\left(\frac{4U_{oi}}{D_i}\right) + \frac{8N\,m_f C_f}{\pi(D_a^2 - D_i^2)L} + \frac{4U_{oi}}{D_a\cdot\left(\frac{D_a}{D_i}\right)\cdot\left(1-\left(\frac{D_i}{D_a}\right)^2\right)} + \frac{4U_{ao}}{D_a\left[1-\left(\frac{D_i}{D_a}\right)^2\right]}} \tag{B-11}$$

For the absorber tube temperatures stability

$$1 - (G_{ao} + G_{ac})\,\Delta\theta_a \geq 0$$

or

$$\Delta\theta \leq \frac{\rho_a C_a \delta_a}{(U_{ao} + U_{ac})} \tag{B-12}$$

For the cover tube temperature stability

$$1 - (G_{ac} + G_{cb} + G_{cs})\,\Delta\theta_c \geq 0$$

or

$$\Delta\theta \leq \frac{\rho_c C_c \delta_c}{\left(U_{ac}\frac{D_a}{D_c} + U_{cr} + U_{rl}\right)} \tag{B-13}$$

V. Example of Computations for the Critical Time Increment

To determine which of the above four conditions, Eqs. (B-10), (B-11), (B-12) and (B-13) yield the most critical time increment $\Delta\theta$ to ensure stable temperature computations the following numerical values are assigned from a typical running condition:

$D_i = 0.0105$ m, $\quad \delta_a = \delta_c = 0.004$ m

$D_a = 0.041$ m, $\quad C_f = 11.634 \times 10^{-4}$ kWh/Kg · °C (water)

$D_c = 0.051$ m, $\quad C_c = C_a = 2.094 \times 10^{-4}$ kWh/Kg · °C (glass)

$L = 1.067$ m, $\quad \rho_f = 1000$ kg/m³ (water)

$N = 4$ $\quad \rho_c = \rho_a = 2468$ kg/m³ (glass)

$m_f = 5$ kg/h

$U_{oi} = 56.53 \times 10^{-3}$ kW/m² · °C

$U_{ao} = 113.06 \times 10^{-3}$ kW/m² · °C

$U_{ac} = 0.80 \times 10^{-3}$ kW/m² · °C

$U_{cr} = 18.62 \times 10^{-3}$ kW/m² · °C

$U_{rl} = 4.99 \times 10^{-3}$ kW/m² · °C

Condition (B-10) yields $\Delta\theta \leq 0.0022$ h (7.8 s)

Condition (B-11) yields $\Delta\theta \leq 0.0166$ h (59.7 s)

Condition (B-12) yields $\Delta\theta \leq 0.0182$ h (65.4 s)

Condition (B-13) yields $\Delta\theta \leq 0.0852$ h (306.7 s)

The above indicates that Condition (B-10) is the most critical condition that must be satisfied in order to ensure stable computations. It can be seen from Condition (B-10) that the resulting minimum increment of time is inversely proportional with the mass flowrate. In the limit, with zero fluid flowrate, Condition (B-10) yields $\Delta\theta \leq 0.0505$ h (181.8 s) and in this case Condition (B-12) will impose the minimum time required for stable computations.

With regard to accuracy, the round-off errors have little or no effect on the solution if the restrictions of stability are observed, while the truncation errors decrease as we select smaller time and space increments.

Radio-Frequency Boresight Analysis of the Low-Cost 64-Meter Antenna

M. S. Katow
DSN Engineering Section

Two configurations of the reflector-only assemblies, using different width backup cones, are analyzed for RF boresight direction changes and wind distortions. The wider backup cone is best for minimum weight; however, there is an optimum weight which minimizes the RF boresight errors for a wind load that produces the maximum pitching moment of both configurations.

I. Introduction

One of the important performance characteristics of a large ground antenna is the pointing accuracy of its RF boresight with respect to the indicated positions on the axes angle measuring devices. As the beamwidth of the RF pattern decreases with increases in operating frequency and antenna diameter, the pointing changes due to the environmental (gravity, wind, temperature) load changes must be limited to a fraction of the beamwidth to prevent excessive gain loss.

The DSN ground antenna must operate continuously through day and night and, on occasions, in wind gusts up to 84 km/h (55 mi/h) on S-band frequency. Operation under a limited environment is considered to be satisfactory for X-band as a balanced requirement to the frequent occurrences of large gain loss of X-band through a moisture-laden atmosphere.

The use of the conical scan pointing system relieves the pointing requirements but "blind" pointing again becomes important when very-long baseline interferometry (VLBI) is activated.

Radio-frequency boresight errors due to gravity loading can be calibrated and compensation applied by many means, such as the future minicomputer in the pointing equipment, so these errors will not be considered here. Errors from wind loads will be difficult to model and calibrate; hence, minimizing by design would probably be the best solution.

Since the connections between the symmetric reflector structure and the alidade under consideration are at only two points with the forces or reactions determinant, the reflector can be analyzed by itself and its reactions applied to the alidade. By this method, the complete antenna can be analyzed.

This reporting will be on the analysis of the wind load resulting in the maximum pitch or yaw moments on the reflector-only configuration. The follow-on reporting will describe the overall effects of the selected wind load on the complete antenna.

The asymmetry of the maximum pitching moment wind load, 60-deg elevation angle with wind from the back, results in the maximum distortion of the reflector as well as the RF boresight deflection. A design that can minimize and compensate for the RF boresight error may be adequate to cover other operating conditions where the gain loss is less and accurate boresight compensations are thus not as critical.

It should be noted here that large gain losses can occur at high RF frequency use with symmetric winds, winds directly into or back of the reflector, as a result of axial RF phase center offsets to the best-fit paraboloid.

The reflector structural configuration and its backup structure is a follow-on of that described in Ref. 1.

The JPL-IDEAS (Ref. 2) computer programs and special programs, as described in Ref. 1, were used to generate most of the computer data which saved both generation and verification time.

II. Antenna Description

A. Reflector Structure

As shown in Fig. 1, the radial distances to the hoops were made up of four increments of 3.05 m (120 in.), one of 3.56 m (140 in.) and four of 4.06 m (160 in.). These spacings can be changed slightly and not affect the distortion characteristics of the reflector. Equal distances along the parabolic arc might be in order to reduce tooling costs of the surface panels.

Two alternate backup cones were used. The standard configuration attached to the fourth hoop and the wider cone attached to the fifth hoop.

A diaphragm or plate flexture-type structural member covers only the bottom of the center bay, and, with the center connection to the backup structure, only lateral reflector support is provided at the center. The axial as well as the second lateral support point is provided by the apex of the backup cone assembly. A torsion constraint link would be required for the actual antenna, but for the one-half symmetrical computer model, constraints on the symmetry plane prevent this torsional motion. Diagonals in at least one bay or space between two ribs would also be required in the actual antenna or constraints would have to be provided by the surface panels.

The center bay is hollow to provide for easy access to the cassegrain cone mounted on hoop 1. Face diagonals are used between hoop 1 and hoop 2 on both top and bottom surfaces to essentially form a torus structure. Otherwise, no other face diagonals are used except between hoops 5 and 6 to tie the intermediate ribs to the main ribs.

As stated previously, the reflector-only configuration is analyzed in this reporting with two different backup cones. Other configuration changes, such as a deeper reflector and thicker outer edges, have been computed, but not completely analyzed at this point.

Since this reflector-cone assembly is connected to the backup structure with the statically determinable two points, the reflector-only configuration can be analyzed by itself, and the reaction loads can then be applied to the backup structure and alidade assembly in order to obtain the total system deflections.

B. Backup Structure and Alidade

The backup structure and alidade is shown in isometric view as Fig. 2. The four-point azimuth wheel supports at ⑤⑥⑦ and ⑧ provide a wide support base which insures stability against overturning from the survival wind loads. At the same time, the four wheel loads are about equal for gravity load because the alidade lacks torsional rigidity about the elevation axis. The rigidity is supplied by the wheels. Loads in the elevation axis direction on elevation bearings ③ and ④ are transmitted to the center radial bearing by diagonal bars ③-⑨ and ④-⑨.

The reflector is attached at points ① and ②.

III. Analysis Description

As stated previously, the wind direction producing the maximum pitching moment occurs with the antenna at 60-deg elevation and the wind from the back. Since the quadripod is protected by the reflector, no wind loads will be assumed on it. The reflector surface is 50-percent porous in the outer 50-percent radius, the same configuration as the present Mars 64-m antenna.

The pressure difference coefficients were developed by the method described in Ref. 2.

The JPL-IDEAS program first minimized the gravity distortions, maintaining the structural integrity for the stow wind loads of 44.70 m/s (100 mi/h). By multiplying the resulting bar areas by 2 and again input to the JPL-IDEAS program using a ratio of 0.2, the output resulted in weight reduction steps with the gravity distortion figures remaining substantially the same, just slightly above the minimums resulting from the first computations. In this way, the data for structural weight vs. the distortion rms for the 31.29-m/s (70-mi/h) wind velocity were developed as well as parameters of the best-fit paraboloid.

The above follows from the theory that, if the surface panels and the cassegrain cone loads are not considered, fixed percentage changes of all of the bars of the reflector structures result in no change in the gravity distortion rms.

IV. Analysis Results

The outputs from the JPL-IDEAS programs related to the 60-deg elevation back-wind load input are detailed in Tables 1 and 2 for the standard and the wider backup cones, respectively.

Offset F figures were calculated from the lateral motion required of the RF phase center in order to maintain the original undeflected RF boresight direction. Radio-frequency ray tracing was used with a reflection factor of 0.85 applicable for a uniformly illuminated reflector as illustrated in Fig. 3.

Figure 4 shows the results of Tables 1 and 2 plotted with respect to the reflector structural weight variations. The rms and offset F curves are almost identical by chance.

V. Conclusions

It must be concluded that the RF boresight direction error for a particular wind load is a function of the structural weight of the reflector.

The wider backup cone decreases both the offset F and the distortion rms for the maximum pitching moment wind load.

The other factors that must be taken into account are: (a) displacement of the RF phase center at the paraboloid's focus, and (b) the deflection characteristics of the reflector's backup wheel and alidade that affect the differences between the indicated positions of the axes angle transducers and the true pointing directions. These factors will be discussed in follow-on reporting.

References

1. Levy, R., "Conceptual Studies for New Low-Cost 64-m Antennas," in *The Deep Space Network Progress Report 42-33*, Jet Propulsion Laboratory, Pasadena, Calif., pp. 55–61, June 15, 1976.
2. Katow, M. S., "Aerodynamic Static Differential Pressure Values for the 50 Percent Porous Reflector Dish," in *The Deep Space Network Progress Report 42-29*, Jet Propulsion Laboratory, Pasadena, Calif., pp. 60–65, Oct. 15, 1975.

Table 1. Parameters of the best-fit paraboloid (Fig. 3) reflector only with standard backup cone

Sequence	Structural weight, kg (kips)	Rms, mm (in.)	Focal length, m (in.)	A Y-coord, cm (in.)	B Z-coord, cm (in.)	C X-rotation, rad	D Offset, cm (in.)	E Offset, cm (in.)	F Offset, cm (in.)
1	482,100 (1063)	2.21 (0.087)	27.1041 (1067.089)	9.972 (3.926)	0.053 (0.021)	0.002061	5.585 (2.199)	4.387 (1.727)	2.184 (0.860)
2	386,900 (853)	2.74 (0.108)	27.1018 (1067.0)	12.466 (4.908)	0.066 (0.026)	0.002576	6.983 (2.749)	5.484 (2.159)	2.731 (1.075)
3	310,700 (685)	3.40 (0.134)	27.1011 (1066.974)	15.583 (6.135)	0.084 (0.033)	0.003220	8.730 (3.437)	6.853 (2.698)	3.419 (1.346)
4	260,800 (575)	4.01 (0.158)	27.1000 (1066.927)	15.583 (6.887)	0.109 (0.043)	0.003861	9.921 (3.906)	7.572 (2.981)	4.100 (1.614)
5	241,300 (532)	4.39 (0.173)	27.0989 (1066.884)	19.944 (7.852)	0.107 (0.042)	0.004122	11.171 (4.398)	8.773 (3.454)	4.369 (1.720)

Wind load = 60° elevation back wind
Dynamic pressure = 84.9 kN/m² (12.3 psi)
Wind velocity = 31.3 m/s (70 mi/h)
F = (D/0.85) − E
Rms = distortion in one-half pathlength errors
A, B, C, D, E, F = Fig. 3

Table 2. Parameters of the best-fit paraboloid (Fig. 3) reflector only with wider backup cone

Sequence	Structural weight, kg (kips)	Rms, mm (in.)	Focal length, m (in.)	A Y-coord, cm (in.)	B Z-coord, cm (in.)	C X-rotation, rad	D Offset, cm (in.)	E Offset, cm (in.)	F Offset, cm (in.)
1	525,500 (1160)	1.37 (0.054)	27.1063 (1067.175)	4.702 (1.851)	0.061 (0.024)	0.001031	2.794 (1.100)	1.908 (0.751)	1.379 (0.543)
2	423,600 (935)	1.70 (0.067)	27.1055 (1067.146)	5.873 (2.312)	0.076 (0.030)	0.001288	3.493 (1.375)	2.380 (0.937)	1.730 (0.681)
3	338,400 (747)	2.11 (0.083)	27.1046 (1067.109)	7.338 (2.889)	0.097 (0.038)	0.001610	4.364 (1.718)	2.974 (1.171)	2.159 (0.850)
4	271,800 (600)	2.77 (0.109)	27.1031 (1067.051)	8.649 (3.405)	0.127 (0.050)	0.001941	5.260 (2.071)	3.388 (1.334)	2.799 (1.102)

Wind load = 60° elevation back wind
Dynamic pressure = 84.9 kN/m² (12.3 psi)
Wind velocity = 31.3 m/s (70 mi/h)
F = (D/0.85) − E
Rms = distortion in one-half pathlength errors
A, B, C, D, E, F = Fig. 3

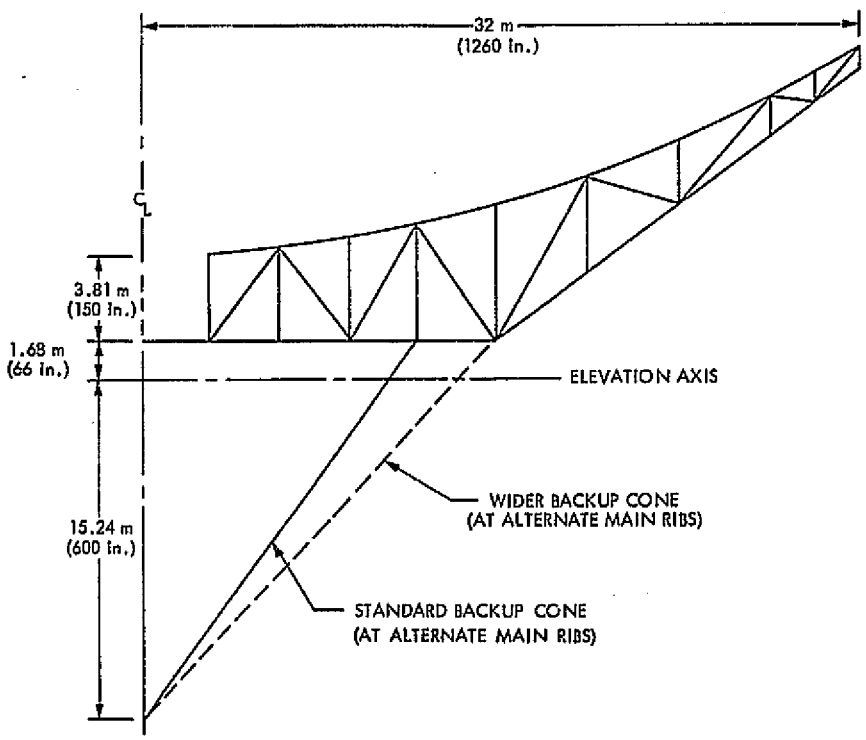

Fig. 1. Reflector structure with backup cone

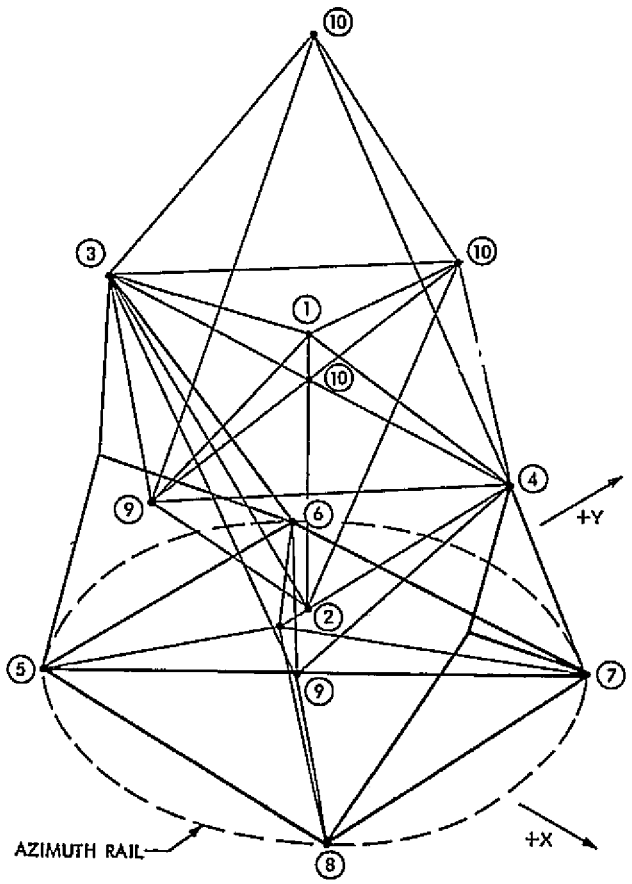

Fig. 2. Reflector backup structure with alidade

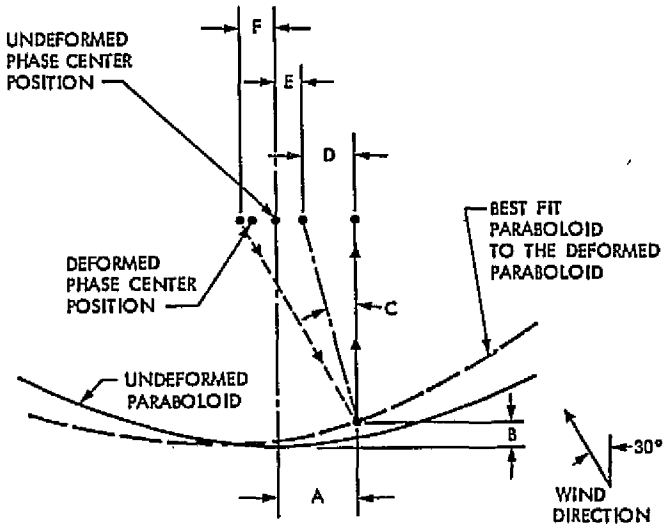

Fig. 3. Best-fit paraboloid parameters

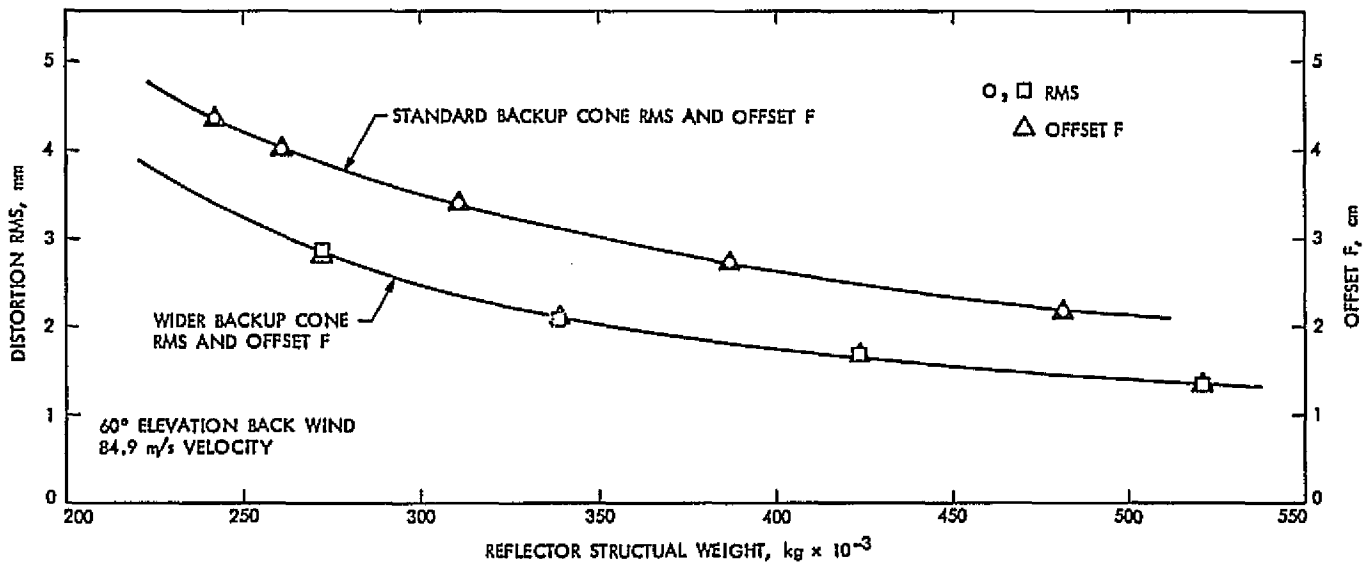

Fig. 4. Reflector distortion rms and offset F vs structural weight

The Pioneer 11 1976 Solar Conjunction: A Unique Opportunity to Explore the Heliographic Latitudinal Variations of the Solar Corona

A. L. Berman, J. A. Wackley, S. T. Rockwell, and J. G. Yee
DSN Network Operations Section

The 1976 Pioneer 11 Solar Conjunction provided the opportunity to accumulate a substantial quantity of doppler noise data over a dynamic range of signal closest approach point heliographic latitudes. The observed doppler noise data were fit to the (previously developed) doppler noise model "ISED," and the deviations of the observed doppler noise data from the model were used to construct a (multiplicative) function to describe the effect of heliographic latitude (ϕ_s):

$$f(\phi_s) = 10^{-0.0(\phi_s/90\ \mathrm{deg})}$$

This expression was then incorporated (back) into the ISED model to produce a new doppler noise model — "ISEDB."

I. Introduction

In a previous report (Ref. 1), A. Berman and J. Wackley, after extensively analyzing the 1975 solar conjunctions of Pioneer 10, Pioneer 11, and Helios 1, concluded that observed doppler noise (rms phase jitter) was directly proportional to integrated signal path electron density. As a direct consequence of that hypothesis, it was possible to construct a geometrical model for observed doppler noise —ISED (Integrated Solar Electron Density)—as follows:

$$\mathrm{ISED} = A_0\left[\frac{\beta}{(\sin\alpha)^{1.3}}\right] F(\alpha,\beta) + A_1\left[\frac{1}{(\sin\alpha)^5}\right]$$

$$F(\alpha,\beta) = 1 - 0.05\left\{\frac{(\beta - \frac{\pi}{2} + \alpha)^3 - (\alpha - \frac{\pi}{2})^3}{\beta}\right\}$$

$$-0.00275\left\{\frac{(\beta - \frac{\pi}{2} + \alpha)^5 - (\alpha - \frac{\pi}{2})^5}{\beta}\right\}$$

α = Sun–Earth–probe angle (SEP), radians

β = Earth–Sun–probe angle (ESP), radians

A best fit of this model to the combined Pioneer 10, Pioneer 11, and Helios 1 1975 solar conjunction doppler noise produced the following fit parameters:

$$A_0 = 9.65 \times 10^{-4}$$

$$A_1 = 5 \times 10^{-10}$$

Additional information concerning the development of the ISED model can be found in Refs. 2, 3, and 4.

If 1975 could be considered as a bountiful year for collection of solar conjunction data, then 1976 must be considered nothing short of a bonanza: six spacecraft undergoing a variety of solar conjunction phases, crowned by a Helios 2 triple occultation. On the face of it, the Pioneer 11 solar conjunction would definitely appear to be least interesting of the lot, a the SEP only reached a minimum of about 12 deg, which in turn results in only weak to moderate solar plasma effects on the spacecraft signal. However, during the period when the SEP was small enough to allow solar plasma effects to be seen in the doppler noise, i.e.,

$$\text{SEP} \lesssim 50 \text{ deg}$$

the heliographic latitude of the signal's closest approach point to the Sun varied slowly from approximately 10 deg to a maximum of approximately 78 deg, and then back to 10 deg again, thus allowing a large amount of noise data to be accumulated over a dynamic range of heliographic latitudes. Figure 1 presents the heliographic latitude of the Pioneer 11 signal closest approach point as a function of day of year (DOY), 1976. A similar curve for Pioneer 10 is included by way of comparison. At this point one is led to consider the following opportunity: why not fit the Pioneer 11 observed doppler noise with the ISED model, and then attempt to correlate the residuals ($\cong 10 \log_{10}(N_d/N_p)$) with the heliographic latitude? If correlation is evident as expected, the variation with heliographic latitude can be modeled and further incorporated (back) into the ISED model. In this process the Pioneer 11 observed doppler noise formed the bulk of the data base; however, a (much) smaller amount of data was available from the Pioneer 10 (1976) solar conjunction, and hence was additionally included.

II. Calculation of Signal Closest Approach Point Heliographic Latitude

The Sun-Earth–spacecraft geometry referenced to the ecliptic plane is shown in Fig. 2, with the appropriate quantities labeled. One easily obtains the following relationships:

$$X = r_e \sin \alpha$$

$$Z = r_e \cos \alpha$$

$$Y = Z \sin \phi_e$$

$$= r_e \cos \alpha \sin \phi_e$$

$$\phi_s = \sin^{-1}(Y/X)$$

$$= \sin^{-1}(r_e \cos \alpha \sin \phi_e / r_e \sin \alpha)$$

$$= \sin^{-1}(\cot \alpha \sin \phi_e)$$

Now the ecliptic latitude (ϕ_e) is defined in terms of the spacecraft right ascension and declination as follows:

$$\sin \phi_e = -\cos \delta_d \sin \alpha_{ra} \sin \epsilon + \sin \delta_d \cos \epsilon$$

where

α_{ra} = right ascension

δ_d = declination

ϵ = obliquity of ecliptic (23.445 deg)

so that

$$\phi_s = \sin^{-1}[\cot \alpha(-\cos \delta_d \sin \alpha_{ra} \sin \epsilon + \sin \delta_d \cos \epsilon)]$$

The above derivation assumes that the pole of the Sun is perpendicular to the ecliptic plane; however, in fact, the pole of the Sun is inclined approximately 7.2 deg from the perpendicular to the ecliptic, so that the heliographic latitude ϕ_s as defined will include an error Δ:

$$0 \text{ deg} \leq |\Delta| \lesssim 7.2 \text{ deg}$$

However, because of the already large spread in the observed doppler noise data, it was felt that this inaccuracy in the computation of heliographic latitude would not substantially degrade any correlation present, and hence (the inaccuracy) was not worth eliminating for the purposes of this study.

III. Correlation of Observed Doppler Noise With Heliographic Latitude

Observed doppler noise (pass average, good two-way, 60-second count doppler) from the 1976 solar conjunctions of Pioneer 10 and Pioneer 11 was compared to the ISED model, and the residuals, in "dB" ($\triangleq 10 \log_{10} N_A/N_P$) were plotted against the heliographic latitude, as seen in Fig. 3. A very strong correlation is immediately apparent. It was assumed that a multiplicative factor $f(\phi_s)$ could be constructed for ISED such that:

$$f(\phi_s) < 1, \qquad \phi_s > 0$$

$$f(0) = 1$$

The simplest expedient was to fit the (logarithmic) residuals as a linear function of heliographic latitude, or

$$f(\phi_s) = 10^{-A(\phi_s/90\ \text{deg})}$$

This function was appended to the ISED formulation and the standard deviation of the combined Pioneer 10 and Pioneer 11 residuals was minimized by choosing:

$$A = 0.9$$

or

$$f(\phi_s) = 10^{-0.9(\phi_s/90\ \text{deg})}$$

Since it has been assumed that doppler noise is proportional to (integrated) electron density, this relationship can be used to obtain a rough measure of the ratio of the (signal path integrated) polar coronal electron density to the (signal path integrated) equatorial coronal electron density, as follows:

$$\frac{\text{Polar density}}{\text{Equatorial density}} \approx 10^{-0.9} \approx \frac{1}{8}$$

IV. Comparison With Other Models of Latitudinal Variation in Electron Density

In Ref. 5, C. C. Counselman III indicates that good results were obtained with the term:

$$\cos^2 \phi_s$$

when modeling electron density as a function of heliographic latitude. In Ref. 6, K. Saito presented a complete expression for electron density as follows:

$$N_e(r, \phi_s) = \frac{3.09 \times 10^8}{r^{10}}(1 - 0.5 \sin \phi_s) + \frac{1.58 \times 10^8}{r^6}(1 - 0.95 \sin \phi_s) + \frac{0.0251 \times 10^8}{r^{2.5}}(1 - \sqrt{\sin \phi_s})$$

For this set of Pioneer 10 and Pioneer 11 data, only the lowest order term is significant, so that one is interested only in the term:

$$(1 - \sqrt{\sin \phi_s})$$

A comparison of the three functions is presented in Fig. 4, and Fig. 5 presents the ratios:

$$\frac{\cos^2 \phi_s}{10^{-0.9(\phi_s/90\ \text{deg}}} ; \frac{1 - \sqrt{\sin \phi_s}}{10^{-0.9(\phi_s/90\ \text{deg}}}$$

An examination of Figs. 4 and 5 reveals that the expression determined from the Pioneer 10 and Pioneer 11 data is a good compromise between the two referenced expressions up until about $\phi_s \approx 60$ deg, but from that point on, both of the referenced expressions fall off far more rapidly than the determined expression. It must be borne in mind, however, that both of the referenced expressions must be considered unrealistically low as ϕ_s approaches 90 deg, since they both are exactly zero when $\phi_s = 90$ deg.

V. The ISEDB Model

Two changes were made to the ISED model to obtain the "ISEDB" model; these are described in this section.

A. Incorporation of Functional Variation With Heliographic Latitude

The previous ISED model is multiplied by the expression determined in this report, or

$$\text{ISEDA} = [\text{ISED}]10^{-0.9(\phi_s/90\ \text{deg})}$$

B. Incorporation of Small, Non-Plasma-Related Noise Sources

Obviously, a conglomerate noise value due to non-plasma-related sources should be added (rms) to the ISED model to obtain more realistic results under low plasma conditions. The noise value adopted here for this purpose is 0.0015 Hz, so that

$$\text{ISEDB} = [(\text{ISEDA})^2 + (0.0015)^2]^{1/2}$$

or

$$\text{ISEDB} = \left[\left(\left\{A_0\left[\frac{\beta}{(\sin\alpha)^{1.3}}\right]F(\alpha,\beta) + A_1\left[\frac{1}{(\sin\alpha)^5}\right]\right\}10^{-A_8(\phi_s/90\ \text{deg})}\right)^2 + (0.0015)^2\right]^{1/2}$$

where

$$F(\alpha,\beta) = 1 - 0.05\left\{\frac{\left(\beta - \frac{\pi}{2} + \alpha\right)^3 - \left(\alpha - \frac{\pi}{2}\right)^3}{\beta}\right\} - 0.00275\left\{\frac{\left(\beta - \frac{\pi}{2} + \alpha\right)^5 - \left(\alpha - \frac{\pi}{2}\right)^5}{\beta}\right\}$$

and

$$A_0 = 9.65 \times 10^{-4}$$

$$A_1 = 5 \times 10^{-10}$$

$$A_8 = 9 \times 10^{-1}$$

The observed doppler noise accumulated during the Pioneer 10 and Pioneer 11 1976 solar conjunctions can be seen and compared to the ISED and ISEDB formulations in Figs. 6 and 7.

VI. Pioneer 11/Saturn Encounter Doppler Noise Prediction

To illustrate the effect of the correction for heliographic latitude, the ISED and ISEDB models have been computed for the Saturn encounter period, and are presented in Fig. 8. For instance, for the planned encounter day (DOY 244, 1979) and for the minimum SEP point (DOY 254, 1979), the reduction due to heliographic latitude is as follows:

DOY, 1979	ISED, Hz	ISEDB, Hz	Reduction, %
244	0.031	0.024	23
254	0.221	0.048	78

VII. Summary

The 1976 solar conjunctions of Pioneer 10 and particularly of Pioneer 11 allowed a large data base of observed doppler noise to be accumulated over a dynamic range of signal closest approach point heliographic latitudes. These data were processed with a previously developed doppler noise model (ISED), and the residuals are shown to correlate strongly with heliographic latitude. An expression for the heliographic latitude effect is constructed as follows:

$$10^{-0.9(\phi_s/90\ \text{deg})}$$

and this term is then (multiplicatively) applied to the ISED model to produce a new model — ISEDB. Finally, the substantial effect of the heliographic latitude effect is illustrated by comparing ISED to ISEDB during the Pioneer 11/Saturn encounter period.

References

1. Berman, A. L., and Wackley, J. A., "Doppler Noise Considered as a Function of the Signal Path Integration of Electron Density," in *The Deep Space Network Progress Report 42-33*, Jet Propulsion Laboratory, Pasadena, Calif., June 15, 1976.

2. Berman, A. L., "Analysis of Solar Effects Upon Observed Doppler Data Noise During the Helios 1 Second Solar Conjunction," in *The Deep Space Network Progress Report 42-32*, Jet Propulsion Laboratory, Pasadena, Calif., Apr. 15, 1976.

3. Berman, A. L., and Rockwell, S. T., "Correlation of Doppler Noise During Solar Conjunctions With Fluctuations in Solar Activity," in *The Deep Space Network Progress Report 42-30*, Jet Propulsion Laboratory, Pasadena, Calif., Dec. 15, 1975.

4. Berman, A. L., and Rockwell, S. T., "Analysis and Prediction of Doppler Noise During Solar Conjunctions," in *The Deep Space Network Progress Report 42-30*, Jet Propulsion Laboratory, Pasadena, Calif., Dec. 15, 1975.

5. Counselman, C. C., III, and Rankin, J. M., "Density of The Solar Corona From Occultations of NP0532," *Astrophys. J.*, Vol. 175, Aug. 1, 1972.

6. Saito, K., "A Non-Spherical Axisymmetric Model of The Solar K Corona of The Minimum Type," *Ann. Tokyo Astron. Observ.*, University of Tokyo, Second Series, Vol. XII, No. 2, Mitaka, Tokyo, 1970.

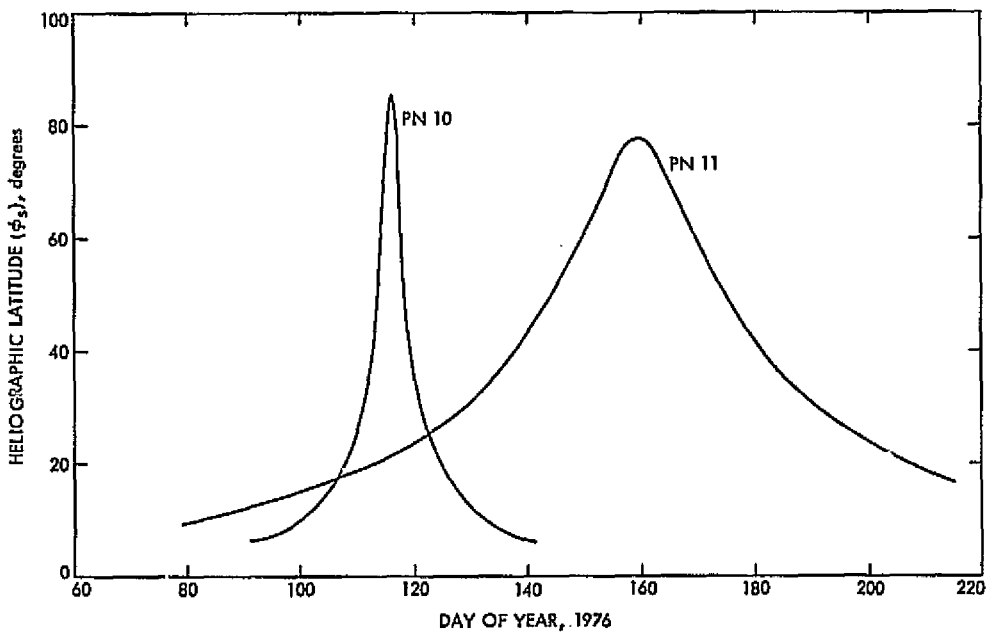

Fig. 1. Pioneer 10 and 11 signal closest approach point heliographic latitude

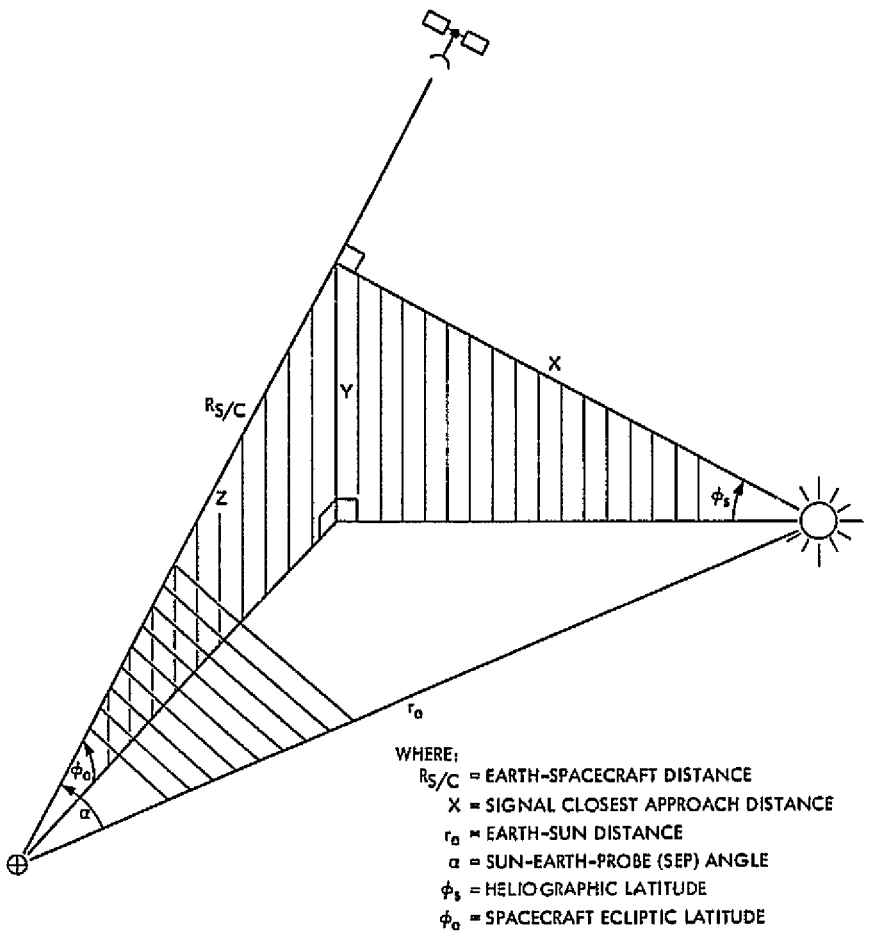

Fig. 2. Signal closest approach heliographic latitude

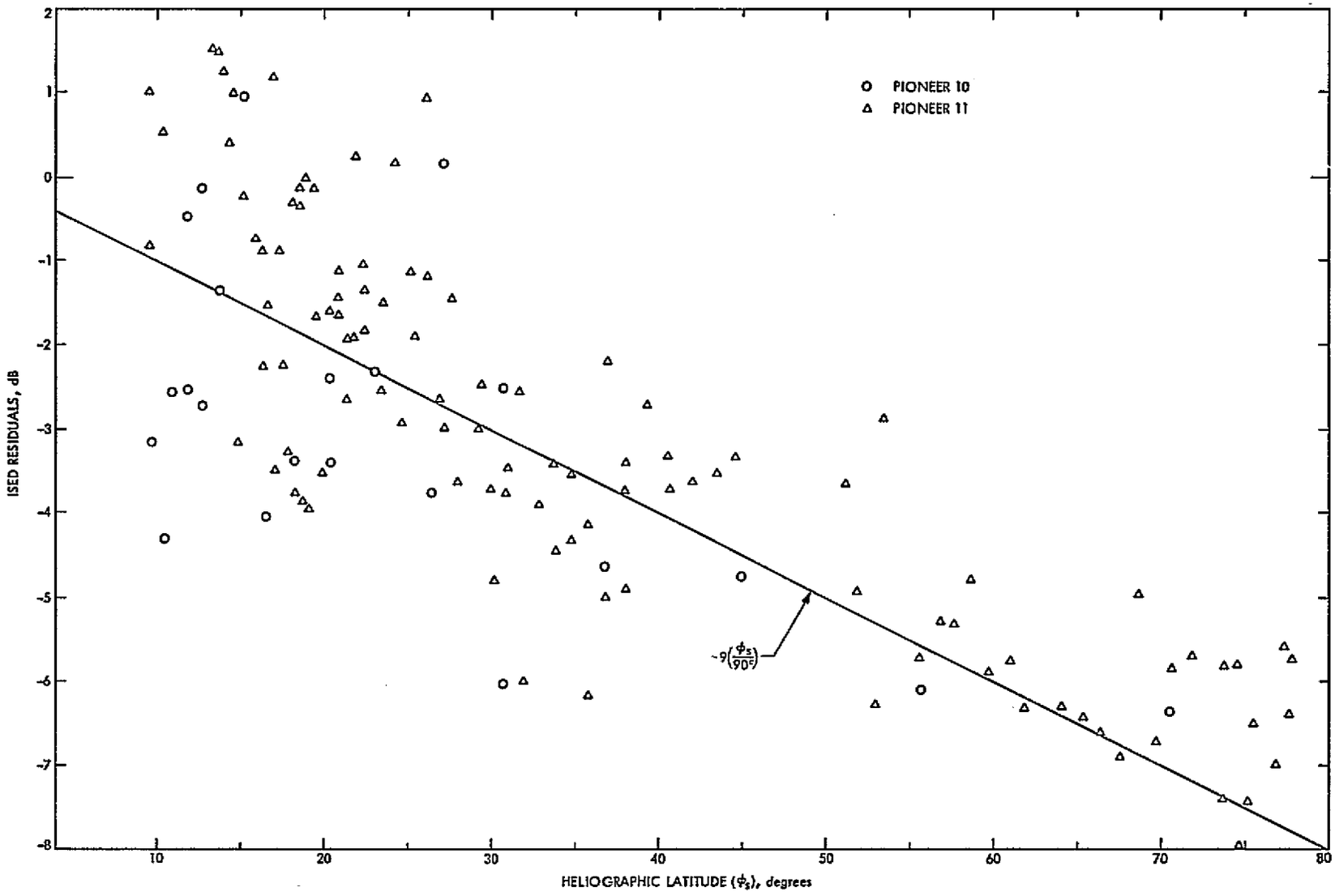

Fig. 3. Pioneer 10 and 11 ISED residuals vs heliographic latitude

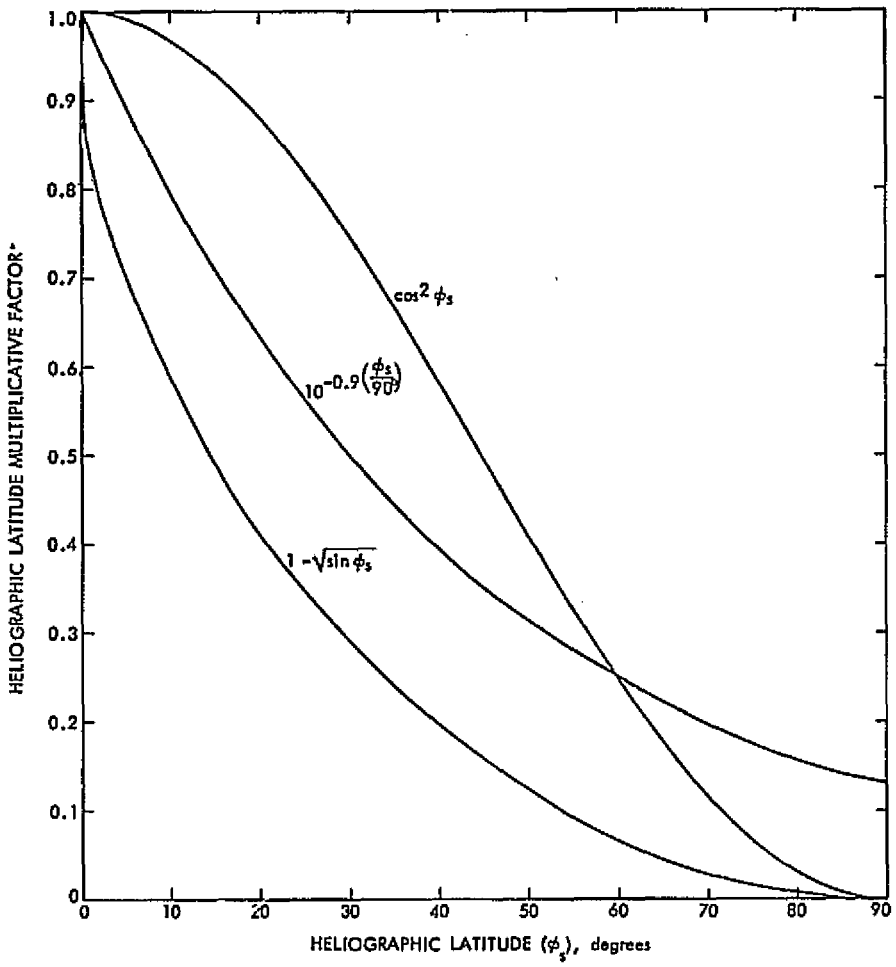

Fig. 4. Comparison of heliographic latitude factors

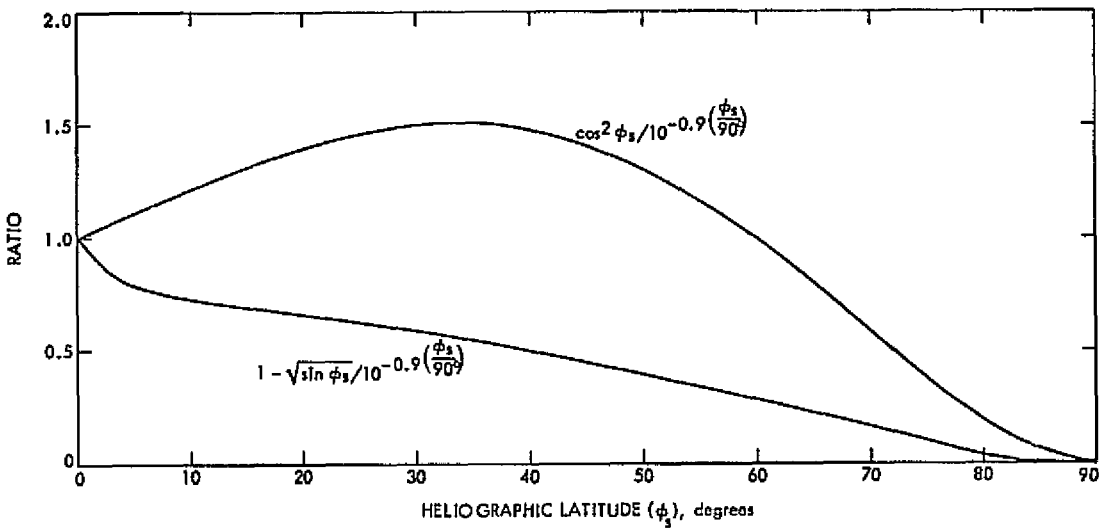

Fig. 5. Ratio comparison of heliographic latitude factors

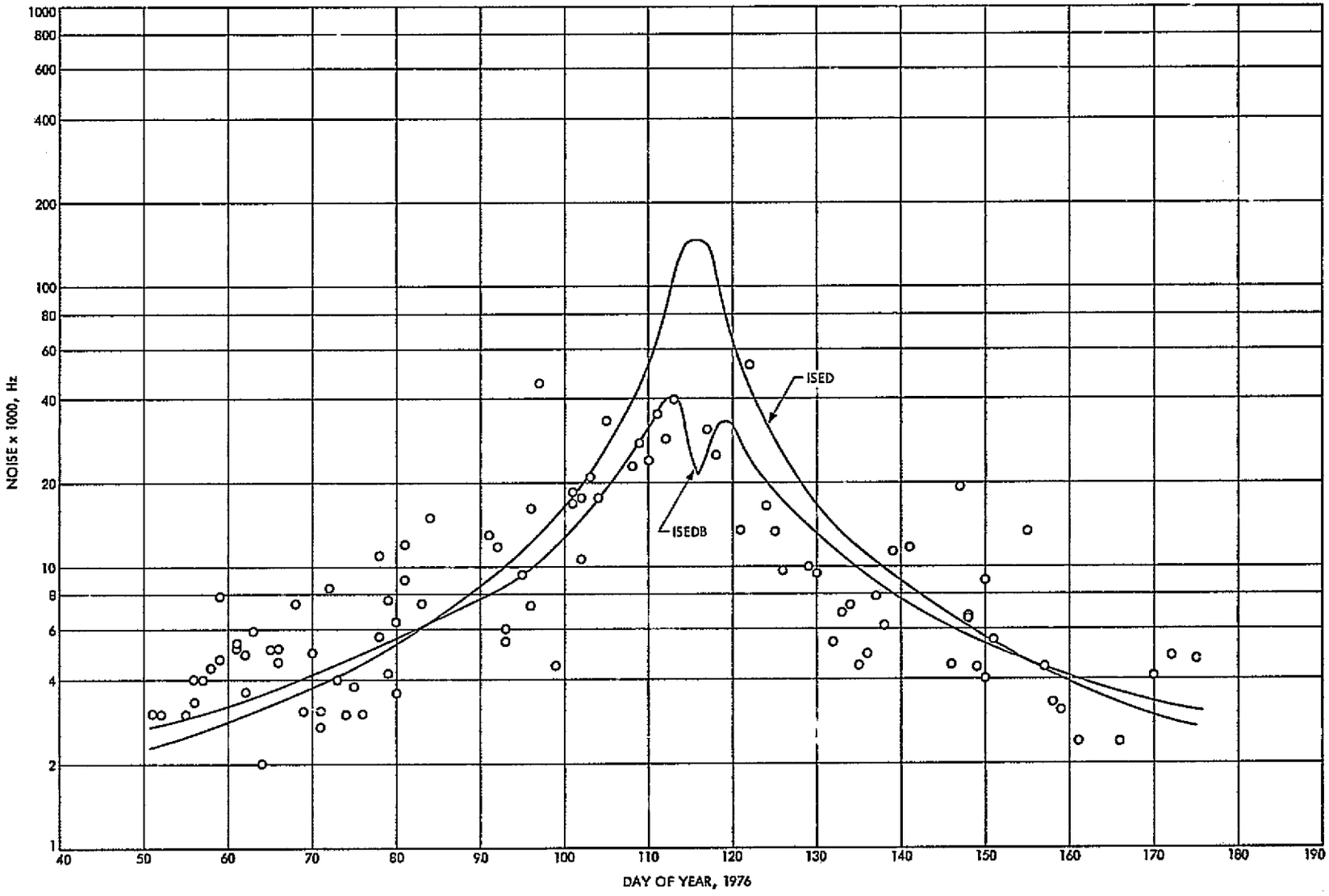

Fig. 6. Pioneer 10 actual noise vs day of year

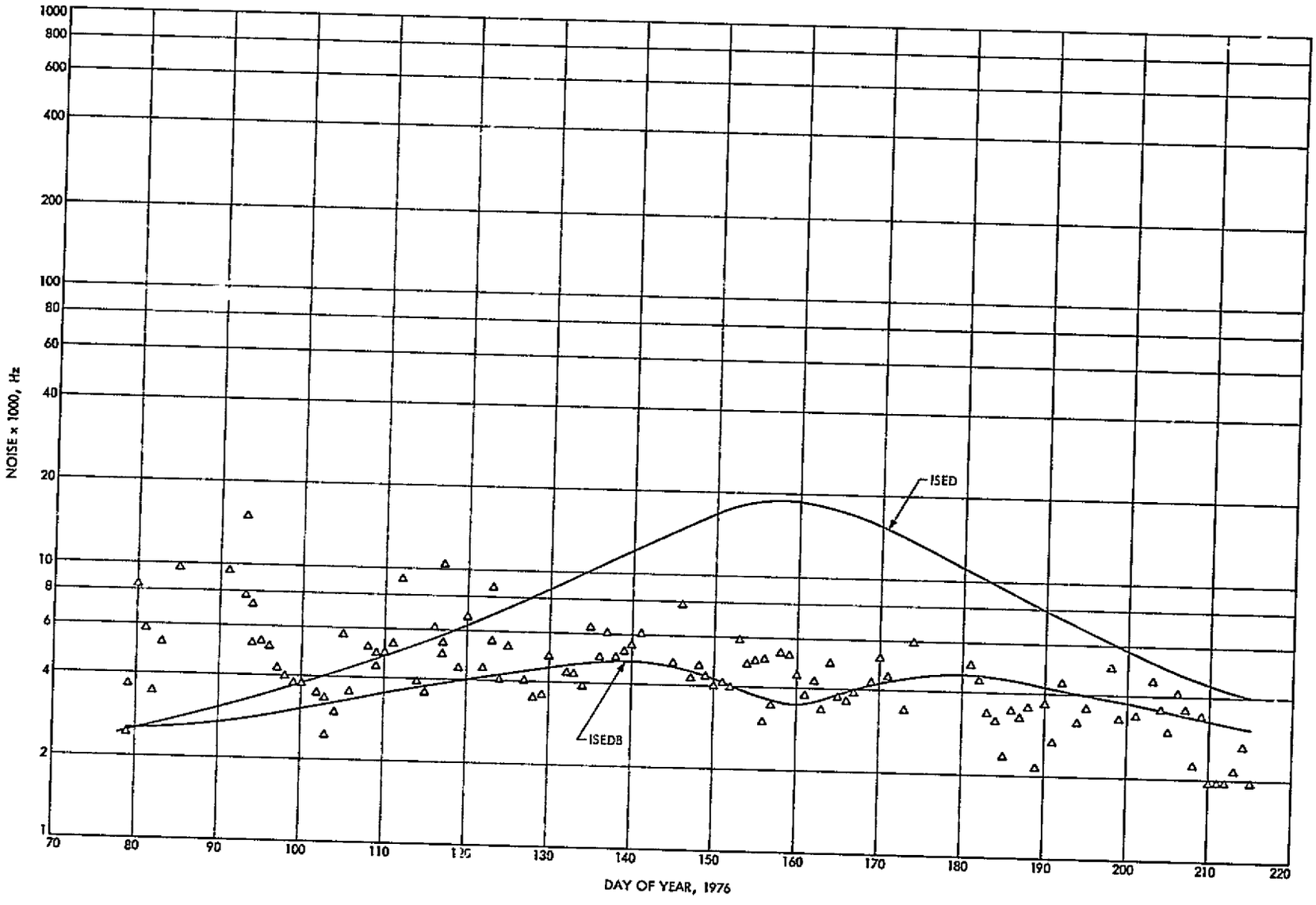

Fig .7. Pioneer 11 actual noise vs day of year

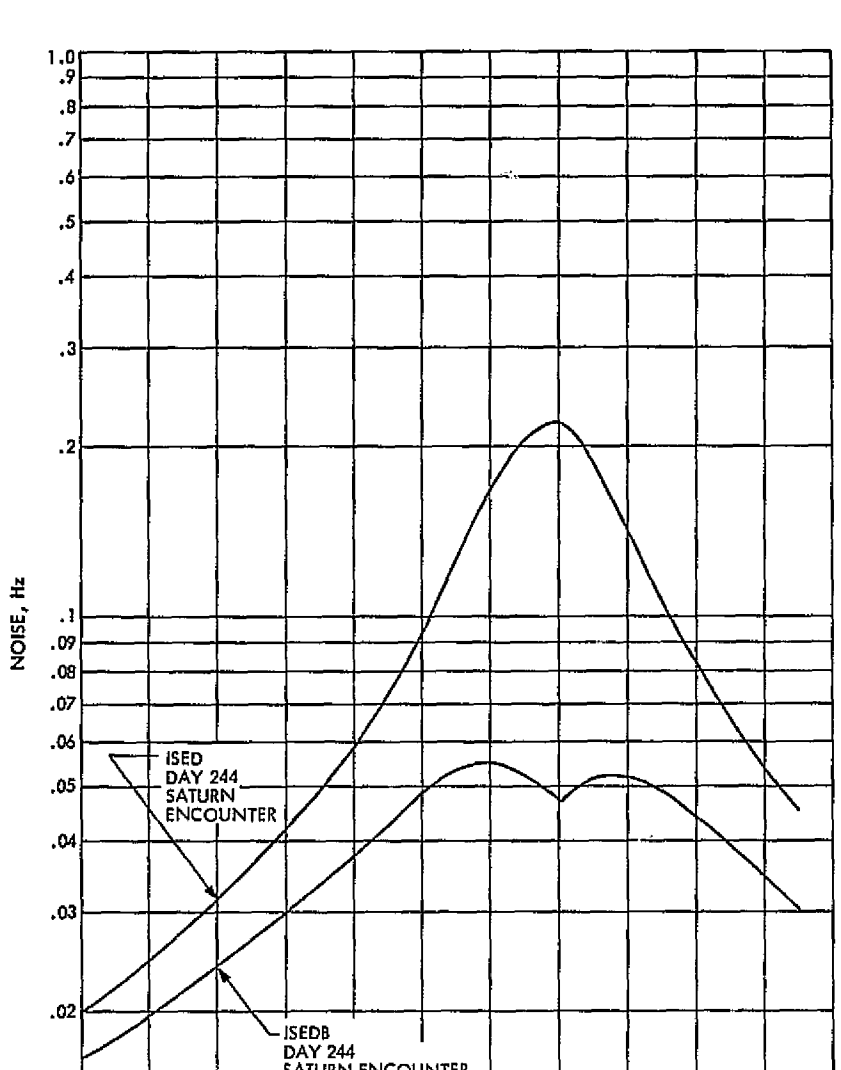

Fig. 8. Saturn encounter predicted doppler noise

Viking 1 Planetary Phase Tracking Operations: Mars Orbit Insertion Through Landing

A. L. Berman and J. A. Wackley
DSN Network Operations Section

This article describes tracking operations during the Viking 1 planetary phase. Particular attention is paid to special planning for critical phase tracking operations, and to the degree of success subsequently achieved by these special plans during the actual operations. In-depth coverage is provided for Mars orbit insertion (MOI), periapsis passage tracking, and Lander direct links. The article concludes that on balance, tracking operations during the Viking 1 planetary phase (to date) have been effectively implemented and quite successful.

I. Introduction

On June 19, 1976 at 22:20:35 GMT the Viking 1 spacecraft initiated a 38-min motor ignition that subtracted sufficient velocity from the spacecraft to place it in a highly elliptical orbit about the planet Mars. The Viking 1 spacecraft had been launched from the Air Force Eastern Test Range (AFETR) almost exactly 10 months earlier (Aug. 20, 1975, at 21:22:00.6 GMT), and the successful completion of the Mars orbit insertion (MOI) motor burn dramatically marked the ending of the long (relatively) dormant cruise phase and the beginning of the intensely active planetary phase.

The initial stage of the planetary phase consisted of a photographic exploration of the Martian surface by the Viking 1 Orbiter spacecraft (VO1) in an attempt to find a safe haven for the Viking 1 Lander spacecraft (VL1). The successful landing on the Martian surface of the Viking 1 Lander on July 20, 1976, at 12:12:07.1 GMT, marked the initiation of the second stage of the planetary phase—a detailed all-encompassing scientific exploration of the Martian surface and atmosphere.

The complete success of the Mars Orbit Insertion was an absolute requirement for realization of the central Viking mission objectives. The criticality and difficulty in establishing and maintaining the telecommunications links to the spacecraft by the Deep Space Network during the MOI phase were second only to the launch phase, and hence a very intensive effort was jointly mounted by the Viking Project and the DSN to devise various tracking strategies to optimize tracking operations and attain all mission goals during the critical MOI period.

This report will detail the preplanning for the MOI period, as well as for the subsequent orbital operations and the direct Lander links. The performance of the DSN during the critical planetary periods will then be analyzed; in particular, the report will focus on the success of the various tracking strategies devised for these periods.

II. MOI Overview

In order to properly align the Viking 1 spacecraft so that its 38-min MOI motor burn would place it into the correct Mars-centered orbit, the spacecraft was programmed to undergo a sequence of three turns: a roll turn, a yaw turn, and a second roll turn. The combination of the resulting geometric orientation (unfavorable cone and clock angles) and the use of the low-gain antenna was expected to cause the loss of both the uplink and downlink signals from shortly after the start of the yaw turn until the end of the second roll turn and return to the high-gain antenna. Following the burn, the spacecraft was to go through the same turns and undergo loss of signal in reverse order to restore it to its original orientation.

In view of the above, it was considered necessary to design uplink and downlink strategies which would:

(1) Give the best opportunity for a fast uplink reacquisition prior to the start of the MOI burn

(2) Allow quick acquisition of the downlink prior to the start of the burn

(3) Have the overall effect of allowing the burn to be observed in the two-way mode with undisturbed radio metric and telemetry data.

(4) Enable reacquisition of the uplink and downlink as soon as is practical foliowing the turn unwinds

During April 1976, a series of meetings was held between representatives of the Orbiter Performance Analysis Group (OPAG), Flight Path Analysis Group (FPAG), and the DSN to work out the specific details of the uplink frequency strategy. As a result of these meetings, the key features of the Viking 1 MOI were formulated as follows:

(1) The ground transmitter would be maintained (on) throughout the critical MOI period.

(2) Uplink ramping would be performed during the preburn period of low uplink signal level.

(3) An "insurance" sweep would be performed immediately after the uplink ramping (in item 2) to insure an uplink in the contingency of the uplink being lost during the ramping period.

(4) The reacquisition of the uplink during the post-burn period would be delayed (by approximately 10 min from the earliest opportunity) so that FPAG could clearly gauge in near-real-time the end of the MOI burn and the beginning of the post-burn roll turn in the doppler data (earlier uplink tuning would have disrupted the doppler (ground) reference frequency).

The downlink strategies for the MOI period were devised by the DSN Tracking Network Operations Analyst (Track NOA).

A detailed description of both uplink and downlink strategies is presented in Sections III and IV.

III. MOI Uplink Strategy

A. Preburn Uplink Strategy

The pre-MOI burn uplink strategy, in accordance with the Section II guidelines, was designed with the intent of acquiring the spacecraft receiver at the earliest possible time, perhaps before the switch back to the high-gain antenna with its subsequent return of the downlink signal.

During the course of the yaw and roll turns, the uplink signal strength was expected to gradually decrease and a series of antenna nulls would then be encountered. Near the end of the roll turn the signal strength would begin to gradually increase. To take advantage of this situation, Deep Space Station (DSS) 14 at Goldstone DSCC would ramp the uplink frequency in a linear approximation of the change of XA (spacecraft receiver best lock with doppler accounted for), starting at the beginning (ground transmit time) of the yaw turn. By doing this, the spacecraft receiver would receive a constant frequency and could be expected to be reacquired whenever the signal rose above its threshold. To insure reacquisition, an "insurance" sweep covering approximately 50 Hz (at voltage controlled oscillator (VCO) level) around XA was designed to be executed coincident with the switch to the high gain antenna. The result of either (or both) of these sweeps would be the reacquisition of an uplink and good two-way data approximately five minutes before the start of the burn.

Figure 1 illustrates this tuning strategy as compared to the significant spacecraft events.

The detailed tuning instructions for DSS 14, based on a nominal burn start time of 22:03:08 GMT, (DSS transmit time), were as follows (with frequencies at digital controlled oscillator (DCO) level):

Start tuning	21:27:00	GMT
Tuning rate	+0.0275	Hz/s (DCO)
Start frequency	43993800	Hz (DCO)
Start insurance sweep	21:57:00	GMT
End insurance sweep	21:59:25	GMT
Sweep lower limit	43993750	Hz (DCO)
Sweep upper limit	43993940	Hz (DCO)
Tuning rates	+2.0000	Hz/s (DCO)
	−1.9900	Hz/s (DCO)

B. Post-Burn Uplink Strategy

Approximately 4 min after the end of the MOI burn the turn unwinds (the mirror image of the turns) were to commence, with their associated losses in uplink and downlink. It would not be possible to ramp the uplink in a manner similar to the pre-MOI burn strategy as these ramps would have to occur during the observation of the burn itself, thus perturbing the radio metric data. The Flight Path Analysis Group (FPAG), in order to accurately assess the burn in near real-time, required that the two-way radio metric data have an unperturbed reference frequency. Additionally, FPAG desired to observe the start of the first roll unwind. Thus, the post-MOI uplink reacquisition was to be delayed until one minute after observing the start of the roll unwind, thereby simplifying the acquisition procedure.

The post-MOI burn uplink strategy, as designed to accommodate the above constraints, consisted of a single sweep from the pre-burn Track Synthesizer Frequency (TSF2) to a new tracking synthesizer frequency (TSF3) at a rate of 1 Hz/s (DCO). This sweep would effectively encompass the XA frequency plus 100 Hz and minus 50 Hz (VCO), accommodating any trajectory uncertainties as a result of the burn. Start time of the sweep was to be one minute after the start of the roll turn unwind in Earth return time (ERT), and coincident with the loss of downlink due to turn.

The post-burn uplink tuning instructions for DSS 14 were as follows:

Start tuning	23:22:00 GMT
Start frequency (TSF2)	43993940 Hz (DCO)
Tuning rate	−1.0000 Hz/s (DCO)
End frequency (TSF3)	43993640 Hz (DCO)
Sweep duration	5 min

The above described tuning can be seen in Fig. 1.

IV. MOI Downlink Strategy

A. Preburn downlink strategy

As described earlier, because of unfavorable antenna orientation, the downlink signal level was expected to gradually degrade to approximately −186 dBm during the yaw turn and further decrease during the second roll turn. It would be necessary then to quickly acquire the signal after the end of the roll turn in order to have solid telemetry lock throughout the ground data system before the start of the burn.

To accomplish this, the station was to sweep the prime receiver (Receiver 3, Block IV) at a high rate (2000 Hz/s S-band) using the acquisition (ACQ) mode with the acquisition-trigger-at-zero-beat (ATZ) signal enabled. The sweeping was to start five minutes before the end of the roll turn in order to ensure receiver lock as early as possible. In order to accommodate any trajectory uncertainties and the contingency of a missed uplink acquisition, the receiver sweep would be wide enough (frequencies corresponding to two-way doppler (D2) ±12 kHz) to detect both the one- and two-way signals. Additionally, since there would be the possibility (however remote) that glitches between the one- and two-way mode would be seen on the ground before the end of the roll turn, the receiver operator was to be prepared to restart the ACQ mode receiver sweeps if the signal was lost.

The actual tuning instructions given to DSS 14 for this downlink acquisition were as follows:

Sweep start	22:25:00 GMT
Sweep upper limit	44678710 Hz (DCO)
Sweep lower limit	44677510 Hz (DCO)
Sweep rate	100.0 Hz/s (DCO)

B. Postburn Downlink Strategy

Since the uplink acquisition sweep was required to be delayed (as described in Sec. III, Paragraph B.), there would be a period of one-way tracking following the end of the yaw turn unwind. It would be necessary then to sweep the receiver through a range of one-way frequencies large enough to account for the high doppler rates due to periapsis passage, trajectory uncertainties introduced by the insertion burn, and auxiliary oscillator frequency uncertainties.

During the yaw unwind following the burn, the downlink signal level was expected to gradually increase from threshold (−175 dBm in 10 Hz RF filter) to approximately −162 dBm. The strategy to secure a reasonably fast downlink acquisition under these difficult conditions was composed of two elements as follows:

(1) The receiver to be set at the predicted D1 when the signal level reaches −170 dBm, in the hope of allowing the signal to "walk through" the receiver.

(2) If this fails, the receiver to be swept in the ACQ mode at a time when the signal level reaches −167 dBm, and at a sweep rate calculated for a signal level of −165 dBm. Specifically, the receiver was to be swept through frequencies equivalent to D1 ± 500 Hz (S-band) and at a rate of 100 Hz/s (S-band) while in ACQ mode with ATZ enabled, and in a radio frequency (RF) bandwidth of 10 Hz.

The specific receiver instructions given to DSS 14 are as follows:

Receiver set to	44678151.5 Hz
Start sweep	23:44:10 GMT
Upper limit	44678195 Hz (DCO)
Lower limit	44678145 Hz (DCO)
Rate	5.0 Hz/s (DCO)

The change from one-way to two-way mode was expected to occur approximately 15 min after the end of the yaw turn (ERT).

The instructions given to DSS 14 for this two-way reacquisition were as follows:

Frequency upper limit	44678335 Hz (DCO)
Frequency lower limit	44678135 Hz (DCO)
Sweep rate	25.0 Hz/s (DCO)

C. "Fast" X-Band Acquisition

A concern of the OPAG during the MOI sequence was the possible loss of Canopus lock. One of the contingencies advanced in response to this concern was the use of X-band to determine the spacecraft orientation. Basically, this entailed having the DSS able to acquire an X-band downlink within a few seconds after its appearance, and, at a time when the signal level would be in the area of only −155 to −160 dBm. To meet this objective, the Track NOA proposed the following acquisition sequence, to be tried at the end of roll unwind 2, following the MOI burn:

(1) Block IV X-band receiver to be used in ACQ MODE, ATZ enabled, and with an RF bandwidth of 10 Hz

(2) Sweep to start 5 min before end of roll turn

(3) Sweep to be D2 ± 850 Hz (X-band)

(4) Sweep rate to be 850 Hz/s (X-band)

(5) Data rate to be 1/s from sweep start to end of roll turn plus 5 min.

If successful, this procedure would be expected to lock the X-band signal some 6 or 8 s prior to the end of the roll turn.

V. MOI Burn Profile

The actual MOI burn parameters are as follows:

Burn start	22:38:03 GMT (ERT)
Burn stop	23:15:52 GMT (ERT)
Magnitude (ΔV)	405 m/s (radial component)

A profile of the two-way doppler rate of change (DD2) during the burn is seen in Fig. 2. Additionally, Figs. 1 and 3 illustrate the effect of the burn and subsequent periapsis passage on the XA frequency (in DSS transmit time) and the two-way doppler (ERT). Figure 4 provides an overall time line for the significant MOI events.

VI. Periapsis Receiver Ramping

A. Introduction

During the Viking 1 orbital phase, X-band radiometric data are being used as an important data type in several radio science experiments including studies of the Martian gravity field, atmosphere and ephemerides as well as

relativity and solar corona experiments. It was and continues to be important, therefore, to maximize the quality of the radio metric data especially at periapsis.

To assure good data, it is necessary to ramp the X-band receivers. Ramps were designed, therefore, with an emphasis on:

(1) Minimizing receiver phase error, with the intention of keeping phase error less than 10 deg

(2) Minimizing the number of cycle slips (<19 in a 12-h period)

(3) Keeping the receivers in lock during the periods of high frequency rates and

(4) Operational simplicity

By executing the designed ramps, it was hoped that good quality X-band radio metric data through the periapsis period could be attained.

B. Receiver Ramp Design

During the period near periapsis the nominal X-band two-way doppler frequency rates extended from a maximum positive excursion of ~40 Hz/s (X-band) to a maximum negative excursion of ~ −40 Hz/s (X-band). This region of high rates lasted approximately four hours starting at 2 h before periapsis.

A sequence of receiver ramps, spanning this time period, was designed that would allow good X-band radio metric data to be acquired. Generally, each ramp was to start and stop when the doppler rate was one-third of its maximum positive or negative excursion. The ramp rate was to be equal to two-thirds of the receiver frequency change rate. Starting frequency for the ramps was to be the frequency at the start time of the first periapsis ramp. By choosing the ramps in this manner, there would be three ramps, the optimum number since this would require no reprogramming of the rate and frequency registers of the programmable oscillator control assembly. For rates above 40 Hz/s (X-band), additional ramps would have to be added. These ramps would be chosen in a manner similar to that of the initial three ramps.

A typical X-band receiver ramp sequence (with ramp frequency inverted for better comparison to D2 frequency) is shown in Fig. 5. The receiver frequencies for this periapsis are shown in Fig. 6.

Parameters for this sequence are:

Start ramping	06:55:00 GMT
Frequency	41368020 Hz (DCO)
Ramp rate 1	−0.3035 Hz/s (DCO)
Start ramp 2	08:06:00 GMT
Ramp rate 2	0.0000 Hz/s (DCO)
Start ramp 3	08:14:00 GMT
Ramp rate 3	0.2173 Hz/s (DCO)
End ramping	09:32:00 GMT
Ramp duration	157 min

C. Phase Error Analysis

Of prime consideration in designing the ramping strategy is the need to minimize phase error, consistent with the minimization of operational difficulty. Figure 5 illustrates the dynamic phase error of a typical ramping sequence. As can be seen, the dynamic phase error generally lies within the 10 deg desired limit. Figure 6 shows the static phase error for the same sequence. It can be seen here that the SPE remains well under the 10 deg desired maximum.

The total phase error is shown in Fig. 7. Here, it can be seen that the dynamic and static phase errors interact in such a way as to generally keep the total phase error below the 10 deg desired maximum. This limit is exceeded slightly for approximately 15 minutes during the period of highest (positive) two-way doppler rates.

Finally, all phase error was computed for a bandwidth of 10 Hz, and a receiver margin of 15 dB. By increasing this bandwidth, it would be possible to further reduce total phase error.

VII. Lander Tracking Operations

A. Introduction

On July 20, 1976, approximately sixteen hours after the first Viking Lander was to touch down on the surface of Mars, DSS 43, Australia, was to commence the initial direct link with the lander. This acquisition, as

well as subsequent acquisitions would have the following characteristics:

(1) The uplink acquisition would be made in the "blind," that is, with no downlink signal from the lander.

(2) Two receivers, each connected to a different antenna and with a 15- to 20-dB difference in signal level, were to be acquired.

(3) There would be, initially at least, large frequency and temperature uncertainties.

(4) The total acquisition time would be limited.

In order to accommodate these characteristics, very conservative uplink and downlink acquisition strategies were devised. These strategies were also to be used on all subsequent lander direct links including those of the second Viking Lander. A typical timeline for the lander direct link is seen in Fig. 8.

B. Uplink Acquisition

Frequency estimates specifying the uplink tuning pattern were provided to the DSN by the Lander Performance Analysis Group (LPAG). The choice of frequencies to be swept became quite complicated when one considered that the lander radio frequency subsystem (RFS) would be undergoing temperature (hence, frequency) changes due to:

(1) The Martian atmospheric effects, such as wind and diurnal temperature cycles.

(2) The turning on and off of the traveling wave tube amplifier (TWTA).

Using models of these effects, LPAG would determine an estimate of RFS temperatures and frequencies. The large temperature uncertainties combined with rather large frequency uncertainties for Lander 1:

$$3\sigma \text{ XA receiver 1} \sim 123 \text{ Hz (VCO)}$$

$$3\sigma \text{ XA receiver 2} \sim 116 \text{ Hz (VCO)}$$

resulted in the need for a very large uplink sweep range. The nominal lander uplink acquisition sweep (until in situ measurements of the temperature and frequency measurements allowed for change) was to have a range of channel 13 center frequency (22,010,119 Hz) plus and minus 470 Hz.

The starting frequency of the sweep would be chosen such that the start frequency and channel center frequency were in the same direction away from the receiver best lock frequency (XMTREF). Thus, for example, the initial acquisition sweep was to start 470 Hz above the channel 13 center frequency (or 22,010,589 Hz), since the XMTREF was approximately 16 Hz below the center frequency. Upon completion of the sweep, the station was to tune to a tracking synthesizer frequency (TSF) chosen to minimize the SPE of the primary command receiver (Receiver 1) during the remainder of the direct communication system (DCS) link.

Information supplied by LPAG indicated a frequency tuning rate region (at S-band) of:

$$44 \text{ Hz/s} < \text{frequency rate} < 219 \text{ Hz/s}$$

The choice of a sweep rate was influenced by:

(1) The desire to allow no more than 20 deg phase error due to both dynamic and static effects

(2) The need to complete a large sweep in a limited period of time

(3) The need to acquire receiver 1 through the low-gain antenna

Thus, the sweep rate (conservatively) chosen was 44 Hz/s or approximately 0.45 Hz/s (VCO).

Finally, the transmitter on-time was to be chosen to accommodate an expected 25 deg elevation landmask for the lander and the time necessary to slew the high gain antenna (HGA; a 0.76-m-diam, az/el drive antenna) from its stowed position to its tracking position. Combining all of the above mentioned parameters, the uplink acquisition procedure was planned to be as follows:

(1) Transmitter on at the HGA at "track" position time minus a one-way light time and at a power level of 20 kW.

(2) Tuning rate to be 0.45 Hz/s (VCO).

(3) The sweep to cover, at most, Channel 13 center frequency ± 470 Hz.

(4) The duration of the sweep to be approximately 51 minutes.

The uplink sweep pattern in terms of spacecraft received frequencies is shown in Fig. 9.

C. Downlink Acquisition

Due to temperature and power constraints the Viking Lander S-band transmitter was to be turned on for at most 92 min (for long DCS links) starting approximately 70 min after the completion of the uplink acquisition sweep. It would therefore be necessary to sweep the receivers in such a manner as to quickly acquire the two-way downlink and to allow for the acquisition of a one-way downlink as a contingency.

The following information concerning the one-way and two-way downlink frequency was available:

(1) The frequency uncertainties for the lander auxiliary oscillator frequencies were quite large:

3σ AUX OSC 1 frequency $\sim$ 8200 Hz

3σ AUX OSC 2 frequency $\sim$ 2200 Hz

(2) The two-way doppler frequencies were expected to be highly accurate.

(3) The difference between one- and two-way doppler was to be approximately 12,000 Hz with one-way doppler (D1) at the higher frequency, i.e.,

$$-\text{TFREQ} + 96\,\frac{240}{221}\,\text{XMTREF} \cong 12\ \text{kHz}$$

This information, as well as the fact that the station configuration (configuration code 61) called for a Block IV receiver as prime with a Block III receiver as backup led to the choice of an easily workable, albeit unique receiver sweep strategy that had a high probability of acquiring either the one- or two-way downlink.

Basically, the Block IV receiver would be swept at a very high rate (2000 Hz/s, (S-band) through the range of doppler frequencies defined by

$$(\text{D1} - X) \pm (12000 + X)\ \text{Hz}$$

where X would, in general, equal $\sim$ 2 kHz.

Thus, the sweep was to encompass both the one- and two-way downlink frequencies. The sweep was to be executed with the receiver programmed oscillator control assembly in ACQ mode with the ATZ signal enabled. This would automatically terminate the sweep upon detection of the downlink signal. Additionally, the sweep was to start approximately 5 min before the time that the downlink signal was expected to be seen. Using this high sweep rate, the entire range of frequencies would be swept approximately every 12 s.

The downlink acquisition procedure planned was therefore:

(1) The receiver DCO programmed to be swept at 2000 Hz/s (S-band) or 100 Hz/s (DCO) through receiver frequencies corresponding to the range:

$\text{D1} - 16\ \text{kHz} \leq \text{frequency} \leq \text{D1} + 12\ \text{kHz}$ (where $\text{D1} > \text{D2}$)

(2) At expected downlink minus 5 min flag doppler as two-way data and start receiver using ACQ mode with ATZ.

D. Lander Tracking Predictions

Since the ephemeris of Mars is fairly well known, predicts were expected to be highly accurate, with the exception of the observables D1 and XA. These frequencies, as mentioned earlier, would have quite large uncertainties. Thus, to accommodate these uncertainties, predicts were to be generated twice a week during the early tracking period. As more experience was gained, the predicts would be generated on a weekly schedule.

E. Ranging

Approximately 2 h after the start of the short downlink lander pass and after the period of real-time imaging, a short period ($\sim$10 min) of time was to be allocated for ranging to the lander.

The ranging accuracy requirements supplied by LPAG were quite liberal, calling for 15 m acceptable one-way 1σ range jitter and 15 components to resolve range ambiguity; these under conditions of -2 dB carrier suppression and an expected ranging power to noise ratio of 1.75 dB. Additionally, since a precise lander location needed to be determined quickly, pipelining of the range code to acquire multiple range points was considered. Pipelining is a previously unused option of the planetary ranging assembly (PRA) which simply allows sequential retransmission of the ranging code, thus making possible many repeated acquisitions within a limited time. With the additional help of an option to transmit immediately, it was felt that three range points of good accuracy could be acquired in less than 10 min.

The ranging parameters chosen under the guidelines of project requirements were: T1, 38 s; T2, 9 s; and 15 components, for a total integration time of 2 min, 44 s. An additional 20 s would also be added before the start of transmission to allow the lander ranging subsystem to settle into normal operating condition.

VIII. Viking 1 Planetary Phase Operations Analysis

A. MOI Uplink Acquisition Performance

1. Preburn period. As mentioned in Sec. III, Paragraph A., it was expected that the uplink would be lost during the yaw and roll 2 turns; in anticipation of this circumstance the uplink was ramped to closely match XA and an "insurance" sweep was performed immediately after the end of the roll 2 turn. Subsequent to the event, Viking Project (OPAG) analysis showed the uplink was maintained throughout the ramping period, attesting to the efficacy of the ramping procedure and thus additionally having rendered the insurance sweep unnecessary.

2. Postburn period. The postburn uplink acquisition subsequent to the conclusion of the yaw unwind turn (described in Section III, Paragraph B.) was successful, and the uplink was maintained routinely from this period forward.

In summation, MOI uplink acquisitions were exactly according to plan and completely successful.

B. MOI Downlink Acquisition Performance

1. Preburn acquisition. According to plan, the Block IV S-band Receiver (No. 3) was placed in the ACQ mode (ATZ enabled) 5 min prior to expected signal reappearance after roll 2 turn (at approximately 22:32:00 GMT). The Receiver 3 sweep pattern and acquisition is seen in Fig. 10. The expected time of signal reappearance was 22:31:52 GMT, and Receiver 3 locked the downlink at 22:32:00 GMT, which can be seen in Fig. 10 to be the first zero crossing after signal emergence. The Block III S-band receiver lock time was 22:31:58 GMT.

2. Postburn one-way downlink acquisition. As described in Section IV., Paragraph B., the first phase in the attempt to acquire the one-way downlink shortly after its emergence at threshold was to allow the doppler to "walk through" the receiver (which was set at a constant frequency). This plan was unsuccessful, and the receiver "tuning" (i.e., referenced to the predicted doppler value) can be seen in Fig. 11. The signal passed through the receiver at 23:42:26 GMT, and at a signal level of approximately −168 dBm. One can see in Fig. 11 that at the expected acquisition time, three receiver frequency "spikes" occurred, which might easily explain the aborted acquisition. Upon careful examination, almost all of the spikes seen in Fig. 11 have a value very close to: ±n {20}, S-band Hz (n = small integer). 20 Hz S-band is exactly equal to 1 Hz DCO, so it would appear quite possible that the misacquisition was ultimately due to an erratic synthesizer.

The second phase in the acquisition plan was to place the Block IV Receiver (3) in the ACQ mode at 23:44:10. Goldstone DSS 14 elected (at their option) not to use the ACQ mode, but instead to try and lock the Block IV Receiver using the lockup frequency from the Block III S-band receiver. Block IV receiver lock to the downlink was not achieved until 23:46:41 GMT, and (with hindsight!) the ACQ mode plan for 23:44:10 might have achieved a quicker acquisition. The Block III S-band receiver lock-up time was 23:43:40 GMT.

3. Postburn two-way downlink acquisition. At 00:00:22 GMT, the ground receivers were thrown out of lock by the one-way/two-way downlink transition. The Block IV S-band Receiver (3) was put in the ACQ mode according to plan (and as described in Section IV., Paragraph B.) and acquired the downlink very rapidly – at 00:03:12 GMT, well ahead of the Block III acquisition at 00:04:42 GMT.

C. Fast X-Band Acquisition

As previously mentioned (Sec. IV., Paragraph C.), the DSN would attempt to lock the X-band signal within seconds after its reappearance at the conclusion of roll 2 unwind. The Orbiter Performance Analysis Group predicted a roll 2 unwind time of 00:23:03 GMT, June 20, with the X-band signal crossing (above) threshold some 10 to 20 s prior to that time. The instructions given to DSS 14 were as follows:

Start sweep time	00:18:00 GMT
Frequency upper limit	41368122 Hz (DCO)
Frequency lower limit	41368102 Hz (DCO)
Sweep rate	10.0 Hz/s (DCO)

The Viking 1 Fast X-band acquisition results are seen in Fig. 12. Acquisition of the X-band signal occurred at 00:22:52 GMT, a full 11 s before the end of roll 2 unwind.

Since the OPAG criterion for a successful fast acquisition was an acquisition at least several seconds before the end of the (roll 2) turn, the procedure as demonstrated here must be adjudged a complete success.

In summation, except for the (relatively insignificant) failure to lock at a very low signal level during the one-way signal reappearance post MOI burn, all Block IV receiver acquisitions were extremely rapid and successful. The failure to lock during the one-way signal reemergence is attributed to an erratic synthesizer.

D. Periapsis Receiver Ramping

The periapsis receiver ramping strategy described in Sec. VI was predicated on usage of the high-gain antenna (HGA) during the periapsis pass. However, because of photographic requirements, many of the periapsis passes utilized the low-gain antenna (LGA), and in fact, the LGA orientation on some passes caused the signal to degrade from a nominal −161 dBm to threshold (−175 dBm) or below. During the LGA periapsis passes, it was found that the receiver ramping scheme (appropriately translated from X-band to S-band levels) was very helpful in just keeping the S-band Block IV receiver in lock! The receiver ramping strategy was thus amended to:

HGA passes: Ramp Block IV X-band receiver

LGA passes: Ramp Block IV S-band receiver

The effectiveness of the S-band receiver ramping has been attested to by the DSS receiver operators, while Viking Radio Science has to date been satisfied with the X-band receiver ramping operations.

E. Lander Operations

1. Uplink acquisition. At 05:10:00 GMT on July 21, DSS 43 turned on its transmitter and began the initial uplink acquisition with the Viking Lander precisely as described in Section VII., Paragraph B. This strategy translated to frequencies for July 21, had the following parameters:

Transmitter on	05:10:00 GMT
Start tuning	05:10:40 GMT
Starting frequency	22011247 Hz (VCO)
Tuning rate	−0.45 Hz/s (VCO)
Tune to	22010302 Hz (VCO)
Start tuning to TSF	05:45:40 GMT
TSF	22010770 Hz (VCO)
Tuning rate	+0.45 Hz/s (VCO)
Stop tuning	06:03:00 GMT
Sweep duration	52 min 20 s

The acquisition sweep was executed with precision and without complication. However, following the acquisition of the Lander downlink signal approximately one hour after the end of the sweep, it was found that Receiver 1, the primary (and emergency) command receiver connected to the low-gain antenna, had not been acquired during the sweep. In fact, this receiver was actually observed to "lock up" in telemetry received several minutes after the downlink was acquired. This anomalous behavior became the subject of much study by the Lander Performance Analysis Group, including lengthy (up to eight hours in one case) sweeps attempted in order to acquire the receiver and has not, as of this writing, been fully explained.

2. Downlink acquisition. At 07:10:00 GMT, following the guidelines of the downlink acquisition strategy, Australia DSS 43 began sweeping its receivers to find the Viking Lander signal. The planned acquisition sweep had the following parameters:

Start acquisition sweep		07:10:00 GMT
Expected downlink		07:12:47 GMT
Sweep upper limit		44753046.55 Hz (DCO)
	or	D1 − 12000 Hz (S-band)
Sweep lower limit		44751846.55 Hz (DCO)
	or	D1 + 12000 Hz (S-band)
D1 − D2		~7000 Hz (S-band)
Sweep rate		2000 Hz/s (S-band)

As can be seen, the sweep encompassed both the one- and two-way downlink frequencies as well as reasonable uncertainties in these frequencies. Approximately two minutes later than expected, 07:14:31 GMT, the two-way downlink was acquired. This acquisition confirmed the efficacy of the uplink acquisition procedures but brought up a question concerning the downlink acquisition procedures: Was the sweep rate too fast for this signal level (−148 dBm)? A similar difference between expected and actual acquisition of signal (AOS) times occurred on the

next Lander direct link as well. After consultations with the Lander Performance Analysis Group it was learned that the expected AOS time was actually the time that the traveling wave tube amplifier was turned on and a radio frequency downlink would not be observed until approximately 90 s later. Thus, the downlink was actually acquired the first time that the receiver swept through the downlink signal.

3. Ranging. Ranging modulation was turned on at DSS 43 at 07:20:20 GMT and the transmission of the ranging code began 20 s later, according to the procedures described earlier. Integration of the third range point was completed at approximately 08:08:13 GMT; the range channel was observed to be shut off at 08:08:25 GMT. Pseudo-DRVID, a comparison of differenced range points with integrated doppler to provide validation of the range points, was computed with the following results:

Acquisitions	Pseudo-DRVID (RU)
1/2	4.6
1/3	16.5
2/3	11.9

Thus, three good range points were indeed acquired in the allotted ranging time and with 13 s to spare!

IX. Prediction Accuracy

The predictions used for the MOI period were generated from a polynomial coefficient tape (PCT) delivered by the FPAG approximately 24 h prior to MOI. The accuracy of these predictions (identified as set VA 58) can easily be gauged by an examination of the Network Operations Control Center (NOCC) pseudo-residual program output. Doppler pseudo-residual data (defined as actual data − predicted data) for selected times throughout the DSS 14 MOI pass are presented in Table 1.

The prediction accuracy as seen in the pseudo-residual output is quite good, particularly when considering that the accuracy (after the burn) is dependent upon both inherent trajectory uncertainties and the accuracy of the MOI burn itself. The prediction accuracy before the burn (~22:38) is at least as good as the accuracies which have been obtained on recent planetary flybys.

X. Summary

The Viking 1 MOI period, with its crucial need for the acquisition and maintenance of the telecommunications links, effectively challenged the DSN tracking system. The Viking project and the DSN jointly evolved strategies to accommodate the MOI complexities, and these strategies were successful. Overall, tracking operations during the Viking 1 MOI period and subsequent planetary phase must be considered an unqualified success.

Table 1. Doppler pseudo-residuals, June 19 and 20

Time (GMT)	Δ(A−P), Hz	Doppler mode	Event
17:52:02	+ 0.3	2	Start of pass
22:37:00	+12.5	2	Before MOI burn
23:17:00	−98.8	2	After MOI burn
23:47:02	−33.6	1	High doppler rate period
00:04:02	+34.0	2	High doppler rate period
05:26:02	+28.3	2	End of pass

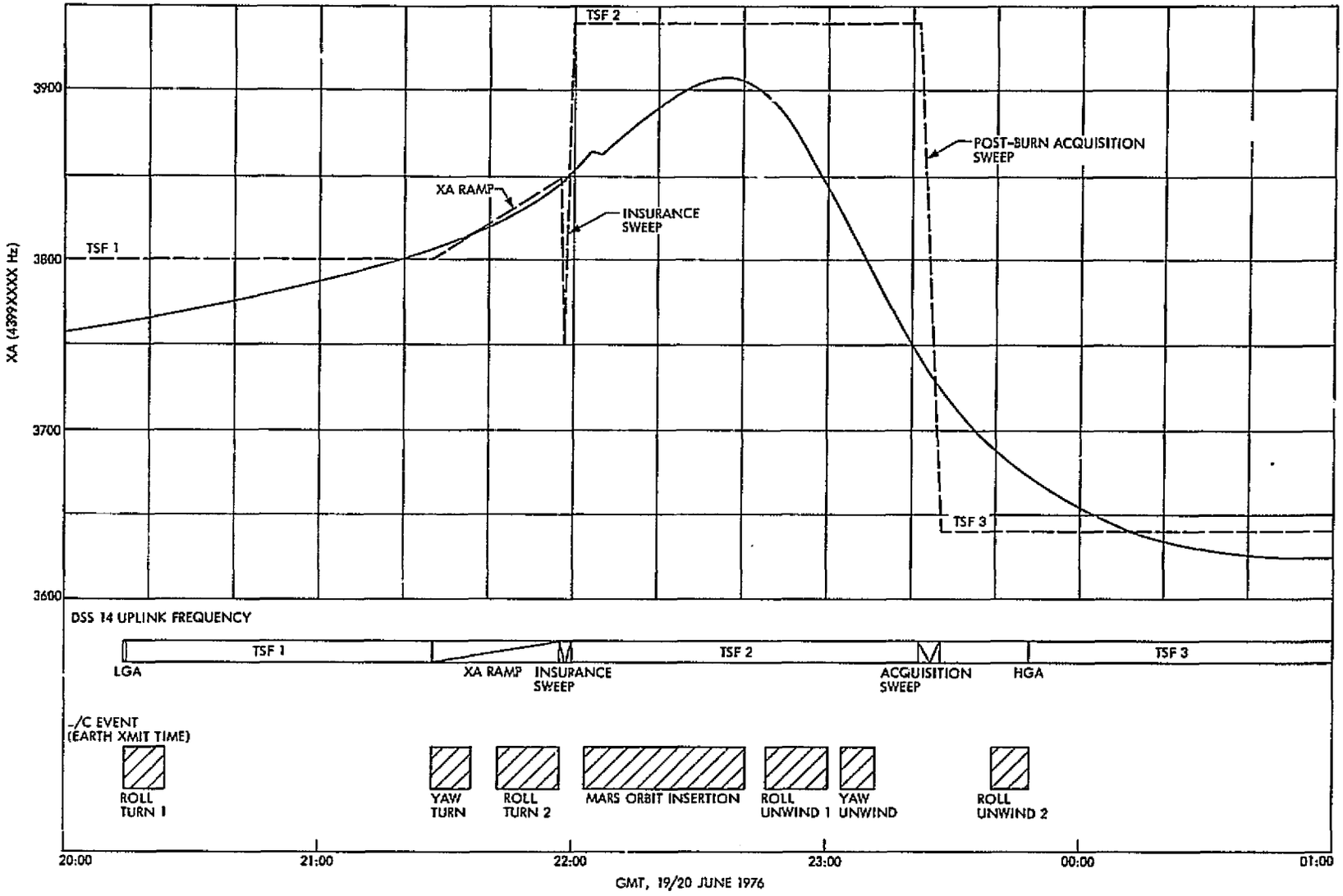

Fig. 1. Actual MOI XA with uplink sequence versus GMT

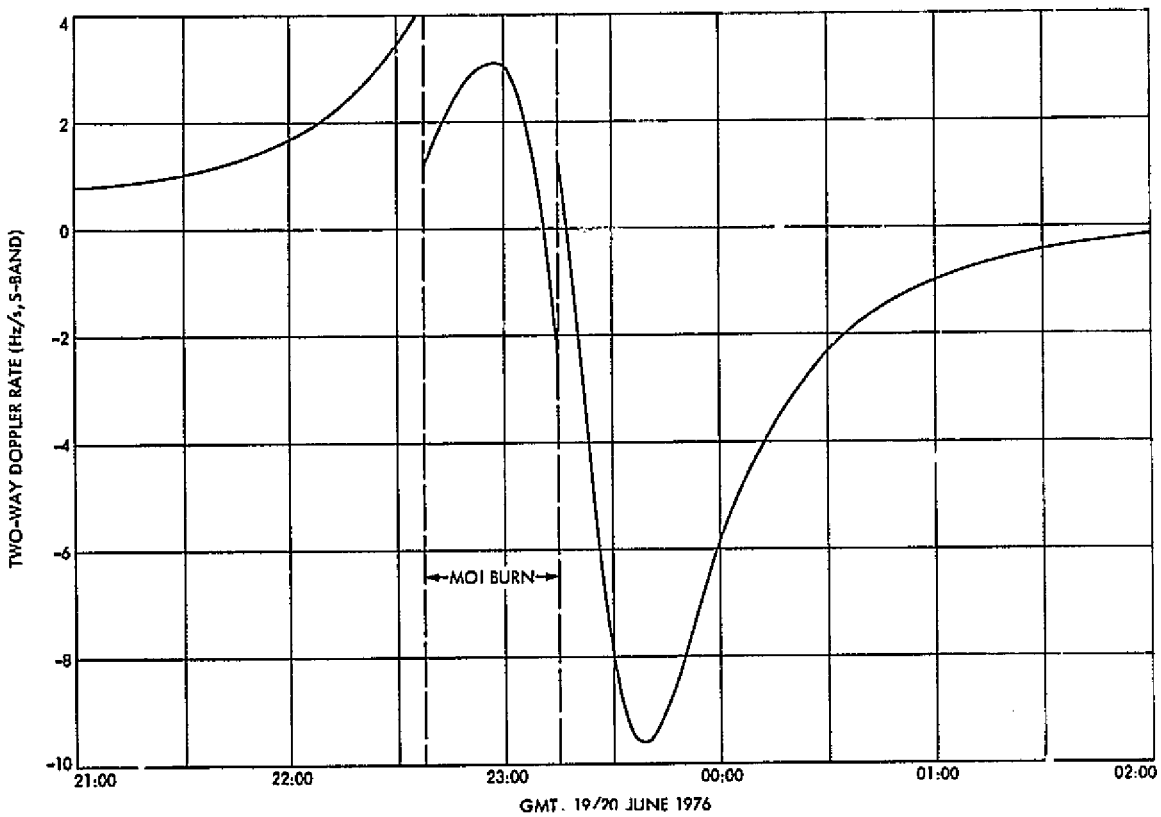

Fig. 2. Viking 1 two-way doppler rate

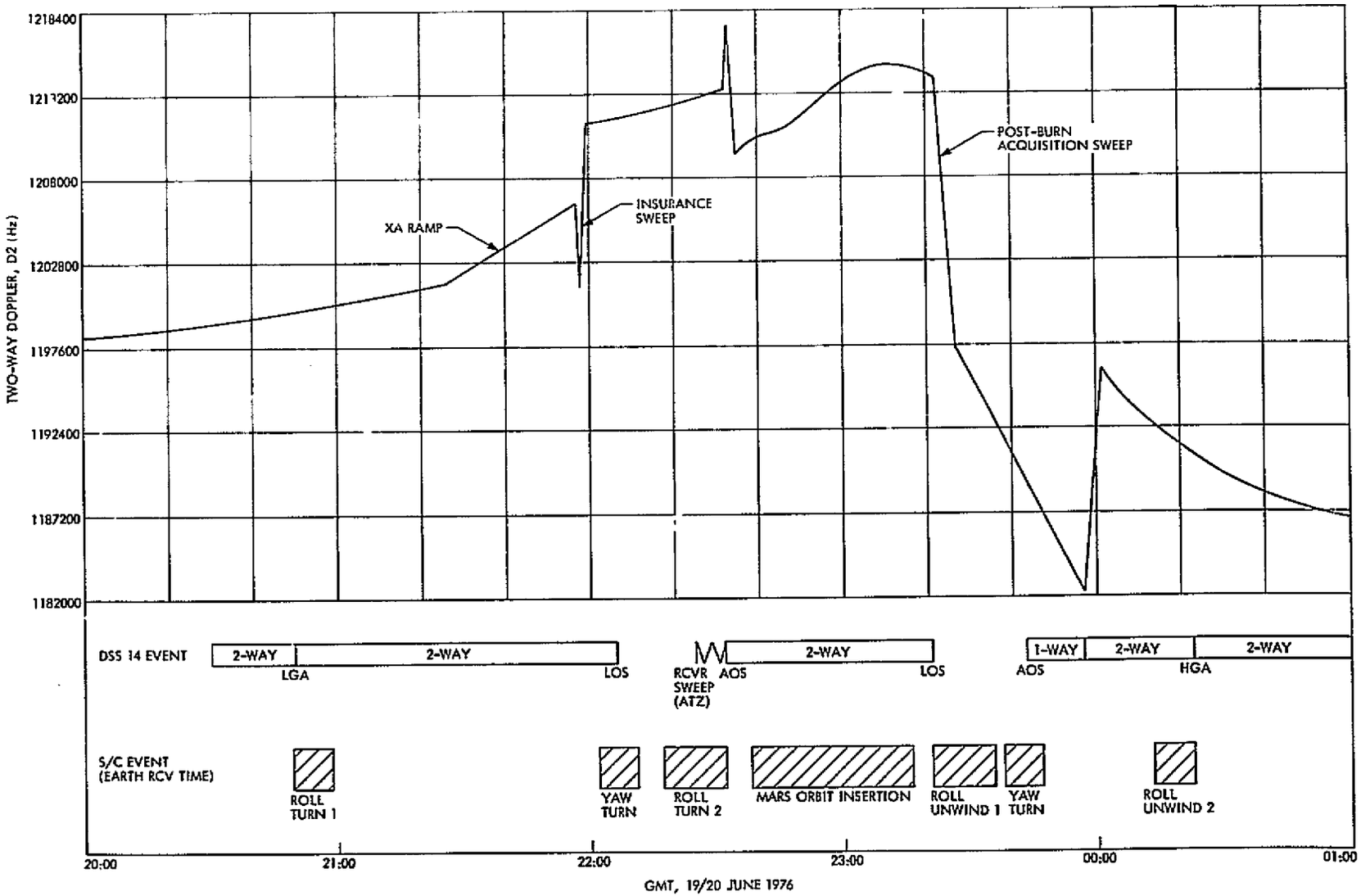

Fig. 3. MOI two-way doppler with downlink sequence versus GMT

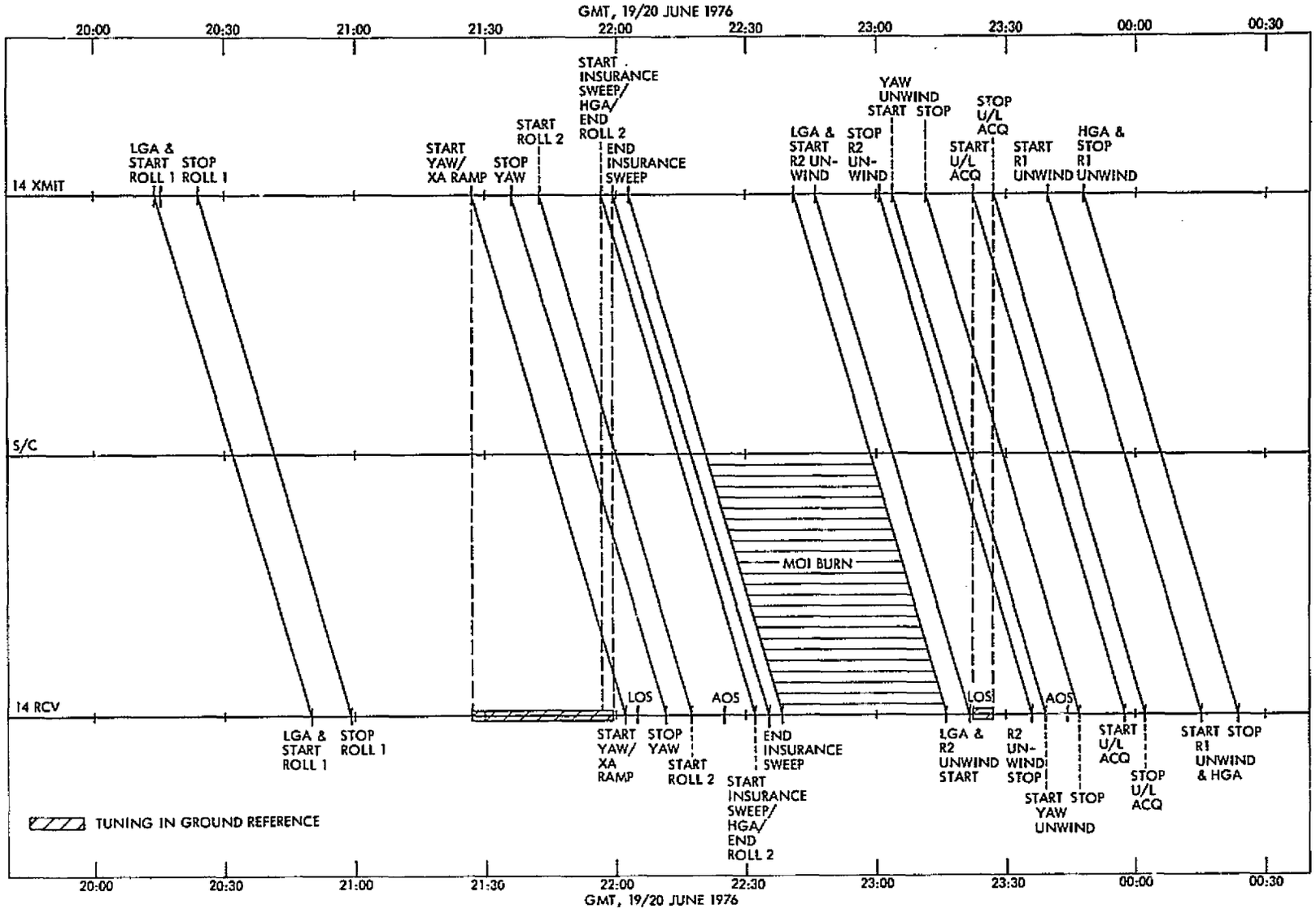

Fig. 4. Viking 1 MOI timeline

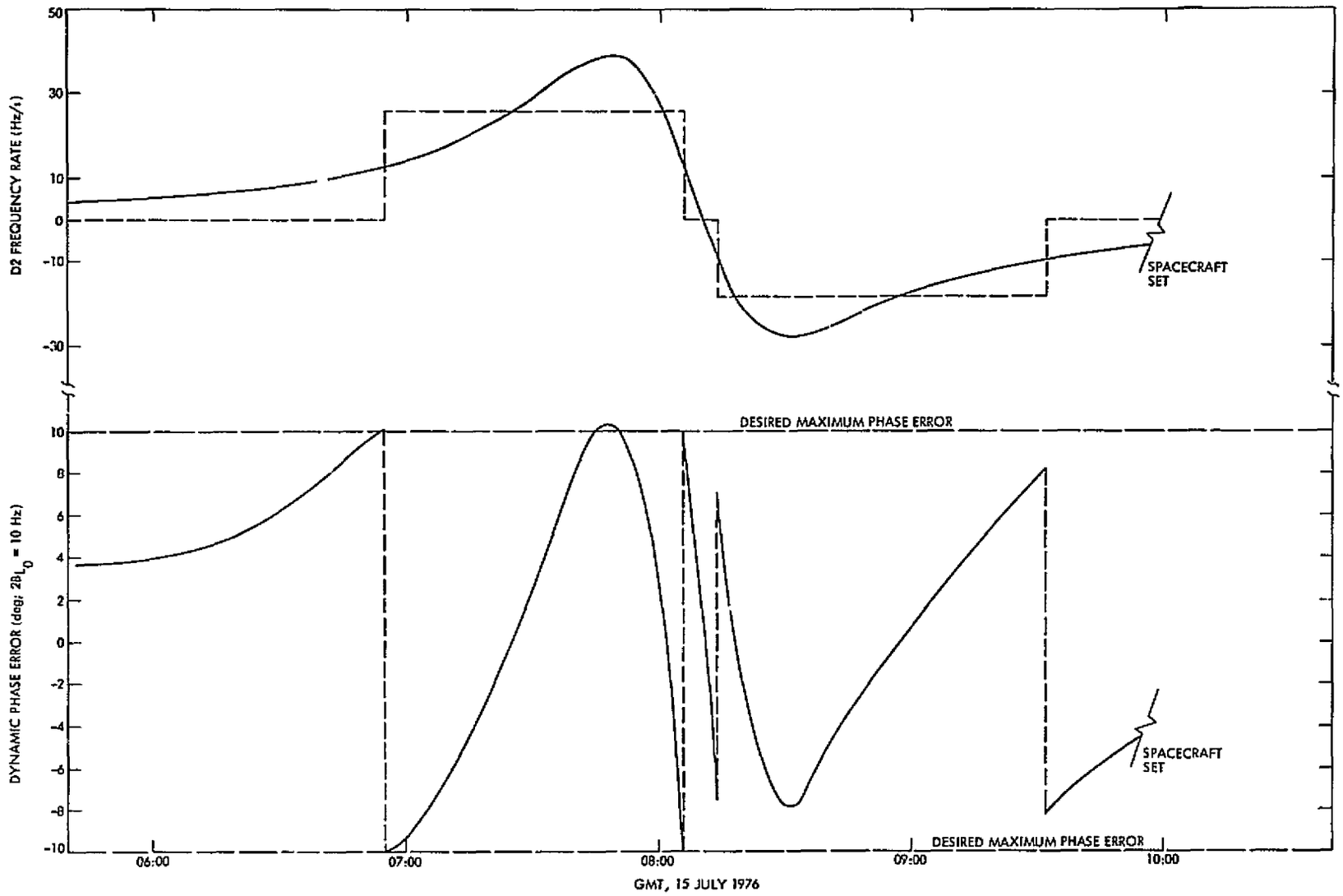

Fig. 5. Typical X-band receiver ramp with dynamic phase error versus GMT (DSS 43, Viking 1)

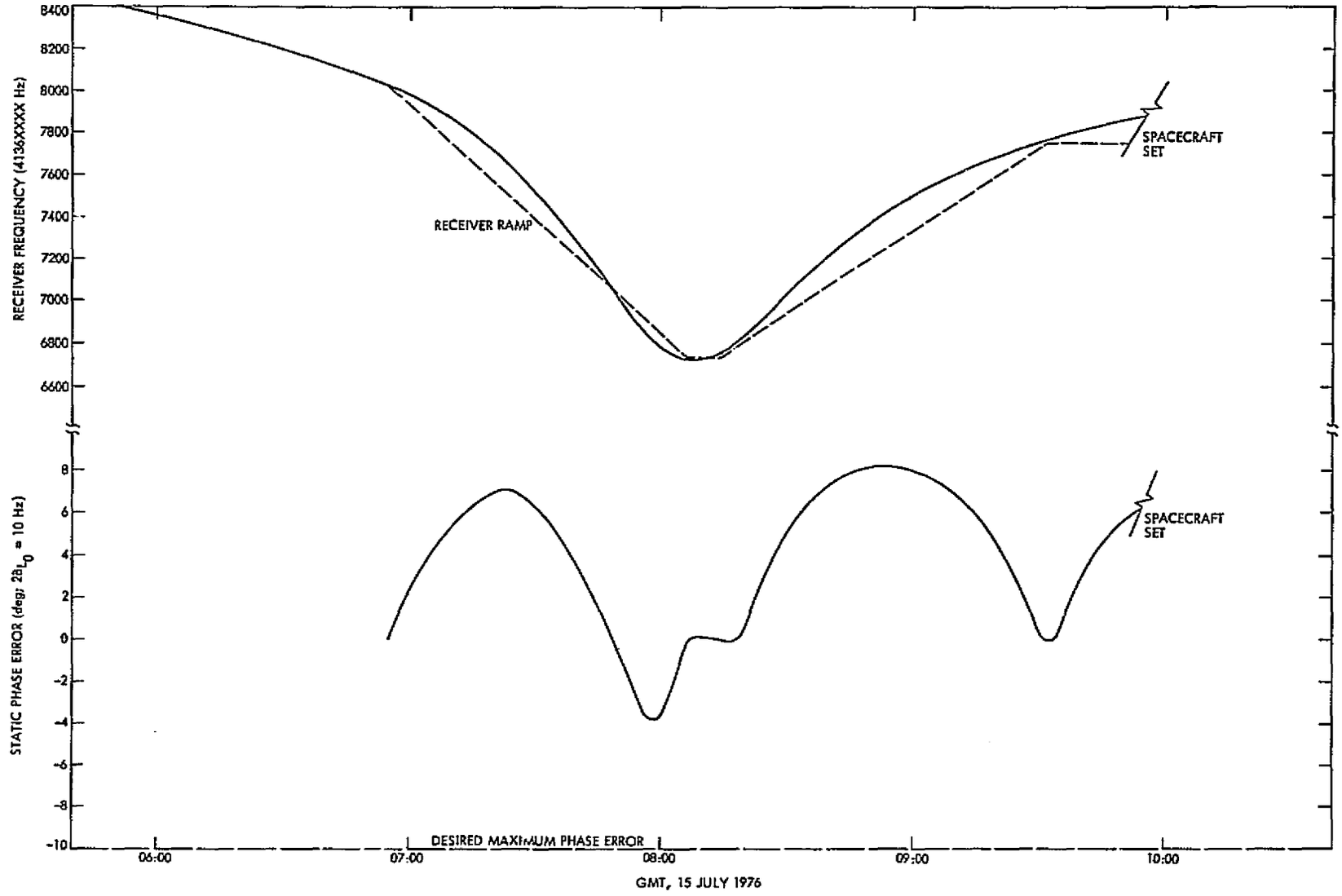

Fig. 6. Typical X-band receiver frequencies with static phase error versus GMT (DSS 43, Viking 1)

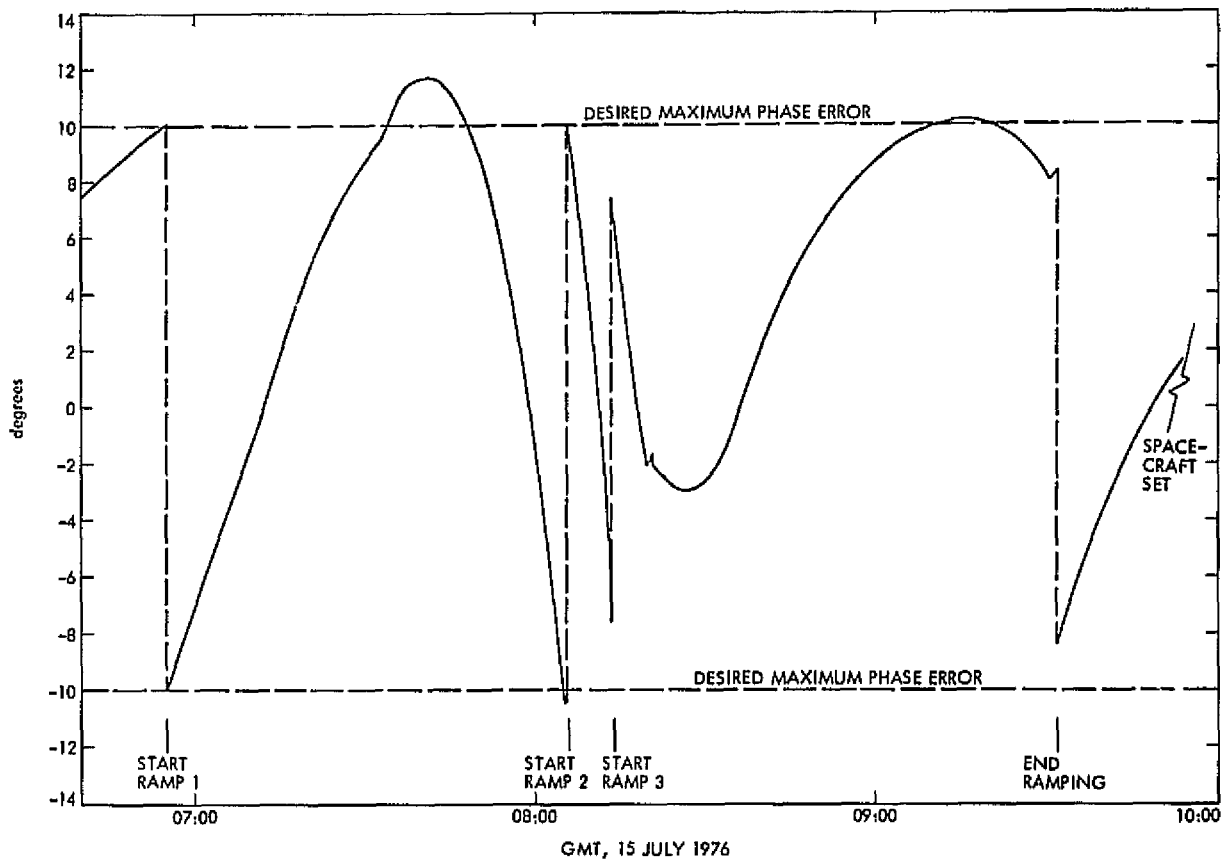

Fig. 7. Total phase error, typical X-band receiver ramp

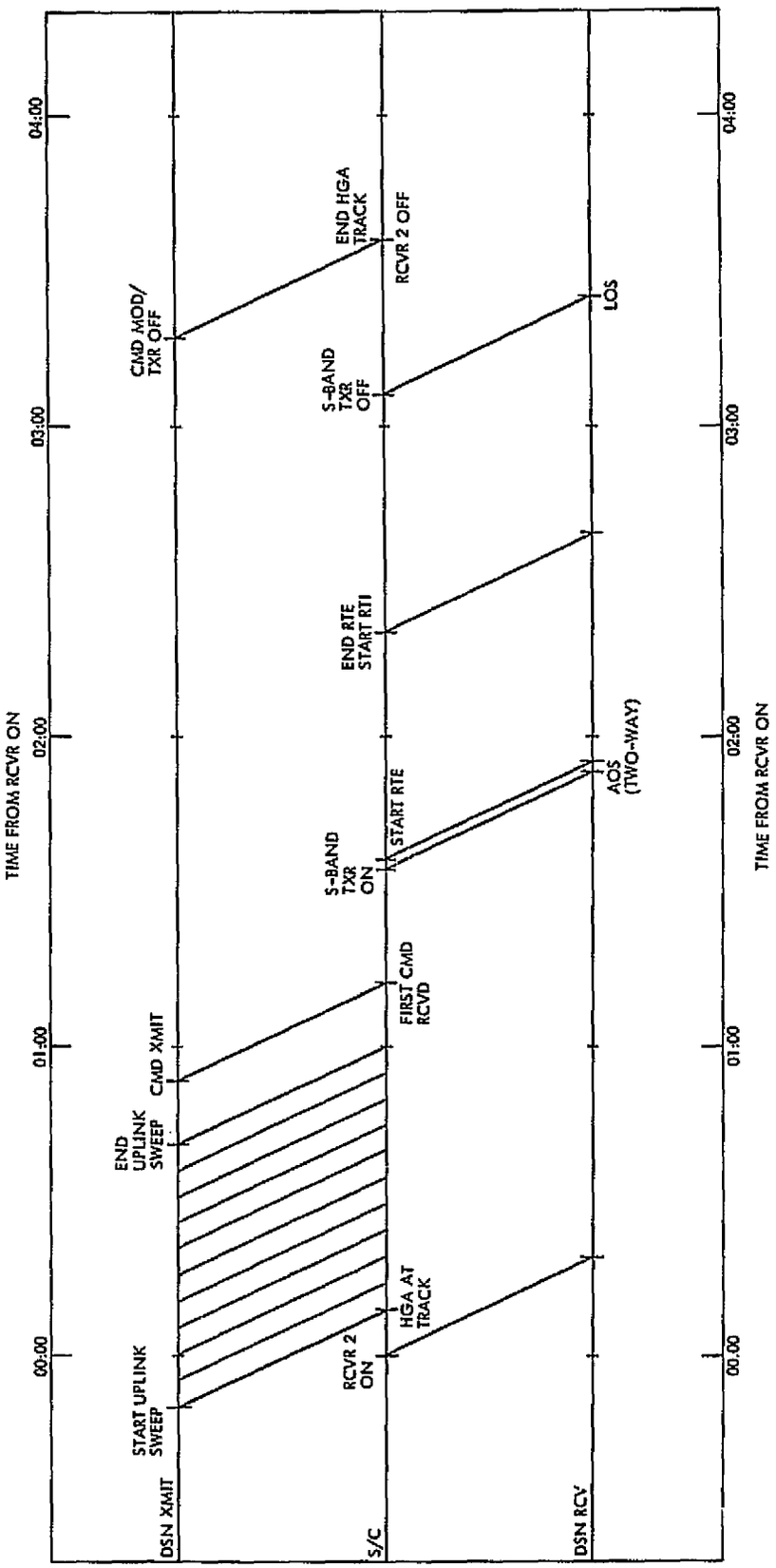

Fig. 8. Viking lander 1 long downlink timeline (1 round trip light = 38 min)

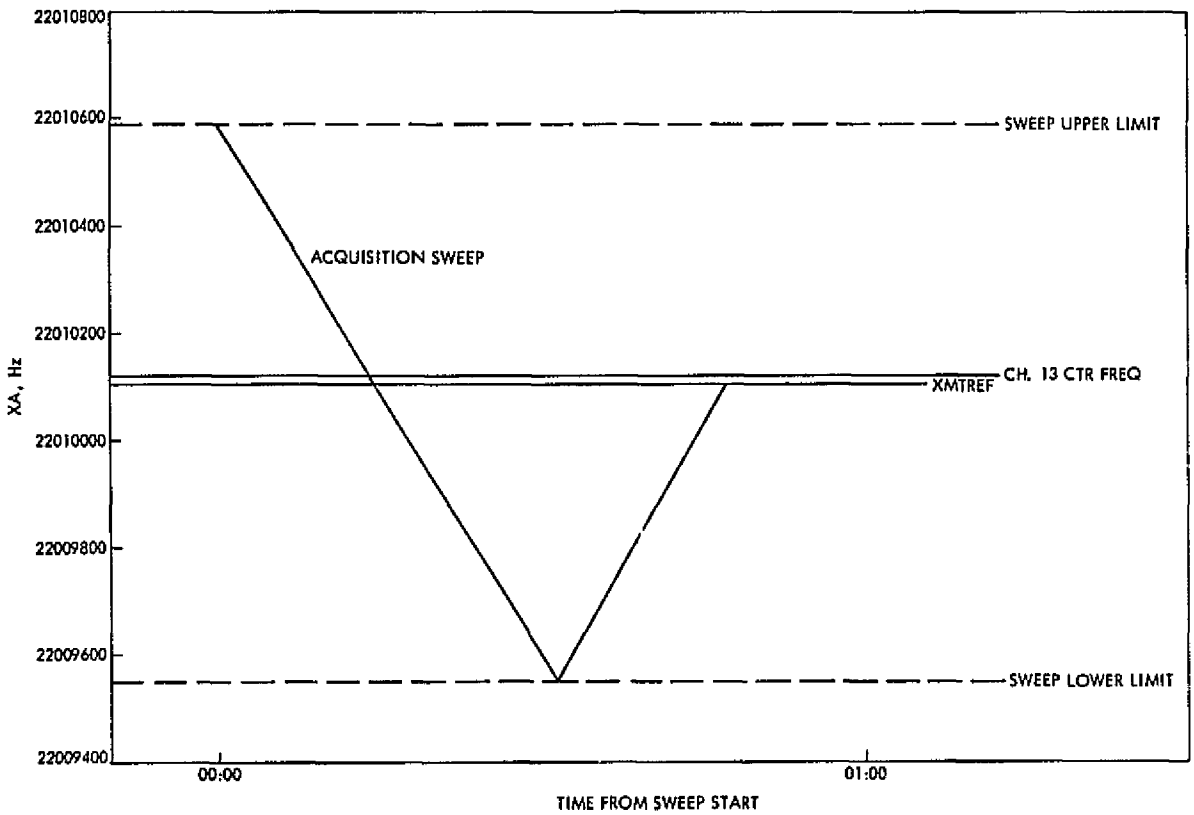

Fig. 9. Typical uplink acquisition sweep—Viking lander 1 (spacecraft received frequencies)

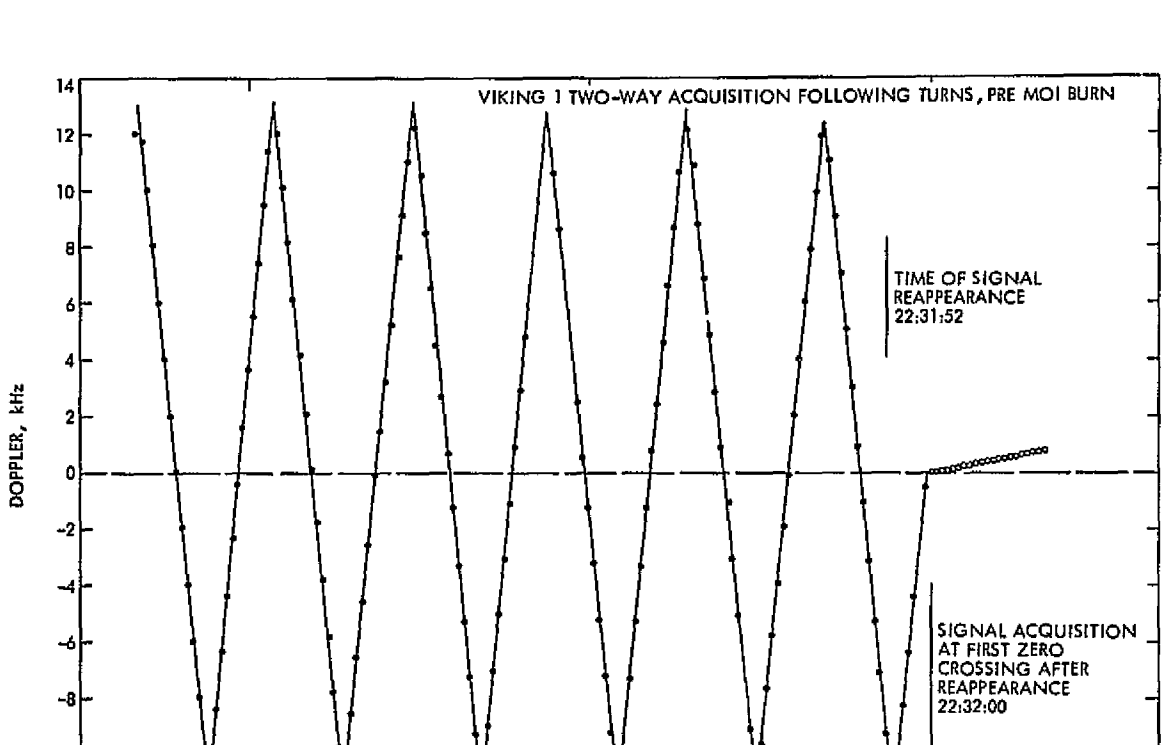

Fig. 10. Viking 1 two-way acquisition following turns, pre-MOI burn

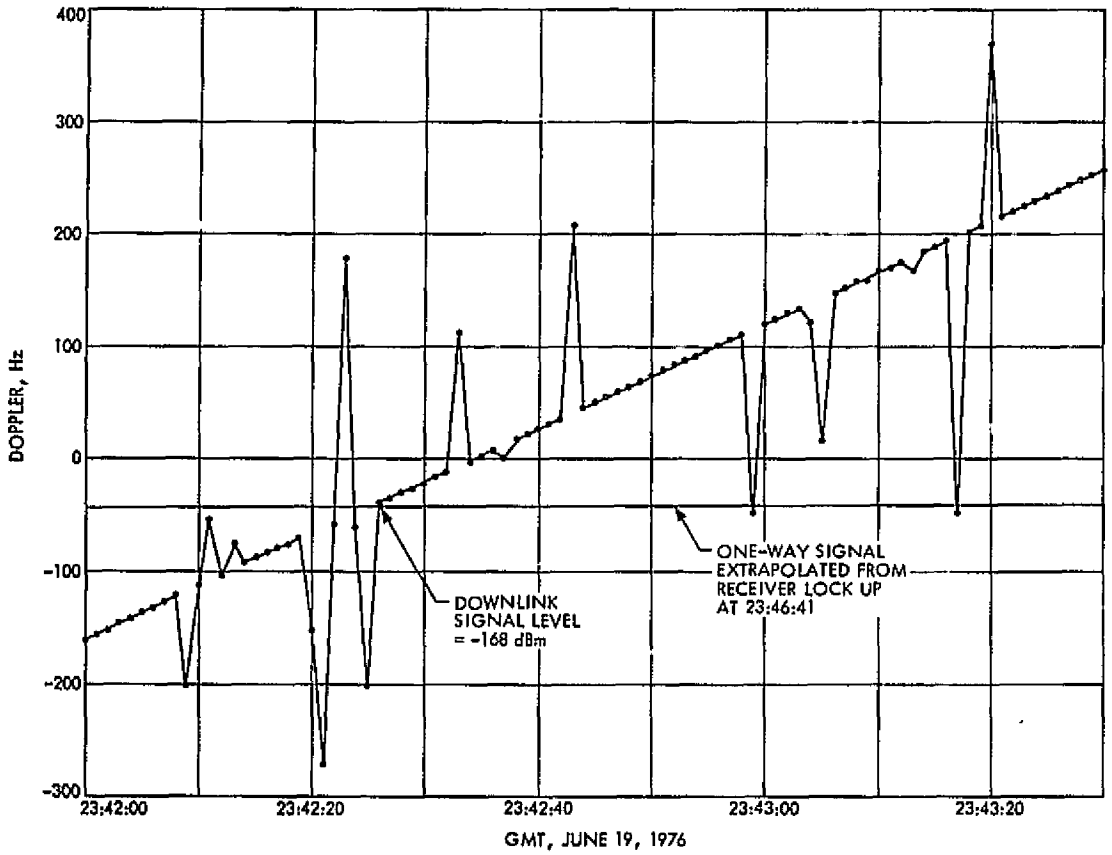

Fig. 11. Attempt to lock one-way signal, Viking 1 post-MOI burn

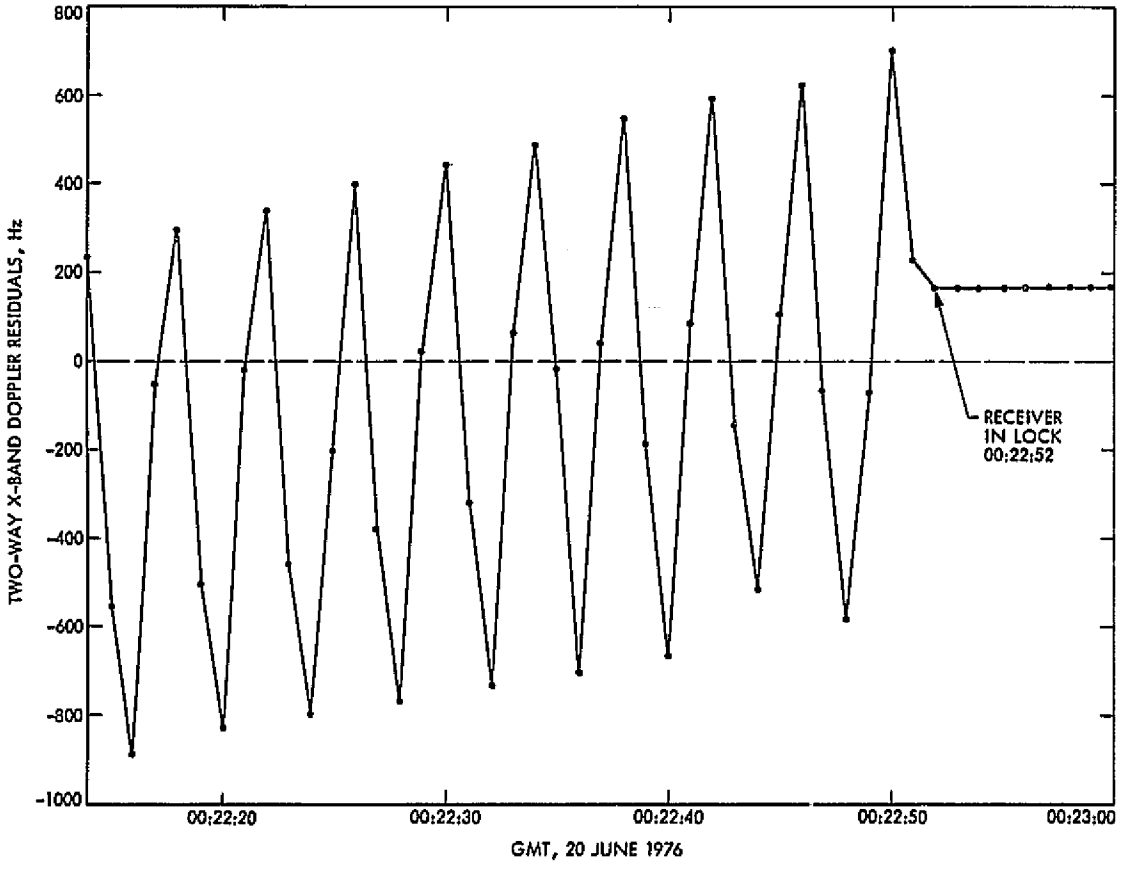

Fig. 12. Viking 1 fast X-band reacquisition following MOI burn

An Approach to Improve Management Visibility Within the Procurement and Financial Group at Goldstone

F. R. Maiocco and J. B. Rozek
DSN Facility Operations Section

This article is one in a series of articles which have been written and pertains to improvements in the operational efficiency of the data management systems at the Goldstone Deep Space Communications Complex (GDSCC). This particular article addresses the existing procurement and financial management data system at GDSCC, identifies management requirements for better visibility, describes a proposed computerized data management system, summarizes results to date, and identifies plans for future development.

I. Present System

The current GDSCC Procurement and Financial (GPF) data management system is a manual data acquisition, information handling, retrieval, processing, and reporting system. The GPF group maintains records of all purchase requests, status of such records, purchase orders, receipts, invoices, and disbursements of funds for material and supplies under their cognizance.

Purchase requisitions which are prepared by various cost centers are forwarded to the GPF group and contain basic requisition data such as: cost account number, cost center identification, purchase requisition (PR) number, PR date of preparation, GPF receiving date, description of item to be ordered, quantity requested, unit of measurement, unit number, and unit price. Figure 1 is a sample PR worksheet.

Purchase orders are prepared by the GPF group after a supplier has been selected and a contract secured. Data contained on the purchase order (PO) reflect the confirmation of the ordered quantity, unit of measurement, PO item number, PO unit price as well as the PO number, PO preparation date, and vendor promise date. Figure 2 is a sample purchase order form.

Receiving Reports contain information on actual items received from the vendor. Figure 3 is a sample form in use at GDSCC.

Transactions or queries regarding the status of any item in the existing data base are documented via manual data entries, sorting, updating, and processing. This type of data handling is somewhat laborious, inefficient, time-consuming, and susceptible to data errors. To acquire data for several standard procurement and financial reports from the existing data management system for decision making requires the GPF group to invest on the average 32 man-hours per report.

II. Requirements

Over and above the general requirements identified in Ref. 1, i.e., provide support with reduced resources, implementation of a centralized management data base system, and permit analytical assessment of manpower planning and budget estimating, the DSN management imposed the following guidelines to improve the operational efficiency of the GPF group:

(1) Provide the capability to effectively respond to budget variation in a timely manner.

(2) Provide a cost-effective capability for financial analysis and planning.

(3) Provide more efficient control techniques with respect to cost center expenditures and budget projections.

(4) Reduce the per unit cost and man-hours expended per report generated.

(5) Improve the integrity (reliability) of the GPF data base.

III. Proposed Computerized Data Management System

To facilitate the above requirements, it was determined after reviewing the various functions performed by the GPF personnel that file updating, searching, data processing, information handling, and the report generation functions were tractable to a computerized system.

Figure 4 shows an overview of the proposed computerized GPF data management system. It indicates that the GPF personnel will input pertinent data, via remote data entry terminals, to the data base and all information handling, updating, sorting, searching of files, storage, and report generation will be performed by the computer.

Users of the data base have been identified to be: JPL/DSN management, GDSCC Operations management, GPF management, GDSCC Facility Maintenance Work Control Center (WCC) planners, and, finally, the originator of the initial PR.

The data requirements and information needs of these users vary. The JPL and Goldstone Facility Management's interest leans toward expenditures versus budget situations. The Goldstone Procurement Section and the Goldstone Facility Maintenance WCC planners are interested in outstanding Purchase Requisitions/ Purchase Orders in reference to functional planning and work load analysis. Financial Planning is concerned about the committed and obligated funds and the disbursement of various cost center funds. And, finally, the originator is concerned with status of his requested items.

Typical reports required by management are:

(1) Monthly/Quarterly Expenditure Reports

(2) Material Budget Account Reports

(3) Disbursement to Small Vendors Report

(4) Weekly Procurement Activity Reports

(5) Cost Accounting Reports

(6) Followup Status Reports (overdue items)

Three major files are required to accommodate the financial related data and provide the essential statistics for management reports. They are: (1) a Vendor File which contains eight fields per computer record; (2) the Purchase File containing a total of 23 data fields per record; and (3) a Disbursement File consisting of 7 fields per record.

The structure of the computer files is shown in Tables 1–3, and sample Computer Status Codes for PR/POs are tabulated in Table 4.

IV. Status of the GPF Data Base

In addition to establishing the major data files, their contents and record layouts per file, a file generator program and an update program have been developed.

A file generator program is required to input data to computer-generated files; housekeeping routines are necessary for file updating and querying the GPF data base; and special purpose application programs are necessary for generating management reports and analyses.

The file generator program permits the GPF personnel to enter initial PR data, PO data, receiving report information, invoice data, freight charge statistics, dis-

bursement, and vendor information into the computer. This program is end-user oriented in that it permits PR/PO data and receiving report information which arrives at a different point in time at the purchasing group to be stored in the computer in a similar fashion. Prompting information for the user is available to minimize an extensive training program and permits front end editing to improve data base integrity.

As for housekeeping functions, an update program was developed to update computer files for those items most frequently modified by the GPF personnel. Specifically, this program allows purchase requisition changes in the account number, quantity requested, unit of measurement, unit price, and PR status. It further permits PO-related changes of a similar nature. To accommodate other changes, the existing MBASIC editor and edit-aid program are available for performing limited housekeeping and modifications of GPF files.

Application programs are currently being developed to achieve the specified management requirements. It is anticipated that as the data base expands during FY77, budget analysis per cost center and account, work load analysis of the GPF group, and vendor performance analyses can be conducted. Under the assumption that certain application programs have been written and given the basic data in the three major files, the GPF data management system will be able to respond to such queries as identified in Table 5. This latter list is by no means exhaustive.

V. Anticipated Results of Development Work

With the capability described above, it is assumed that the following improvements in the GPF group's operating efficiency will be detected:

(1) A reduction in man-hours expended on report preparation or analyses conducted.

(2) Elimination of computational error.

(3) An increase in GPF data base integrity.

(4) Development of efficient data acquisition, information handling, and processing procedures.

(5) An expanded capability in GPF reporting not previously available in the manual data recording system.

Additional areas where improvement is anticipated encompass such categories as: manpower utilization, organization of data files, timeliness of management reports based on current data, planning and availability of more pertinent information on overall obligated, committed, and disbursed funds per cost center or account.

VI. Future Plans

The major tasks planned for this fiscal year are as follows:

(1) Train GPF users on how to interface with the computer, create data and history files, and initiate management reports.

(2) Determine approximately six specific application programs required for management decision making.

(3) Develop and implement management programs.

(4) Transfer operations of GPF data management system to GPF group.

VII. Conclusion

The GPF on-line computerized data management system will contribute to increasing GDSCC Procurement and Planning group's efficiency and provide added visibility to JPL/DSN management with respect to GDSCC's expenditures and disbursements. Utilizing modern computer technology will result in further benefits, namely, a speedup in decision making, a reduction in clerical tasks, rapid data retrieval, and a general streamlining of the organization's operation.

Reference

1. Maiocco, F. R., and Hume, J. P., "Computerizing Goldstone Facility Maintenance Data for Management Decisions," in *The Deep Space Network Progress Report 42-32*, pp. 310–330, Jet Propulsion Laboratory, Pasadena, Calif., Apr. 15, 1976.

Table 1. Structure of Purchase File

Field	Item	Field size	Format
1	Account	5	N
2	Cost Center	4	A/N
3	Purchase Requisition Number	6	N
4	Purchase Requisition Date	6 (MMDDYY)	N
5	Purchase Requisition Receiving Date	6 (MMDDYY)	N
6	Quantity Requested	4	N
7	Purchase Requisition Unit of Measurement	2	A
8	Purchase Requisition Item	2	N
9	Purchase Requisition Unit Price	8	N
10	Status*	1	A/N
11	Revision	1	N
12	Purchase Order Number	6	N
13	Purchase Order Date	6 (MMDDYY)	N
14	Vendor Promise Date	6 (MMDDYY)	N
15	Vendor Code	4	A/N
16	Quantity Ordered	4	N
17	Purchase Order Unit of Measurement	2	A
18	Purchase Order Item	2	N
19	Purchase Order Unit Price	8	N
20	Receiving Report Number	6	N
21	Receiving Report Date	6 (MMDDYY)	N
22	Quantity Received	4	N
23	Receiving Report Unit of Measurement	2	A

A = alpha character
N = numeric character
A/N = alphanumeric character
*See Table 4.

Table 2. Structure of Disbursement File

Field	Item	Field size	Format
1	Purchase Order	6	N
2	Invoice Number	6	N
3	Invoice Date	6 (MMDDYY)	N
4	Freight Charge	5	N
5	Check Number	8	N
6	Date Paid	6 (MMDDYY)	N
7	Dollar Value	10	N

N = numeric character

Table 3. Structure of Vendor File

Field	Item	Field size	Format
1	Vendor Code	4	A/N
2	Vendor Name	36	A
3	Vendor Address	36	A/N
4	Zip Code	5	N
5	Vendor Size	1	A
6	Rating	2	A/N
7	Vendor Phone Nr.	10	N
8	Contact	15	A

A = alpha character
N = numeric character
A/N = alphanumeric character

Table 4. Sample status codes for computer input

Status code	Description
0	Routine
1	Urgent
2	Subcontract
3	Repair
4	Urgent, Subcontract
5	Urgent, Repair
6	Subcontract, Repair
7	Urgent, Subcontract, Repair
8	Petty Cash
9	Quotation
A	Quotation, Urgent
B	Quotation, Subcontract
C	Quotation, Repair
D	Quotation, Urgent, Subcontract
E	Quotation, Urgent, Repair
F	Quotation, Subcontract, Repair
G	Quotation, Urgent, Subcontract, Repair
X	Cancellation

Table 5. Possible aspects to be analyzed

Number of Purchase Requisitions written per month
Number of Purchase Requisitions written per Cost Center
Number of Purchase Requisitions written per account
Outstanding Purchase Requisitions per Cost Center
Outstanding Purchase Requisitions per account
Total outstanding Purchase Requisitions at any given time
Number of cancelled Purchase Requisitions per Cost Center
Total number of cancelled Purchase Requisitions at any given time
Number of urgent Purchase Requisitions written per Cost Center
Number of urgent Purchase Requisitions written at any given time
Number of revisions made per Cost Center
Number of revisions made at any given time
Number of Purchase Orders written per month
Number of Purchase Orders written per Cost Center
Number of Purchase Orders written per account
Outstanding Purchase Orders per Cost Center
Outstanding Purchase Orders per account
Outstanding Purchase Orders at any given time
Time period to convert Purchase Requisitions to Purchase Orders
Time period between *promised* and *actual* delivery dates
Number of outstanding items per Purchase Order
Number of cancelled Purchase Orders per Cost Center
Number of cancelled items per Cost Center
Total Number of cancelled Purchase Orders at any given time
Total Number of Invoices received at any given time
Number of outstanding invoices at any given time
Freight Charges paid out per account
Freight Charges paid out to individual Vendors
Number of checks written toward a given Purchase Order
Total Disbursement per Cost Center
Total Disbursement per account
Total Disbursement of petty cash per Cost Center
Total Disbursement of petty cash at any given time
Performance rating of vendors
Total Disbursement to small business
Total Disbursement to large business

Aeronutronic Ford Corporation
COMMUNICATIONS AND TECHNICAL SERVICES DIVISION
HEADQUARTERS • 4700 WISSAHICKON AVE.
PHILADELPHIA, PA. 19144

SMALL VALUE PURCHASE ORDER No.

SHOW THESE NUMBERS ON ALL SHIPMENTS AND CORRESPONDENCE

AMENDMENT NO. | RELEASE NO.

REQ. DATE | REQUISITION [X] | SMALL VALUE PURCHASE ORDER [ ] | BLANKET RELEASE [ ]

GOVT. CONTRACT NO. NAS 7-100/954150 | PRIORITY RATING CERTIFIED UNDER DMS REG. DOA 2

PHILCO-FORD CORPORATION, BUYER, HEREBY AGREES TO PURCHASE AND RECEIVE, AND

SELLER, AGREES TO SELL AND DELIVER SUPPLIES OR SERVICES SPECIFIED HEREIN UNDER THE TERMS AND CONDITIONS ON THE FACE AND REVERSE SIDE HEREOF.

SUPPLIER NO. | D/S | TERMS | VENDOR PROMISE DATE | ORDER DATE

INSPECTION REQUIREMENTS

GOVERNMENT SOURCE INSPECTION APPLICABLE IF CHECKED [ ]

MIL-Q-9858A [ ] A [ ] SAMPLE(S) APPROVAL REQ'D BY PHILCO-FORD [ ] B [ ]

ATTACHMENTS – COMPLETE THOSE INDICATED AND ATTACH TO SHIPPING PAPERS

1. TEST & INSPECTION DATA [ ] 2. TOOL ATTACHMENT [ ] 4. CHEMICAL & PHYSICAL ANAL. [ ] 6. CERTIF. OF COMPLIANCE [ ]

INSPECTION CODE | INSPECTION REQUIRED: SEE ATTACHMENT [ ] INCOMING [ ]

SHIP TO | INVOICE TO

SHIP VIA | SHIPPING POINT

F.O.B. CARRIER SELLERS PLANT [ ] DESTINATION [ ] | TRANSPORTATION TERMS PREPAID & CHARGE [ ] PREPAID [ ] COLLECT [ ] | PROJECT/CONTRACT | SMALL BUSINESS [ ]

QUANTITY	UNIT MEASURE	ITEM	UNIT PRICE DOLLARS	UNIT PRICE CENTS	PART NUMBER/DESCRIPTION

DATE REQUIRED | CONFIRMING ON | BY | TO

PAGE | OF | MARK FOR ATTENTION OF

AERONUTRONIC FORD CORPORATION

BY _____ PURCHASING

BUYER _____

ADDRESS ALL COMMUNICATIONS TO THE BUYER

REQUISITION NO. 19546 | BUYER'S ADDRESS IF DIFFERENT FROM ABOVE:

SINGLE/SOLE SOURCE REQUEST ATTACHED [ ]	ESTIMATED COST	DELIVERY REQUIRED	SUBJECT TO SALES/USE TAX YES [ ] NO [ ]	APPROPRIATION NO.	ACCOUNT CLASSIFICATION

NOTES:

ACCOUNT/WORK ORDER CHARGED

BUYER CODE | DEPT./STORES STOCK

JPL APPROVAL | DATE | ON SITE DATE

APPROVALS

REQUESTER'S SIGNATURE	DATE	DEPT.	EXT.	MANAGER	DATE	MAT'L CONTROL	DATE	ACCOUNTING	DATE	QUALITY ASSURANCE	DATE

REQUISITION WORK SHEET PROCUREMENT 1

Fig. 1. Requisition Work Sheet

Aeronutronic Ford

COMMUNICATION SYSTEMS DIVISION

HEADQUARTERS • 3900 WELSH ROAD WILLOW GROVE, PA. 19090

SHOW THESE NUMBERS ON ALL SHIPMENTS AND CORRESPONDENCE | PURCHASE ORDER NO. | RELEASE NO.

PRIME CONTRACT NO. | PRIORITY RATING CERTIFIED UNDER DMS REG. 1

REQ DATE | REQUISITION ☐ | SMALL VALUE PURCHASE ORDER ☐ | BLANKET RELEASE ☐

SUPPLIER NO. | B/S | PAYMENT TERMS | VENDOR PROMISE DATE | ORDER DATE

Aeronutronic Ford Corporation, BUYER, HEREBY AGREES TO PURCHASE AND RECEIVE AND

SUPPLIER PRODUCT ASSURANCE REQUIREMENTS

THE FOLLOWING CLAUSES OF SPAR ATTACHMENT. CTS 243. ARE INVOKED ON THIS ORDER:

INSPECTION CODE | DATA | CODE | CONTRACT OR PROJECT ▶

SELLER AGREES TO SELL AND DELIVER SUPPLIES OR SERVICES SPECIFIED HEREIN UNDER THE TERMS AND CONDITIONS ON THE FACE AND REVERSE SIDE HEREOF.

SHIP TO | MARK FOR / STOREROOM

SHIP VIA | SHIPPING POINT

F.O.B. | TRANSPORTATION TERMS

☐ CARRIER SELLER'S PLANT ☐ DESTINATION | ☐ PREPAID & CHARGE ☐ PREPAID ☐ COLLECT

QUANTITY	UNIT MEAS.	ITEM	UNIT PRICE DOLLARS	UNIT PRICE CENTS	PART NUMBER	DESCRIPTION	REQUISITION NUMBER	POINT NO.	CODE

UNIT MEAS. CODE: 01 EACH, 02 PKG, 03 GAL, 05 FEET, 08 PAIR, 11 PINTS, 14 DOZEN, 90 LOT

TOTAL PRICE ▶

☐ CONFIRMING THE ORDER PLACED ON: BY TO

PAGE OF

INVOICE TO ACCOUNTS PAYABLE: (ATTACH PROOF OF SHIPMENT: POSTAL RECEIPT: BILL OF LADING: ETC.)

HEADQUARTERS ☐ ADDRESS ☐

Aeronutronic Ford Corporation

BY PURCHASING CODE

REQUISITION NUMBER 545349

BUYER'S ADDRESS WHEN DIFFERENT FROM HEADQUARTERS ADDRESS

BUYER

ADDRESS ALL COMMUNICATIONS TO THE BUYER

SINGLE/SOLE SOURCE ☐ REQUEST ATTACHED	ESTIMATED COST	DELIVERY REQUIRED		ACCOUNT CLASSIFICATION	EXP. CLASS.	

NOTES:

ACCOUNT / WORK ORDER CHARGED

BUYER CODE | APPROPRIATION NO.

ON-SITE DATE

APPROVALS

REQUESTER'S SIGNATURE	DATE	DEPT.	EXT.	MANAGER	DATE	MAT'L CONTROL	DATE	ACCOUNTING	DATE	QUALITY ASSURANCE	DATE

CTS 120 7/75 PREVIOUS EDITIONS MAY NOT BE USED PRINTED IN U.S.A.

2

Fig. 2. Purchase order form

GOLDSTONE RECEIVING REPORT

NO. 006102

SUPPLIER NAME				P O NO	
PACKING SLIP NO	PREPARED BY		VIA		
REC STATION	DEPT NO OR AREA		ATTENTION OF		
DATE RECEIVED	DISC CODE	DISP CODE	RATE	DATE INSPECTED	STAMP

LINE ITEM	QTY & UNIT	PART NO./DESCRIPTION	QTY REJ	QTY ACC

REMARKS

VOUCHER NO

RECEIVED BY DATE

Accounting JPL 5790/DSIF (12/71)

Fig. 3. Goldstone Receiving Report

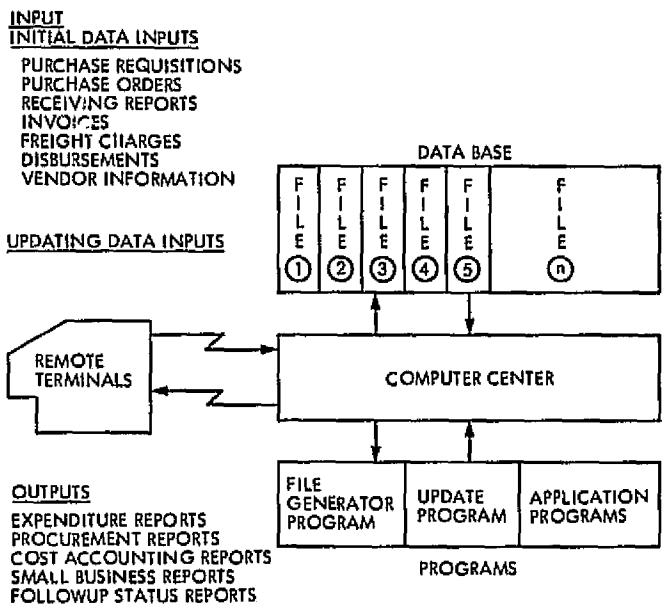

Fig. 4. General view of the computer data base system

N77 10110

A Technique for Generating Correlated X-Band Weather Degradation Statistics

E. C. Posner and F. J. Zeigler
TDA Planning Office

Flight projects relying on the DSN's X-band receiving facilities for X-band telemetry and/or tracking require some technique for generating test cases of degradations to use in mission sequence planning exercises and even in data rate selection. It is, for example, known that the X-band noise temperature of DSN receivers can go up from 20 K to over 100 K or more, if the air is heavily laden with water vapor, although that is an uncommon occurrence. It is proposed that the DSN furnish flight projects relying on X-band degradation models, one for each DSN Complex. Such models would be in the form of a random process generator, say in an MBASIC program, that would permit the project to generate X-band degradation data with the right autocorrelations for periods of interest to the Projects. The autocorrelation modeling is especially important because bursts of degradation lasting several days can affect data storage and mission sequence design strategy. This article therefore presents one approach which works if the degradation statistics obey a half-gaussian law. That is, the random variables are formed by taking the absolute values of another set of random variables, themselves having a (two-sided) gaussian distribution. The technique of this paper then permits the half-gaussian random variables to have given one- and two-step correlation coefficients.

I. Introduction

Flight projects relying on the DSN's X-band receiving facilities for X-band telemetry and/or tracking require some technique for generating test cases of degradations to use in mission sequence planning exercises and even in data rate selection. It is, for example, known that the X-band noise temperature of DSN receivers can go up from 20 K to over 100 K or more, if the air is heavily laden with water vapor, although that is an uncommon occurrence. It is proposed that the DSN furnish flight projects relying on X-band degradation models, one for each DSN Complex. Such models would be in the form of a random process generator, say in an MBASIC program, that would permit the project to generate X-band degradation data with the right autocorrelation for peri-

ods of interest to the projects. The autocorrelation modeling is especially important because bursts of degradation lasting several days can affect data storage and mission sequence design strategy. This article therefore presents one approach which works if the degradation statistics obey a half-gaussian law. That is, the random variables are formed by taking the absolute values of another set of random variables, themselves having a (two-sided) gaussian distribution. The technique of this paper then permits the half-gaussian random variables to have given one- and two-step correlation coefficients, if non-negative. A modification, to be reported separately, can be used to match negative correlations.

Mathematically, the primary problem is to find correlation coefficients ρ_1, ρ_2 for the intermediate gaussian random variables which will lead to the desired correlations λ_1 and λ_2 for the half-gaussian variables. Thus, we need to find $\rho_1(\lambda_1)$, and $\rho_2(\lambda_2)$. The nature of the bivariate gaussian distribution makes the calculation of $\lambda(\rho)$ feasible. A two-step process is therefore followed: the function $\lambda(\rho)$ is found (see Section II), then is inverted to get $\rho(\lambda)$ by numerical means (Section III).

In Section IV we outline a method for generating a sequence of gaussian random variables with one- and two-step correlations ρ_1, ρ_2, from an uncorrelated set of normal gaussian random variables. The algorithm described in Section IV can easily be extended to the case of more than two correlations. Section V briefly describes a program written in the MBASIC language implementing the above algorithms, and it describes how to create a set of standard gaussian random numbers from a set of random variables distributed uniformly. Some sample output from the program is also given. Section VI is an informal "Software Specification Document" (SSD) for the program.

II. Determining the Intermediate Correlation

Given two normally distributed random variables X_1,X_2 with mean 0, variance 1 and correlation $\rho(X_1,X_2)$, we wish to find Corr $(|X_1|,|X_2|) = \lambda(\rho)$. Our starting point is the distribution function

$$F(a_1,a_2) = \int_{-\infty}^{a_1}\int_{-\infty}^{a_2} f(X_1,X_2,\rho)dX_1dX_2$$

for X_1,X_2, where f is the bivariable normal density centered at the origin:

$$f(X_1,X_2,\rho) = \frac{1}{2\pi\sqrt{1-\rho^2}} \times \exp\left[\frac{-1}{2(1-\rho^2)}(X_1^2 - 2\rho X_1X_2 + X_2^2)\right]$$

Let $G(a_1,a_2)$ denote the distribution function for $|X_1|,|X_2|$. If either a_1 or a_2 is less than 0 then $G(a_1,a_2) = 0$; otherwise we have

$$\begin{aligned} G(a_1,a_2) &= \rho(|X_1| \le a_1, |X_2| \le a_2) \\ &= \int_{-a_1}^{a_1}\int_{-a_2}^{a_2} f(X_1,X_2,\rho)dX_1dX_2 \\ &= \int_0^{a_1}\int_0^{a_2} 2[f(X_1,X_2,\rho) + f(X_1,X_2,-\rho)]dX_1dX_2 \end{aligned}$$

Therefore, $2[f(X_1,X_2,\rho) + f(X_1,X_2,-\rho)]$ represents the joint density of $|X_1|,|X_2|$

The next step is to calculate the expectation of $|X_1|,|X_2|$:

$$\begin{aligned} &E(|X_1|,|X_2| \\ &2\int_0^\infty\int_0^\infty X_1X_2[f(X_1,X_2,\rho) + f(X_1,X_2,-\rho)]dX_1dX_2 \\ &= 2\Phi(\rho) + 2\Phi(-\rho) \end{aligned}$$

where

$$\Phi(\rho) = \int_0^8\int_0^\infty X_1X_2f(X_1,X_2,\rho)dX_1dX_2$$

A variable change to polar coordinates gives

$$\begin{aligned} \Phi(\rho) &= \frac{1}{4\pi\sqrt{1-\rho^2}}\int_0^\infty\int_0^{\pi/2} r^3\sin 2\theta \cdot \exp\left[\frac{-1}{2(1-\rho)}(r^2 - \rho r^2\sin 2\theta)\right]dr\,d\theta \\ &= \frac{1}{4\pi\sqrt{1-\rho^2}}\int_0^{\pi/2}\sin 2\theta\int_0^\infty r^3\cdot\exp\left(-r^2\cdot\frac{1-\rho\sin 2\theta}{2(1-\rho^2)}\right)dr\,d\theta \\ &= \frac{(1-\rho^2)^{3/2}}{2\pi}\int_0^{\pi/2}\frac{\sin 2\theta d\theta}{1-\rho\sin 2\theta} = \frac{\sqrt{1-\rho^2}}{2\pi} + \frac{\rho}{4} + \frac{\rho\arcsin\rho}{2\pi} \end{aligned}$$

Thus,

$$E(|X_1|,|X_2|) = \frac{2}{\pi}(\sqrt{1-\rho^2} + \rho \arcsin \rho)$$

For $\rho = 1$ we obtain $E(X_i^2) = 1$; $\rho = 0$ implies

$$[E|X_i|]^2 = \frac{2}{\pi}, \text{so} \quad \text{var}(X_i) = 1 - \frac{2}{\pi}$$

Therefore

$$\text{Corr}(|X_1|,|X_2|) = \frac{\frac{2}{\pi}(\sqrt{1-\rho^2} + \rho \arcsin \rho - 1)}{1 - \frac{2}{\pi}}$$

$$= \frac{\sqrt{1-\rho^2} + \rho \arcsin \rho - 1}{\frac{\pi}{2} - 1} = \lambda(\rho)$$

III. Calculation of $\rho(\lambda)$

We calculate $\rho(\lambda)$ given the relation

$$\lambda(\rho) = \frac{\sqrt{1-\rho^2} + \rho \arcsin \rho - 1}{\frac{\pi}{2} - 1}, \qquad (0 \le \lambda \le 1) \quad (1)$$

A useful observation is $(\pi/2 - 1)\, d\lambda/d\rho = \arcsin \rho = \rho + 1/6\,\rho^3 + 3/40\,\rho^5 + \ldots$. Integrating this formula gives a Taylor series for $(\pi/2 - 1)\lambda$ and, upon formal inversion, we obtain:

$$\rho^2(\lambda) = 2\lambda_1 - 1/3\,\lambda_1^2 - 4/45\,\lambda_1^3 - 11/189\,\lambda_1^4 - 722/14175\,\lambda_1^5 - 0.05203\,\lambda_1^6 - 0.05087\,\lambda_1^7$$

where $\lambda_1 = (\pi/2 - 1)\lambda$. Over the interval [0,0.5] this seven-term series will find ρ to within the theoretical error bound of $2 \cdot 10^{-4}$. An actual computer calculation using this series, then converting back via Eq. (1) gives an accuracy to within 10^{-5} over [0,0.5] with the largest error at $\lambda = 0.5$. (The difference between the two numbers is simply an example of the fact that calculations often work out much better than theoretical error bounds would indicate.)

When λ approaches 1, the above series gives inaccurate results. An alternate method is to use the Lagrange Interpolation polynomial for ρ over the interval [0.5,1], with mesh points 0.5, 0.6,..,1. The result is $\rho(\lambda) = 0.2862 + 1.0558\lambda - 0.0470\lambda^2 - 0.9506\lambda^3 + 1.0072\lambda^4 - 0.3516\lambda^5$. The theoretical error bound is $7 \cdot 10^{-4}$, mainly due to rounding. A computer calculation using this formula gave accuracy to within $4 \cdot 10^{-4}$ over [0.5,1].

IV. Generating Random Variables With Given One and Two-Step Correlations

We now give a method for generating a sequence $\{X_i\}$ of gaussian random variables with given one-step correlation $\rho_1(X_i,X_{i+1})$ and two-step correlation $\rho_2(X_i,X_{i+2})$. Consider a process of the form

$$X_{i+2} = \alpha X_{i+1} + \beta X_i + y_{i+2} \qquad (1)$$

where α and β are coefficients to be determined, and the y_i are standard normal gaussian random variables.

Multiplying Eq. (1) by X_i,X_{i+1} and taking expectations, we find that $\rho_1\sigma_{i+2}^2 = \alpha\sigma_{i+1}^2 + \beta\rho_1\sigma_i^2$ and $\rho_2\sigma_{i+2}^2 = \alpha\rho_1\sigma_{i+1}^2 + \beta\sigma_i^2$ where $\sigma_i^2 = E(X_i^2)$. For Eq. (1) to be a stationary process it is required that $\sigma_i = \sigma_{i+k}$ for $k > 0$; in this case we may solve for α and β, giving $\alpha = \rho_1 - \rho_2\rho_2/1 - \rho_1^2$ and $\beta = \rho_2 - \rho_1^2/1 - \rho_1^2$. It is also possible to solve for $\sigma_i = \sigma$. Writing $E(X_{i+2} - \alpha X_{i+1} - \beta X_i)^2 = Ey_{i+2}^2 = 1$ we find $\sigma^2 = 1 - \rho_1^2/(1 - \rho_2)(1 + \rho_2 - 2\rho_1^2)$. Since $\sigma^2 \ge 0$ this gives us the inequality $1 + \rho_2 - 2\rho_1^2 \ge 0$.

To begin generating $\{X_i\}$ we normalize X_1,X_2 using the above value for σ as follows:

$$X_1 = \sigma\sqrt{\frac{1+\rho_1}{2}}\,y_1 + \sigma\sqrt{\frac{1-\rho_1}{2}}\,y_2,$$

$$X_2 = \sigma\sqrt{\frac{1+\rho_1}{2}}\,y_1 - \sigma\sqrt{\frac{1-\rho_1}{2}}\,y_2$$

This gives the proper correlation and variance for X_1,X_2. Equation (1) may now be used to calculate $X_3,X_4,\ldots$.

V. Program Organization

A program has been written in the MBASIC[1] language to carry out the generation of a sequence of correlated "half gaussian" random variables, relying on the procedures described above.

The MBASIC random number generator gives numbers which are uniformly distributed, so the first step is to produce a sequence of standard normal gaussian numbers from the uniform distribution, via the central limit

[1]The DSN standard nonreal-time language.

theorem. If y_i is the ith standard gaussian, X_K the Kth random number from the MBASIC generator, we may write

$$y_i = \sum_{K=1} (X_{12(i-1)+K} - 1/2)$$

A uniform distribution over [0,1] has mean 1/2, variance 1/12, so each $X_K - 1/2$ has mean 0, and adding 12 of them gives a random variable with variance 1. In addition, the y_i will be very nearly gaussian, as a result of the central limit theorem.

Using the numerical methods described above, the next step in the program is to calculate the intermediate correlations. Then the stationary random process is used (if the correlations satisfy the required inequality) to generate random variables with the intermediate correlations. The absolute values of these random variables are then taken to give our desired sequence of "half gaussian" random variables with the given correlations.

A word of caution. We have not yet proved that any non-negative two-step correlation function $\{\lambda_1, \lambda_2\}$ which can arise as the correlation function of some stationary process whose 1-dimensional marginals have the same distribution as the absolute value of a centered gaussian can also arise as the two-step correlation function of the absolute value of a centered jointly (the key word) gaussian process. We can prove, however, that this is the case provided.

$$\lambda_1 \leq \lambda\left(\frac{1}{\sqrt{2}}\right) \simeq 0.4598$$

Since in most applications λ_1 and λ_2 would be reasonably close to 0, this gap should not arise in practice, if indeed it can arise at all.

A typical run of the program is shown in Fig. 1.

VI. Program Description

A. General Description

This section is essentially a Software Specification Document (SSD) for an MBASIC program CORGS2. The purpose of CORGS2 is the generation of a set of "half-gaussian" random variables (the elements of which are formed by taking the absolute values of the members of a set with a normal distribution) with given one- and two-step correlations. The subsequent numbering refers to module numbers in the structured flowcharts. Three main steps are involved. First, a set of random variables (normal distribution) is produced with mean 0, variance 1. Then these are used to generate a new set of gaussian random variables with known one- and two-step correlations, via a stationary gaussian stochastic process. Finally, the absolute values of these numbers are taken (with the appropriate scaling factor introduced to give the correct standard deviation) to produce our set of half-gaussian random numbers.

B. Level 1 Detailed Description

1.1

This module has two purposes. The first is the declaration of the subroutine addresses for the subprograms of CORGS2. Then input is obtained for N, the number of half-gaussian random variables to be produced by the user response to a prompting message.

Variables:

N: user response to the prompting message, the number of half-gaussians to be generated.

1.2 (ASSIGN)

In this module all necessary variables are declared and the random number generator is initialized to some positive value in order to insure a repeatable sequence of random variables.

1.3 (INPT)

Input is obtained for LAMBDA(1), LAMBDA(2) (the one- and two-step correlations) and sigma (the final scaling factor) by means of user response to prompting messages.

Variables

LAMBDA(1): The one-step correlation of the half-gaussian random variables.

LAMBDA(2): The two-step correlation of the half-gaussian random variables.

SIGMA: The scaling factor which determines the final standard deviation.

1.4 (INDGS)

In this module we generate an array (G01) of gaussian random variables with mean 0, variance 1, by means of two nested loops.

Variable:

G01: A numeric array variable of length N consisting of uncorrelated standard normal random numbers.

1.5 (CORGS)

An array (GRHO) of random numbers is generated with intermediate one-step correlation RHO(1), two-step correlation RHO(2).

Variable:

GRHO: A numeric array of length N consisting of random variables with mean 0, variance 1 and one-step correlation RHO(1), two-step correlation RHO(2).

1.6 (HALFGS)

An array of half-gaussian random numbers (GHALF) is produced with one-step correlation LAMBDA(1), two-step correlation LAMBDA(2).

Variable:

GHALF: A numeric array variable of length N, the "half-gaussian" random variables.

1.7 (PRNT)

A prompting question determines whether the user wants a printout of the array GHALF of half-gaussian random numbers; with an affirmative answer the array GHALF is printed.

Variables:

ANS$: A simple string variable accepting only the initial character of the user's response. ANS$='Y' means output is desired, ANS$='N' means the opposite.

OK: A simple numeric variable, the condition of a correct user response to the prompting question.

See Fig. 2 for flowchart.

C. Level 2 Detailed Design

1.1

The subroutine addresses are first declared as follows: ASSIGN = 100200, INPT = 100300, INDGS = 100500, CORGS = 100600, HALFGS = 100800, PRNT = 100900. Then a prompting message is printed asking for the number of random variables needed. The message is "ENTER N, THE NUMBER OF CORRELATED HALF-GAUSSIAN RANDOM NUMBERS DESIRED:".

Variable defined

N, a simple numeric variable input in 1.1.

1.2 ASSIGN Detailed Design: Level 2

The purpose of ASSIGN is to declare all necessary variables and to initialize the random number generator at a positive value to produce a repeatable sequence of random numbers.

1.2.1 Declare variables with explicit declarations. The declaration of the numeric variables is: Real G01(N), X(N), GRHO(N), GHALF(N), LAMBDA(2), RHO(2), SIGMA, ADJ, OK, R, S. The string declaration is: STRING ANS$:1.

Variable definitions

G01 a numeric array of length N generated in 1.4.1–1.4.3; X, a numeric array of length N generated in 1.5.8–1.5.10; GHALF, a numeric array of length N (consisting entirely of positive numbers) calculated in 1.6.1–1.6.2; LAMBDA, a numeric array of length 2 input in 1.3.1–1.3.2; SIGMA, a simple numeric variable input in 1.3.3; RHO, a numeric array of length 2 calculated in 1.5.1–1.5.4; ADJ, a simple numeric variable defined in 1.5.3; OK, a simple numeric variable defined in 1.7.1 and reevaluated in 1.7.4; ANS$, a simple string variable input in 1.6.3.

1.2.2 Initialize the random number generator with the declaration: RANDOMIZE 518997. Any positive number may be used, but the following should be noted. Large positive numbers seem to give the best results, so six digits are advisable. Also, they should be chosen by some random means, which in this case consisted of choosing cards from a deck, face cards removed, and sampling with replacement.

See Fig. 3 for flowchart.

1.3 INPT Detailed Design: Level 2

In this module we obtain from user, via a series of prompting messages, values which will determine the statistical characteristics of the half-gaussian random variables.

Inputs

A. LAMBDA(1), a numeric variable input in 1.3.1 which must satisfy $0 \leq \text{LAMBDA}(1) \leq 1$.

B. LAMBDA(2), a numeric variable input in 1.3.2 which must also satisfy $0 \leq \text{LAMBDA}(2) \leq 1$.

C. SIGMA, a numeric variable input in 1.3.3 which must be positive.

Outputs

A. Prompting message "ENTER LAMBDA(1), THE ONE-STEP CORRELATION OF THE HALF-GAUSSIAN RANDOM NUMBERS (NOTE THAT LAMBDA(1) MUST BE NON-NEGATIVE AND LESS THAN 1):"

B. Prompting message "ENTER LAMBDA(2), THE TWO-STEP CORRELATION OF THE HALF-GAUSSIAN RANDOM NUMBERS (NOTE THAT LAMBDA(2) MUST BE NON-NEGATIVE AND LESS THAN 1:"

C. Prompting message "ENTER SIGMA, THE STANDARD DEVIATION OF THE FULL-GAUSSIAN DISTRIBUTION (NOTE THAT SIGMA MUST BE POSITIVE):"

1.3.1 Print prompting message A to user asking for the final one-step correlation.

Variable defined

LAMBDA(1), a numeric variable input in 1.3.1.

1.3.2 Print prompting message B to user asking for the final two-step correlation.

Variable defined

LAMBDA(2), a numeric variable input in 1.3.2.

1.3.3 Print prompting message C to user asking for the final scaling factor.

Variable defined

SIGMA, a simple numeric variable input in 1.3.3. The standard deviation of the half-gaussian random variables should be approximately SIGMA*$\sqrt{(1-2/\pi)}$.

See Fig. 4 for flowchart.

1.4 INDGS Detailed Design: Level 2

In this module an array (G01) of gaussian random variables is generated with mean 0, variance 1, by means of two nested loops.

1.4.1 The index I is first initialized to 1. At each execution of the loop it is determined whether I>N; if not, control is passed on to 1.4.2; if the inequality holds, then control is transferred to 1.5.1.

1.4.2 This loop starts with J=1; if J≤12 control is passed to 1.4.3 then back to 1.4.2 where J is incremented by 1, if J>12 control is transferred to 1.4.1.

1.4.3 A random variable is produced with mean 0, variance 1. From an MBASIC random number (RNDM) 1/2 is subtracted to produce a random variable with mean 0, variance 1/2. Each time control is passed from 1.4.2 another of these random variables is added on to the previous result, which increments the variance by 1/12; the basic step is G01(I)=G01(I)+RNDM−1/2. After control is passed to 1.4.3 for the twelfth time, G01 will have variance 1 (and still have mean ϕ). Control is then returned to 1.4.1.

Variable definition

G01, a numeric array variable generated in 1.4.1–1.4.3.

See Fig. 5 for flowchart.

1.5 CORGS Detailed Design: Level 2

The purpose of CORGS is to produce an array (GRHO) with proper one- and two-step correlations so that when the absolute values of the elements of GRHO are taken, the new array has our desired correlations LAMBDA(1) and LAMBDA(2). Therefore we must first determine the correct intermediate correlations (RHO(1) and RHO(2)) which will lead to the final correlations (LAMBDA(1) and LAMBDA(2)), then produce GRHO using the array G01 by means of a stationary stochastic process.

It is possible that the numbers RHO(1) and RHO(2) will not lead to a stationary process; if they do not, an error message will be printed and the program terminated.

Outputs

A. Error message: "LAMBDA(1) AND LAMBDA(2) ARE NOT ACCEPTABLE CORRELATIONS"

B. TERMINATING MESSAGE "CORGS2 TERMINATED"

C. "THE INTERMEDIATE ONE-STEP CORRELATION IS:"

D. "THE INTERMEDIATE TWO-STEP CORRELATION IS:"

1.5.1 Initialize the index I to 1 and pass control to 1.5.2. Control will be passed back to 1.5.1 from 1.5.3 and I is incremented by 1 at that stage; then if I>N, control is transferred to 1.5.4; if not, control is again passed on to 1.5.2.

1.5.2 The correlation RHO(I) is determined for the interval $0 \leq LAMBDA(I) \leq 1/2$ by the formula RHO(I)=SQR(2*ADJ**2−(4/45)*ADJ**3−(11/189)*ADJ**4−(722/14175)*ADJ**5−(.05203)*ADJ**6−(.05087)*ADJ**7) where ADJ=LAMBDA(I)*(π/2−1) (this is the first seven terms of a Taylor series). Control is passed to 1.5.3.

Variable definitions

LAMBDA(I), a numeric variable input in 1.3.1 or 1.3.2; RHO(I), a numeric variable calculated in 1.5.1–1.5.3; ADJ, a simple numeric variable defined in 1.5.2.

1.5.3 RHO(I) is calculated over the interval $.5 < LAMBDA(I) \leq 1$ by the formula RHO(I)=.2862+1.0558*LAMBDA(I)−.0470*LAMBDA(I)**2−.9506*LAMBDA(I)**3+1.0072*LAMBDA(I)**4−.3516*LAMBDA(I)**5. This is the "Lagrange interpolation polynomial" for RHO(I) of degree 5 over [.5,1] with equally spaced points. Control is passed to 1.5.1.

Variable definitions

RHO(I), a numeric variable calculated in 1.5.1–1.5.3; LAMBDA(I), a numeric variable input in 1.3.1 or 1.3.2.

1.5.4 We now use the calculated values of RHO(1), RHO(2), and the array G01 to produce an array GRHO of correlated random variables. This is done by means of a stationary stochastic process and an intermediate array, X, which will give us our array GRHO when its members are normalized. However, if $1+RHO(2)-2*RHO(1)**2 \leq 0$ then the stochastic scheme will not be stationary. In this case, we cannot generate an array of half-gaussians corresponding to the values of LAMBDA originally input, so control is passed to 1.5.5 and the program is terminated. If the correlations are valid (i.e., the above inequality does not hold) then control goes to 1.5.6.

Variable definition

RHO(I), a numeric variable calculated in 1.5.1–1.5.3.

1.5.5 Print error messages A and B, then terminate program.

Variable defined

LAMBDA, a numeric variable input in 1.3.1 and 1.3.2.

1.5.6 Print messages C and D along with RHO(1), and RHO(2) to four-decimal-place accuracy.

Variable defined

RHO, a numeric array variable calculated in 1.5.1–1.5.3.

1.5.7 The first two random variables (G01(1) and G01(2) produced in 1.4.3 must be normalized to begin the stationary stochastic process which will lead to the correlated gaussian array GRHO. We set X(1)=R*G01(1)+S*G01(2), X(2)=R*G01(1)−S*G01(2) where

$$R = \sqrt{(1-RHO(1)**2)*(1+RHO(1))} \Big/ \sqrt{2*(1-RHO(2))*(1+RHO(2)-2*RHO(1)**2)}$$

and

$$S = \sqrt{(1-RHO(1)**2)*(1-RHO(1))} \Big/ \sqrt{2*(1-RHO(2))*(1+RHO(2)-2*RHO(1)**2}.$$

Variable definitions

G01, a numeric array generated in 1.4; GRHO, a numeric array generated in 1.5.10–1.5.11; X, a numeric array generated in 1.5.7–1.5.9; R, S, simple numeric variables defined in 1.5.7.

1.5.8 This loop generates the rest of the array X. The index I is first set to 3, it is increased by one every time control returns from 1.5.9. If I>N control is transferred to 1.5.10, if not, control passes to 1.5.9.

Variable defined

X, a numeric array generated in 1.5.7–1.5.9.

1.5.9 The elements of X are calculated according to the formula X(I)=(RHO(1)*(1−RHO(2))/(1−RHO(1)**2))*X(I−1)+((RHO(2)−RHO(1)**2)/(1−RHO(1)**2))*X(I−2)+G01(I). Control is passed to 1.5.8.

Variable definitions

X, a numeric array generated in 1.5.7–1.5.9; RHO, a numeric array calculated in 1.5.1 to 1.5.3; G01, a numeric array generated in 1.4.

1.5.10 This loop generates the array GRHO. I is set to 1, and each time control is returned to 1.5.11 from 1.5.12 it is increased by 1. If I>N, control passes to 1.6.1; if not, control goes to 1.5.12.

Variable defined

GRHO, a numeric array generated in 1.5.10–1.5.11.

1.5.11 The elements of GRHO are calculated by the formula

$$GRHO(I)=$$

$$\sqrt{(1-RHO(2))*(1+RHO(2)-2*RHO(1)**2)}*$$

$$(1/\sqrt{1-RHO(I)**2})*X(I)$$

Control returns to 1.5.10.

Variable definitions

X, a numeric array generated in 1.5.7–7.5.9; GRHO, a numeric array generated in 1.5.10–1.5.11.

See Fig. 6 for flowchart of 1.5.

1.6 HALFGS Detailed Design: Level 2

In this module we generate the set of half-gaussian random variables with one-step correlation LAMBDA(1), two-step correlation LAMBDA (2). This set will have standard deviation SIGMA*$\sqrt{1-2/\pi}$ after multiplication by the scaling factor SIGMA.

1.6.1 This loop generates the set of half-gaussians. I is set to 1 then increased by 1 when control returns from 1.6.2. If I > N, control goes to 1.7.1, otherwise control passes to 1.6.2.

1.6.2 Each half-gaussian is calculated by the formula GHALF(I)=ABS(SIGMA*GRHO(I)).

Variable definitions

SIGMA, a simple numeric variable input in 1.2.3; GRHO, a numeric array generated in 1.5.11–1.5.12; GHALF, a numeric array generated in 1.6.

See Fig. 7 for flowchart.

1.7 PRNT Detailed Design: Level 2

This module prints out the array GHALF when required by the user.

Input

ANS$, a simple string variable accepting only 1 character. If ANS$='Y', the array GHALF is printed. If ANS$='N', the array is not printed. If ANS$≠'Y' or 'N' an error message is given and the loop is repeated until a correct response is given by the user.

Outputs

A. Prompting message "DO YOU WANT A PRINTOUT OF THE CORRELATED HALF-GAUSSIAN RANDOM NUMBERS? (ANSWER YES OR NO):"

B. Error message "ONLY YES OR NO ANSWERS, PLEASE"

C. Optional message "THE CORRELATED HALF-GAUSSIAN RANDOM NUMBERS ARE"\I, GHALF(I) for I=1 to N (GHALF is the array of half-gaussians)

D. Terminating message "END OF CORGS2"

1.7.1 We set OK=0 and let this be the condition that an incorrect user response has been given (something other than 'Y' or 'N').

Variable definition

OK, a simple numeric variable defined in 1.7.1 and reevaluated in 1.7.4.

1.7.2 We set LOOP=1 and ask if OK=0. If OK=0 then control passes to 1.7.3, otherwise control is transferred to 1.7.7.

Variable definition

OK, a simple numeric variable defined in 1.7.1 and reevaluated in 1.7.4.

1.7.3 Give prompting message A asking whether the user wants a printout of the array GHALF.

Variable definition

GHALF, a numeric array generated in 1.6.

1.7.4 We set OK=1*(ANS$='Y')+2*(ANS$='N'). If OK=0 is still true, the loop will be repeated because a correct user response to A has not been given.

Variable definitions

OK, a simple numeric variable defined in 1.7.1 and reevaluated in 1.7.4; ANS$, a simple string variable input in 1.7.3.

1.7.5 Determine if OK=0. If it does, pass control to 1.7.6; if not, control goes to 1.7.2.

Variable definition

OK, a simple numeric variable defined in 1.7.1 and reevaluated in 1.7.4.

1.7.6 Print error message B and return control to 1.7.2.

1.7.7 If OK=1, control passes to 1.7.8; if OK=2, control goes to 1.7.9.

Variable definition

OK, a simple numeric variable defined in 1.7.1 and reevaluated in 1.7.4.

1.7.8 Print message C, with the array GHALF given to four decimal places.

Variable definition

GHALF, a numeric array generated in 1.6.

1.7.9 Print terminating message D.

See Fig. 8 for flowchart.

```
>RUN


ENTER N, THE NUMBER OF CORRELATED HALF GAUSSIAN NUMBERS DESIRED:  10

ENTER LAMBDA(1), THE ONE-STEP CORRELATION OF THE HALF GAUSSIAN RANDOM
NUMBERS (NOTE THAT LAMBDA(1) MUST BE NON-NEGATIVE AND LESS THAN 1): .53

ENTER LAMBDA(2), THE TWO-STEP CORRELATION OF THE HALF GAUSSIAN RANDOM
NUMBERS (NOTE THAT LAMBDA(2) MUST BE NON-NEGATIVE AND LESS THAN 1): .28

ENTER SIGMA, THE STANDARD DEVIATION OF THE FULL GAUSSIAN DISTRIBUTION (NOTE
THAT SIGMA MUST BE POSITIVE): 3.1

THE INTERMEDIATE ONE-STEP CORRELATION IS:  0.7558

THE INTERMEDIATE TWO-STEP CORRELATION IS:  0.5574

DO YOU WANT A PRINTOUT OF THE CORRELATED HALF GAUSSIAN DISTRIBUTION?
(ANSWER YES OR NO): YES

THE CORRELATED HALF GAUSSIAN RANDOM NUMBERS ARE

   1       .7006
   2      1.1159
   3       .6289
   4      2.0626
   5      1.7033
   6      2.6059
   7      3.6343
   8      1.8570
   9      3.0022
  10      2.3408

END OF CORGS2
```

Fig. 1. Typical CORGS2 run

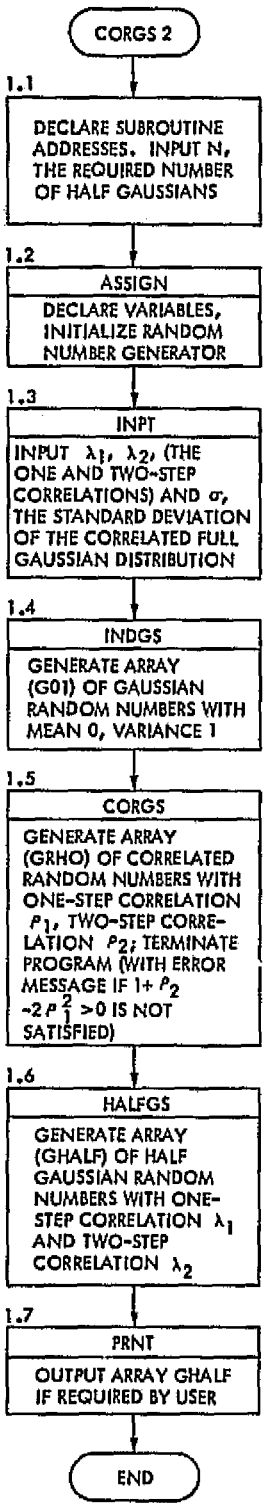

Fig. 2. CORGS2 Level 1 flowchart

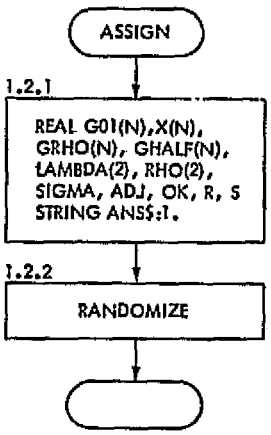

Fig. 3. Module 1.2 flowchart

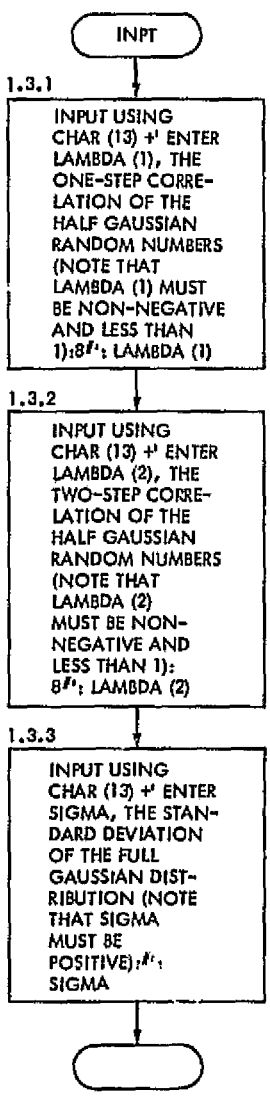

Fig. 4. Module 1.3 flowchart

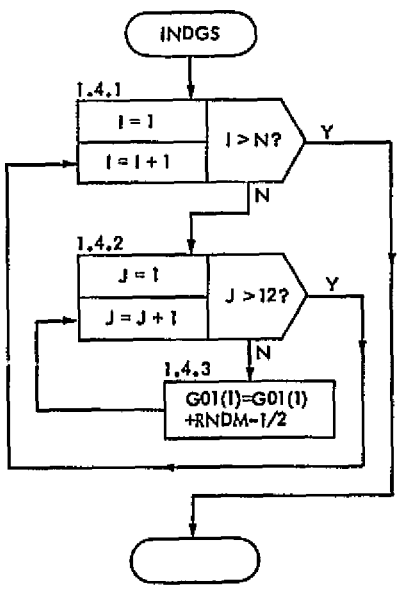

Fig. 5. Module 1.4 flowchart

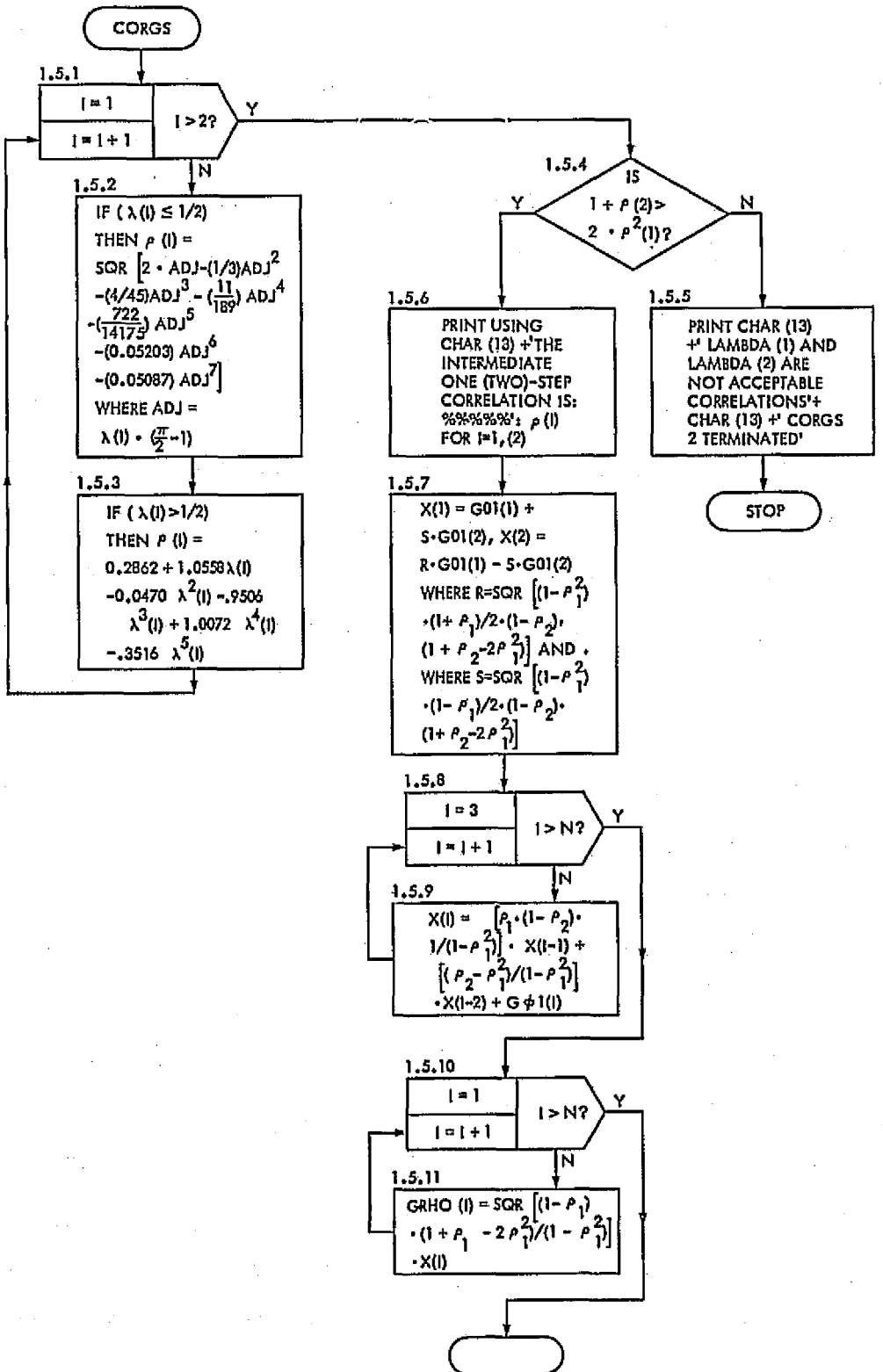

Fig. 6. Module 1.5 flowchart

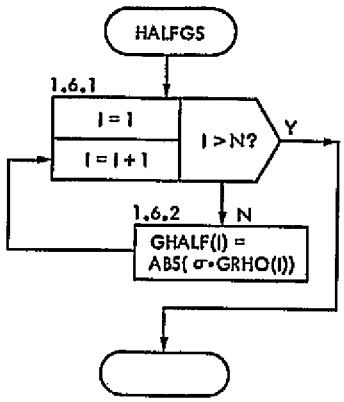

Fig. 7. Module 1.6 flowchart

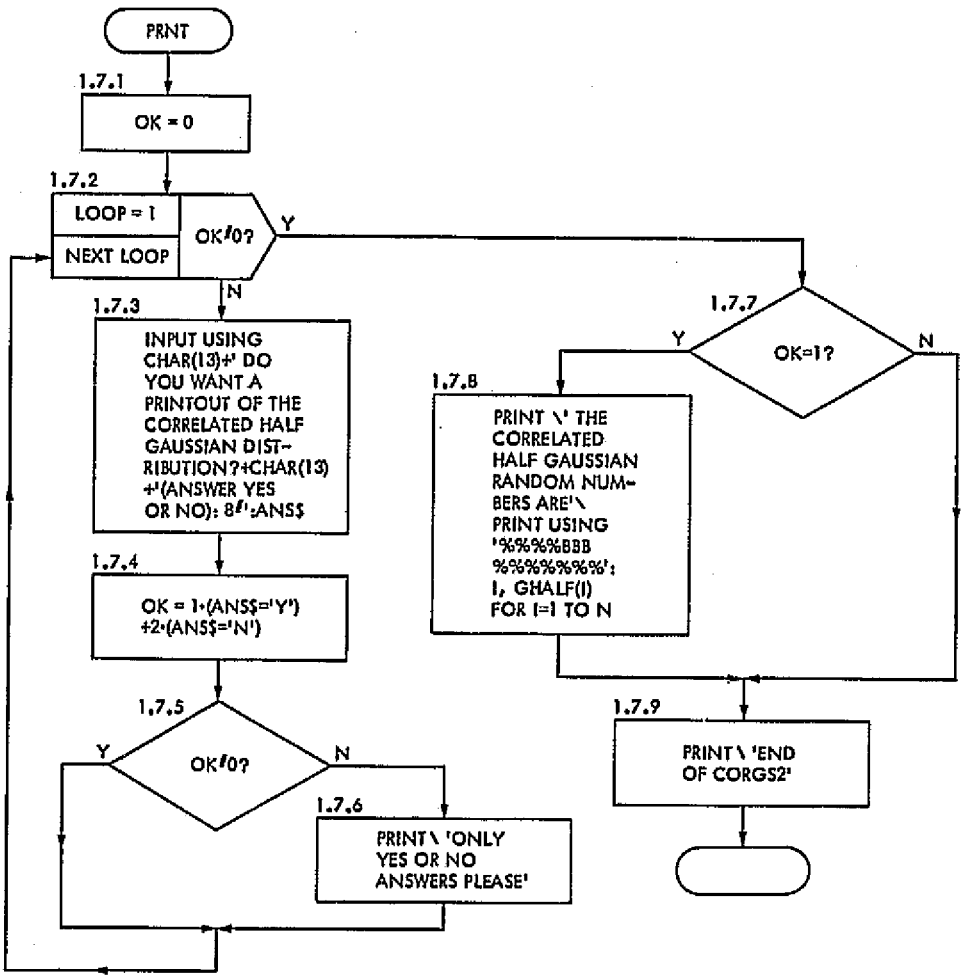

Fig. 8. Module 1.7 flowchart

```
100010   !CORGS2---MODULE 1

100020     ASSIGN=100200, INPT=100300, INDGS=100500, CORGS=100600,
             HALFGS=100800, PRNT=100900
100030     !NPUT USING CHAR(13)+CHAR(13)+'ENTER N, THE NUMBER OF CORRELATED'
             +' HALF GAUSSIAN NUMBERS DESIRED:#  ':N      !MODULE #1.1

100040     GOSUB ASSIGN        !MODULE #1.2
100050     GOSUB INPT          !MODULE #1.3
100060     GOSUB INDGS         !MODULE #1.4
100070     GOSUB CORGS         !MODULE #1.5
100080     GOSUB HALFGS        !MODULE #1.6
100090     GOSUB PRNT          !MODULE #1.7

100100     END                 !END MODULE #1


100200   !ASSIGN-DECLARE VARIABLES; INITIALIZE RANDOM NUMBER GENERATOR
           ---MODULE #1.2

100210     REAL G01 (N), X(N), GRHO(N), GHALF(N), LAMBDA(2), RHO(2), SIGMA
             ADJ, OK, R, S
100220     STRING ANS$:1       !MODULE #1.2.1

100230     RANDOMIZE 518997    !MODULE #1.2.2

100240     RETURN              !END MODULE #1.2


100300   !INPT-ENTER PROGRAM PARAMETERS---MODULE #1.3

100310     INPUT USING CHAR(13)+'ENTER LAMBDA(1), THE ONE-STEP CORRELATION'
             +' OF THE HALF GAUSSIAN RANDOM'+CHAR(13)+'NUMBERS (NOTE THAT'
             +' LAMBDA(1) MUST BE NON-NEGATIVE AND LESS THAN 1): 8#':LAMBDA(1)
             !MODULE #1.3.1

100320     INPUT USING CHAR(13)+'ENTER LAMBDA(2), THE TWO-STEP CORRELATION'
             +' OF THE HALF GAUSSIAN RANDOM'+CHAR(13)+'NUMBERS (NOTE THAT'
             +' LAMBDA(2) MUST BE NON-NEGATIVE AND LESS THAN 1): 8#':LAMBDA(2)
             !MODULE #1.3.2

100330     INPUT USING CHAR(13)+'ENTER SIGMA, THE STANDARD DEVIATION OF THE'
             +' FULL GAUSSIAN DISTRIBUTION (NOTE'+CHAR(13)+'THAT SIGMA MUST'
             +' BE POSITIVE):  #':SIGMA      !MODULE #1.3.3

100340     RETURN       !END MODULE #1.3
```

Fig. 9. CORGS2 listing

```
100500    !NDGS-GENERATE ARRAY OF RANDOM NUMBERS (NORMAL DISTRIBUTION)
            WITH MEAN 0, VARIANCE 1---MODULE#1.4

100510      G01(I)=G01 (I)+RNDM-1/2 FOR J=1 TO 12  FOR I=1 TO N
              MODULES #1.4.1,.2,.3

100520      RETURN      !END MODULE #1.4


100600    !CORGS-GENERATE ARRAY OF RANDOM NUMBERS (NORMAL DISTRIBUTION)
            WITH MEAN 0, VARIANCE 1; ALSO WITH ONE-STEP CORRELATION RHO(1),
            AND TWO-STEP CORRELATION RHO(2)---MODULE #1.5

100610      FOR I=1 TO 2        MODULE#1.5.1

100620        IF (LAMBDA(I)<=1/2) THEN
                RHO(I)=SQR(2*ADJ-(1/3)*ADJ**2-(4/45)*ADJ**3-(11/189)*ADJ**4
                -(722/14175)*ADJ**5-(.05203)*ADJ**6-(.05087)*ADJ**7)
                  WHERE ADJ=LAMBDA(I)*(PI/2-1)       !MODULE #1.5.2

100630        IF (LAMBDA(I)>1/2)  THEN
                RHO(I)=.2862+1.0558*LAMBDA(I)-.0470*LAMBDA(I)**2
                -.9506*LAMBDA(I)**3+1.0072*LAMBDA(I)**4-.3516*LAMBDA(I)**5
                  MODULE #1.5.3

100640      NEXT I

100650      IF (1+RHO(2)-2*RHO(1)**2<=0) THEN STOP CHAR(13)+
              'LAMBDA(1) AND LAMBDA(2) ARE NOT ACCEPTABLE CORRELATIONS'+CHAR(13)+
              'CORGS2 TERMINATED'       !MODULES #1.5.4,.5

100660      PRINT USING CHAR(13)+'THE INTERMEDIATE ONE-STEP CORRELATION IS:'
              +' %.%%%%%%':RHO(1)
100670      PRINT  USING CHAR(13)+'THE INTERMEDIATE TWO-STEP CORRELATION IS:'
              +'%.%%%%%%':RHO(2)        !MODULE #1.5.6

100680      R=SQR((1-RHO(1)**2)*(1+RHO(1))/2*(1-RHO(2))*(1+RHO(2)-2*RHO(1)**2))
100690      S=SQR((1-RHO(1)**2)*(1-RHO(1))/2*(1-RHO(2))*(1+RHO(2)-2*RHO(1)**2))
100700      X(1)=R*G01(1)+S*G01(2)
100710      X(2)=R*G01(1)-S*G01(2)      !MODULE #1.5.7

100720      X(I)=G01(I)+(RHO(1)*(1-RHO(2))/(1-RHO(1)**2))*X(I-1)+
              ((RHO(2)-RHO(1)**2)/(1-RHO(1)**2))*X(I-2)  FOR I=3 TO N
                MODULES #1.5.8,.8

100730      GHRO(1)=SQR((1-RHO(2))*(1+RHO(2)-2*RHO(1)**2)/(1-RHO(1)**2))*X(1)
              FOR I=1 TO N   !MODULES #1.5.10,.11

100740      RETURN      !END MODULE #1.5
```

Fig. 9 (contd)

```
100800    HALFGS-GENERATE ARRAY OF CORRELATED HALF GAUSSIAN RANDOM NUMBERS
            ---MODULE #1.6

100810      GHALF(I)=ABS(SIGMA*GRHO(I))  FOR I=1 TO N

100820      RETURN      !END MODULE #1.6


100900    PRNT-GENERATES OUTPUT WHEN REQUESTED---MODULE #1.7

100910      FOR LOOP=1 UNTIL OK WHERE OK=0       MODULES #1.7.1,.2

100920        INPUT USING CHAR(13)+'DO YOU WANT A PRINTOUT OF THE CORRELATED'
                +' HALF GAUSSIAN DISTRIBUTION?'+CHAR(13)+'(ANSWER YES OR'
                +' NO):  #':ANS$      !MODULE #1.6.3

100930        OK=1*(ANS$='Y')+2*(ANS$='N')      !MODULE #1.6.4
100940        IF (NOT OK) THEN PRINT\'ONLY YES OR NO ANSWERS, PLEASE'
                MODULES 1.7.5,.6

100950      NEXT LOOP       !MODULE #1.7.2

100960      IF OK=1 THEN PRINT\' THE CORRELATED HALF GAUSSIAN RANDOM NUMBERS ARE'\
              ELSE GO TO 100980

100970      PRINT USING'%%%%%%  %%%%.%%%%':I, GHALF(I)  FOR I=1 TO N
              MODULES #1.7.7,.8

100980      !DECISION COLLECTOR NODE FOR 100960

100990      PRINT\'END OF CORGS2'       !MODULE #1.7.9

101000      RETURN      !END MODULE #1.7
```

Fig. 9 (contd)